

**Document Version**

Final published version

**Citation (APA)**

van Hattem, A. (2026). *Chemistry of irradiated fuel-coolant interaction in lead-cooled fast reactors: A structural and thermodynamic study*. [Dissertation (TU Delft), Delft University of Technology]. <https://doi.org/10.4233/uuid:88376c91-8d57-4d3c-9e94-e972de4e64b6>

**Important note**

To cite this publication, please use the final published version (if applicable).  
Please check the document version above.

**Copyright**

In case the licence states "Dutch Copyright Act (Article 25fa)", this publication was made available Green Open Access via the TU Delft Institutional Repository pursuant to Dutch Copyright Act (Article 25fa, the Taverne amendment). This provision does not affect copyright ownership.  
Unless copyright is transferred by contract or statute, it remains with the copyright holder.

**Sharing and reuse**

Other than for strictly personal use, it is not permitted to download, forward or distribute the text or part of it, without the consent of the author(s) and/or copyright holder(s), unless the work is under an open content license such as Creative Commons.

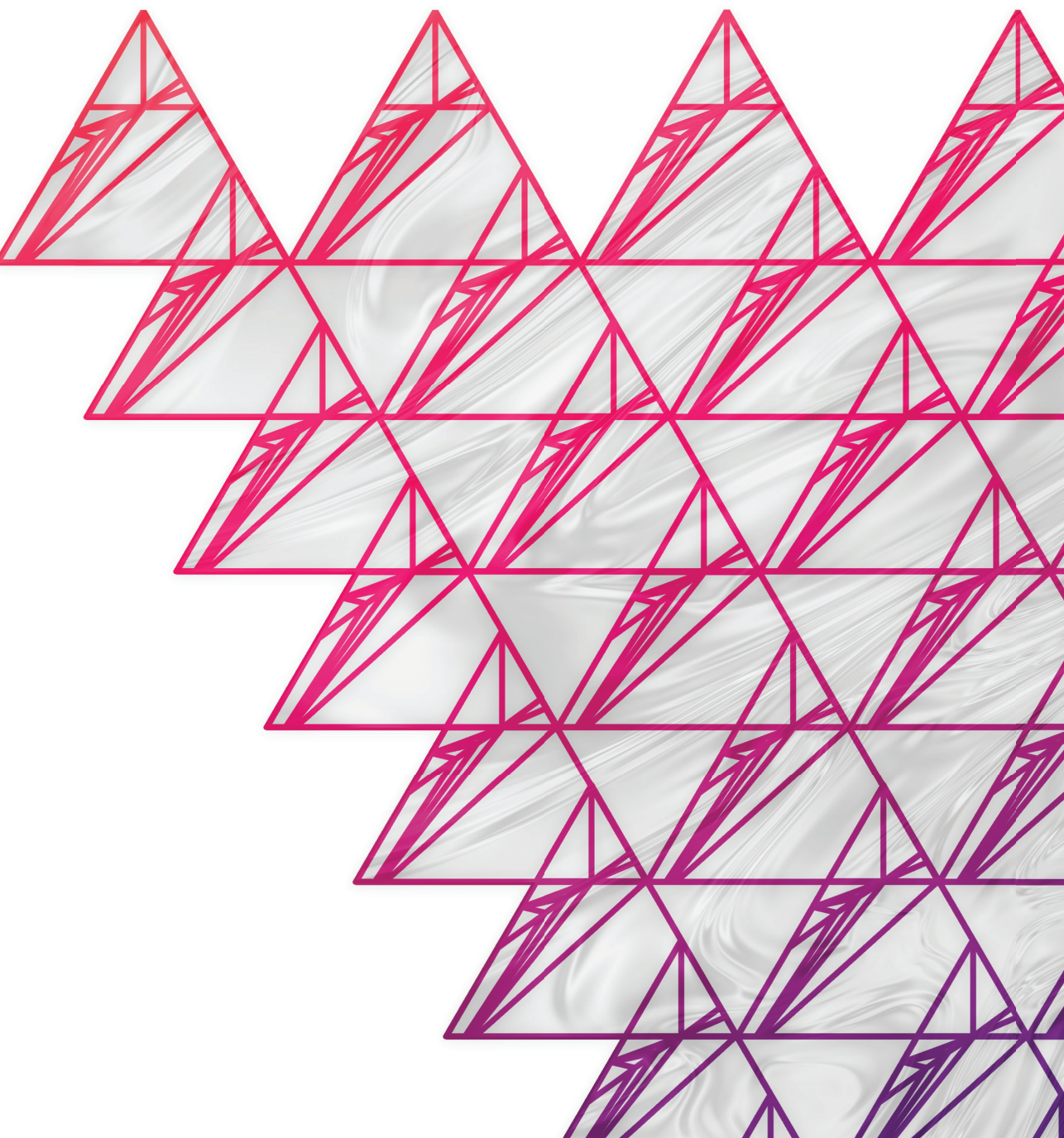
**Takedown policy**

Please contact us and provide details if you believe this document breaches copyrights.  
We will remove access to the work immediately and investigate your claim.

# **CHEMISTRY OF IRRADIATED FUEL-COOLANT INTERACTION IN LEAD-COOLED FAST REACTORS**

A STRUCTURAL AND THERMODYNAMIC STUDY

Andries van Hattem





**CHEMISTRY OF IRRADIATED FUEL-COOLANT  
INTERACTION IN LEAD-COOLED FAST REACTORS**

A STRUCTURAL AND THERMODYNAMIC STUDY



# **CHEMISTRY OF IRRADIATED FUEL-COOLANT INTERACTION IN LEAD-COOLED FAST REACTORS**

A STRUCTURAL AND THERMODYNAMIC STUDY

## **Proefschrift**

ter verkrijging van de graad van doctor  
aan de Technische Universiteit Delft,  
op gezag van de Rector Magnificus prof. dr. ir. H. Bijl  
voorzitter van het College voor Promoties,  
in het openbaar te verdedigen op maandag 9 februari 2026 om 10:00 uur

door

**Andries VAN HATTEM**

Master of Science in Chemische wetenschappen,  
Universiteit Utrecht, Nederland  
geboren te Elburg, Nederland.

Dit proefschrift is goedgekeurd door de promotoren.

Samenstelling promotiecommissie:

Rector magnificus	voorzitter
prof. dr. R.J.M. Konings	TU Delft, promotor
dr. A.L. Smith	TU Delft, promotor

*Onafhankelijke leden:*

em. prof. dr. P. Dorenbos	TU Delft
prof. dr. F.M.F. de Groot	Universiteit Utrecht
dr. C. Guéneau	Université Paris-Saclay
dr. G.L. Murphy	Forschungszentrum Jülich
dr. M. Verwerft	SCK-CEN
prof. dr. E.H. Brück	TU Delft, reservelid



*Keywords:* Physical chemistry, LFR, JOG-phase, Fission product chemistry

*Printed by:* ProefschriftMaken

*Front & Back:* Jozua Koffeman

*Funding:* This research was performed in the Reactor Physics & Nuclear Materials group of the department Radiation Science & Technology, faculty Applied Physics, Delft University of Technology.

This work has received funding from the Euratom research and training programme 2019-2020 through the research project PASCAL (Proof of Augmented Safety Conditions in Advanced Liquid-metal-cooled systems) under grant agreement N<sup>o</sup> 945341.

The Institute for Beam Physics and Technology is acknowledged for the operation of the Karlsruhe Research Accelerator at the INE and CAT-ACT beamline at the KIT Light Source.

Data reported herein were partially generated at the JRC Karlsruhe of the European Commission via ActUsLab projects PACIFIED-LFR, PARTICULAR (N<sup>o</sup> 36345/01 and 36345/02) and REPUBLIC (N<sup>o</sup> 36619/07).

Copyright © 2026 by A. van Hattem

ISBN 978-94-6534-149-1

An electronic version of this dissertation is available at  
<http://repository.tudelft.nl/>.

Voor Jenthe en Gemma

Voor Sandra

Voor mijn ouders



# CONTENTS

<b>Samenvatting</b>	<b>xi</b>
<b>Summary</b>	<b>xiii</b>
<b>Preface</b>	<b>xv</b>
<b>1 Introduction</b>	<b>1</b>
1.1 Chemistry of the fast-spectrum nuclear fuel pin . . . . .	1
1.2 Lead-cooled fast reactors . . . . .	4
1.3 Cladding failure in lead-cooled fast reactors . . . . .	7
1.3.1 Research questions . . . . .	8
1.3.2 Methods and scope . . . . .	8
1.3.3 Thesis outline . . . . .	9
<b>2 Methodology</b>	<b>13</b>
2.1 Synthesis . . . . .	14
2.2 X-ray and neutron diffraction . . . . .	14
2.3 X-ray absorption spectroscopy . . . . .	15
2.3.1 XAS at the Mo <i>K</i> -edge . . . . .	15
2.3.2 XAS at the Pu <i>L</i> <sub>3</sub> - and <i>M</i> <sub>5</sub> -edges . . . . .	15
2.4 Differential scanning calorimetry . . . . .	17
2.5 Solution calorimetry . . . . .	17
2.6 Thermal-relaxation calorimetry . . . . .	18
2.7 Magnetometry using SQUID-VSM . . . . .	20
2.8 Thermodynamic modelling . . . . .	20
<b>3 The Pb-Mo-O system</b>	<b>25</b>
3.1 Introduction and context . . . . .	26
3.2 Review of literature data on the Pb-Mo-O system . . . . .	26
3.2.1 Constituting binary sub-systems . . . . .	26
3.2.2 Structural data for the ternary Pb-Mo-O phases . . . . .	28
3.2.3 Thermodynamic data for ternary Pb-Mo-O phases . . . . .	29
3.2.4 Phase diagram data in the Pb-Mo-O system . . . . .	32
3.2.5 Thermodynamic modelling . . . . .	32
3.2.6 Thermal expansion studies . . . . .	32
3.3 Experimental results . . . . .	33
3.3.1 Structural analysis . . . . .	33
3.3.2 X-ray absorption spectroscopy at the Mo <i>K</i> -edge . . . . .	33
3.3.3 Thermal expansion of PbMoO <sub>4</sub> and Pb <sub>2</sub> MoO <sub>5</sub> . . . . .	35
3.3.4 Melting enthalpy of PbMoO <sub>4</sub> . . . . .	36
3.3.5 Low-temperature heat capacity of PbMoO <sub>4</sub> and Pb <sub>2</sub> MoO <sub>5</sub> . . . . .	36

3.4	Thermodynamic modelling . . . . .	37
3.4.1	Development of model. . . . .	37
3.4.2	Optimised model . . . . .	42
3.5	Summary and recommendations . . . . .	47
	Experimental details . . . . .	47
<b>4</b>	<b>The Pb-Cs-Mo-O system</b>	<b>55</b>
4.1	Introduction . . . . .	56
4.2	Structural characterisation of $\alpha$ -Cs <sub>2</sub> Pb(MoO <sub>4</sub> ) <sub>2</sub> . . . . .	57
4.3	Structural characterisation of $\beta$ -Cs <sub>2</sub> Pb(MoO <sub>4</sub> ) <sub>2</sub> . . . . .	61
4.4	Thermal expansion of Cs <sub>2</sub> Pb(MoO <sub>4</sub> ) <sub>2</sub> . . . . .	63
4.5	X-ray absorption spectroscopy at the Mo K-edge . . . . .	66
4.6	Phase equilibria in the Cs <sub>2</sub> MoO <sub>4</sub> -PbMoO <sub>4</sub> phase diagram. . . . .	67
4.6.1	Transition temperatures of the end-members and intermediate compound Cs <sub>2</sub> Pb(MoO <sub>4</sub> ) <sub>2</sub> . . . . .	67
4.6.2	Solid solubility . . . . .	68
4.6.3	Phase diagram equilibria in the Cs <sub>2</sub> MoO <sub>4</sub> -PbMoO <sub>4</sub> section . . . . .	70
4.7	Thermodynamic properties of $\alpha$ -Cs <sub>2</sub> Pb(MoO <sub>4</sub> ) <sub>2</sub> . . . . .	71
4.7.1	Enthalpy of formation at 298.15 K . . . . .	71
4.7.2	Low-temperature heat capacity and standard entropy . . . . .	74
4.8	Conclusions. . . . .	76
	Experimental details . . . . .	76
<b>5</b>	<b>The compound CsBi(MoO<sub>4</sub>)<sub>2</sub></b>	<b>83</b>
5.1	Introduction . . . . .	84
5.2	X-ray absorption spectroscopy at the Mo K-edge . . . . .	85
5.3	Solving the room-temperature crystal structure. . . . .	86
5.3.1	Towards understanding the antiferroelectric phase . . . . .	86
5.3.2	Crystal structure and antiferroelectricity mechanism . . . . .	87
5.4	Temperature dependence of crystal properties . . . . .	95
5.5	Conclusions. . . . .	96
	Experimental details . . . . .	97
<b>6</b>	<b>The CsI-PbI<sub>2</sub>-BiI<sub>3</sub> system</b>	<b>101</b>
6.1	Introduction . . . . .	102
6.2	Literature review . . . . .	103
6.2.1	The CsI-BiI <sub>3</sub> system . . . . .	103
6.2.2	The CsI-PbI <sub>2</sub> system . . . . .	104
6.2.3	The BiI <sub>3</sub> -PbI <sub>2</sub> system . . . . .	105
6.2.4	The ternary phase field CsI-PbI <sub>2</sub> -BiI <sub>3</sub> . . . . .	105
6.2.5	Data used for thermodynamic modelling . . . . .	105
6.3	Characterisation of synthesised ternary salts . . . . .	107
6.4	Low-temperature heat capacity. . . . .	108
6.4.1	Low-temperature heat capacity of $\delta$ -CsPbI <sub>3</sub> . . . . .	108
6.4.2	Low-temperature heat capacity of Cs <sub>4</sub> PbI <sub>6</sub> . . . . .	112
6.4.3	Low-temperature heat capacity of Cs <sub>3</sub> Bi <sub>2</sub> I <sub>9</sub> . . . . .	112

6.5	Phase transition determinations of the end members and compounds . . .	120
6.6	Binary phase diagrams: calorimetric measurements and modelling . . .	120
6.6.1	The binary system CsI-BiI <sub>3</sub> . . . . .	121
6.6.2	The binary system CsI-PbI <sub>2</sub> . . . . .	122
6.6.3	The binary system BiI <sub>3</sub> -PbI <sub>2</sub> . . . . .	123
6.7	Ternary phase diagram studies: modelling and experiments . . . . .	125
6.7.1	Ternary eutectic equilibria . . . . .	126
6.7.2	The pseudo-binary section Cs <sub>3</sub> Bi <sub>2</sub> I <sub>9</sub> -CsPbI <sub>3</sub> . . . . .	126
6.7.3	The ternary system: miscellaneous points . . . . .	127
6.8	Conclusions. . . . .	129
	Experimental details . . . . .	130
<b>7</b>	<b>The BaO-deficient Ba<sub>3</sub>PuO<sub>6</sub> compound</b>	<b>139</b>
7.1	Introduction . . . . .	140
7.2	Results and discussion . . . . .	142
7.2.1	The oxidation state of Pu. . . . .	143
7.2.2	The Ba:Pu ratio. . . . .	144
7.2.3	Physical property measurements . . . . .	152
7.3	Conclusions. . . . .	157
	Experimental details . . . . .	158
<b>8</b>	<b>Conclusions and outlook</b>	<b>167</b>
8.1	Coolant-JOG interaction for Pb-cooled systems. . . . .	167
8.2	Coolant-JOG interaction for LBE-cooled systems . . . . .	174
8.3	Coolant-volatile fission product interaction. . . . .	174
8.4	Coolant-grey phase interaction . . . . .	176
8.5	General implications and outlook. . . . .	177
	<b>Acknowledgements</b>	<b>181</b>
<b>A</b>	<b>Supporting information to the Pb-Mo-O system</b>	<b>185</b>
<b>B</b>	<b>Experimental data in the CsI-PbI<sub>2</sub>-BiI<sub>3</sub> system</b>	<b>193</b>
<b>C</b>	<b>Thermodynamic model of the CsI-PbI<sub>2</sub>-BiI<sub>3</sub> system</b>	<b>203</b>
<b>D</b>	<b>Supporting information to BaO-deficient Ba<sub>3</sub>PuO<sub>6</sub></b>	<b>213</b>
	<b>Curriculum vitae- NL</b>	<b>219</b>
	<b>Curriculum vitae- EN</b>	<b>221</b>
	<b>List of publications</b>	<b>223</b>



# SAMENVATTING

Kernreactoren met een snel neutronenspectrum kunnen koolstofvrij energie opwekken uit splijtbare uranium en plutonium isotopen met een beter gebruik van de brandstof vergeleken met de momenteel gebruikte lichtwaterreactoren, waarmee ze bijdragen aan het sluiten van de nucleaire brandstofcyclus. Het toegenomen brandstofgebruik beïnvloedt de chemie van de brandstofstaaf; het leidt onder meer tot de vorming van de zogenaamde JOG-laag (joint-oxyde gaine, Frans voor de verbinding tussen de oxide-brandstof en de metalen bekleding). Deze fase benaderen we chemisch als  $\text{Cs}_2\text{MoO}_4$ . In tegenstelling tot conventionele lichtwaterreactoren worden vloeibare metalen gebruikt als koelmiddel om het snelle neutronenspectrum te accommoderen. In deze dissertatie worden vloeibaar lood (Pb) en lood-bismuth eutectic (LBE), een vloeibaar mengsel van lood en bismuth, beschouwd. De klasse reactoren die deze koelmiddelen gebruikt staat bekend als loodgekoelde snelle reactoren (LFRs, van het Engelse 'lead-cooled fast reactors'). Deze dissertatie bestudeert chemische interacties die kunnen plaatsvinden tussen koelmiddel en splijtingsproducten als gevolg van het falen van de bekleding in LFRs, waarbij het eerst focust op de interactie tussen het koelmiddel en de JOG-laag. Andere belangrijke splijtingsproducten om te bestuderen zijn cesium (Cs) en jodium (I), zogenaamde vluchtige splijtingsproducten en barium (Ba), dat aanwezig is in de zogenaamde grijze fase. In deze dissertatie wordt de methode van de chemische thermodynamica gebruikt, die complementair is aan onderzoek van bestraalde monsters, kinetische studies en studies naar het vrijkomen van materiaal.

Chemische thermodynamica draait om een juiste beschrijving van de Gibbsenergie van de mogelijke fases. Deze beschrijving van de Gibbsenergie bevat beschikbare experimentele data. Belangrijke verbindingen worden meestal gesynthetiseerd via vastestofsynthese. Hun karakterisatie geschiedt met Röntgen- en neutronendiffractie bij verschillende temperaturen, en soms ook Röntgenabsorptiespectroscopie. Na karakterisatie worden thermodynamische eigenschappen als vormingswarmte en standaard entropie bepaald. Fasediagrammen worden gemeten met differentiële scanning calorimetrie om faseovergangen te bestuderen en de aggregatietoestand van mengsels in de (compositie, temperatuur)-ruimte te kennen. De verkregen thermodynamische data worden gebruikt om thermochemische berekeningen uit te voeren of om thermodynamische modellen te ontwikkelen via de zogeheten CALPHAD methode.

In dit werk wordt de mogelijkheid van chemische interactie tussen het Pb-koelmiddel en de JOG-laag bestudeerd. Thermodynamische eigenschappen van de verbindingen  $\text{PbMoO}_4$ ,  $\text{Pb}_2\text{MoO}_5$  en  $\text{Cs}_2\text{Pb}(\text{MoO}_4)_2$ , zoals standaard entropie, vormingswarmte en smeltwarmte zijn experimenteel bepaald. Hierop gebaseerd is een compleet thermodynamisch model van het Pb-Mo-O systeem ontwikkeld, met daarin  $\text{PbMoO}_4$ ,  $\text{Pb}_2\text{MoO}_5$  en  $\text{Pb}_5\text{MoO}_8$  met behulp van computationele thermodynamische software (ThermoCalc). Uiteindelijk laten thermodynamische berekeningen zien dat  $\text{Cs}_2\text{Pb}(\text{MoO}_4)_2$ ,  $\text{PbMoO}_4$ ,  $\text{Pb}_2\text{MoO}_5$  en  $\text{Pb}_5\text{MoO}_8$  kunnen vormen in bedrijfscondities van LFRs. Anders gezegd:

deze stoffen kunnen vormen bij de typische zuurstofconcentraties aanwezig in het koelmiddel. Hiernaast zijn de thermische uitzetting en Mo-oxidatietoestand van  $\text{PbMoO}_4$ ,  $\text{Pb}_2\text{MoO}_5$  en  $\text{Cs}_2\text{Pb}(\text{MoO}_4)_2$  gemeten, zodat bijvoorbeeld de mechanische interactie van deze fasen na vorming beoordeeld kan worden.

De verbinding  $\text{CsBi}(\text{MoO}_4)_2$  is bestudeerd als een mogelijk vormingsproduct tussen LBE en de JOG-laag. Een oud vraagstuk rondom de kristalstructuur van deze verbinding is opgelost met neutronendiffractie. De thermische uitzetting van  $\text{CsBi}(\text{MoO}_4)_2$  werd bepaald.

Om de interactie tussen koelmiddel en vluchtige splijtingsproducten te beoordelen is het systeem CsI-PbI<sub>2</sub>-BiI<sub>3</sub> experimenteel bestudeerd. De warmtecapaciteit bij lage temperatuur van de drie verbindingen in het systeem,  $\text{CsPbI}_3$ ,  $\text{Cs}_4\text{PbI}_6$  en  $\text{Cs}_3\text{Bi}_2\text{I}_9$  werd bepaald en de standaard entropiën werden berekend. De fase diagrammen CsI-PbI<sub>2</sub>, CsI-BiI<sub>3</sub> en PbI<sub>2</sub>-BiI<sub>3</sub> werden gemeten met differentiële scanning calorimetrie. Een thermodynamisch model werd ontwikkeld om het *liquidus*-oppervlak van het CsI-PbI<sub>2</sub>-BiI<sub>3</sub> te voorspellen. De accuraatheid van het model werd bevestigd met geselecteerde metingen van de ternaire eutectische punten en het pseudo-binaire systeem  $\text{CsPbI}_3$ - $\text{Cs}_3\text{Bi}_2\text{I}_9$ .

Een studie van de interactie tussen het splijtingsproduct uit de grijze fase, Ba, brandstof en koelmiddel werd gestart. Tijdens dit werk werd een BaO-deficiënte, plutonium-bevattende perovskietfase met een compositie dicht bij  $\text{Ba}_3\text{PuO}_6$  gesynthetiseerd. De kristalstructuur van deze verbinding werd bestudeerd, evenals de faseovergangen bij hoge temperatuur. De standaardentropie en de magnetische susceptibiliteit van deze verbinding werden experimenteel bepaald. Dit werk, waardevol in zichzelf als bijdrage aan het begrijpen van de bestraalde nucleaire brandstofstaaf, is nodig als bouwblok voor de studie van de interactie tussen het koelmiddel en de grijze fase.

Samenvattend beschrijft deze dissertatie potentiële chemische interactieproducten in het scenario dat de bekleding rond de brandstof in loodgekoelde reactoren faalt. In het afsluitende hoofdstuk wordt getoond dat de zuurstofconcentratie die aanwezig is onder bedrijfsmatige omstandigheden de vorming van verschillende complexe oxideverbindingen toestaat in het scenario van Pb-JOG interactie. In het algemeen voorziet dit werk in nieuwe en noodzakelijke data om de stabiliteit van jodide en oxide verbindingen te beoordelen. De resultaten uit deze dissertatie moeten gecombineerd worden met onderzoek van bestraalde monsters en kinetische studies om het scenario van het falen van de bekleding vanuit verschillende perspectieven te beoordelen.

# SUMMARY

Fast-neutron spectrum nuclear reactors allow generating carbon-free energy from fissionable uranium and plutonium isotopes with increased fuel utilisation compared to currently used light-water reactors (LWRs), whereby they contribute to closing the nuclear fuel cycle. The increased fuel utilisation influences the chemistry of the fuel pin, leading among others to the formation of the so-called JOG-layer (joint oxide-gaine, French for the connecting layer between the oxide fuel and cladding material). This JOG-phase is chemically approximated as  $\text{Cs}_2\text{MoO}_4$ . Unlike conventional LWRs, liquid metals are used as coolant to accommodate the fast-neutron spectrum. In this work, liquid lead (Pb) and lead-bismuth eutectic (LBE), a liquid mixture of lead and bismuth (Bi) are considered. The class of reactors using these coolants and a fast neutron spectrum is known as Lead-cooled Fast Reactors (LFRs). This dissertation studies chemical interactions that can occur between coolant and fission products following cladding failure in LFRs, first focussing on the interaction between coolant and JOG-layer. Other important fission products to assess are cesium (Cs) and iodine (I), so-called volatile fission products and barium (Ba), present in the so-called grey phase. It uses the chemical thermodynamics approach, as complementary to post-irradiation examinations and kinetic and release studies.

Chemical thermodynamics centres around a proper description of the Gibbs energy of the possible phases. This Gibbs energy description is informed by available experimental data. Important compounds are typically synthesised using solid state synthesis. Their characterisation involves X-ray and neutron diffraction at ambient and non-ambient temperatures, along with X-ray absorption spectroscopy. After the characterisation, thermodynamic properties like the enthalpy of formation and standard entropy are determined. Phase diagrams are measured using differential scanning calorimetry to study phase transition points and know the aggregation state of mixtures in (composition, temperature)-space. The acquired thermodynamic data are used to perform thermochemical calculations or to develop thermodynamic models using the so-called CALPHAD approach.

In this work, the possibility of chemical interaction between Pb-coolant and JOG-layer was studied. Thermodynamic properties of the compounds  $\text{PbMoO}_4$ ,  $\text{Pb}_2\text{MoO}_5$  and  $\text{Cs}_2\text{Pb}(\text{MoO}_4)_2$ , such as standard entropy, enthalpy of formation and melting enthalpy were determined experimentally. Based on this, a complete thermodynamic model of the Pb-Mo-O system, including  $\text{PbMoO}_4$ ,  $\text{Pb}_2\text{MoO}_5$  and  $\text{Pb}_5\text{MoO}_8$  was developed using computational thermochemical software (ThermoCalc). Finally, thermodynamic calculations show that  $\text{Cs}_2\text{Pb}(\text{MoO}_4)_2$ ,  $\text{PbMoO}_4$ ,  $\text{Pb}_2\text{MoO}_5$  and  $\text{Pb}_5\text{MoO}_8$  can form in LFR operating conditions *i.e.* with typical oxygen concentrations present in the coolant. Next to this, thermal expansion and Mo-oxidation state of  $\text{PbMoO}_4$ ,  $\text{Pb}_2\text{MoO}_5$  and  $\text{Cs}_2\text{Pb}(\text{MoO}_4)_2$  were measured, in order to for example assess the mechanical interaction of these phases after formation.

The compound  $\text{CsBi}(\text{MoO}_4)_2$  was studied as a possible formation product between LBE and JOG-phase. A long-standing issue in the understanding of the crystal structure of this compound has been solved using neutron diffraction. The thermal expansion of  $\text{CsBi}(\text{MoO}_4)_2$  was determined.

To assess the interaction between coolant and volatile fission products, the system  $\text{CsI-PbI}_2\text{-BiI}_3$  was studied experimentally. The low-temperature heat capacity of the three compounds in the system ( $\text{CsPbI}_3$ ,  $\text{Cs}_4\text{PbI}_6$  and  $\text{Cs}_3\text{Bi}_2\text{I}_9$ ) were determined and the standard entropy was calculated. The phase diagrams  $\text{CsI-PbI}_2$ ,  $\text{CsI-BiI}_3$  and  $\text{PbI}_2\text{-BiI}_3$  were measured using differential scanning calorimetry. A thermodynamic model was developed to predict the liquidus surface of the  $\text{CsI-PbI}_2\text{-BiI}_3$  system. The accuracy of the model was confirmed by selective measurements of the ternary eutectics and the pseudo-binary  $\text{CsPbI}_3\text{-Cs}_3\text{Bi}_2\text{I}_9$ .

Study of the interaction between the grey-phase element Ba, fuel and coolant was initiated. During this work, a BaO-deficient plutonium-based perovskite with a composition close to  $\text{Ba}_3\text{PuO}_6$  was synthesised. Its crystal structure was studied, as well as the phase transitions at high temperature. The standard entropy of the compound and magnetic susceptibility were determined experimentally. This work, valuable in itself as a contribution to the understanding of the irradiated nuclear fuel pin, is needed as a building block to study coolant-grey phase interaction.

Overall, this thesis describes potential chemical interaction products in the scenario of cladding failure in LFRs. In the concluding chapter, it is shown that the oxygen concentration present in operating conditions allows for the formation of several complex oxide compounds in case of Pb-JOG interaction. In general, this work provides new and necessary data to assess the stability of iodide and oxide compounds. The results present in this thesis should be combined with post-irradiation examination and kinetic studies to assess the scenario of cladding failure from different perspectives.

# PREFACE

It should have been in a meeting about a year after the start of my project that my promoters asked me whether I would like to graduate as a nuclear engineer or as a nuclear chemist. As the reader of this thesis will find out, there is quite some fundamental physics, thermodynamics and chemistry in here for a pure engineer. However, the engineers among the readers will find some application calculations in the concluding chapter. Hopefully, this dissertation saves the engineers some future work, while the academic physical-chemists will find enough to their liking as well.

*Andries van Hattem  
Nunspeet, Summer 2025*



# 1

## INTRODUCTION

Fission of uranium or plutonium atoms in a nuclear reactor releases a lot of energy, neutrons and a range of fission products. The thermal energy is released as heat and transported via the primary and secondary coolant to be converted to electricity or used directly. In normal operating conditions, the fission products are retained inside the nuclear fuel pin, where a complex chemistry emerges. In case the cladding that separates the primary coolant and fuel pin fails during incident or accident scenarios, some of the fission products may be released into the primary coolant. In this dissertation, chemical scenarios are investigated to assess the so-called source-term for radionuclide release in lead-cooled nuclear systems.

Fission products of primary concern in a possible accident scenario will be introduced in Section 1.1, with some context towards reactor design, fuel choice and irradiated fuel. In Section 1.2, the use of liquid lead as innovative primary coolant is discussed, together with an identification of the chemical systems that have to be investigated in order to understand clad breach in lead-cooled nuclear reactors. Section 1.3 presents the research questions of this thesis, methods and scope, and gives an outline of this thesis.

### 1.1. CHEMISTRY OF THE FAST-SPECTRUM NUCLEAR FUEL PIN

The principle of nuclear energy generation relies on the splitting of fissile isotopes like uranium ( $^{235}\text{U}$ ) and plutonium ( $^{239}\text{Pu}$ ) [1]. After the first man-made splitting of the nucleus of the atom at the end of the 1930s, the nuclear binding energy was soon exploited for energy production. In a few decades time, civilian use of nuclear energy was established in multiple countries, providing a fossil-free energy alternative for electricity generation [2]. Besides, radionuclides for health started being produced in nuclear reactors by irradiation of target materials [3, 4]. Nowadays, the current (mainly light-water reactor (LWR)) reactor fleet provides clean and affordable electricity, while new nuclear reactor designs are proposed for various purposes like electricity production, district heating, closure of the fuel cycle and transmutation. These designs excel in improving or exceeding existent techniques with regard to among others efficiency and safety. Among

the proposed innovative reactor designs, fast-neutron spectrum reactors play a key role [5–7].

Fast-neutron reactors operate typically with a fuel mixture of uranium (U) and plutonium (Pu), unlike the U-based fuel used in most LWRs [6]. The choice of nuclear fuel depends on several criteria, among which are intrinsic material properties, resource and energy policies, and available knowledge and industrial infrastructure. From a material properties perspective, one considers particularly the density of fissile elements, the oxidative properties, the neutronic properties, the melting point and the thermal conductivity, and how these properties influence the margin to melting. Inertness to cladding and coolant are also important. Fuels in the classes metal, oxide, nitride, carbide, silicide and boride have been investigated and compared [8]. From a resource and energy policy, the availability of mineable uranium (U) or thorium (Th) and plutonium (Pu) and minor actinide (MA, a.o. neptunium, americium and curium isotopes) management play key roles in decision making. The availability of knowledge and infrastructure, moreover, plays a pivotal role in investment strategies as dedicated facilities for enrichment, fuel production and reprocessing are large and expensive industries.

Historically, metallic fuel was employed during early breeding activities in the 1950s in the US and UK, but since the 1960s mixed oxide fuel (MOX, (U,Pu)O<sub>2</sub>) was selected as reference fuel because of its more apt radiation tolerance. Next to this, metallic fuel has several polymorphs and anisotropic thermal expansion that complicate its use. For transuranium management reasons, MOX has been used in breeder and fast-neutron spectrum reactors, and is proposed to be used in several new fast-neutron reactor designs. In sodium-cooled fast reactor (SFR) irradiation experiments, hypostoichiometric MOX was used with a O/M ratio of the as-fabricated pellets in the range 1.93-1.99. In general, despite its relatively low heavy metal atom density and poor thermal conductivity, oxide fuel has been employed most often in Europe, because early irradiation experiments were successful [6].

The first rise to power influences as-fabricated MOX fuel in a fast-neutron reactor significantly. The enormous temperature and radiation effects change the structural and thermal properties of the fuel pin element via effects like central hole formation, plutonium redistribution, cracking and grain growth. The start of the fission reaction considerably affects the radioactive inventory of the fuel pin and multiple chemical elements (fission products) are formed. The exact elemental yield depends on the starting fissile isotope ratio and the neutronic spectrum, but yields a peak around mass number 100 and mass number 140. This means that the fission products such as Zr, Mo and Ru are abundant, as well as I, Xe, Cs, Ba, Ce, Nd. Due to their short half-life, some isotopes decay in other elements. Chemically, the fission products are present all over the fuel pin but migrate and redistribute in four types of phases, which are indicated in Figure 1.1:

1. Fission products in solid solution in the UO<sub>2</sub> fluorite structure
2. Metallic precipitates (white phase inclusions)
3. Oxide precipitates (the so-called grey phase inclusions, and, at higher burn-up, the joint oxide gain (JOG) phase), like Ba, Cs, Mo
4. Gaseous or volatile species, like Cs, I, Xe, Kr

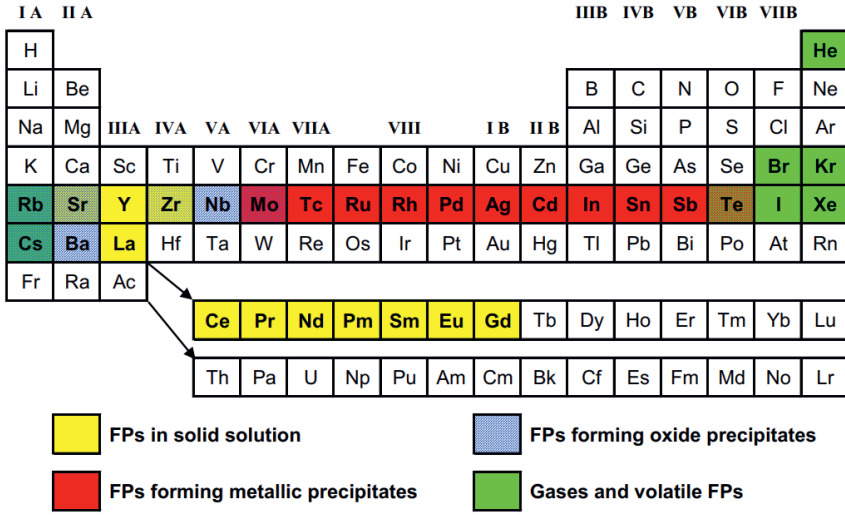


Figure 1.1: Main fission products (FPs) in their preferred chemical phase. Reproduced with permission from Pelletier and Guérin [6]. Copyright Elsevier, 2020.

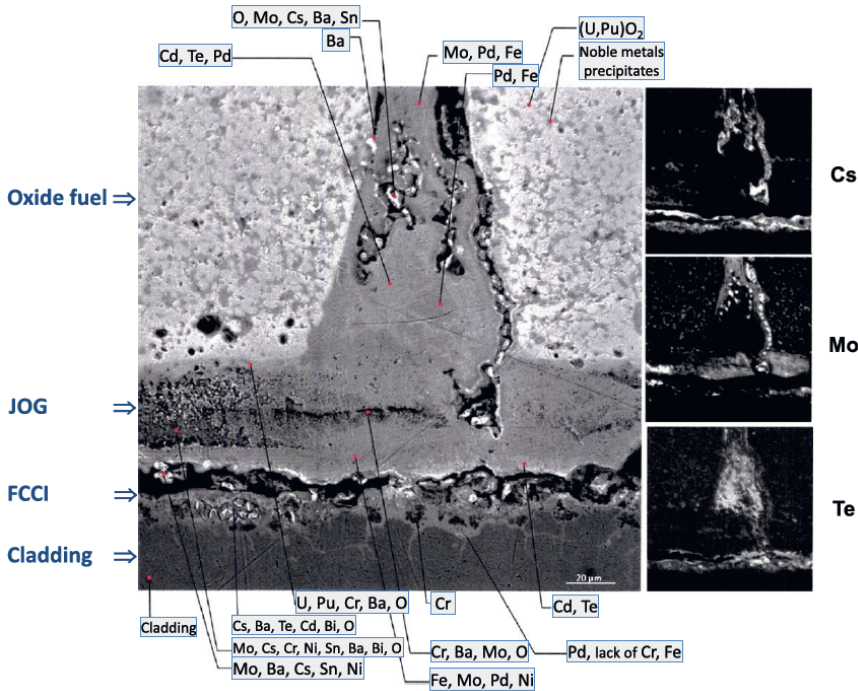


Figure 1.2: Elemental analysis on a Prototype Fast Reactor pin irradiated at very high burnup (23 at-%). Reproduced with permission from Pelletier and Guérin [6]. Copyright Elsevier, 2020.

Fast-neutron reactors reach a higher burn-up percentage compared to LWRs. In thermal-spectrum reactors, the fuel is refreshed rather soon, but fast-spectrum neutron reactors continue to burn-up values of 10 to 25% FIMA (Fissions per Initial Metal Atom) [6]. The increased fuel utilisation related to the higher burn-up influences the chemistry of the fuel pin considerably. The so-called grey phase consists of a  $\text{BaZrO}_3$  perovskite phase, with other elements dissolved in it. Together with these other elements, it forms the oxide precipitate  $(\text{Ba,Sr,Cs})(\text{Zr,U,Pu,Mo,REE})\text{O}_3$  where REE = rare-earth elements [6]. At 7-8% burn-up of the fissile initial metal atoms (FIMA), an oxide-rich layer starts to fill the small gap between the fuel pellet rim and the cladding material [9]. This so-called JOG-layer (see Figure 1.2), from the French acronym joint-oxyde gainé [10], influences the thermal conductivity and local pressure and can be several hundreds of micrometers thick [6].

The JOG-layer is a multi-element material. Its thermal conductivity is lower than that of MOX fuel but higher than gas filling this area and because of the temperature at the rim of fuel pellets, the JOG-layer is partially viscous. Highly abundant fission product elements in the JOG are caesium (Cs), molybdenum (Mo), tellurium (Te) and iodine (I), while one can also find barium (Ba) and cladding elements like iron (Fe), chromium (Cr) and nickel (Ni) [6]. In case the cladding material fails at higher burn-up, these elements will be the first layer interacting with the coolant material, and their interaction with coolant thus forms an important part of this dissertation. The JOG-phase can be approximated as  $\text{Cs}_2\text{MoO}_4$ , which is the most abundant phase according to thermochemical calculations coupled to post-irradiation examinations [6, 9–12].

## 1.2. LEAD-COOLED FAST REACTORS

As a promising fast-neutron spectrum design, the lead-cooled fast reactor (LFR) was selected by the Generation IV forum around the start of this millennium [13]. The Generation IV Forum listed five designs next to the LFR, *viz.* the gas-cooled fast reactor (GFR), the molten salt reactor (MSR), the sodium-cooled fast reactor (SFR), the supercritical-water-cooled reactor (SCWR) and the very-high-temperature reactor (VHTR) [5]. They also drafted a list of prerequisites for the new generation of nuclear power plants. Using an innovative reactor design or another coolant than water does not directly qualify as Generation IV, but a reactor has to comply and excel with all four selection criteria: sustainability, economic competitiveness, safety and reliability, and proliferation resistance and physical protection. The Lead-cooled Fast Reactor general design is reminiscent of a Light-water Reactor design, Figure 1.3. The fuel pin assembly (reactor core) is immersed in the primary coolant (liquid lead), which transfers the produced heat to a secondary coolant which drives a turbine. The main differences between LFRs and LWRs, besides the coolant material, are in the neutron spectrum and fuel choice as explained supra. The coolant material for LFRs is either liquid lead (Pb) or a liquid eutectic mixture of lead and bismuth (Bi), also known as lead-bismuth eutectic (LBE). The chemical composition of LBE is  $\text{Pb}_{45}\text{Bi}_{55}$  [14].

Similar to selecting the nuclear fuel, there are multiple criteria for a nuclear coolant, as are listed in Table 1 [15]. The main differences between Pb and LBE are the melting point and thus lower limit of the operating temperature (600 K for Pb, 398 K for LBE), the short-term induced radioactivity, and the lower abundance and thus higher price of

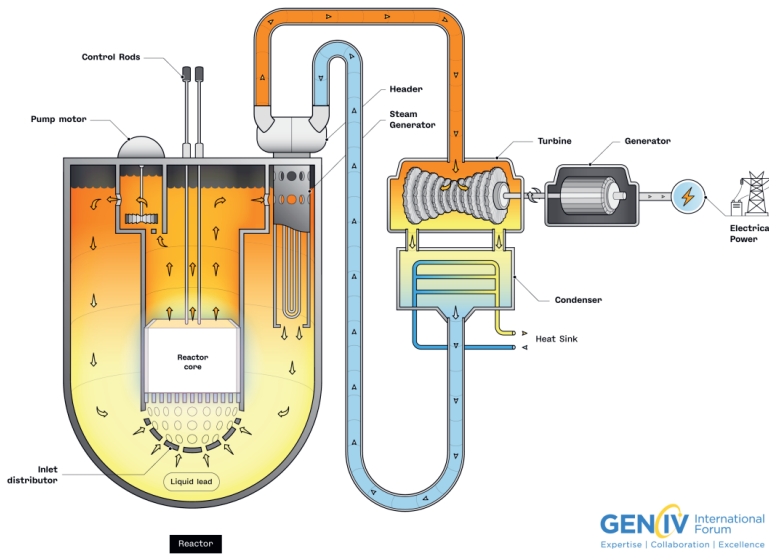


Figure 1.3: Schematic overview of the Lead-cooled Fast reactor. Picture slightly adapted from Generation IV International Forum.

Bi. One of the often mentioned challenges of using Pb or Bi as nuclear coolant is the formation of the neutron activation product  $^{210}\text{Po}$ . This effect is present for both liquid Pb and LBE, but orders of magnitude larger for LBE. According to Zhang, the polonium hazards are always overestimated, as evidenced by a long operational experience [15]. Given the lower natural abundance of Bi, LBE-cooled designs should not be used for a large energy production fleet, but for dedicated applications. Materials compatibility and corrosion resistance are the other big challenge, more specifically for Pb-cooled systems, because the higher melting point inherently dictates higher operating temperatures, opening other corrosion pathways.

The cladding materials of choice for LFRs differ from conventional LWR cladding materials like Zircaloy. The cladding material in a LFR should be able to resist several corrosion mechanisms at much higher temperatures and to withstand wear in flowing liquid metal. In other words, it should be both chemically and mechanically stable. Cladding materials that received attention for LFRs are the steels 316L, 15-15Ti austenitic steel, ferritic-martensitic T91, martensitic steel HT-9, and alumina forming austenitic steels [16, 17]. Non-ferrous alloys are also considered, as well as oxide dispersive steels and composite materials [17]. Coatings are moreover used to enhance the performance of several types of structural materials [16]. From a chemical thermodynamics perspective, the corrosion mechanisms are distinguished based on three regimes for the oxygen potential in the liquid metal coolant: a too low oxygen potential, an intermediate working regime, and a too high oxygen potential. In the case of a too high oxygen potential, lead oxide (PbO) will be formed, while a too low oxygen potential leads to so-called liquid metal embrittlement. Most of the cited steels are Fe-rich, and they are typically protected by a passivating Fe(-Cr) oxide layer. This means that the operating oxygen concentration

Property	Liquid Pb	Liquid LBE
Low vapour pressure at operating temperatures	Good	Good
High boiling point	Good	Good
Low melting point	Criterion not met	Good
Excellent heat transfer properties	Good	Good
Radiation stability	Good	Good
Thermal stability	Good	Good
Low thermal neutron capture cross section	Good	Good
Short term induced radioactivity	Criterion partially met	Criterion not met
Compatibility with reactor and heat transfer loop materials	Criterion partially met	Criterion partially met
Low cost	Good	Criterion not met
Low pumping power	Criterion not met	Criterion not met
Non-toxic and free from operating hazard	Criterion not met	Criterion not met
Non-reactive with air and water	Good	Good

Table 1.1: Properties of nuclear coolants with a judgment whether liquid Pb and liquid LBE meet these criteria. Taken from Zhang [15].

and thus oxygen potential in liquid metal coolant should read [14]:

$$2\Delta_f G^0(\text{PbO}) > RT \ln p_{\text{O}_2} > \frac{1}{2}\Delta_f G^0(\text{Fe}_3\text{O}_4) \quad (1.1)$$

Herein, Fe-containing cladding materials will be taken as reference, meaning the conditions in Equation 1.1 can be used as reference in application calculations.

In case of cladding failure in a lead-cooled fast-neutron spectrum reactor, the liquid Pb (and Bi) interact chemically and physically with the fuel with fission products. Cladding failure affects the safety and economy of a nuclear reactor, and thus affect two of the Generation IV selection categories. According to Olander, the burnup for LWRs is limited by the increased probability of cladding failure, which should at maximum be of the order of  $10^{-5}$  [2]. Olander considers increased cladding rupture probability of a single fuel element in LWRs to be more an economic than a safety concern. Pelletier and Guérin write that for SFRs, the design criteria include also a cladding failure rate of  $10^{-5}$ , where experience shows that the main failure cause is related to excessive clad deformation because of austenitic steel swelling [6]. They state that the limitation was not on burn-up per se, but on the the maximum dose the cladding material could withstand. Next to this, they point towards fuel-cladding mechanical interaction (FCMI) and fuel-cladding chemical interaction (FCCI) [6]. In general, the economic competitiveness of Generation IV reactors is difficult to assess as the literature is rather scarce [18, 19], but it is self-evident that a too high cladding failure rate has a severely negative effect on the economic competitiveness of nuclear reactors.

The escape of radionuclides from the fuel pin into the primary coolant circuit if the cladding fails, is the first event that may lead to a source term. The source term for LWRs

is defined as “the timing, fraction, speciation of fission products released to the containment during a severe accident and their behaviour when they are suspended in the containment atmosphere” [20].

To assess the source term, both the interaction products of coolant and irradiated fuel, and the retention capacity of the coolant towards the fission products or interaction products are important. Several studies into the retention capacity and release of fuel and fission products are reported in the open literature [21, 22]. In general, good fuel compatibility and fission product retention are claimed for LFRs [23].

The formation of interaction products depends on the location in the reactor where the chemical interaction occurs. Reaction after coolant ingress into the fuel pin, reaction around a cladding failure interface or reaction following fission products release into the rather large volume of coolant material differ from the thermodynamic perspective, as the sketched scenarios translate to other chemical compositions and thus to other stable phases, or at least to other ratios between stable phases. A key parameter for the occurrence and form of the chemical interaction is the oxygen concentration in liquid Pb or LBE. The operating conditions of a LFR balance between a too low and a too high oxygen concentration to prevent liquid metal corrosion towards structural materials on the one hand, and PbO(s) formation in the coolant on the other hand. This results in a non-negligible oxygen concentration, which in thermodynamic language means an oxygen potential determining the stability range wherein oxygen is present as dissolved in liquid metal [14, 24, 25]. This non-negligible oxygen concentration is the thermodynamic driver for the formation of interaction compounds in equilibrium conditions. The stability range or concentration of oxygen dissolved in liquid Pb is  $c_O = 8 \cdot 10^{-7}$  to  $10^{-4}$  wt-% in the temperature window 673-873 K; for liquid LBE, this is  $c_O = 4 \cdot 10^{-10}$  to  $10^{-8}$  wt-% in the temperature window 473-673 K or  $c_O = 2 \cdot 10^{-7}$  to  $10^{-5}$  wt-% in the temperature window 673-873 K [14]. In the case of Na-U-O interactions in sodium-cooled fast reactors (SFRs), the oxygen concentration typically encountered in sodium-coolant in operating conditions is high enough to lead to the formation of interaction products of higher valence state than  $UO_2$  [26]. In the incidental or accidental scenario of oxygen ingress into the coolant vessel, the oxygen potential would increase and open additional oxidation pathways. Whereas oxygen is a necessary present in the coolant, the presence of other trace elements in the coolant depends on initial impurities, release upon cladding failure or spallation processes. The subsequent formation of multi-element compounds would thermodynamically depend on *e.g.* the iodine or caesium potential at extremely low concentrations, for which data are often scarce or non-existent.

### 1.3. CLADDING FAILURE IN LEAD-COOLED FAST REACTORS

In normal operating conditions, the cladding around the nuclear fuel pin separates the coolant and the fuel and fission products. In incidental or accidental conditions, cladding failure leads to physical and chemical interaction between the coolant elements (Pb, Bi) and fission products, which has to be understood for safe handling, cleaning and licensing procedures.

### 1.3.1. RESEARCH QUESTIONS

This thesis focusses on the thermodynamic aspects of the chemical interaction between selected fission products originating from irradiated fuel and Pb or LBE coolant. The main research question can be formulated as follows:

*Which chemical interactions occur between coolant and fission products following cladding failure in a lead-cooled fast reactor?*

The main question is divided into three sub-questions:

1. What chemistry is associated with coolant-JOG phase interaction?
2. What chemistry is associated with coolant-volatile fission product interaction?
3. What chemistry is associated with coolant-grey phase interaction?

### 1.3.2. METHODS AND SCOPE

Nuclear chemistry has three main methods to study the chemical behaviour of the nuclear fuel pin: post-irradiation examination (PIE) [27], kinetic and release studies [22, 28], and thermodynamic studies. In this study, the knowledge obtained on the chemistry of the fast-reactor fuel pin in sodium-cooled fast reactors using PIE serves as starting point for the identification of important fission product phases. The selected fission product phases, together with the coolant elements Pb and Bi, form the chemical systems that will be examined from a thermodynamic point of view in this thesis.

The knowledge obtained on spent fuel originates from data collected via both PIE and thermodynamic studies. While post-irradiation examination gives first-hand insights into the elements that are present over the radius of the fuel pin, it is an extremely costly and complicated process, involving dedicated facilities where radioactive hot materials can be handled and examined. Moreover, the short-lived or volatile nature of several isotopes results in the disappearance of several phases before the actual PIE. Although this can be overcome by short re-irradiation or by ion bombardment, thermodynamic studies add to the understanding of the evolution of the nuclear fuel pin by adding separate effect studies. Moreover, the thermodynamic studies can be performed on inactive or less active isotopes of the elements of interest. Complementary to PIE, kinetic and thermodynamic studies, engineering-related separate effect studies may be performed [29], as *operando* measurements on a nuclear fuel are even more complicated than PIE though not impossible [30].

The herein reported thermodynamic studies typically proceed along the following line: collect from literature what is known on the systems formed with the chemical elements of interest, identify the missing crystallographic or thermodynamic data, perform new experiments and assemble a model to predict which compounds can be formed in operational, incidental or accidental scenarios.

Despite the well-established track record of the thermodynamic approach, there are a few limitations and assumptions when using it to understand the *operando* behaviour of a nuclear fuel pin. A fuel pin under irradiating particle flux has a nonequilibrium point defect concentration, which PIE is also not able to capture, however [30]. The fuel itself gives another example: although often written as  $(U,Pu)O_2$ , implying a full perfect solid

solution, the fabrication method influences the actual fuel homogeneity [31–34]. As a last example, the most recent contribution to the longstanding debate on the presence of CsI in nuclear fuel found that the radiation field destroys CsI that is predicted to be stable by thermodynamic considerations [35].

### 1.3.3. THESIS OUTLINE

The thesis follows the three sub-questions defined above in order to solve the main question. First, the used experimental and modelling methods are described.

#### METHODOLOGY

Chapter 2 outlines the experimental techniques and thermodynamic modelling approach that are used in the later chapters. It also gives details of equipment used in later chapters, giving general information that is supplemented by experimental details at the end of each chapter where necessary.

#### CHEMISTRY ASSOCIATED WITH COOLANT-JOG PHASE INTERACTION

Various aspects of the chemistry associated with coolant-JOG phase interaction are approached via the Pb-(Bi)-Cs-Mo-O system and dealt with in the Chapters 3 to 5. A full thermodynamic model of the Pb-Mo-O system is developed in Chapter 3, based on own thermochemical experiments and literature data. The experimental investigations are continued for the Pb-Cs-Mo-O system in Chapter 4, focussing on the  $\text{Cs}_2\text{MoO}_4$ - $\text{PbMoO}_4$  system with the compound  $\text{Cs}_2\text{Pb}(\text{MoO}_4)_2$ . Next to the crystallographic investigation, the standard thermodynamic properties of  $\text{Cs}_2\text{Pb}(\text{MoO}_4)_2$  are experimentally measured. From literature, two quaternary compounds in the  $\text{Cs}_2\text{MoO}_4$ - $\text{Bi}_2(\text{MoO}_4)_3$  system are identified. In Chapter 5, open issues in the understanding of one of them,  $\text{CsBi}(\text{MoO}_4)_2$  are addressed. A new crystal structure at room temperature is proposed based on non-ambient neutron diffraction results.

#### CHEMISTRY ASSOCIATED WITH COOLANT-VOLATILE FISSION PRODUCT INTERACTION

Chapter 6 deals with the coolant-volatile fission product interaction as studied in the iodide salt limit, *i.e.* the CsI-PbI<sub>2</sub>-BiI<sub>3</sub> system. The standard entropy of the three relevant compounds CsPbI<sub>3</sub>, Cs<sub>4</sub>PbI<sub>6</sub> and Cs<sub>3</sub>Bi<sub>2</sub>I<sub>9</sub> is reported, based on low-temperature heat capacity measurements. Moreover, phase transition temperatures are studied using differential scanning calorimetry. Next to this newly collected thermodynamic data, a full (solid, liquid) phase diagram of the CsI-PbI<sub>2</sub>-BiI<sub>3</sub> system is presented.

#### CHEMISTRY ASSOCIATED WITH COOLANT-GREY PHASE INTERACTION

In an attempt to initiate the study of the Pb-Ba-Pu-O system, many questions in the Ba-Pu-O system were found and Chapter 7 features the results obtained in the study of a Ba-Pu-O compound, important in the understanding of the grey perovskite-containing phase in irradiated fuel. The found compound is experimentally studied, and a model for the crystal structure is proposed. Furthermore, spectroscopic and physical measurements are reported. By this, the compound is characterised by its Ba:Pu ratio and the oxidation state of Pu, after which several of its physical properties are reported.

### CONCLUSIONS AND OUTLOOK

With the new data collected in this dissertation, new insights are gained towards a thorough understanding of the chemical consequences of cladding failure in lead-cooled fast reactors. The open question after studying the thermodynamic stability presented in the earlier chapters is whether these compounds actually are stable in typical LFR operating conditions. This question is answered for the compounds studied in Chapter 3 and 4, for which all necessary experimental data are available. The implications of the other chapters in view of the cladding failure scenario are also discussed. The concluding chapter gives an outlook on the implications for the study of irradiated fuel-coolant interaction via PIE.

# BIBLIOGRAPHY

- (1) Konings, R. J. M.; Wiss, T.; Beneš, O. *Nature Materials* **2015**, *14*, 247–252.
- (2) Olander, D. *Journal of Nuclear Materials* **2009**, *389*, 1–22.
- (3) Krijger, G. C.; Ponsard, B.; Harfensteller, M.; Wolterbeek, H. T.; Nijssen, J. W. F. *Trends in Biotechnology* **2013**, *31*, 390–396.
- (4) Van de Voorde, M.; Van Hecke, K.; Cardinaels, T.; Binnemans, K. *Coordination Chemistry Reviews* **2019**, *382*, 103–125.
- (5) US DOE Nuclear Energy Research Advisory Committee with Generation IV International Forum [https://www.gen-4.org/gif/jcms/c\\_40481/technology-roadmap](https://www.gen-4.org/gif/jcms/c_40481/technology-roadmap) **2002**.
- (6) Pelletier, M.; Guérin, Y. In *Comprehensive Nuclear Materials, 2nd edition*, Konings, R. J. M., Stoller, R. E., Eds.; Elsevier: 2020; Chapter 2.03, pp 72–105.
- (7) Roelofs, F.; Breijder, P.; Habiyaremye, V.; Hussain, M. M. M. D.; Mathur, A.; Nindiyasari, F.; Pangukir, F.; Stempniewicz, M.; van Til, S.; Uitslag-Doolaard, H., et al. *Nuclear Engineering and Design* **2025**, *440*, 114146.
- (8) Konings, R. J. M.; Wiss, T.; Guéneau, C. In *The chemistry of the actinide and transactinide elements*, Morss, L. R., Edelstein, N. M., Fuger, J., Eds.; Springer: 2010; Chapter 34, pp 3665–3811.
- (9) Cappia, F.; Miller, B. D.; Aguiar, J. A.; He, L.; Murray, D. J.; Frickey, B. J.; Stanek, J. D.; Harp, J. M. *Journal of Nuclear Materials* **2020**, *531*, 151964.
- (10) Tourasse, M.; Boidron, M.; Pasquet, B. *Journal of Nuclear Materials* **1992**, *188*, 49–57.
- (11) Kleykamp, H. *Journal of Nuclear Materials* **1985**, *131*, 221–246.
- (12) Smith, A. L.; Thi, T. N. P.; Guéneau, C.; Dumas, J.-C.; Epifano, E.; van Burik, W.; Dupin, N. *Calphad* **2021**, *75*, 102350.
- (13) Alemberti, A. *Engineering* **2016**, *2*, 59–62.
- (14) Müller, G.; Heinzl, A.; Schumacher, G.; Weisenburger, A. *Journal of Nuclear Materials* **2003**, *321*, 256–262.
- (15) Zhang, J. *Advanced Engineering Materials* **2014**, *16*, 349–356.
- (16) Serag, E.; Caers, B.; Schuurmans, P.; Lucas, S.; Haye, E. *Surface and Coatings Technology* **2022**, 128542.
- (17) Bassini, S.; Cataldo, S.; Cristalli, C.; Fiore, A.; Sartorio, C.; Tarantino, M.; Utili, M.; Ferroni, P.; Ickes, M.; Alemberti, A., et al. In *Comprehensive Nuclear Materials, 2nd edition*, Konings, R. J. M., Stoller, R. E., Eds.; Elsevier: 2020; Chapter 4.08, pp 218–241.

- (18) Mignacca, B.; Locatelli, G. *Progress in Nuclear Energy* **2020**, *129*, 103503.
- (19) Tassone, F.; Ricotti, M. E.; Lorenzi, S.; Locatelli, G. *Progress in Nuclear Energy* **2024**, *174*, 105298.
- (20) Engineering Safety Section *A simplified approach to estimating reference source terms for LWR designs (IAEA-TECDOC-1127)*; tech. rep.; International Atomic Energy Agency, 1999.
- (21) Vigier, J.-E.; Popa, K.; Tyrpekl, V.; Gardeur, S.; Freis, D.; Somers, J. *Journal of Nuclear Materials* **2015**, *467*, 840–847.
- (22) Bell, J. S.; Dickson, R. S.; Sheedy, J.; Peplinskie, R. T.; Gauthier, M. D.; Ruhnke, J.; Stoll, K. *Annals of Nuclear Energy* **2020**, *148*, 107683.
- (23) Cacuci, D. G., *Handbook of Nuclear Engineering: Vol. 1: Nuclear Engineering Fundamentals; Vol. 2: Reactor Design; Vol. 3: Reactor Analysis; Vol. 4: Reactors of Generations III and IV; Vol. 5: Fuel Cycles, Decommissioning, Waste Disposal and Safeguards*; Springer Science & Business Media: 2010; Vol. 4.
- (24) Ganesan, R.; Gnanasekaran, T.; Srinivasa, R. S. *Journal of Nuclear Materials* **2006**, *349*, 133–149.
- (25) Zhang, J.; Li, N. *Journal of Nuclear Materials* **2008**, *373*, 351–377.
- (26) Smith, A. L.; Gueneau, C.; Flèche, J.-L.; Chatain, S.; Beneš, O.; Konings, R. J. M. *The Journal of Chemical Thermodynamics* **2017**, *114*, 93–115.
- (27) Degueldre, C.; Bertsch, J.; Martin, M. *Progress in Nuclear Energy* **2016**, *92*, 242–253.
- (28) Wang, M.; Jiang, G.; Cheng, S.; Wang, K. *Nuclear Engineering and Design* **2024**, *419*, 112981.
- (29) Tari, D.; Retegan Vollmer, T.; Geers, C. *Journal of Nuclear Engineering* **2024**, *5*, 57–73.
- (30) Solov'yov, A. V.; Verkhovtsev, A. V.; Mason, N. J.; Amos, R. A.; Bald, I.; Baldacchino, G.; Dromey, B.; Falk, M.; Fedor, J.; Gerhards, L., et al. *Chemical Reviews* **2024**, *124*, 8014–8129.
- (31) Olander, D. R. *Journal of Nuclear Materials* **1976**, *60*, 237–239.
- (32) Boshoven, J.; Vigier, J.-E.; Pöml, P.; Ndiaye, A.; Morel, B.; Konings, R. J. M.; Popa, K.; Cologna, M. *Journal of Nuclear Materials* **2025**, 155800.
- (33) Colle, J.-Y.; Pöml, P.; Boshoven, J.; Konings, R. J. M. *Nuclear Technology* **2025**, *211*, 1103–1110.
- (34) Boshoven, J.; Ndiaye, A.; Morel, B.; Cologna, M.; Vigier, J.-E.; Marquez, R. C.; Konings, R. J. M.; Popa, K. *Journal of Nuclear Materials* **2025**, 155915.
- (35) Colle, J.-Y.; Zappey, J.; Beneš, O.; Cologna, M.; Wiss, T.; Konings, R. J. M. *Journal of Nuclear Materials* **2025**, *608*, 155715.

# 2

## METHODOLOGY

*This chapter explains the methods used in the subsequent chapters. It deals subsequently with solid-state synthesis, X-ray and neutron diffraction, X-ray absorption spectroscopy, differential scanning calorimetry, solution calorimetry, thermal-relaxation calorimetry and magnetometry using SQUID-VSM. Thermodynamic modelling is introduced in the last section.*

---

This chapter contains parts of experimental details from the publications on which the following chapters are based.

## 2.1. SYNTHESIS

Solid-state synthesis of complex oxides (iodides) typically requires intimate mixing of simple oxides (iodides) and heating them together at a high temperature, while staying in the solid-state window. The so-called Tammann-rule dictates that at least two-third of the melting temperatures has to be reached to get a diffusion-controlled reaction in a reasonable time [1]. The atmosphere in the furnace needs to be selected (oxidising, inert, reducing), as well as the crucible material (*e.g.* alumina, boron nitride, Ni, Pt) and crucible shape (open, closed). Typically, more than one heat treatment with intermittent regrinding is used. Instead of starting from oxide precursors, more readily available or more reactive carbonate or nitrate precursors can be used. Alternatively to solid state synthesis, synthesis via the melt phase can also be employed if the compound is congruently melting. Details of the performed syntheses are mentioned at the end of each chapter.

## 2.2. X-RAY AND NEUTRON DIFFRACTION

Crystalline materials exhibit a diffraction pattern because the periodicity of the material causes constructive and destructive interference according to Braggs Law [1, 2]. X-rays are diffracted by the electrons of the material, and the intensity of the obtained diffraction pattern is related to the electric density and thus the atomic number. Neutrons interact with the nuclei in the material, and there is no clear trend in neutronic cross section over the periodic table. Both techniques are thus complementary while studying a crystal structure, where the less commonly used neutrons are very useful in locating small-mass atoms in the crystal structure (*e.g.* oxygen).

Formation and purity of the compounds were confirmed by powder X-ray diffraction (pXRD), while a more detailed picture of the crystal structure was obtained in some specific cases using neutron diffraction (ND). In general, purity up to 99% can be concluded from XRD measurements. In Chapters 3, 4, 5 and 6, a PANalytical X'Pert PRO X-ray diffractometer mounted in the Bragg-Brentano configuration with a Cu-anode was used. The data were collected using an X'Celerator detector. The samples were loaded in airtight sample holders closed with Kapton foil to prevent lead powder spreading or reaction with air. In Chapter 7, pXRD at ambient temperature was measured at the JRC Karlsruhe using a Bruker D8 X-ray diffractometer mounted in the Bragg-Brentano configuration with the Cu  $K_{\alpha 1}$  radiation (40 kV, 40 mA, Ge(111) monochromator). About 10 mg of the specimen was immobilised in bi-component epoxy resin on a sample holder to prevent spreading of radioactive powder. Data were collected from 10-120°  $2\theta$  with a step size of 0.013°  $2\theta$  using a LynxEye detector for up to 24 hours per measurement.

Next to XRD measurements at ambient temperature, measurements were also made at non-ambient temperature. For X-ray diffraction, commercially available strip heaters or furnace heaters are employed. In this work, an XRK-900 (furnace heater) device was used in Chapter 3, while an AntonPaar TTK450 strip heater was used for the work in Chapter 4, both installed in the PANalytical X'Pert PRO X-ray diffractometer mounted in the Bragg-Brentano configuration. In Chapter 7, a second Bruker D8 X-ray diffractometer installed at JRC Karlsruhe was used to collect data at elevated temperatures under vacuum ( $10^{-3}$  bar). The sample was dispersed on the surface of a Pt heating strip using

a few drops of alcohol in a N<sub>2</sub>-filled glove box and measured every 100 K.

ND was performed at the PEARL beam line [3] at the Hoger Onderwijs Reactor (HOR) at TU Delft with a fixed wavelength of 0.166718 nm in the angle range  $11^\circ \leq 2\theta \leq 159^\circ$ . For room-temperature measurements, the sample was encapsulated in a vanadium Null-alloy container hermetically closed with a rubber o-ring. Data analysis was performed using the profile refinement method [4, 5] in the FullProf suite [6]. For neutron-diffraction at non-ambient temperature, in-house built cooling or heating equipment are available at PEARL.

Structural analysis was performed on the diffraction patterns using the Rietveld profile refinement method [4, 5] or the LeBail refinement method [7] in the FullProf suite [6]. Visualisations of the crystal structures were made using VESTA [8].

## 2.3. X-RAY ABSORPTION SPECTROSCOPY

In X-ray absorption spectroscopy (XAS), core level electrons are excited. The absorbance or fluorescence spectrum that is measured is typically divided in the so-called X-ray absorption near edge structure (XANES) spectrum, and the extended X-ray absorption fine structure (EXAFS) spectrum.

### 2.3.1. XAS AT THE MO *K*-EDGE

In this work, XANES spectroscopy measurements were performed for several compounds containing Mo at the INE beamline [9] of the KIT Light Source (Karlsruhe, Germany) with 2.5 GeV and 150–170 mA as operating conditions in the KARA storage ring. The beamline uses a Ge(422) double-crystal monochromator (DCM). Rh-coated mirrors before (flat, cylindrically bent) and after (toroidal) the DCM are used to collimate and focus the synchrotron beam, respectively, producing a spot size of 500 μm by 500 μm at the sample surface. Transmission and fluorescence geometries could be measured in unison.

Samples were probed around the *K*-edge of Mo (20 keV). XAS samples were prepared by mixing some of the compound with boron nitride (BN), which around the Mo *K*-edge is almost transparent to X-rays. The samples mixed with BN were pressed into a circular pellet of 8 mm diameter and enclosed in Kapton foil.

The energy  $E_0$  of the edge absorption threshold position was taken at the inflection point of the spectrum using the the zero-crossing of the second derivative. The position of the pre-peak was selected as the peak maximum, using the zero crossing of the first derivative. Several acquisitions were performed on the same sample and summed up to improve the signal-to-noise ratio. Before averaging the scans, each spectrum was aligned using the XANES spectrum of a metallic molybdenum reference foil measured simultaneously. The ATHENA software was used to normalise and analyse the spectra [10].

### 2.3.2. XAS AT THE PU *L*<sub>3</sub>- AND *M*<sub>5</sub>-EDGES

For the Pu-containing sample studied in Chapter 7, about 1 mg sample was mounted with bi-component glue on a sample holder and doubly encapsulated with 12 μm Kapton. XANES and EXAFS spectroscopy at the Pu *L*<sub>3</sub>-edge were measured at the INE beamline [9] and high-energy resolution fluorescence detected (HERFD) X-ray absorption

spectroscopy at the Pu  $M_5$ -edge was performed at the ACT station of the CAT-ACT beam-line of the KIT Light Source in Karlsruhe, Germany [11, 12]. The storage ring operates at 2.5 GeV and has a maximum stored current of 170 mA.

The Pu  $L_3$  edge (18057 eV) was measured in both transmission and fluorescence mode. For calibration, the  $K$ -edge of a metallic Zr foil (17998 eV) was measured between the second and third ionisation chamber. Ge(422) crystals were used in the double-crystal monochromator (DCM). The X-ray beam is collimated and focussed to a spot size of  $500\ \mu\text{m} \times 500\ \mu\text{m}$  by means of two Rh-coated mirrors, respectively located before (cylindrically bent) and after (toroidal) the DCM. EXAFS spectra were collected at room temperature in fluorescence mode, using a combination of two silicon drift detectors, *viz.* a Vortex- ME4 (4 elements) and a Vortex-60EX (1 element, Hitachi/SIINT). The transmission data were exploited for XANES and the fluorescence signal was used for EXAFS.

The XANES-region of the spectrum was analysed using the ATHENA software and the inflection point of the edge was taken as the threshold position  $E_0$  [10]. The white line position is the maximum of the spectrum. The EXAFS data were collected up to  $16\ \text{\AA}^{-1}$  and Fourier-transformed using the Hanning window over the  $k$ -range 3.5 to  $14.5\ \text{\AA}^{-1}$  ( $dk = 2$ ). The ARTEMIS software suite was used to fit the data in  $k^2$ -space [10]. The *ab initio* code FEFF8.40 was used to calculate the phases and amplitudes for the interatomic scattering paths. The shift in the threshold energy ( $\Delta E_0$ ) was varied as a global parameter. The bond distances were optimized, but the coordination numbers were kept constant. The amplitude for all paths  $S_0^2$  was fixed to 0.9. A single value of  $\Delta E_0$  for all scattering paths was allowed to vary, while the Debye-Waller parameters  $\sigma^2$  were allowed to vary as well. The distance resolution  $\Delta R$ , i.e. the ability to differentiate neighbouring atom shells in the EXAFS spectrum, is given by  $\Delta R = \pi / (2 \cdot \Delta k)$  where  $\Delta k$  is the  $k$ -range of the spectra, resulting in  $\Delta R = 0.14\ \text{\AA}$  for the present  $k$ -range. This means that distances with differences shorter than  $0.14\ \text{\AA}$  cannot be fitted independently.

Pu  $L_3$ -edge XANES spectra have been calculated with the Finite Difference Method Near Edge Structure (FDMNES) code using the herein proposed crystal structure and earlier published BaPuO<sub>3</sub> [13–15]. The simulations were performed with a cluster radius of  $6\ \text{\AA}$  using Greens function, relativistic effect and spin-orbit coupling. The simulated spectra were normalised and shifted by the Pu  $L_3$  edge (18057 eV) for comparison with the experimental spectrum.

High energy resolution fluorescence detection (HERFD) improves the energy resolution via partial fluorescence yield detection of the X-ray fluorescence (as opposed to the regular absorbance or total fluorescence yield) process [16]. Effectively, this technique removes the core-hole lifetime broadening [17]. HERFD-XANES at the Pu  $M_5$  edge (3775 eV) was collected at the ACT-station of the CAT-ACT beamline, using the Pu  $M_{\alpha_1}$  emission (3351 eV) with a Si(220) analyser crystal of 0.5 m bending radius. Si collimating and focussing mirrors and Si(111) DCM crystals were used and the size of the beam-spot was decreased to  $500\ \mu\text{m} \times 500\ \mu\text{m}$  using slits to increase the energy resolution of the collected spectra. The analyser crystal was positioned at an  $142^\circ$  scattering angle relative to the incident beam. The spectrophotometer was placed in a He-flushed glovebox to minimize tender X-ray absorption in the beam path [11, 12].

## 2.4. DIFFERENTIAL SCANNING CALORIMETRY

Differential scanning calorimetry (DSC) measures the heat-flow difference between a crucible containing a sample and a reference crucible. Zero-heating rate calibration is performed by measuring the melting points of standard high purity metals (In, Sn, Pb, Al, Ag, Au) at 2-4-5-8-10-12 K·min<sup>-1</sup>. The calibration was performed as recommended in ref. [18].

In this work, DSC measurements were performed using two Setaram Multi-Detector HTC Module 96 Line calorimeters. One calorimeter was equipped with a 3D heat flux detector, while another was mounted with a simultaneous thermogravimetry-heat flux detector with plate type sensors, to allow for thermogravimetry-differential scanning calorimetry (TG-DSC).

In the DSC instrument, (mixtures of) the compounds were measured with a sample size of about 100 mg of powder in a closed stainless steel crucible with Ni liner under Ar atmosphere [19]. In the TG-DSC, in general, (mixtures of) the compounds were measured with a sample size of about 100 mg of powder in an open alumina cup under oxygen atmosphere. The heating ramp used was 10 K·min<sup>-1</sup> in both cases.

The transition temperatures were derived on the heating ramp as the onset temperature using tangential analysis of the recorded heat flow if the event was interpreted as polymorphism, congruent melting or eutectic. Liquidus event temperatures were based on the peak maximum of the last event collected on the heating ramp [20]. The melting point of the compound was based on the determination of the onset temperature of the event. The estimated uncertainty on measured temperatures is estimated to be ± 5 K for pure compounds and ± 10 K for mixtures.

Next to phase transition temperatures, the enthalpy of a transition (*e.g.* melting) can be determined by using a reference material with a known transition enthalpy in the reference crucible, and measuring both the sample and the reference material in the same cycle. The detector sensitivity  $s_{ref}$  for each measurement is equal to:

$$s_{ref} = \frac{M_{ref} \cdot A_{ref}}{m_{ref} \cdot \Delta_{tr} H_m^{\circ}(T_{tr,ref})} \quad (2.1)$$

where  $s_{ref}$  is in  $\mu\text{V}\cdot\text{mW}^{-1}$ ,  $M_{ref}$  the molar mass of the reference material in  $\text{g}\cdot\text{mol}^{-1}$ ,  $A_{ref}$  the area of the reference sample signal in  $\mu\text{V}\cdot\text{s}$ ,  $m_{ref}$  the sample mass in mg, and  $\Delta_{tr} H_m^{\circ}(T_{tr,ref})$  the transition or melting enthalpy of the reference in  $\text{J}\cdot\text{mol}^{-1}$ . Open alumina crucibles in the DSC were used under oxygen flow at ambient pressure with a heating rate of 10 K·min<sup>-1</sup>.

## 2.5. SOLUTION CALORIMETRY

The enthalpy of formation of a compound at standard conditions is a key ingredient for the Gibbs energy calculation. The enthalpy of formation is the heat associated with the formation of the compound from its constituting elements at standard reference conditions. Nowadays, standard thermodynamic properties of many compounds of two or three elements are known, so thermodynamic cycles can use this auxiliary data.

In this work, the enthalpy of formation of  $\text{Cs}_2\text{Pb}(\text{MoO}_4)$  based on a thermochemical cycle involving  $\text{Cs}_2\text{MoO}_4$  and  $\text{PbMoO}_4$  was measured. The dissolution enthalpies of

a mixture of  $\text{Cs}_2\text{MoO}_4$  and  $\text{PbMoO}_4$  and the dissolution enthalpy of  $\text{Cs}_2\text{Pb}(\text{MoO}_4)_2$  in 2 M NaOH were measured using a Precision Solution Calorimeter from TA Instruments with a TAM IV thermostat. The dissolution experiments were performed in a 25 mL Pyrex glass reaction vessel with a golden stirrer holding a glass ampoule. The 1 mL glass ampoule contained about 100 mg sample per measurement and was sealed with wax. Stabilisation of the baseline and calibration before and after the break were performed using an electrical heater. The accuracy of the equipment was assessed by dissolution of KCl (Merck/Supelco pro analysis) in MilliQ water, yielding a value in line with the study of Kilday from the NBS [21].

## 2.6. THERMAL-RELAXATION CALORIMETRY

The heat capacity below room temperature (low-temperature heat capacity) is important to understand the physics of materials and can moreover be used to derive the standard entropy at 298.15 K. Low-temperature heat capacity was measured on two thermal-relaxation calorimeters, namely a Physical Property Measurement System from Quantum Design (QD-PPMS 14 T, operational window with  $^4\text{He}$  1.9 - 400 K) and a Versalab (operational window 50 - 400 K) equipment system from Quantum Design. The results were collected in the temperature range 2 - 400 K with slight variation of the precise temperature window per sample. Typically, the data were collected with zero magnetic field with exception from Chapter 7.

Poly-crystalline powders were pressed into pellets of 3 mm diameter. The samples were thermally connected to the puck platform using Apiezon N-grease or Apiezon H-grease, depending on the temperature window of the measurement. First, a so-called addenda-curve was measured, giving the heat capacity of the sample puck and the thermal grease. After loading the sample on the puck, the total heat capacity was determined from which the sample heat capacity was extracted. All measurements were performed at very high vacuum ( $10^{-9}$  bar). The heat capacity of the sample was obtained by subtracting the addenda-curve from the total heat capacity, a procedure that is done by the software of the instruments (Multiview from Quantum Design). Some samples have been encapsulated in Stycast 2850 FT as radiation shielding, to improve thermal coupling and/or to reduce potential interaction with atmosphere during installation on the sapphire platform [22]. Heat capacity of Stycast 2850 FT was measured separately and subtracted to obtain the heat capacity of the sample.

The heat capacity at 298.15 K can be estimated using the classical Dulong-Petit limit in its modern formulation ( $C_v = 3nR$ ) or the Neumann-Kopp estimation [23–25]. As was found when cryogenic techniques became available, when going towards 0 K, the heat capacity decreases strongly. For simple systems, the lattice vibrations have been described successfully with the Einstein model and, even better, the Debye model. For complex compounds, it is useful to use a combination of the Debye and Einstein expressions if a model of a single Einstein or Debye expression fails to reproduce the lattice contribution to the low-temperature heat capacity data correctly by itself [26, 27]. In this dissertation, a combination of one Debye ( $D(\Theta_D, T)$ ) and one or more Einstein models ( $E(\Theta_E, T)$ ) were found sufficient to fit the experimental data. The formula used for fitting

in this work reads thus:

$$C_v(T) = n_D \cdot D(\Theta_D, T) + \sum_i n_{E_i} \cdot E(\Theta_{E_i}, T) \quad (2.2)$$

where  $n_D + \sum_i n_{E_i}$  should approximately be equal to the number of atoms in the formula and  $C_p \approx C_v$  in the fitted temperature range. The parameters do not represent the acoustic and optical branches any more, but are rather to be understood as empirical fitting parameters. The formulae for the Debye (with  $x = \Theta_D/T$ ) and Einstein functions read, respectively:

$$D(\Theta_D, T) = 9R \left( \frac{\Theta_D}{T} \right)^3 \int_0^{\Theta_D/T} \frac{e^x x^4}{(e^x - 1)^2} dx \quad (2.3)$$

$$E(\Theta_E, T) = 3R \left( \frac{\Theta_E}{T} \right)^2 \frac{e^{\Theta_E/T}}{(e^{\Theta_E/T} - 1)^2} \quad (2.4)$$

At low temperatures (typically below 10-20 K), the electronic and lattice contribution to the heat capacity are best fitted to a polynomial expression, which is merely a mathematical approach [28]:

$$C_p(T) = \gamma \cdot T + \sum_{n=3,5,7,9} B_n T^n \quad (2.5)$$

where the  $\gamma$ -term, known as Sommerfeld-coefficient, is the electronic contribution, which equals 0 for insulating materials. The other terms represent the lattice contribution to the heat capacity. If the heat capacity rises fast and exceeds the Dulong-Petit limit already at 298.15 K, as is found in two cases in Chapter 6, the Grüneisen parameter and thermal expansion coefficient can be used as correction factors for the anharmonic effects beyond the Dulong-Petit limit, using ref. [29] and substituting  $C_v = 3nR$ :

$$C_p(T) = 3nR \cdot (1 + \alpha_V \cdot \gamma \cdot T) \quad (2.6)$$

where  $\alpha_V$  is the thermal expansion coefficient and  $\gamma$  is the Grüneisen parameter.

In general, a 3% uncertainty on the heat capacity has been used in the error analysis as a conservative error estimate [30, 31].

The standard entropy and low-temperature heat capacity are related via:

$$S^0(T) = \int_0^T \frac{C_p(T)}{T} dT \quad (2.7)$$

The standard entropy value at 298.15 K reported herein was obtained using a numerical integration of the data obtained with QD-PPMS using linear spline interpolation from 0 to 298.15 K. The entropy contribution between 0 K and the lowest measured temperature point of each compound was calculated by integration of a fit through the origin and the lowest measured points. The 3% uncertainty on the measured heat capacity has been used in the error analysis of the standard entropy.

## 2.7. MAGNETOMETRY USING SQUID-VSM

The static magnetic susceptibilities  $M/H$  of several compounds were measured on a MPMS-3 Quantum Design [32] instrument via the SQUID-VSM (superconducting quantum interference device - vibrating sample magnetometer) technique, achieving DC magnetization  $M$  from 2 to 300 K under constant magnetic field  $H$  up to 70 kOe. The samples used were identical to the non-encapsulated heat capacity samples measured on the QD-PPMS instrument, fresh samples or specially encapsulated samples (Chapter 7). Pellets were fixed on a low magnetic contribution quartz support.

Magnetization  $M(T)$  measurements were performed by thermalizing each piece of material using an exchange gas (6N helium) at a partial pressure of 9 Torr. First, cooling was performed without magnetic field applied (Zero Field Cooled, ZFC). After application of static DC magnetic field  $H = 70$  kOe, each measurement point was then obtained by stabilizing the temperature  $T$  and subsequent extraction of  $M(T)$  signal by mechanical oscillation.

The obtained curves allow in most cases to classify the materials as diamagnetic, paramagnetic or (anti-)ferromagnetic. All samples in Chapters 3-6 classify as diamagnetic, and the sample in Chapter 7 is discussed in the chapter.

## 2.8. THERMODYNAMIC MODELLING

Development of thermodynamic models for application calculations starts with assessment of available literature data regarding the phases that exist, and their thermodynamic properties. From this starting point, Gibbs energy descriptions need to be developed. The Gibbs energy functions of all the phases are referred to the enthalpy of the pure elements in their stable state at standard conditions, *i.e.* 298.15 K and 1 bar and the temperature-dependent terms are in Kelvin.

### PURE ELEMENTS

The Gibbs energy functions of the pure elements at temperature  $T$  and in state  $\phi$  with parameters as reported by Dinsdale [33] follow the general equation:

$$G_i^\phi(T) - {}^\circ H_i^{SER}(298.15K) = a + b \cdot T + c \cdot T \cdot \ln T + \sum d_n T^n \quad (2.8)$$

where  $n \in \{2, 3, -1, \dots\}$ .

### STOICHIOMETRIC COMPOUNDS

The Gibbs energy functions have the same form as Equation 2.8:

$$G^\phi(T) - \sum_i n_i^{\phi \circ} H_i^{SER}(298.15K) = a + b \cdot T + c \cdot T \cdot \ln T + \sum d_n T^n \quad (2.9)$$

where  $n_i^\phi$  is the number of atoms of the element in the formula.

### SOLUTION PHASES

For both solid and liquid solution phases, the most general expression for the Gibbs energy is expressed as:

$$G = G_{ref}^\phi + G_{ideal}^\phi + G_{exc}^\phi + G_{phys}^\phi \quad (2.10)$$

Herein,  $G_{ref}^\phi$  refers to a numerical formulation of the Gibbs energy of (liquid) chemical elements or the stoichiometric compounds. In other words, it is the stoichiometric sum of pure end-members. Adding  $G_{ideal}^\phi$  allows to describe an ideal mixture, which equals accounting for the configurational entropy.  $G_{exc}^\phi$  describes the deviation from ideality (a.k.a. excess) using a formalism apt for the application. Finally,  $G_{phys}^\phi$  describes additional physical phenomena like magnetism. Typically, this last term is not applicable in this study. Once the end-members are defined, allowing the calculation of  $G_{ref}^\phi$ ,  $G_{ideal}^\phi$  can be calculated for every mixture based on mole fractions.  $G_{exc}^\phi$  takes a mathematical shape that depends on the used formalism. Two different formalisms and software suites have been used in this work, of which the ionic two-sublattice model is explained in more detail here.

The ionic two-sublattice model as proposed by Hillert *et al.* [34] was used to describe the liquid phase of the Pb-Mo-O system in Chapter 3. In general, the first lattice in this model contains the cationic species, while the second lattice contained anionic and neutral species, including vacancies:



with  $P$  and  $Q$  equal to the average charge of the opposite sub-lattice:

$$P = b \cdot y_B + Q y_{Va^{Q-}} \quad (2.12)$$

$$Q = a \cdot y_A \quad (2.13)$$

and the various site fractions described with the respective  $y$ 's.

### GAS PHASE

The gas phase is described by an ideal mixture. The corresponding Gibbs energy  $G^\phi$  reads:

$$G^\phi = \sum_i y_i^\circ G_i^\phi + RT \sum_i y_i \ln y_i + RT \ln \frac{P}{P^0} \quad (2.14)$$

where the first term includes the fraction of the gas species at any point in the system multiplied by the Gibbs energy of the gaseous species  $i$ , the second term is a mixing entropy term, and the third term the pressure influence as normalised on standard pressure  $P^0$ .



# BIBLIOGRAPHY

- (1) Dronskowski, R.; Kikkawa, S.; Stein, A., *Handbook of Solid State Chemistry, 6 Volume Set*; John Wiley & Sons: 2017.
- (2) Bijvoet, J. M., *Röntgenanalyse van kristallen*; DB Centen: 1948.
- (3) Van Eijck, L.; Cussen, L. D.; Sykora, G. J.; Schooneveld, E. M.; Rhodes, N. J.; Van Well, A. A.; Pappas, C. *Journal of Applied Crystallography* **2016**, 49, 1398–1401.
- (4) Rietveld, H. M. *Journal of Applied Crystallography* **1969**, 2, 65–71.
- (5) Van Laar, B.; Schenk, H. *Acta Crystallographica Section A* **2018**, 74, 88–92.
- (6) Rodríguez-Carvajal, J. *Physica B: Condensed Matter* **1993**, 192, 55–69.
- (7) Le Bail, A.; Duroy, H.; Fourquet, J. L. *Materials Research Bulletin* **1988**, 23, 447–452.
- (8) Momma, K.; Izumi, F. *Journal of Applied Crystallography* **2011**, 44, 1272–1276.
- (9) Rothe, J.; Butorin, S.; Dardenne, K.; Denecke, M. A.; Kienzler, B.; Löble, M.; Metz, V.; Seibert, A.; Steppert, M.; Vitova, T., et al. *Review of Scientific Instruments* **2012**, 83, 043105.
- (10) Ravel, B.; Newville, M. *Journal of Synchrotron Radiation* **2005**, 12, 537–541.
- (11) Zimina, A.; Dardenne, K.; Denecke, M. A.; Doronkin, D. E.; Huttel, E.; Lichtenberg, H.; Mangold, S.; Pruessmann, T.; Rothe, J.; Spangenberg, T., et al. *Review of Scientific Instruments* **2017**, 88.
- (12) Schacherl, B.; Prüssmann, T.; Dardenne, K.; Hardock, K.; Krepper, V.; Rothe, J.; Vitova, T.; Geckeis, H. *Synchrotron Radiation* **2022**, 29, 80–88.
- (13) Christoph, G. G.; Larson, A. C.; Eller, P. G.; Purson, J. D.; Zahrt, J. D.; Penneman, R. A.; Rinehart, G. H. *Acta Crystallographica Section B* **1988**, 44, 575–580.
- (14) Bunău, O.; Joly, Y. *Journal of Physics: Condensed Matter* **2009**, 21, 345501.
- (15) Guda, S. A.; Guda, A. A.; Soldatov, M. A.; Lomachenko, K. A.; Bugaev, A. L.; Lamberti, C.; Gawelda, W.; Bressler, C.; Smolentsev, G.; Soldatov, A. V., et al. *Journal of Chemical Theory and Computation* **2015**, 11, 4512–4521.
- (16) Evans, J., *X-ray absorption spectroscopy for the chemical and materials sciences*; John Wiley & Sons: 2018.
- (17) Hämäläinen, K.; Siddons, D. P.; Hastings, J. B.; Berman, L. E. *Physical review letters* **1991**, 67, 2850.
- (18) Höhne, G. W. H.; Cammenga, H. K.; Eysel, W.; Gmelin, E.; Hemminger, W. *Thermochimica Acta* **1990**, 160, 1–12.

- (19) Beneš, O.; Konings, R. J. M.; Wurzer, S.; Sierig, M.; Dockendorf, A. *Thermochimica Acta* **2010**, *509*, 62–66.
- (20) Boettinger, W. J.; Kattner, U. R.; Moon, K.-W.; Perepezko, J. H. In *Methods for Phase Diagram Determination*, Zhao, J.-C., Ed.; Elsevier Science Ltd: Oxford, 2007, pp 151–221.
- (21) Kilday, M. V. *Journal of Research of the National Bureau of Standards* **1980**, *85*, 467.
- (22) Javorský, P.; Wastin, F.; Colineau, E.; Rebizant, J.; Boulet, P.; Stewart, G. *Journal of Nuclear Materials* **2005**, *344*, 50–55.
- (23) Neumann, F. E. *Annalen der Physik und Chemie* **1831**, *23*, 1–39.
- (24) Kopp, H. *Philosophical Transactions of the Royal Society of London* **1865**, 71–202.
- (25) Leitner, J.; Voňka, P.; Sedmidubský, D.; Svoboda, P. J. T. A. *Thermochimica Acta* **2010**, *497*, 7–13.
- (26) Wu, L.; Schliesser, J.; Woodfield, B. F.; Xu, H.; Navrotsky, A. *The Journal of Chemical Thermodynamics* **2016**, *93*, 1–7.
- (27) Gamsjäger, E.; Wiessner, M. *Monatshefte für Chemie-Chemical Monthly* **2018**, *149*, 357–368.
- (28) Majzlan, J.; Navrotsky, A.; Woodfield, B. F.; Lang, B. E.; Boerio-Goates, J.; Fisher, R. A. *Journal of Low Temperature Physics* **2003**, *130*, 69–76.
- (29) Dekker, A. J., *Solid state physics*; Prentice-Hall: 1957.
- (30) Lashley, J. C.; Hundley, M. F.; Migliori, A.; Sarrao, J. L.; Pagliuso, P. G.; Darling, T. W.; Jaime, M.; Cooley, J. C.; Hults, W. L.; Morales, L., et al. *Cryogenics* **2003**, *43*, 369–378.
- (31) Kennedy, C. A.; Stancescu, M.; Marriott, R. A.; White, M. A. *Cryogenics* **2007**, *47*, 107–112.
- (32) QuantumDesign <https://www.qdusa.com/products/mpms3.html>, SQUID Magnetometer Quantum Design MPMS3, Date of last access: 2023-08-15, 2023.
- (33) Dinsdale, A. T. *Calphad* **1991**, *15*, 317–425.
- (34) Hillert, M.; Jansson, B.; Sundman, B.; Ågren, J. *Metallurgical Transactions A* **1985**, *16*, 261–266.

# 3

## THE Pb-Mo-O SYSTEM

*A combined experimental and modelling study into the Pb-Mo-O system has been conducted in view of the safety analysis for lead-cooled nuclear systems. The thermal expansion and low-temperature heat capacity of the ternary compounds  $\text{PbMoO}_4$  and  $\text{Pb}_2\text{MoO}_5$  have been determined experimentally, as well as the melting enthalpy of  $\text{PbMoO}_4$ . Moreover, XANES measurements have confirmed the hexavalent oxidation state of Mo in  $\text{PbMoO}_4$  and  $\text{Pb}_2\text{MoO}_5$ . A thermodynamic model of the ternary system including the ternary phases  $\text{PbMoO}_4$ ,  $\text{Pb}_2\text{MoO}_5$  and  $\text{Pb}_5\text{MoO}_8$  has also been developed in this work based on the CALPHAD methodology. For the first time, an ionic two-sublattice model is used for the liquid phase, while the compound energy formalism is used for the solid phases.*

---

This chapter is based on: A. van Hattem, R. Dankelman, E. Colineau, J.-C. Griveau, K. Dardenne, J. Rothe, S.D. Couweleers, R.J.M. Konings and A.L. Smith *Experimental investigations and thermodynamic modelling of the ternary system Pb-Mo-O*. Journal of Alloys and Compounds 1003 (2024): 175588

### 3.1. INTRODUCTION AND CONTEXT

Recently, the Pb-Mo-O system has received renewed attention in the field of nuclear engineering for lead-cooled fast reactors (LFRs) and other nuclear systems [1–8]. As explained in Chapter 1, reactor designs differ in fuel [9, 10], neutron spectrum and thus fission product chemistry [11, 12]. In Europe, mixed oxide fuel ((U,Pu)O<sub>2</sub>) is the fuel of reference for LFRs [10]. The numerous fission products that will form during operation, include the high-yield fission products Mo, together with Cs, Te and I. The mentioned fission products tend to migrate to the outer rim of the fuel pin [13], where they form the so-called JOG-layer above 7-8% burn-up as found in post-irradiation experiments and thermochemical calculations for breeder reactors [13–15].

More general, although the ternary system Pb-Mo-O has been the subject of many investigations, driven both by fundamental interests and diverse technological applications [16–21], some fundamental properties of these materials have never been experimentally studied and a recent thermodynamic model is lacking in literature. Already in 1921, a phase diagram of the PbO-PbMoO<sub>4</sub> section has been published by Jaeger and Germs [22], and thermodynamic studies into the Pb-Mo-O system have recently been performed to understand the formation and thermochemical stability of passive oxide films formed during operation [6, 7], although some experimental gaps remain to be filled.

In this chapter, the literature on the Pb-Mo-O system is thoroughly reviewed, several physical properties are measured and reported for the first time and a full thermodynamic model is developed. This thermodynamic model of the Pb-Mo-O is of interest both for the accidental scenario of cladding failure as part of the multi-element chemistry [23], but also to understand structural steel-coolant interactions, since Pb and the oxygen dissolved in it can be corrosive for structural and cladding materials, which might be Mo or Mo-containing [10, 24–26].

## 3.2. REVIEW OF LITERATURE DATA ON THE Pb-Mo-O SYSTEM

### 3.2.1. CONSTITUTING BINARY SUB-SYSTEMS

A thermodynamic description of the Pb-O system was published by Risold *et al.* [27]. Since then, new experimental and modelling results were reported. A thermodynamic description of the Mo-O system is available in the TAF-ID database [28]. For the Pb-Mo system, no thermodynamic description is known, though a tentative phase diagram was found [29]. The binary ( $x, T$ )-diagrams are shown in Figure 3.1.

#### BINARY Pb-O SYSTEM

A thermodynamic modelling assessment of the Pb-O system was published by Risold *et al.* [27]. This work assessed the thermodynamics of the Pb-O system, complementing a review of structural studies by Wriedt [30]. The Pb-O system includes the following binary compounds: PbO(L) (litharge, red), PbO(M) (massicot, yellow), Pb<sub>3</sub>O<sub>4</sub>, Pb<sub>12</sub>O<sub>17</sub>, Pb<sub>12</sub>O<sub>19</sub> and PbO<sub>2</sub>. Risold *et al.* modelled the liquid phase in the ionic two-sublattice model. Since the publication by Risold *et al.* in 1998, some additional thermodynamic investigations were reported.

Kobertz studied yellow PbO [31]. He reported vaporisation behaviour and measured

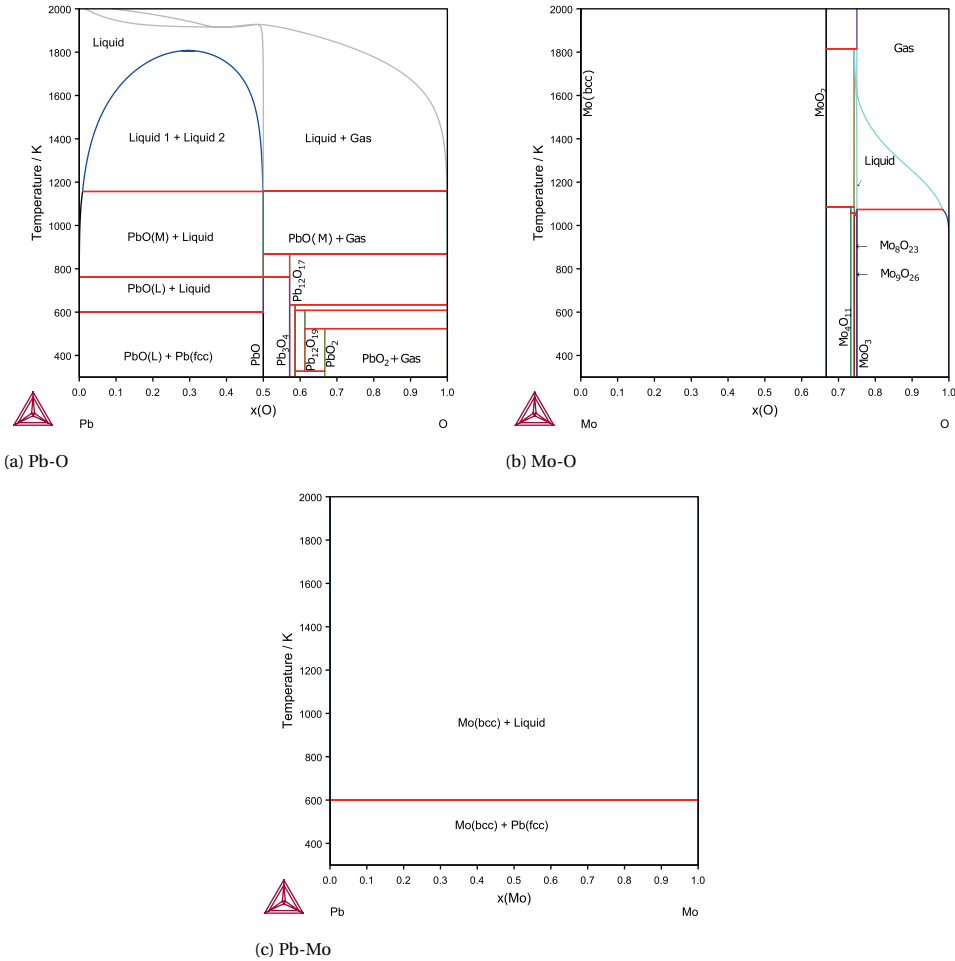


Figure 3.1: Binary phase diagrams used in the current work.

the heat capacity of yellow PbO using DSC in the temperature range 298-1100 K. However, the heat capacity function for PbO he reported deviates significantly from previous results, see Figure A.1. Since the heat capacity value reached at melting cannot be matched to existing enthalpy increment data [32, 33] and the total heat capacity as calculated using *ab initio* methods also supports the existing data set [34], the data set of Risold is retained. Moreover, Liu *et al.* did some DSC experiments in the Pb-PbO phase diagram [35]. Their results are in line with the phase diagram by Risold *et al.* [27].

Ganesan *et al.* measured the standard molar Gibbs free energy of formation of PbO(s) via electromotive force measurements (e.m.f.) [36]. The solubility of oxygen in liquid lead was investigated at least twice more: Ganesan *et al.* derived the solubility of oxygen in liquid Pb in the temperature range 815 - 1090 K from e.m.f. measurements [37],

while Lim *et al.* studied the solubility of oxygen by coulometric titration [38] in the range 623 - 823 K. In 2005, a thermodynamic assessment of the ternary Cu-Pb-O system was published [39], in which the high-temperature equilibria between Pb and PbO were re-optimised compared to the assessment by Risold on the basis of a selection of available solubility data. This re-optimisation was deemed necessary to be able to model the ternary Cu-Pb-O system accurately. However, the solubility of oxygen in molten lead as recommended in the *Handbook on Lead-bismuth Eutectic Alloy and Lead Properties, Materials Compatibility, Thermohydraulics and Technologies* [40] is better reproduced by the model of Risold *et al.* In this work, the model of Risold *et al.* [27] and the selection of [40] are retained. A visualisation of the difference is given in Figure A.2.

It is important to note that we also found two typographic errors in the publication by Risold *et al.*. For  $\text{Pb}_3\text{O}_4\text{-T}$ , the equation should read:

$$G(T) = -802140 + 1112 \cdot T/K - 194.5 \cdot T/K \cdot \ln(T/K) - 0.0025 \cdot (T/K)^2 + 1566000 \cdot (T/K)^{-1} \quad (3.1)$$

where the fourth term changed sign. The function  $G_{\text{Pb}}^{0,G}$  for  $2000 < T < 3700$  K should have a minus sign for the term with  $T^2$ .

### BINARY Mo-O SYSTEM

The thermodynamic description of the Mo-O system is taken from the work of Corcoran *et al.* [41], with the updated liquid phase parameters by Kauric [42]. In this model the compounds  $\text{MoO}_2$ ,  $\text{Mo}_4\text{O}_{11}$ ,  $\text{Mo}_8\text{O}_{23}$ ,  $\text{Mo}_9\text{O}_{26}$  and  $\text{MoO}_3$  are treated as stoichiometric. By using this model, we assure that the results of this study are consistent with work on the Ba-Mo-O system [43] as well as the international TAF-ID project [28].

### BINARY Pb-Mo SYSTEM

Mo is stable as bcc (A2) phase, while Pb is stable as fcc (A1) phase [44]. The metals are practically immiscible. A phase diagram of Mo-Pb is reported in the Landolt-Börnstein New Series [29]. As cited by [29], Parkman *et al.* found that less than  $10^{-4}$  at-% Mo is soluble in liquid Pb between 1150 and 1280 K, while Alden *et al.* found solubility of less than 0.011 at-% Mo at 1479 K [45]. Landolt-Börnstein constructed its phase diagram based on estimations by Brewer *et al.* [46] and improvements by Massalski *et al.* [47]. Recently, two studies were published reporting co-deposition to form a film [48, 49]. It seems possible to form a thin film or compound with composition  $\text{Mo}_3\text{Pb}$ , that is thermally stable up to a minimum of 523 K and a maximum of 573 K [48]. This phase is not taken into account in this assessment: first, it is not reported as bulk compound; second, no thermodynamic information is available; last, a LFR cooled with liquid Pb operates at temperatures above the melting point of lead, so this phase would not be thermally stable under operating conditions. The Pb-Mo system has been modelled herein using arbitrarily high thermodynamic parameters to destabilise the solution phases, as given in Table 3.5. The resulting phase diagram was already shown in Figure 3.1.

### 3.2.2. STRUCTURAL DATA FOR THE TERNARY Pb-Mo-O PHASES

The number of compounds in the Pb-Mo-O system is rather limited. Recently, isotherms at 773 K and 998 K were investigated by Aiswarya *et al.* [6]. The reader is referred to their

literature review for the discussion of the literature before 2017. Here, the structural data are summarised:  $\text{PbMoO}_4$  and  $\text{Pb}_2\text{MoO}_5$  are established for over a century [22], while  $\text{Pb}_5\text{MoO}_8$  was for the first time reported in 1965 [50]. Later on,  $\text{PbMo}_5\text{O}_8$  [51] and  $\text{Pb}_3\text{Mo}_{16}\text{O}_{24}$  [52] were reported. Aiswarya *et al.* [6] tried to reproduce the syntheses reported for  $\text{PbMo}_5\text{O}_8$  and  $\text{Pb}_3\text{Mo}_{16}\text{O}_{24}$ , but they were not able to synthesise  $\text{PbMo}_5\text{O}_8$  using the reaction conditions reported by [51], nor using lower temperatures.  $\text{Pb}_3\text{Mo}_{16}\text{O}_{24}$  was only partially found via synthesis at 1215 K for 240 h, starting from Mo,  $\text{MoO}_3$  and  $\text{PbMoO}_4$  in a closed ampoule. A similar result was found by Xu [53]. Aiswarya *et al.* also found that a synthesis temperature of 998 K is insufficient [6]. According to Feja [54], the composition  $\text{Pb}_3\text{Mo}_{16}\text{O}_{24}$  shifts to  $\text{PbMo}_5\text{O}_8$  at 1523 K. Besides these compounds, the perovskite phase  $\text{PbMoO}_3$  was also reported recently [55]. However, since  $\text{PbMoO}_3$  is only reported to form as high temperature-high pressure phase, it is excluded from the present model. The ( $p$ ,  $T$ )-conditions (1273 K, 7 GPa, [55]) typically necessary for the formation of  $\text{PbMoO}_3$  do not occur upon release of Mo from the fuel pin upon cladding failure nor in the case of the chemical interaction between coolant and structural materials. Moreover, experiments with partial reduction under hydrogen at 773 K and 998 K on  $\text{PbMoO}_4$  resulted in a mixture of Pb,  $\text{MoO}_2$  and  $\text{PbMoO}_4$  [6].

Thus, the hexavalent Mo phases  $\text{PbMoO}_4$ ,  $\text{Pb}_2\text{MoO}_5$  and  $\text{Pb}_5\text{MoO}_8$  are left for consideration, together with the exotic couple  $\text{Pb}_3\text{Mo}_{16}\text{O}_{24}$ - $\text{PbMo}_5\text{O}_8$ . The reported crystallographic data (at ambient pressure) for each phase are listed in Table 3.1.  $\text{Pb}_2\text{MoO}_5$  and  $\text{Pb}_5\text{MoO}_8$  are classified as compounds containing chains of  $\text{OPb}_4$  tetrahedra [56]. The exotic couple  $\text{Pb}_3\text{Mo}_{16}\text{O}_{24}$ - $\text{PbMo}_5\text{O}_8$  was not further included in the thermodynamic assessment, since Aiswarya *et al.* were not able to reproduce the claims of their formation [6] and because of the lack of experimental thermodynamic data. (In)homogeneity of the compounds was investigated for both  $\text{PbMoO}_4$  [57] and  $\text{Pb}_2\text{MoO}_5$  [58]. The small extent of the homogeneity range of  $\text{PbMoO}_4$  (reported as 49.85-50.50 mol-%  $\text{MoO}_3$ ) allows us to neglect this effect herein and treat the compounds as line compounds.

### 3.2.3. THERMODYNAMIC DATA FOR TERNARY Pb-Mo-O PHASES

Of the *supra* selected compounds, thermodynamic data are only available for  $\text{PbMoO}_4$  and  $\text{Pb}_2\text{MoO}_5$ , so these are the only two compounds discussed here. For reported melting temperatures, the reader is referred to Table 3.8.

#### PbMoO<sub>4</sub>

The standard enthalpy of formation of  $\text{PbMoO}_4$  was investigated many times, see Table 3.2; the most recent investigation is by Aiswarya *et al.* [7], who reviewed all earlier data. The data reported by Muldrow and Hepler [62], Dellien *et al.* [63], Bissengaliyeva *et al.* [64] and Aiswarya *et al.* [7], based on direct calorimetric measurements, are used to calculate a weighted mean that is selected as reference for the present thermodynamic model, yielding  $\Delta_f H_m^\circ(\text{PbMoO}_4, \text{cr}, 298.15 \text{ K}) = -(1052.9 \pm 0.5) \text{ kJ} \cdot \text{mol}^{-1}$ . The other values are not used in the current weighted mean, since they are already an assessment or because it was not a direct enthalpy measurement.

The standard entropy of  $\text{PbMoO}_4$  at 298.15 K is given in the NBS Tech Note 270-4 (1969) to be  $S_m^\circ = 166.1 \text{ J} \cdot \text{K}^{-1} \cdot \text{mol}^{-1}$  [65], based on low-temperature heat capacity measurements by Weller and Kelley (1964) in the temperature range 51 to 298 K [66]. Bis-

Phase	Mo ox. state	Space group	Cell parameters (Å or °)	Ref.
PbMoO <sub>4</sub>	+6	<i>I</i> 4 <sub>1</sub> / <i>a</i> (88)	<i>a</i> = 5.424 <i>c</i> = 12.076	[59]
Pb <sub>2</sub> MoO <sub>5</sub>	+6	<i>C</i> 2/ <i>m</i> (12)	<i>a</i> = 14.2221(11) <i>b</i> = 5.7852(5) <i>c</i> = 7.3262(6) <i>β</i> = 114.168(2)	[60]
Pb <sub>5</sub> MoO <sub>8</sub>	+6	<i>P</i> 2 <sub>1</sub> / <i>c</i> (14)	<i>a</i> = 15.330(1) <i>b</i> = 11.829(2) <i>c</i> = 11.631(2) <i>β</i> = 90.104(14)	[61]
PbMo <sub>5</sub> O <sub>8</sub>	+2.8	<i>P</i> 2 <sub>1</sub> / <i>c</i> (14)	<i>a</i> = 9.993(2) <i>b</i> = 9.247(1) <i>c</i> = 7.536(2) <i>β</i> = 109.39(2)	[51]
Pb <sub>3</sub> Mo <sub>16</sub> O <sub>24</sub>	+2.625	<i>P</i> 4/ <i>mnc</i> (128)	<i>a</i> = 9.615(1) <i>c</i> = 11.362(3)	[52]

Table 3.1: Crystallographic data at ambient pressure on the reported compounds in the Pb-Mo-O system.

sengaliyeva calculated a value of  $S_m^\circ = (168.33 \pm 2.06) \text{ J} \cdot \text{K}^{-1} \cdot \text{mol}^{-1}$  when measuring the low-temperature heat capacity from 320 K down to 55 K [67]; when they also measured the region from 80 to 4.3 K, they obtained a value of  $S_m^\circ = (161.5 \pm 0.3) \text{ J} \cdot \text{K}^{-1} \cdot \text{mol}^{-1}$  [64, 68]. The latter value of Bissengaliyeva *et al.* is preferred over the former ones, since it includes actual measured data between 4.3 and 55 K. A calculation with all data, including new data obtained in this work, yielded for the standard entropy:  $S_m^\circ = (160.9 \pm 0.3) \text{ J} \cdot \text{K}^{-1} \cdot \text{mol}^{-1}$ , where the uncertainty has been estimated to be equal or better than the uncertainty reported by Bissengaliyeva *et al.* [68].

Aiswarya *et al.* also published a study in which they carried out e.m.f. measurements, yielding the Gibbs energy of reaction between 772 and 1017 K [6]. As is given in Table 3.2, the enthalpy of formation at 298.15 K deduced using a second-law analysis deviates from the other values. A third-law analysis performed in the current work yields a value closer to the selected value, but also a small drift was observed. The data are further discussed in Appendix A.

Heat capacity measurements at standard and high temperatures are reported by several authors. Weller and Kelley give a value of  $C_p(298.15 \text{ K}) = (119.7 \pm 2.1) \text{ J} \cdot \text{K}^{-1} \cdot \text{mol}^{-1}$  [66], while Bissengaliyeva *et al.* report  $C_p(298.15 \text{ K}) = (119.4 \pm 0.13) \text{ J} \cdot \text{K}^{-1} \cdot \text{mol}^{-1}$  [67]. Aiswarya *et al.* reported heat capacity measurements using DSC over the temperature range 313-798 K as well [6]. At 298.15 K, the equation of Aiswarya *et al.* yields  $C_p(298.15 \text{ K}) = 116.23 \text{ J} \cdot \text{K}^{-1} \cdot \text{mol}^{-1}$ . To avoid a small mismatch between low- and high-temperature heat capacity data, the heat capacity function was re-fitted to both the high-temperature data and a part of the low-temperature data:

$$C_p / \text{J} \cdot \text{K}^{-1} \cdot \text{mol}^{-1} = 112.192 + 65.55 \cdot 10^{-3} \cdot T / \text{K} - 965693 \cdot (T / \text{K})^{-2} - 2.317 \cdot 10^{-5} \cdot (T / \text{K})^2 \quad (3.2)$$

Reference	$\Delta_f H_m^\circ$ (298.15 K) / $\text{kJ}\cdot\text{mol}^{-1}$	Method
Muldrow & Hepler, [62]	$-1049.1 \pm 3.7$	Precipitation reaction calorimetry
Dellien <i>et al.</i> , [63]	$-1052.66 \pm 0.5$	Solution calorimetry
Bissengaliyeva [64]	$-1051.2 \pm 4.3$	High-temperature melt calorimetry
Aiswarya <i>et al.</i> , [7]	$-1059.6 \pm 2.2$	Solution calorimetry
This work, assessment	<b><math>-1052.9 \pm 0.5</math></b>	Recommended, see text
Wagman <i>et al.</i> , <sup>+</sup>	$-1051.9 \pm 0.85$	Compilation
O'Hare <i>et al.</i> , <sup>+</sup>	$-1025.08$	Estimation
Feja, [54]	$-1042.1$	Estimation
Aiswarya <i>et al.</i> , [6]	$-1036.6 \pm 0.7$	e.m.f., 2 <sup>nd</sup> law
Aiswarya <i>et al.</i> , [6]	$-1055.5 \pm 1.6$	e.m.f., 3 <sup>rd</sup> law*

Table 3.2: Enthalpy of formation  $\Delta_f H_m^\circ$  ( $\text{kJ}\cdot\text{mol}^{-1}$ ) of  $\text{PbMoO}_4$ . The value for this work was calculated using Equations A.1 and A.2. Uncertainties as reported by the original sources.<sup>+</sup> cited via [7]. \* analysis in this work, see text for explanation.

with  $C_p(298.15 \text{ K}) = 118.8 \text{ J}\cdot\text{K}^{-1}\cdot\text{mol}^{-1}$ .

### $\text{Pb}_2\text{MoO}_5$

The enthalpy of formation of  $\text{Pb}_2\text{MoO}_5$  is estimated by Feja to be  $\Delta_f H_m^\circ(\text{Pb}_2\text{MoO}_5, \text{cr}, 298.15 \text{ K}) = -1294.6 \text{ kJ}\cdot\text{mol}^{-1}$  [54]. More recently, Aiswarya *et al.* reported the enthalpy of formation as determined by solution calorimetry to be  $\Delta_f H_m^\circ(\text{Pb}_2\text{MoO}_5, \text{cr}, 298.15 \text{ K}) = -(1274.7 \pm 2.3) \text{ kJ}\cdot\text{mol}^{-1}$  [7]. These two values are the only values known. The value of Aiswarya *et al.* is favoured, since it is based on experimental measurement.

The standard entropy at 298.15 K was estimated by Feja to be  $S_m^\circ = 209 \text{ J}\cdot\text{K}^{-1}\cdot\text{mol}^{-1}$  [54]. This is in the expected order of magnitude as calculated from the method of Glasser [69], yielding  $215.4 \text{ J}\cdot\text{K}^{-1}\cdot\text{mol}^{-1}$ . No experimental data (low-temperature heat capacity) are reported until now; *infra* the value obtained in the current work will be discussed, *viz.*  $S_m^\circ = (244.8 \pm 7.4) \text{ J}\cdot\text{K}^{-1}\cdot\text{mol}^{-1}$ .

Aiswarya *et al.* published a study where they performed e.m.f. measurements, yielding the Gibbs energy of reaction between 741 and 1021 K [6]. Again, these e.m.f. results are discussed in-depth in Appendix A.

The heat capacity at high temperature was reported twice. In 2004, Feja published an estimation [54]. Aiswarya published a measurement using DSC in the range 308 to 798 K [7].

$$C_p \pm 6.2/\text{J}\cdot\text{K}^{-1}\cdot\text{mol}^{-1} = 169.20 + 66.69 \cdot 10^{-3} \cdot T/\text{K} - 1.99 \cdot 10^6 \cdot (T/\text{K})^{-2} \quad (3.3)$$

At 298.15 K, the equation of Aiswarya *et al.* yields  $C_p(298.15 \text{ K}) = 166.7 \text{ J}\cdot\text{K}^{-1}\cdot\text{mol}^{-1}$ . This curve matches well with the low-temperature heat capacity measured in this work (*vide infra*), so this fit is retained.

### THERMODYNAMIC PROPERTIES OF GASEOUS SPECIES

A mass spectrometry study was reported by Nikolaev *et al.* [70]. The authors refer to three earlier publications that report that upon heating  $\text{PbMoO}_4(\text{s})$ , mass spectrometric investigations indicate that congruent vaporisation, *i.e.*  $\text{PbMoO}_4(\text{s}) = \text{PbMoO}_4(\text{g})$  is practically the only occurring process. They conclude the gas phase over lead molybdate

to consist mostly of  $\text{PbMoO}_4(\text{g})$  molecules, but also of minor amounts of  $\text{PbMo}_2\text{O}_7(\text{g})$ ,  $\text{Pb}_2\text{MoO}_5(\text{g})$ ,  $\text{Mo}_3\text{O}_9(\text{g})$ ,  $\text{Pb}_2\text{O}_2(\text{g})$ ,  $\text{PbO}(\text{g})$  and atomic  $\text{Pb}(\text{g})$ .

A combined mass spectrometry and density functional study of the gas phase of the  $\text{PbO-MoO}_3$  system was published by Kunkel *et al.* [71] more recently. The authors made three samples, mixing  $\text{PbO}$  and  $\text{MoO}_3$  in the ratios (2:3), (1:1) and (3:1). They detected four parent ions ( $\text{PbMo}_3\text{O}_{10}^+$ ,  $\text{PbMo}_2\text{O}_7^+$ ,  $\text{PbMoO}_4^+$  and  $\text{Pb}_2\text{Mo}_2\text{O}_7^+$ ). They also compare the experimental enthalpies of formation of the gaseous molecules with quantum chemical calculations, see also Table A.1. To the best of our knowledge, no function of experimental vapour pressure against temperature is reported in the literature.

### 3.2.4. PHASE DIAGRAM DATA IN THE Pb-Mo-O SYSTEM

Over the time span of a century, several phase diagram studies were reported. Combined, they provide a rather well-established insight into the pseudo-binary section  $\text{PbO-MoO}_3$ , while leaving some open questions for some specific regions. The first report is by Jaeger and Germs (1921), who investigated the phase diagram section  $\text{PbO-PbMoO}_4$  [22]. Besides the end-members, they found  $\text{Pb}_2\text{MoO}_5$ . Belyaev and Smolyaninov (1962) report the whole section  $\text{PbO-MoO}_3$  [72]. The authors found the same compounds as Jaeger and Germs. Kunev *et al.* published a paper in 1966 on the  $\text{MoO}_3\text{-PbMoO}_4$  system [73]; they found a single eutectic. The existence of  $\text{Pb}_5\text{MoO}_8$  was first reported in 1965 by Doyle and Forbes [50]. Bukhalova *et al.* studied the section  $\text{PbO-MoO}_3$  in 1971 [74] and reported only  $\text{PbMoO}_4$  and  $\text{Pb}_2\text{MoO}_5$ . Eissa *et al.* reported in 1996 on the phase diagram  $\text{PbO}_2\text{-Pb-MoO}_3$  in air [75]. Nihtianova *et al.* studied the  $\text{Pb}_5\text{MoO}_8$  crystal growth together with the phase diagram closely to the  $\text{Pb}_5\text{MoO}_8$  composition in 1997 [76].

Feja (2004) investigated the phase fields in the  $\text{Pb-Mo-O}$  section [54]. The author investigated the oxygen rich phase field, which is above the line  $\text{Pb-MoO}_2$ . Given the temperatures necessary to synthesise ternary compounds, the lead oxides of concern are limited to  $\text{PbO}$  and  $\text{Pb}_3\text{O}_4$ . Phase fields  $\text{Pb}_3\text{O}_4\text{-MoO}_3\text{-PbMoO}_4$  and  $\text{Pb}_3\text{O}_4\text{-PbMoO}_4\text{-Pb}_2\text{MoO}_5$  were found to be unstable at 773 K and atmospheric pressure. At 773 K, the coexistence line  $\text{Pb}_2\text{MoO}_5\text{-Pb}_3\text{O}_4$  was found to exist, besides the section  $\text{PbO-MoO}_3$ . Within the  $\text{Pb-MoO}_2\text{-MoO}_3\text{-PbO}$  boundaries and at 773 K, lines between  $\text{Pb}_5\text{MoO}_8$  and  $\text{Pb}$ ,  $\text{Pb}_2\text{MoO}_5$  and  $\text{Pb}$ , and  $\text{PbMoO}_4$  and  $\text{Pb}$  were found, besides the  $\text{PbMoO}_4\text{-MoO}_2$  line. Aiswarya *et al.* studied the phase fields of the  $\text{Pb-Mo-O}$  section at 773 and 998 K in 2017 [6]. They focused on the field between  $\text{Pb-PbO-MoO}_3\text{-Mo}$ . At 773 K, they found the compound  $\text{Pb}_5\text{MoO}_8$  to be not (yet) stable. At 998 K, it was found to be stable.

### 3.2.5. THERMODYNAMIC MODELLING

Feja applied a modelling approach in his study of the  $\text{Pb-Mo-O}$  system [54] using Redlich-Kister-Murkschano-models for the liquid phase, but no parameters were reported. The  $\text{Mo(VI)}$ -compounds  $\text{PbMoO}_4$ ,  $\text{Pb}_2\text{MoO}_5$  and  $\text{Pb}_5\text{MoO}_8$  are included, as well as an attempt to model the  $\text{PbMo}_5\text{O}_8$  phase.

### 3.2.6. THERMAL EXPANSION STUDIES

Some crystallographic studies into  $\text{PbMoO}_4$  and  $\text{Pb}_2\text{MoO}_5$  at non-ambient temperature are reported in the literature. For  $\text{PbMoO}_4$ , the crystal structure was studied using X-ray diffraction in the range 303 - 623 K [77]. The average coefficients of linear thermal ex-

pansion were found to be  $\alpha_a = 12.19 \cdot 10^{-6} \text{ K}^{-1}$  and  $\alpha_c = 24.45 \cdot 10^{-6} \text{ K}^{-1}$ . The authors cite unpublished work that reported  $\alpha_a = 10.38 \cdot 10^{-6} \text{ K}^{-1}$  and  $\alpha_c = 25.31 \cdot 10^{-6} \text{ K}^{-1}$  using interferometric measurements. Recently, Achary *et al.* used neutron diffraction to study the evolution of the lattice parameters between 5 and 300 K [78]. They found the average axial thermal expansion coefficients in this temperature region to be  $\alpha_a = 9.39 \cdot 10^{-6} \text{ K}^{-1}$  and  $\alpha_c = 20.61 \cdot 10^{-6} \text{ K}^{-1}$ . The volumetric thermal expansion is plotted for comparison in Figure 3.4. For completeness, the first study reporting linear thermal expansion is mentioned here too: Argyle *et al.* measured the dilation of  $\text{PbMoO}_4$  [79], but it is unclear how to use and how to compare their reported data to the other data, since  $\text{PbMoO}_4$  expands anisotropically. If their data is taken as unity for  $\alpha_a$  and multiplied by an anisotropy factor of 2.5 for  $\alpha_c$ , their data agrees with the data obtained in the current work; this reading of their paper remains speculative, however. Therefore, we did not include their data in Figure 3.4.

The crystal structure of  $\text{PbO} \cdot \text{PbXO}_4$  with  $X = \text{S, Cr, Mo}$  at 5 K was reported by Mentzen *et al.* [80], using neutron diffraction. To the best of our knowledge, this is the only diffraction study of  $\text{Pb}_2\text{MoO}_5$  at non-ambient temperature.

### 3.3. EXPERIMENTAL RESULTS

#### 3.3.1. STRUCTURAL ANALYSIS

$\text{PbMoO}_4$  and  $\text{Pb}_2\text{MoO}_5$  were prepared and characterised in this work following the procedures described in detail at the end of this chapter. The obtained diffraction patterns for  $\text{PbMoO}_4$  and  $\text{Pb}_2\text{MoO}_5$  are shown in Figure 3.2. No unaccounted peaks were found on the X-ray diffraction patterns. The cell parameters as obtained after refinement of the models against the data are listed in Table 3.3. The cell parameter values are in line with those reported in literature, *e.g.* the values in Table 3.1.

Compound	a (Å)	b (Å)	c (Å)	$\beta$ (°)
$\text{PbMoO}_4$	5.4365(10)	5.4365(10)	12.1109(3)	90
$\text{Pb}_2\text{MoO}_5$	14.2168(5)	5.7866(2)	7.3292(2)	114.142(2)

Table 3.3: Cell parameters of the powders used in this research as found after refinement of the models against the X-ray diffraction data. The space groups for  $\text{PbMoO}_4$  and  $\text{Pb}_2\text{MoO}_5$  are  $I4_1/a$  (88) and  $C2/m$  (12), respectively. Both compounds have  $Z = 4$ .

#### 3.3.2. X-RAY ABSORPTION SPECTROSCOPY AT THE MO K-EDGE

The oxidation state of Mo was studied via XANES spectroscopy. Since no XANES measurements on  $\text{Pb}_2\text{MoO}_5$  were reported previously, the  $\text{Pb}_2\text{MoO}_5$  K-edge was probed and is shown in Figure 3.3. In this figure,  $\text{Pb}_2\text{MoO}_5$  is compared to  $\text{Mo}^0$ ,  $\text{Mo}^{\text{IV}}\text{O}_2$ ,  $\text{Mo}^{\text{VI}}\text{O}_3$  and  $\text{PbMo}^{\text{VI}}\text{O}_4$ . The derived absorption edge threshold and pre-peak features are listed in the table in Figure 3.3. The measured  $E_0$  value for  $\text{Pb}_2\text{MoO}_5$  is close to that of  $\text{PbMoO}_4$  and  $\text{MoO}_3$ , indicating a Mo valence state of +6. The intrinsic features of  $\text{Mo}^0$ ,  $\text{Mo}^{\text{IV}}$ ,  $\text{Mo}^{\text{VI}}$  can be seen in the increase in  $E_0$ -position with increasing Mo valence state. Moreover, while Mo and  $\text{MoO}_2$  have a simple edge, Mo(VI) in  $\text{MoO}_3$  has a characteristic pre-edge feature. This pre-edge feature is also found in  $\text{PbMoO}_4$  and  $\text{Pb}_2\text{MoO}_5$  and originates from the tetrahedral environment of the oxygen atoms around the Mo centre [81, 82].

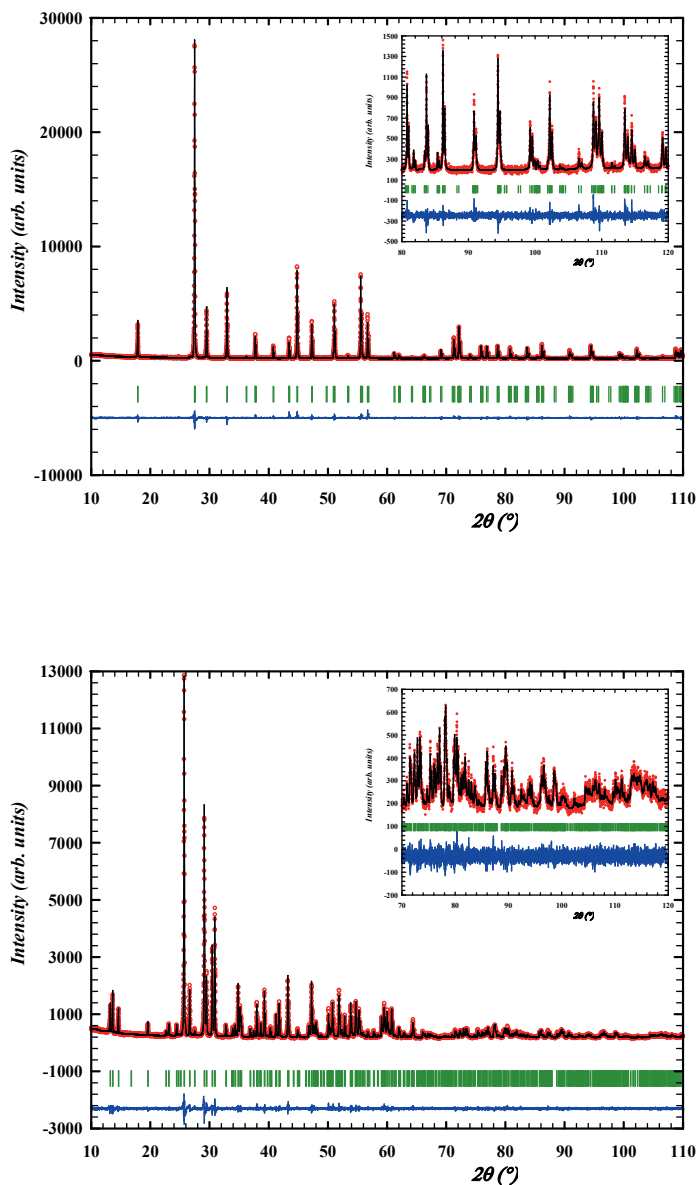


Figure 3.2: Experimental ( $Y_{obs}$ , in red) and calculated ( $Y_{calc}$ , in black) XRD patterns of  $\text{PbMoO}_4$  (top) and  $\text{Pb}_2\text{MoO}_5$  (bottom) at ambient temperature. The difference between the calculated and the experimental intensities  $Y_{obs} - Y_{calc}$  is shown in blue. The angular positions of the Bragg reflections are shown in green. Measurement at  $\lambda = \text{Cu } K\alpha$ .

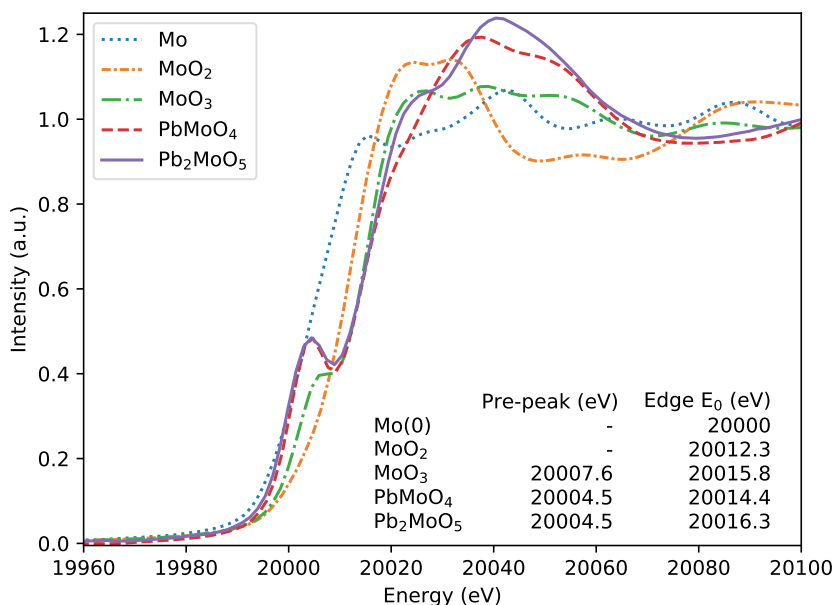


Figure 3.3: X-ray Absorption Near-Edge Structure (XANES) spectra around the Mo K-edge with energy values of the pre-peak and edge in the normalised XANES spectra. The edges are determined based on the inflection points in the normalised XANES spectra at the Mo K-edge. The pre-peaks are determined via the maximum.

### 3.3.3. THERMAL EXPANSION OF $\text{PbMoO}_4$ AND $\text{Pb}_2\text{MoO}_5$

High-temperature XRD measurements were performed on  $\text{PbMoO}_4$  and  $\text{Pb}_2\text{MoO}_5$ . The obtained volumetric thermal expansion of  $\text{PbMoO}_4$  is plotted in Figure 3.4. As can be seen in this figure, the current data between 298 K and 1173 K is in line with the data reported by Suryanarayana and Deshpande [77] and joins with the low-temperature data of Achary *et al.* [78]. In the inset of Figure 3.4, the expansion of the cell parameters  $a$  ( $=b$ ) and  $c$  relative to 298 K is shown. Based on this fit, the thermal expansion values between 298 and 1173 K of the  $a$ - and  $c$ -axes are given by  $12.3 \cdot 10^{-6} \text{ K}^{-1}$  and  $30.5 \cdot 10^{-6} \text{ K}^{-1}$ . Using the same fitting method, the volumetric thermal expansion gives  $56 \cdot 10^{-6} \text{ K}^{-1}$ . As can be seen from the fits, the behaviour is slightly non-linear: upon increasing temperature, there is an increasing expansion rate for the cell parameters and thus for the volume. The volume of  $\text{PbMoO}_4$  is best described with the second order polynomial:

$$V(T) = 353.9 + 0.0117 \cdot T/K + 6.34 \cdot 10^{-6} \cdot (T/K)^2 \quad (3.4)$$

with temperature in Kelvin and the volume in  $\text{\AA}^3$ . Overall, the parameters obtained in this work are consistent with the values found in literature as discussed *supra*. The lattice parameters at non-ambient temperature are given in Table A.2

The volumetric thermal expansion of  $\text{Pb}_2\text{MoO}_5$  is plotted in Figure 3.4.  $\text{Pb}_2\text{MoO}_5$

crystallises in the monoclinic space group  $C2/m$  (12). The  $a$ -axis evolves linearly with temperature, while the expansion of the  $b$  and  $c$  axis are non-linear. Describing the whole temperature range 298 K till 1073 K linearly, one obtains for the thermal expansion coefficient of the lattice parameters  $a$ ,  $b$  and  $c$ ,  $8.6 \cdot 10^{-6} \text{ K}^{-1}$ ,  $29 \cdot 10^{-6} \text{ K}^{-1}$  and  $40 \cdot 10^{-6} \text{ K}^{-1}$ , respectively. Using a polynomial of degree 2, the volume of  $\text{Pb}_2\text{MoO}_5$  is described by:

$$V(T) = 540 + 0.0295 \cdot T/K + 1.21 \cdot 10^{-5} \cdot (T/K)^2 \quad (3.5)$$

with temperature in Kelvin and the volume in  $\text{\AA}^3$ . The cell parameters at non-ambient temperature are given in Table A.3.

### 3.3.4. MELTING ENTHALPY OF $\text{PbMoO}_4$

The enthalpy of melting of  $\text{PbMoO}_4$  was measured 4 times against the enthalpy of transition and enthalpy of melting of  $\text{Cs}_2\text{MoO}_4$  [83] using DSC. The results are shown in Table 3.4. The enthalpy of the solid-liquid transition was calculated using the sensitivity factor as given in Equation 2.1. The obtained melting enthalpy is  $(62.3 \pm 3) \text{ kJ} \cdot \text{mol}^{-1}$  with the corresponding melting point  $(1338 \pm 5) \text{ K}$ . A similar analysis using the  $\alpha$ - $\text{Cs}_2\text{MoO}_4 = \beta$ - $\text{Cs}_2\text{MoO}_4$  transition yields  $(66.7 \pm 3) \text{ kJ} \cdot \text{mol}^{-1}$ . The former value is preferred since the melting temperature of  $\text{Cs}_2\text{MoO}_4$  is closer to the melting temperature of  $\text{PbMoO}_4$ , so the derived sensitivity is expected to be more accurate.

$m_{\text{PbMoO}_4}$ (mg)	$T_{tr}$ (K)	$m_{\text{Cs}_2\text{MoO}_4}$ (mg)	$A_{sample}$ ( $\mu\text{V} \cdot \text{s}$ )	$A_{ref}$ ( $\mu\text{V} \cdot \text{s}$ )	$s_{ref}$ ( $\mu\text{V} \cdot \text{mW}^{-1}$ )	$\Delta_{tr} H_m^o$ ( $\text{kJ} \cdot \text{mol}^{-1}$ )
74.10	1338.4	39.89	70.24	16.25	0.00545	63.8 $\pm$ 5
76.05	1338.7	67.59	70.01	28.27	0.00560	60.4 $\pm$ 6
50.89	1336.9	63.88	71.52	39.89	0.00836	61.7 $\pm$ 8
49.43	1338.3	67.66	75.34	44.74	0.00885	63.2 $\pm$ 8
<b>Average</b>	1338 $\pm$ 5					62.3 $\pm$ 3

Table 3.4: Experimental results of the DSC measurements of  $\text{PbMoO}_4(\text{s}) = \text{PbMoO}_4(\text{l})$  versus  $\beta$ - $\text{Cs}_2\text{MoO}_4(\text{s}) = \text{Cs}_2\text{MoO}_4(\text{l})$ . The average and standard deviation are calculated using Equations A.1 and A.2.

### 3.3.5. LOW-TEMPERATURE HEAT CAPACITY OF $\text{PbMoO}_4$ AND $\text{Pb}_2\text{MoO}_5$

Thermal-relaxation calorimetry was used to measure the low-temperature heat capacity of  $\text{PbMoO}_4$  and  $\text{Pb}_2\text{MoO}_5$ . The low-temperature heat capacity of  $\text{PbMoO}_4$  is shown in Figure 3.5. The results obtained in this work agree well with literature. The small anomaly as reported by Bissengaliyeva *et al.* [68] at 273 K was not observed in this work and might be attributed to water, because there seems to be no structural or other physical reason to have any transition inherent to  $\text{PbMoO}_4$ . This means the *supra* selected entropy value can be retained. In Figure A.5, the magnetic susceptibility is shown, confirming the absence of any anomaly in the studied temperature range. In this work, the heat capacity between 2 and 4 K has been measured for the first time. Only lattice contributions to the heat capacity are present, as shown in Figure A.7.

The low-temperature heat capacity of  $\text{Pb}_2\text{MoO}_5$  was measured on three different pellets. As shown in Figure 3.5, the heat capacity joins the high-temperature data as re-

ported by Aiswarya *et al.* around room temperature [6]. The heat capacity at 298.15 K obtained here equals  $C_p(298.15 \text{ K}) = (172 \pm 5) \text{ J} \cdot \text{K}^{-1} \cdot \text{mol}^{-1}$ , which is in line with the extrapolation from the high-temperature heat capacity of Aiswarya *et al.* [7], *viz.*  $(166.7 \pm 6.2) \text{ J} \cdot \text{K}^{-1} \cdot \text{mol}^{-1}$ . The lower temperature range was plotted, as shown in Figure A.7. As can be concluded from this fit, there is no electronic contribution to the heat capacity, as expected for an insulating material. In Figure A.6, the magnetic susceptibility is shown, confirming the absence of any anomaly in the studied temperature range. The data of the 11.21(5) mg sample joins best with the data of Aiswarya *et al.* at higher temperatures. The sample of 12.79(5) mg was encapsulated in stycast, which adds an extra error source. Typically, the corresponding uncertainty on the heat capacity can be estimated to be 3%. To obtain the standard entropy at 298.15 K, the curve of the 11.21(5) mg sample was selected; extension below 50 K was done using the curve of the 12.79(5) mg sample joint to the 11.21(5) mg sample curve. A standard entropy at 298.15 K of  $(244.8 \pm 7.4) \text{ J} \cdot \text{K}^{-1} \cdot \text{mol}^{-1}$  was obtained. Integration of the curve obtained on the 12.79(5) mg sample on itself yields  $(252 \pm 7) \text{ J} \cdot \text{K}^{-1} \cdot \text{mol}^{-1}$ , which is just within error limits of the selected curve. The third curve is in line with the other two samples, but is only measured between 50 and 200 K and therefore not used for entropy determination at 298.15 K. Thus, the entropy used in this work is  $S_m^\circ(298.15 \text{ K}) = (244.8 \pm 7.4) \text{ J} \cdot \text{K}^{-1} \cdot \text{mol}^{-1}$ .

### 3.4. THERMODYNAMIC MODELLING

The model with thermodynamic parameters to be optimised to the the data on the Pb-Mo-O system using the CALculation of PHase Diagrams (CALPHAD) approach is detailed first, after which the optimised parameters are discussed.

#### 3.4.1. DEVELOPMENT OF MODEL

##### PURE ELEMENTS

Metallic Pb was included in the description of the fcc (A1) phase as (Pb,Mo)(O,Va) (Va being a vacancy), while Mo is stable as bcc (A2) phase with sub-lattices (Mo,Pb,Va)(O,Va)<sub>3</sub>. The Pb-Mo system is effectively defined by the pure element functions given in Table 3.5.

Phase	Gibbs energy ( $\text{J} \cdot \text{mol}^{-1}$ )	Ref.
<i>fcc</i> (A1)	$G[(\text{Pb})(\text{Va})] = G_{\text{Pb}}^{\text{SER}}$	[44]
	$G[(\text{Mo})(\text{Va})] = G_{\text{Mo}}^{\text{fcc}}$	[44]
	$L[(\text{Mo}, \text{Pb})(\text{Va})] = +300000$	This work
<i>bcc</i> (A2)	$G[(\text{Pb})(\text{Va})_3] = G_{\text{Pb}}^{\text{bcc}}$	[44]
	$G[(\text{Mo})(\text{Va})_3] = G_{\text{Mo}}^{\text{SER}}$	[44]
	$L[(\text{Mo}, \text{Pb})(\text{Va})_3] = +300000$	This work
Liquid	$L^0(\text{Pb}^{2+})_P(\text{Va}^{Q^-})_Q = G_{\text{Pb}}^{\text{Liq}}$	[44]
	$L^0(\text{Mo}^{4+})_P(\text{Va}^{Q^-})_Q = G_{\text{Mo}}^{\text{Liq}}$	[44]
	$L^0(\text{Mo}^{4+}, \text{Pb}^{2+})_P(\text{Va}^{Q^-})_Q = +300000$	This work

Table 3.5: Thermodynamic functions used in the model of the Pb-Mo system.

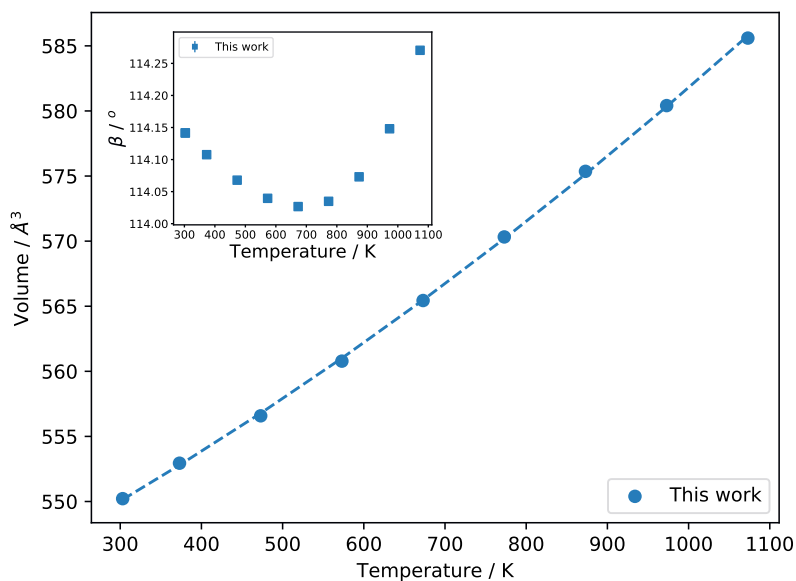
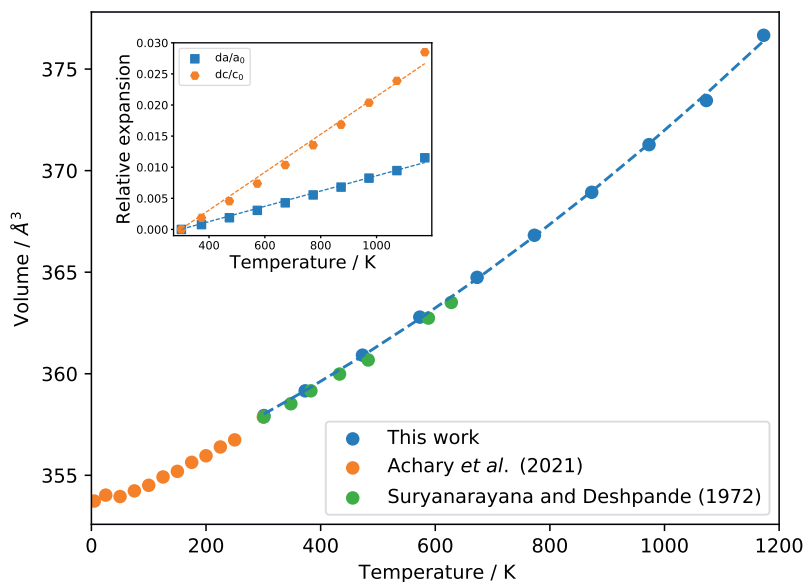


Figure 3.4: Top: Volumetric thermal expansion of  $\text{PbMoO}_4$  as measured in this work (blue), by Suryanarayana and Deshpande [77] and by Achary *et al.* [78]. The inset shows the relative lattice parameter expansion on the  $a$ - and  $c$ -axes. Bottom: Volumetric thermal expansion of  $\text{Pb}_2\text{MoO}_5$  as measured in this work (blue). The inset shows the evolution of angle  $\beta$  with increasing temperature.

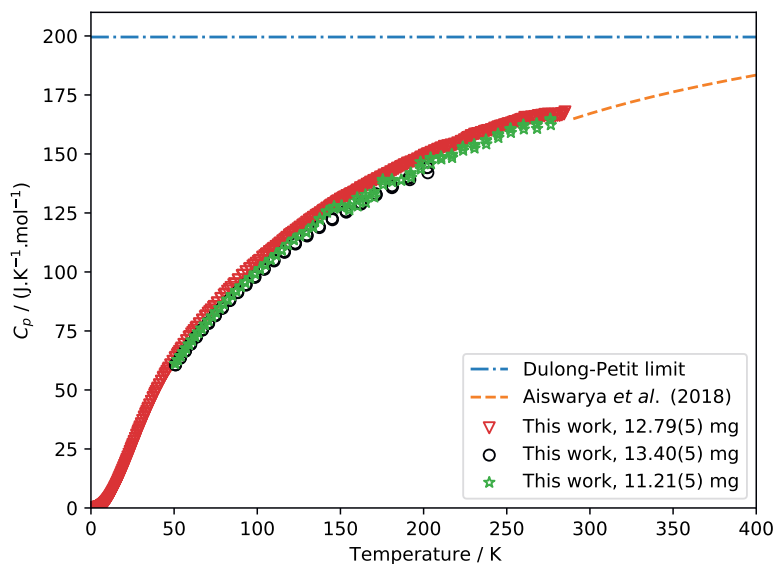
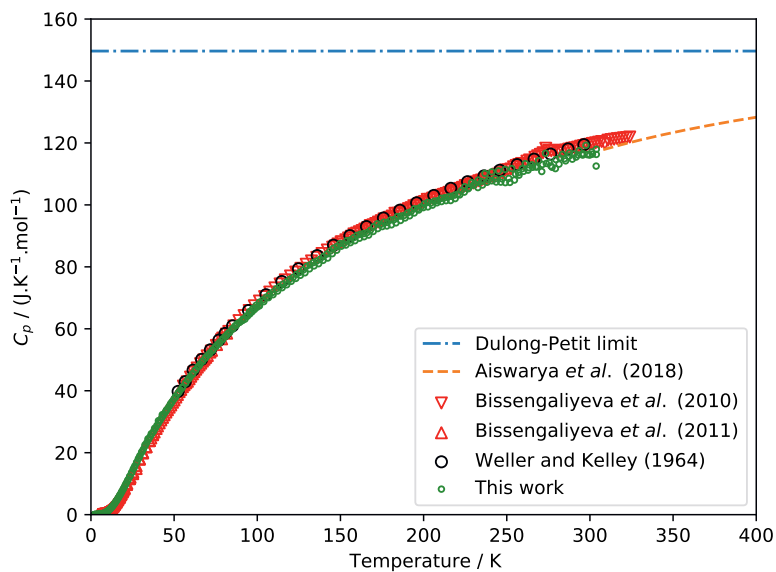


Figure 3.5: Top: Low-temperature heat capacity of  $\text{PbMoO}_4$  as measured by Weller and Kelley [66], Bissengaliyeva *et al.* [67, 68] and in this work, as compared to the high-temperature heat capacity as measured by Aiswarya *et al.* [7] and the Dulong-Petit limit. Bottom: Low-temperature heat capacity of  $\text{Pb}_2\text{MoO}_5$  as measured in this work and compared to the high-temperature heat capacity as measured by Aiswarya *et al.* [7] and the Dulong-Petit limit.

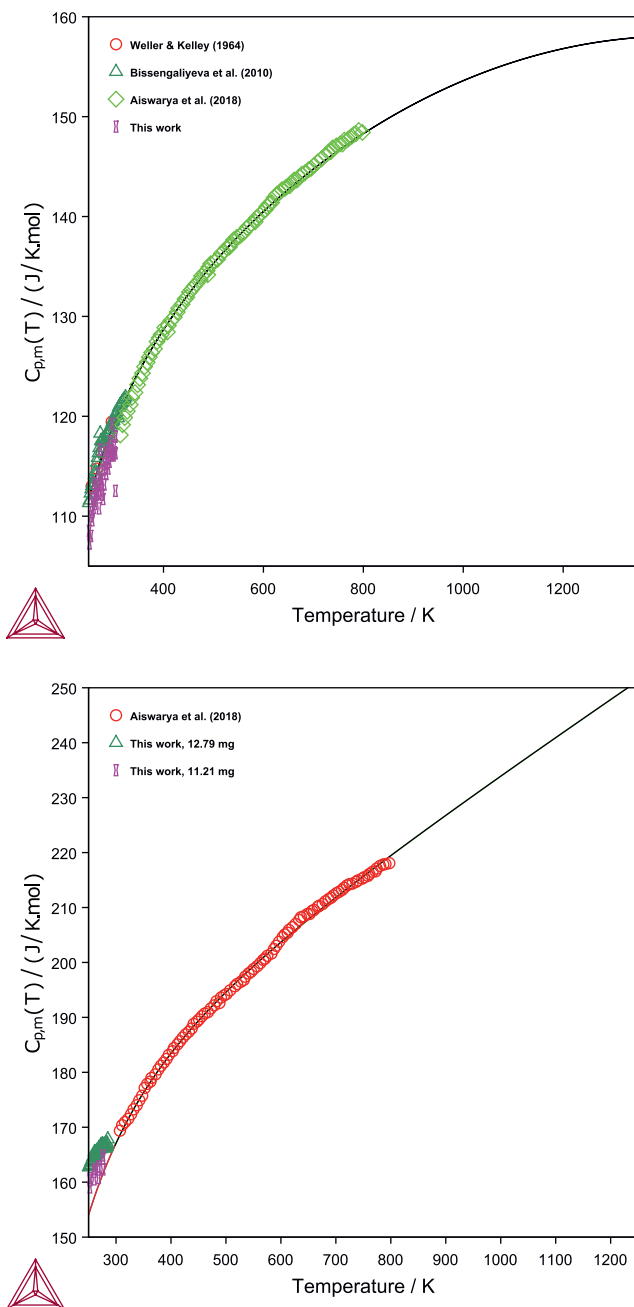


Figure 3.6: Top: Heat capacity of  $\text{PbMoO}_4$  in the model compared with data from refs. [7, 66–68]. Bottom: Heat capacity of  $\text{Pb}_2\text{MoO}_5$  in the model compared with data from ref. [7].

### BINARY OXIDES

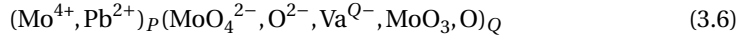
The binary oxides of the Mo-O system ( $\text{MoO}_2$ ,  $\text{Mo}_4\text{O}_{11}$ ,  $\text{Mo}_8\text{O}_{23}$ ,  $\text{Mo}_9\text{O}_{26}$ ,  $\text{MoO}_3$ ) and of the Pb-O ( $\text{PbO}$ ,  $\text{Pb}_3\text{O}_4$ ,  $\text{Pb}_{12}\text{O}_{17}$ ,  $\text{Pb}_{12}\text{O}_{19}$  and  $\text{PbO}_2$ ) system were described as stoichiometric compounds. The functions were taken from Corcoran *et al.* and Kauric [41–43] and Risold *et al.* [27] for the Mo-O and the Pb-O systems, respectively.

### HEXAVALENT TERNARY MOLYBDATES

The complex molybdates formed on the section PbO-MoO<sub>3</sub> were described as stoichiometric compounds with a three-sub-lattice model of the form  $(\text{Pb}^{2+})_x(\text{Mo}^{6+})_y(\text{O}^{2-})_{x+3y}$ . As a starting point, available experimental enthalpy of formation, entropy and heat capacity data were used to express the Gibbs energy functions for  $\text{PbMoO}_4$  and  $\text{Pb}_2\text{MoO}_5$ . The functions are given in Table 3.6.  $\text{Pb}_5\text{MoO}_8$ , for which no experimental thermodynamic data is available, was modelled using a combination of the Gibbs energy functions of  $\text{Pb}_2\text{MoO}_5$  and PbO matching its stoichiometry, after which its enthalpy and entropy at 298.15 K were optimised.

### LIQUID PHASE

The ionic two sub-lattice model as proposed by Hillert *et al.* [84] was used to describe the liquid phase. The first lattice in this model contained the cationic species, while the second lattice contained anionic and neutral species, including vacancies:



with  $P$  and  $Q$  equal to the average charge of the opposite sub-lattice:

$$P = 2y_{\text{MoO}_4^{2-}} + 2y_{\text{O}^{2-}} + Qy_{\text{Va}^{Q-}} \quad (3.7)$$

$$Q = 2y_{\text{Pb}^{2+}} + 4y_{\text{Mo}^{4+}} \quad (3.8)$$

where the various site fractions are described with the respective  $y$ 's.

The Gibbs energy of the liquid phase for any composition in the Pb-Mo-O system is given by the sum of the reference terms of the end-member species (Pb, Mo, O,  $\text{PbMoO}_4$ , ...) multiplied by their fractions, a configurational entropy term on the cationic and the anionic lattices and an excess term:

$$\begin{aligned} G^{\text{liquid}} = & y_{\text{Pb}^{2+}} y_{\text{MoO}_4^{2-}} \circ G_{(\text{Pb}^{2+})_2(\text{MoO}_4^{2-})_2} + y_{\text{Pb}^{2+}} y_{\text{O}^{2-}} \circ G_{(\text{Pb}^{2+})_2(\text{O}^{2-})_2} \\ & + Q y_{\text{Pb}^{2+}} y_{\text{Va}^{Q-}} \circ G_{(\text{Pb}^{2+})_1(\text{Va}^{1-})_2} + y_{\text{Mo}^{4+}} y_{\text{MoO}_4^{2-}} \circ G_{(\text{Mo}^{4+})_2(\text{MoO}_4^{2-})_4} \\ & + y_{\text{Mo}^{4+}} y_{\text{O}^{2-}} \circ G_{(\text{Mo}^{4+})_2(\text{O}^{2-})_4} + Q y_{\text{Mo}^{4+}} y_{\text{Va}^{Q-}} \circ G_{(\text{Mo}^{4+})_1(\text{Va}^{1-})_4} \\ & + Q y_{\text{MoO}_3} \circ G_{\text{MoO}_3} + Q y_{\text{O}} \circ G_{\text{O}} \\ & + RT(P[y_{\text{Pb}^{2+}} \ln(y_{\text{Pb}^{2+}}) + y_{\text{Mo}^{4+}} \ln(y_{\text{Mo}^{4+}})]) \\ & + Q[y_{\text{MoO}_4^{2-}} \ln(y_{\text{MoO}_4^{2-}}) + y_{\text{O}^{2-}} \ln(y_{\text{O}^{2-}})] \\ & + y_{\text{Va}^{Q-}} \ln(y_{\text{Va}^{Q-}}) + y_{\text{MoO}_3} \ln(y_{\text{MoO}_3}) + y_{\text{O}} \ln(y_{\text{O}})] + G^{\text{excess}} \quad (3.9) \end{aligned}$$

The excess Gibbs energy is described by the parameters  $L^0(\text{Pb}^{2+})_P(\text{MoO}_4^{2-}, \text{O}^{2-})_Q$  and  $L^1(\text{Pb}^{2+})_P(\text{MoO}_4^{2-}, \text{O}^{2-})_Q$  for the PbO-PbMoO<sub>4</sub> range, while the PbMoO<sub>4</sub>-MoO<sub>3</sub> range is described by the parameters  $L^0(\text{Pb}^{2+})_P(\text{MoO}_4^{2-}, \text{MoO}_3)_Q$  and  $L^1(\text{Pb}^{2+})_P(\text{MoO}_4^{2-}, \text{MoO}_3)_Q$ .

## GAS PHASE

The gas phase is described by an ideal mixture of Mo, Mo<sub>2</sub>, Mo<sub>2</sub>O<sub>6</sub>, Mo<sub>3</sub>O<sub>9</sub>, Mo<sub>4</sub>O<sub>12</sub>, Mo<sub>5</sub>O<sub>15</sub>, MoO, MoO<sub>2</sub>, MoO<sub>3</sub>, O, O<sub>2</sub>, O<sub>3</sub>, Pb, Pb<sub>2</sub>, Pb<sub>2</sub>O<sub>2</sub>, Pb<sub>3</sub>O<sub>3</sub>, Pb<sub>4</sub>O<sub>4</sub>, Pb<sub>5</sub>O<sub>5</sub>, Pb<sub>6</sub>O<sub>6</sub>, PbO, PbMoO<sub>4</sub>, Pb<sub>2</sub>MoO<sub>5</sub>, PbMo<sub>2</sub>O<sub>7</sub> and PbMo<sub>3</sub>O<sub>10</sub>. The Gibbs energy expression of PbMoO<sub>4</sub>(g), PbMo<sub>2</sub>O<sub>7</sub>(g), Pb<sub>2</sub>MoO<sub>5</sub>(g), and PbMo<sub>3</sub>O<sub>10</sub>(g) are taken from Kunkel *et al.* [71].

## 3.4.2. OPTIMISED MODEL

The PARROT module of the ThermoCalc software (Version 2023b) was used [85, 86]. The optimised parameters for the Pb-Mo-O system are summarised in Table 3.6. The selected and optimised enthalpies of formation and standard entropy are compared in Table 3.7. The selected values for PbMoO<sub>4</sub> and Pb<sub>2</sub>MoO<sub>5</sub> allow for a successful optimisation, proving the consistency of the data. No experimental data for Pb<sub>5</sub>MoO<sub>8</sub> is available, so no comparison can be made. The melting enthalpy of PbMoO<sub>4</sub> as found in the optimised model equals 59.9 kJ·mol<sup>-1</sup> at 1346 K (measured: (62.3±3 kJ·mol<sup>-1</sup>) at 1338±5 K). The calculated melting enthalpy of Pb<sub>2</sub>MoO<sub>5</sub> equals 80.6 kJ·mol<sup>-1</sup> at 1215 K. The heat capacities of PbMoO<sub>4</sub> and Pb<sub>2</sub>MoO<sub>5</sub> as used in the model are plotted in Figure 3.6.

Phase	Gibbs energy (J·mol <sup>-1</sup> )
Liquid	${}^{\circ}G(\text{Pb}^{2+})_2(\text{MoO}_4^{2-})_2 - 2^{\circ}H_{\text{Pb}}^{SER} - 2^{\circ}H_{\text{Mo}}^{SER}$ $- 8^{\circ}H_{\text{O}}^{SER} = 2G_{\text{PbMoO}_4} + \mathbf{41600-26.6} \cdot T$ $L^0(\text{Pb}^{2+})_P(\text{MoO}_4^{2-}, \text{O}^{2-})_Q = \mathbf{+171000-196.7} \cdot T$ $L^1(\text{Pb}^{2+})_P(\text{MoO}_4^{2-}, \text{O}^{2-})_Q = \mathbf{+46250}$ $L^0(\text{Pb}^{2+})_P(\text{MoO}_4^{2-}, \text{MoO}_3)_Q = \mathbf{147825-151} \cdot T$ $L^1(\text{Pb}^{2+})_P(\text{MoO}_4^{2-}, \text{MoO}_3)_Q = \mathbf{126960-75.5} \cdot T$
Hexavalent molybdates	$G_{\text{PbMoO}_4} = -1092267.81 + 614.510765 \cdot T - 112.192229 \cdot T \cdot \ln(T) - 0.032775 \cdot T^2$ $+ 482846.944 \cdot T^{-1} + 3.86243333 \cdot 10^{-6} T^3$ $G_{\text{Pb}_2\text{MoO}_5} = -1334786 + 920.31 \cdot T - 169.2 \cdot T \cdot \ln(T) - 0.033345 \cdot T^2 + 995000 \cdot T^{-1}$ $G_{\text{Pb}_5\text{MoO}_8} = G_{\text{Pb}_2\text{MoO}_5} + 3^* G_{\text{PbO}} - \mathbf{4380}$

Table 3.6: Thermodynamic functions used in the optimisation of the Pb-Mo-O model. Optimised values are given in **bold**.

Compound	$\Delta_f H_m^{\circ}(298.15 \text{ K})$ (kJ·mol <sup>-1</sup> )		$S_m^{\circ}(298.15 \text{ K})$ (J·K <sup>-1</sup> ·mol <sup>-1</sup> )	
	Optimised	Selected*	Optimised	Selected*
PbMoO <sub>4</sub>	-1052.9	-(1052.9±0.5)	160.9	160.9
Pb <sub>2</sub> MoO <sub>5</sub>	-1274.7	-(1274.7±2.3)	244	244.8±7.4
Pb <sub>5</sub> MoO <sub>8</sub>	-1936.2	n.a.	443	n.a.

Table 3.7: Optimised standard enthalpies of formation and standard entropies of the ternary lead molybdates. \*Values selected after literature review, see Section 3.2.

The calculated PbO-MoO<sub>3</sub> phase diagram is shown in Figure 3.7, together with the available phase diagram data. The optimised invariant equilibria are listed in Table 3.8, together with data from the literature. A zoom of the phase diagram around the peritectic decomposition of Pb<sub>5</sub>MoO<sub>8</sub> is shown in Figure 3.7. The model has been optimised

to the data of Kunev *et al.* [73], Bukhalova *et al.* [74] and Nihtianova *et al.* [76] (filled data points). This equilibrium phase diagram cannot easily be compared to the phase diagram reported by Eissa *et al.* [75] (which is not included in the Figure), because  $\text{PbO}_2$  was used as starting material in their study. The compounds  $\text{Pb}_2\text{MoO}_5$  and  $\text{PbMoO}_4$  in that phase diagram are more unstable than calculated here, likely because of the stability of Pb(IV) at the oxygen potentials in their work. Their findings for the liquidus are in line with the current modelled phase fields, except at the PbO-rich side of the phase diagram.

Ternary isotherms at 298, 773, 998 and 1273 K are calculated and shown in Figures 3.8 and 3.9. There are quite some phase field investigations reported in literature. In the field PbO-MoO<sub>3</sub>-O, the change in stable species results from the changes in the PbO-O phase diagram; no ternary compounds with Pb(IV) are stable. In the fields between PbO-MoO<sub>3</sub>-MoO<sub>2</sub>-Pb at 773 K, the findings of Feja [54] and Aiswarya *et al.* [6] are in agreement with the current model. Feja also reported the presence of  $\text{Pb}_3\text{O}_4$  at 773 K above the line PbO-MoO<sub>3</sub>. The phase fields as analysed by Aiswarya *et al.* [6] were measured after cooling to ambient temperature. In their dozens of samples in the field Pb-Mo-MoO<sub>3</sub>-PbO, they only reported Pb, Mo, MoO<sub>2</sub>, PbMoO<sub>4</sub>, Pb<sub>2</sub>MoO<sub>5</sub> and PbO as formed at 773 K, while at 998 K they also found Pb<sub>5</sub>MoO<sub>8</sub>. As stated above, there remains some contradiction as to the existence of the couple  $\text{Pb}_3\text{Mo}_{16}\text{O}_{24}$ -PbMo<sub>5</sub>O<sub>8</sub>, that would fall in the Pb-MoO<sub>2</sub>-Mo system and thus not influence the chemistry of the remaining fields that are definitely found to be stable.

Invariant equilibrium	Eq. type	$x(\text{MoO}_3)$	T / K	Ref.
$\text{PbO} + \text{Pb}_5\text{MoO}_8 = \text{L}$	E	0.130	1027	This work, opt.
		0.117	1035	[72]
		0.14	1017	[74]
$\text{Pb}_5\text{MoO}_8 = \text{Pb}_2\text{MoO}_5 + \text{L}$	P	0.167	1033	This work, opt.
		0.167	1037	[76]
$\text{Pb}_2\text{MoO}_5 = \text{L}$	C	0.333	1232	This work, opt.
		0.333	1224	[22]
		0.333	1225	[72]
		0.333	1223	[74]
		0.333	1223	[76]
$\text{Pb}_2\text{MoO}_5 + \text{PbMoO}_4 = \text{L}$	E	0.38	1212	This work, opt.
		0.375	1208	[72]
		0.375	1183	[74]
$\text{PbMoO}_4 = \text{L}$	C	0.5	1346	This work, opt.
		0.5	1338±2	This work, exp.
$\text{PbMoO}_4 + \text{MoO}_3 = \text{L}$	E	0.79	943	This work, opt.
		0.825	953	[72]
		0.795	933	[74]
		0.785	945	[73]

Table 3.8: Invariant points on the section PbO-MoO<sub>3</sub>; E = eutectic; P = peritectic decomposition; C = congruent melting; Opt. = optimised in this work; Exp. = experimental.

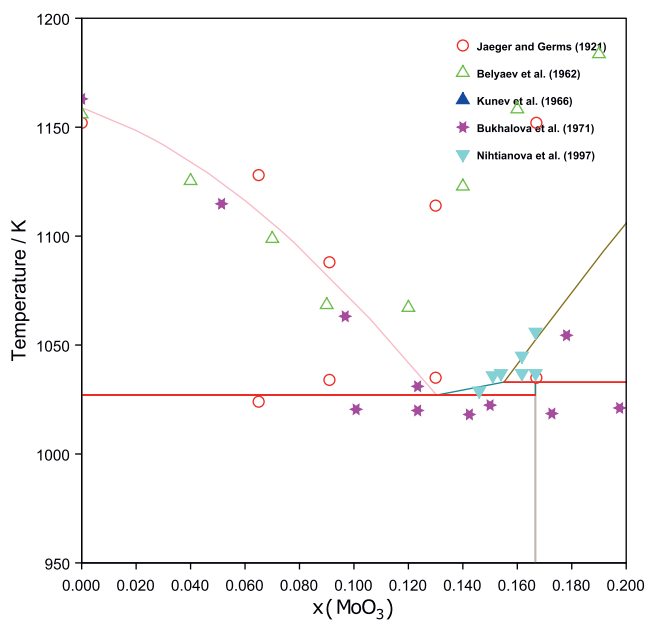
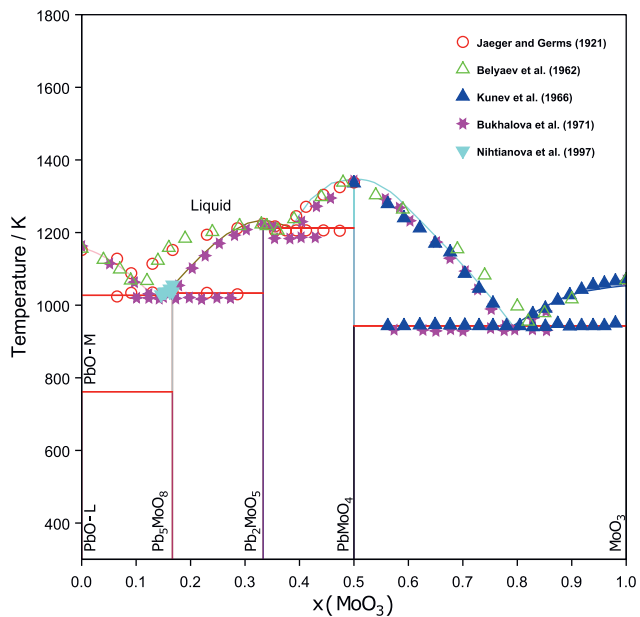


Figure 3.7: Top: Pseudo-binary phase diagram PbO-MoO<sub>3</sub> calculated from the optimised thermodynamic model and compared with literature [22, 58, 72–74]. Bottom: Pseudo-binary phase diagram PbO-MoO<sub>3</sub>, zoomed around the decomposition of Pb<sub>5</sub>MoO<sub>8</sub> as calculated from the optimised thermodynamic model and compared with literature [22, 58, 72–74].

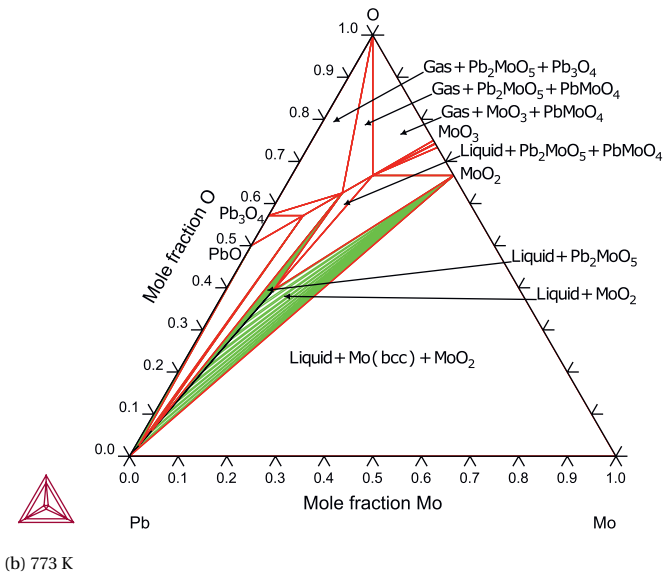
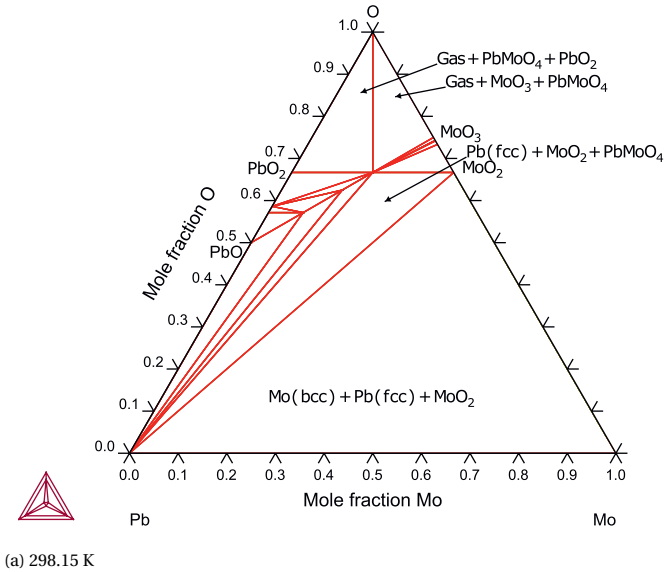


Figure 3.8: Calculated isothermal sections of the Pb-Mo-O system at (a) 298.15 K and (b) 773 K. The green lines are tie-lines.

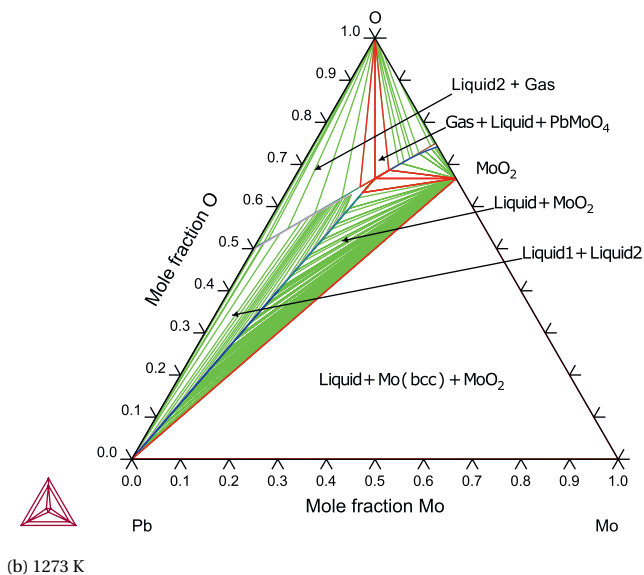
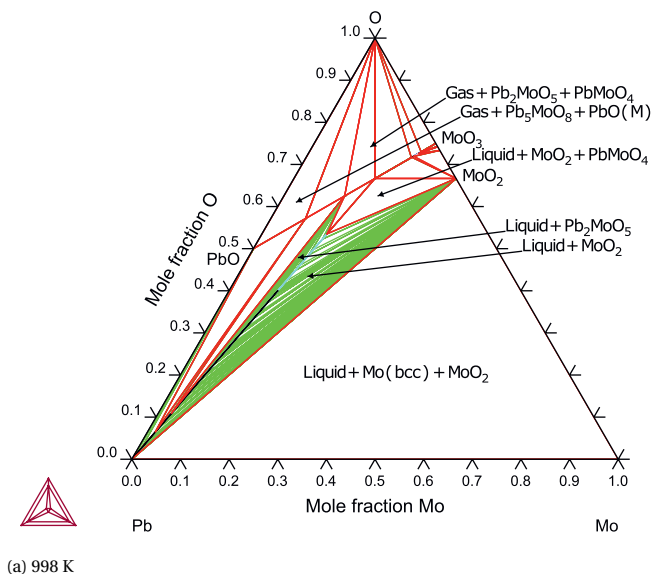


Figure 3.9: Calculated isothermal sections of the Pb-Mo-O system at (a) 998 K and (b) 1273 K. The green lines are tie-lines.

### 3.5. SUMMARY AND RECOMMENDATIONS

A Pb-Mo-O phase diagram featuring the hexavalent molybdates  $\text{PbMoO}_4$ ,  $\text{Pb}_2\text{MoO}_5$  and  $\text{Pb}_5\text{MoO}_8$  has been optimised to experimental thermodynamic data using the CALPHAD method. Moreover, the thermal expansion and low-temperature heat capacity of the compounds  $\text{PbMoO}_4$  and  $\text{Pb}_2\text{MoO}_5$  were measured and the melting enthalpy of  $\text{PbMoO}_4$  was determined experimentally. XANES measurements confirmed the hexavalent oxidation state of Mo of these compounds. The thermodynamic model published in this article includes the phases  $\text{PbMoO}_4$ ,  $\text{Pb}_2\text{MoO}_5$  and  $\text{Pb}_5\text{MoO}_8$ . A model that is consistent with available thermodynamic and phase diagram data was built.

Some recommendations for further experimental work include the measurement of thermodynamic properties (enthalpy of formation, entropy, heat capacity) of  $\text{Pb}_5\text{MoO}_8$  in order to improve the description of the peritectic decomposition; the melting enthalpy of  $\text{Pb}_2\text{MoO}_5$ ; an in-depth structural study of the pair  $\text{Pb}_3\text{Mo}_{16}\text{O}_{24}$ - $\text{PbMo}_5\text{O}_8$ , to be completed with thermodynamic study to resolve whether these are thermodynamically stable phases that should be considered in the phase diagram; and vapour pressure studies to clarify the role of ternary gaseous species.

### EXPERIMENTAL DETAILS

**Synthesis** The chemicals  $\text{PbMoO}_4$  (Merck Sigma, 99.9%), PbO (Merck Sigma, 99.999%) and  $\text{MoO}_3$  (Alfa Aesar, 99.95%) were purchased.  $\text{Pb}_2\text{MoO}_5$  was synthesised via solid state synthesis by mixing PbO and  $\text{MoO}_3$  in a 2:1 ratio. The mixture was ground and heated to 873 K under oxygen atmosphere in an alumina boat, where it was kept for 12h. The sample was subsequently cooled to room temperature and reground, after which the heat treatment was repeated.

**X-ray diffraction (XRD)** Formation and purity of the compounds was confirmed by powder XRD. The XRK-900 furnace was used to heat the sample from ambient temperature up to 1173 K for  $\text{PbMoO}_4$  and 1073 K for  $\text{Pb}_2\text{MoO}_5$ .

**X-ray absorption near edge structure (XANES) spectroscopy** XANES spectroscopy measurements were performed for  $\text{MoO}_2$ ,  $\text{MoO}_3$ ,  $\text{PbMoO}_4$  and  $\text{Pb}_2\text{MoO}_5$  at the INE beamline [87] of the KIT Light Source (Karlsruhe, Germany). Samples were probed around the K-edge of Mo (20 keV). The samples were prepared by mixing the compound with boron nitride (BN) and pressed into a circular pellet of 8 mm diameter and enclosed in Kapton foil.

**Differential scanning calorimetry (DSC)** DSC measurements were performed using the Setaram Multi-Detector HTC Module of the 96 Line calorimeter with 3D heat flux detection. Open alumina crucibles were used under oxygen flow at ambient pressure with a heating rate of  $10 \text{ K}\cdot\text{min}^{-1}$ . The enthalpy of melting of  $\text{PbMoO}_4$  was determined using  $\text{Cs}_2\text{MoO}_4$  as reference material [83].

**Low-temperature heat capacity** The low-temperature heat capacity was measured on two instruments, namely a Physical Property Measurement System from Quantum Design (QD-PPMS 14 T) and a Versalab equipment system from Quantum Design. The results were collected with zero field in the temperature range 2 - 300 K. The samples were thermally connected to the puck platform using Apiezon N-grease. The heat capacity of  $\text{PbMoO}_4$  was measured on a 3.05(5) mg sample using QD-PPMS systems of QuantumDesign.  $\text{Pb}_2\text{MoO}_5$  samples have been measured on the QD-PPMS (full range) and Versalab (50-300 K) on pellets weighing 11.21(5), 12.79(5) and 13.40(5) mg respectively. The 12.79(5) mg sample has been encapsulated in Stycast 2850 FT to a total mass of 13.50(5) mg [88].

**Magnetic susceptibility** The non-encapsulated samples were measured afterwards in a Quantum Design MPMS-7 device to study the magnetic susceptibility. Measurements have been performed by fixing pellets on a low magnetic contribution quartz support and measured in DC magnetic field up to 70 kOe applied field and varying temperature from 2 to 300 K.



# BIBLIOGRAPHY

- (1) Weeks, J. R. *Nuclear Engineering and Design* **1971**, *15*, 363–372.
- (2) Abderrahim, H. A.; Kupschus, P.; Malambu, E.; Benoit, P.; Van Tichelen, K.; Arien, B.; Vermeersch, F.; D’hondt, P.; Jongen, Y.; Ternier, S., et al. *Nuclear Instruments and Methods in Physics Research Section A* **2001**, *463*, 487–494.
- (3) US DOE Nuclear Energy Research Advisory Committee with Generation IV International Forum [https://www.gen-4.org/gif/jcms/sc\\_40481/technology-roadmap](https://www.gen-4.org/gif/jcms/sc_40481/technology-roadmap) **2002**.
- (4) Abderrahim, H. A.; Baeten, P.; De Bruyn, D.; Fernandez, R. *Energy Conversion and Management* **2012**, *63*, 4–10.
- (5) Zhang, J. *Advanced Engineering Materials* **2014**, *16*, 349–356.
- (6) Aiswarya, P. M.; Ganesan, R.; Gnanasekaran, T. *Journal of Nuclear Materials* **2017**, *493*, 310–321.
- (7) Aiswarya, P. M.; Ganesan, R.; Gnanasekaran, T. *The Journal of Chemical Thermodynamics* **2018**, *116*, 21–31.
- (8) Zverev, D. L.; Neevin, S. M.; Doronkov, D. L.; Sokolova, L. B. *Atomic Energy* **2020**, *129*, 1–7.
- (9) Adamov, E. O.; Kapliencko, A. V.; Orlov, V. V.; Smirnov, V. S.; Lopatkin, A. V.; Lemekhov, V. V.; Moiseev, A. V. *Atomic Energy* **2021**, *129*, 179–187.
- (10) Smith, C. F.; Cinotti, L. In *Handbook of Generation IV Nuclear Reactors*; Elsevier: 2016, pp 119–155.
- (11) Pelletier, M.; Guérin, Y. In *Comprehensive Nuclear Materials, 2nd edition*, Konings, R. J. M., Stoller, R. E., Eds.; Elsevier: 2020; Chapter 2.03, pp 72–105.
- (12) Kleykamp, H. *Journal of Nuclear Materials* **1985**, *131*, 221–246.
- (13) Cappia, F.; Miller, B. D.; Aguiar, J. A.; He, L.; Murray, D. J.; Frickey, B. J.; Stanek, J. D.; Harp, J. M. *Journal of Nuclear Materials* **2020**, *531*, 151964.
- (14) Imoto, S. *Journal of Nuclear Materials* **1986**, *140*, 19–27.
- (15) Tourasse, M.; Boidron, M.; Pasquet, B. *Journal of Nuclear Materials* **1992**, *188*, 49–57.
- (16) Danevich, F. A. et al. *Nuclear Instruments and Methods in Physics Research Section A* **2010**, *622*, 608–613.
- (17) Van Loo, W. *physica status solidi (a)* **1975**, *27*, 565–574.
- (18) Van Loo, W. *physica status solidi (a)* **1975**, *28*, 227–235.
- (19) Groenink, J. A.; Blasse, G. *Journal of Solid State Chemistry* **1980**, *32*, 9–20.

- (20) Nedilko, S.; Chornii, V.; Hizhnyi, Y.; Trubitsyn, M.; Volnyanskaya, I. *Optical Materials* **2014**, *36*, 1754–1759.
- (21) Loiacono, G. M.; Balascio, J. F.; Bonner, R.; Savage, A. *Journal of Crystal Growth* **1974**, *21*, 1–11.
- (22) Jaeger, F. M.; Germs, H. C. *Zeitschrift für anorganische und allgemeine Chemie* **1921**, *119*, 145–173.
- (23) Van Hattem, A.; Vlieland, J.; Dankelman, R.; Thijs, M. A.; Wallez, G.; Dardenne, K.; Rothe, J.; Konings, R. J. M.; Smith, A. L. *Inorganic Chemistry* **2023**, *62*, 6981–6992.
- (24) Rivai, A. K.; Takahashi, M. *Progress in Nuclear Energy* **2008**, *50*, 560–566.
- (25) Cairang, W.; Ma, S.; Gong, X.; Zeng, Y.; Yang, H.; Xue, D.; Qin, Y.; Ding, X.; Sun, J. *Corrosion Science* **2021**, *179*, 109132.
- (26) Serag, E.; Caers, B.; Schuurmans, P.; Lucas, S.; Haye, E. *Surface and Coatings Technology* **2022**, 128542.
- (27) Risold, D.; Nagata, J.-I.; Suzuki, R. O. *Journal of Phase Equilibria* **1998**, *19*, 213–233.
- (28) Gueneau, C.; Dupin, N.; Kjellqvist, L.; Geiger, E.; Kurata, M.; Gosse, S.; Corcoran, E.; Quaini, A.; Hania, R.; Smith, A. L., et al. *Calphad* **2021**, *72*, 102212.
- (29) Predel, B. In *Phase Equilibria, Crystallographic and Thermodynamic Data of Binary Alloys Volume 5*, Predel, B., Ed.; Springer: 1997; Chapter Mo-Pb, p 1.
- (30) Wriedt, H. A. *Journal of Phase Equilibria* **1988**, *9*, 106–127.
- (31) Kobertz, D. *Calphad* **2019**, *65*, 155–164.
- (32) Knacke, O. *Erz. Metall* **1964**, *17*, 28–34.
- (33) Rodigina, E. N.; Gomel'skii, K. Z.; Luginina, V. F. *Russian Journal of Physical Chemistry* **1961**, *35*, 884–886.
- (34) Razzazi, V.; Alaei, S. *Chinese Physics B* **2017**, *26*, 116501.
- (35) Liu, X.; Kang, Z.; Shi, Y.; Liu, H.; Zhang, Y.; He, M. *Fluid Phase Equilibria* **2022**, *559*, 113461.
- (36) Ganesan, R.; Gnanasekaran, T.; Srinivasa, R. S. *Journal of Nuclear Materials* **2003**, *320*, 258–264.
- (37) Ganesan, R.; Gnanasekaran, T.; Srinivasa, R. S. *Journal of Nuclear Materials* **2006**, *349*, 133–149.
- (38) Lim, J.; Gladinez, K.; Marino, A.; Rosseel, K.; Aerts, A. *JOM* **2021**, *73*, 4023–4029.
- (39) Čančarević, M.; Zinkevich, M.; Aldinger, F. *International Journal of Materials Research* **2005**, *96*, 879–887.
- (40) OECD–NEA, *Handbook on lead-bismuth eutectic alloy and lead properties, materials compatibility, thermalhydraulics and technologies*; Organisation for Economic Co-Operation and Development: 2015.
- (41) Corcoran, E. C.; Flèche, J.-L.; Dupin, N.; Sundman, B.; Guéneau, C. *Calphad* **2018**, *63*, 196–211.

- (42) Kauric, G. *Study of the Nuclear Fuel-Sodium Coolant Interaction for the Safety Assessment of Sodium-Cooled Fast Reactors (Ph. D. thesis), University Paris-Saclay, France* **2020**.
- (43) Smith, A. L.; Rutten, M.; Herrmann, L.; Epifano, E.; Konings, R. J. M.; Colineau, E.; Griveau, J.-C.; Guéneau, C.; Dupin, N. *Journal of the European Ceramic Society* **2021**, *41*, 3664–3686.
- (44) Dinsdale, A. T. *Calphad* **1991**, *15*, 317–425.
- (45) Alden, T.; Stevenson, D. A.; Wulff, J. *Transactions of the Metallurgical Society of AIME* **1958**, *212*.
- (46) Brewer, L. *International Atomic Energy Authority*, **1980**, 714.
- (47) Thaddeus, B. M. *Materials Park Ohio* **1990**, 2705–2708.
- (48) Volodin, V. N.; Tuleushev, Y.; Tsai, K. V.; Zhakanbaev, E. A. *The Physics of Metals and Metallography* **2014**, *115*, 500–506.
- (49) Petrushenko, S. I.; Dukarov, S. V.; Sukhov, V. N. *Journal of Nano- and Electronic Physics* **2016**, *8*, 04073–1.
- (50) Doyle, W. P.; Forbes, F. *Journal of Inorganic and Nuclear Chemistry* **1965**, *27*, 1271–1280.
- (51) Dronskowski, R.; Simon, A.; Mertin, W. *Zeitschrift für anorganische und allgemeine Chemie* **1991**, *602*, 49–63.
- (52) Wang, S.-L.; Yeh, J.-Y. *Acta Crystallographica Section B* **1991**, *47*, 446–451.
- (53) Jianxiao, X. Thermoelectric properties of transition metal oxides and thallium main group chalcogenides, Ph.D. Thesis, University of Waterloo, 2008.
- (54) Feja, S. Darstellung und Charakterisierung ternärer Molybdate in den Systemen M-Mo-O (M=Sn, Pb, Sb), Ph.D. Thesis, Technischen Universität Dresden, 2004.
- (55) Takatsu, H.; Hernandez, O.; Yoshimune, W.; Prestipino, C.; Yamamoto, T.; Tassel, C.; Kobayashi, Y.; Batuk, D.; Shibata, Y.; Abakumov, A. M., et al. *Physical Review B* **2017**, *95*, 155105.
- (56) Krivovichev, S. V.; Mentre, O.; Siidra, O. I.; Colmont, M.; Filatov, S. K. *Chemical Reviews* **2013**, *113*, 6459–6535.
- (57) Gabrielian, V. T.; Fedorova, L. M.; Tkachenko, E. B.; Neiman, A. Y.; Nikogosian, N. S. *Crystal Research and Technology* **1986**, *21*, 439–448.
- (58) Nihtianova, D. D.; Angelova, S. S.; Djonev, L. K.; Zheleva, T. S.; Tsukeva, E. A.; Petrov, K. P. *Journal of Crystal Growth* **1995**, *148*, 148–154.
- (59) Sillén, L. G.; Nylander, A.-L. *Arkiv för Kemi, Mineralogi och Geologi* **1943**, *17A*, 1–27.
- (60) Atuchin, V. V.; Ivannikova, N. V.; Komonov, A. I.; Kuratieva, N. V.; Loshkarev, I. D.; Pervukhina, N. V.; Pokrovsky, L. D.; Shlegel, V. N. *CrystEngComm* **2015**, *17*, 4512–4516.
- (61) Vassilev, P.; Nihtianova, D. *Acta Crystallographica Section C* **1998**, *54*, 1062–1064.

- (62) Muldrow Jr, C. N.; Hepler, L. G. *The Journal of Physical Chemistry* **1958**, *62*, 982–984.
- (63) Dellien, I.; McCurdy, K. G.; Hepler, L. G. *The Journal of Chemical Thermodynamics* **1976**, *8*, 203–207.
- (64) Bissengaliyeva, M. R.; Ogorodova, L. P.; Vlgasina, M. F.; Mel'chakova, L. V. *Russian Journal of Physical Chemistry A* **2013**, *87*, 163–165.
- (65) Wagman, D. D.; Evans, W. H.; Parker, V. B.; Halow, I.; Bailey, S. M.; Schumm, R. H. NBS Technical Note, 1969.
- (66) Weller, W. W.; Kelley, K. K. *U.S. Bureau of Mines Report of Investigations* **0194**, 6357.
- (67) Bissengaliyeva, M. R.; Bespyatov, M. A.; Gogol', D. B. *Journal of Chemical & Engineering Data* **2010**, *55*, 2974–2979.
- (68) Bissengaliyeva, M. R.; Gogol, D. B.; Bekturganov, N. S.; Taimassova, S. T.; Bespyatov, M. A.; Zhusipov, A. A. *Journal of Chemical & Engineering Data* **2011**, *56*, 1941–1945.
- (69) Glasser, L. *The Journal of Chemical Thermodynamics* **2022**, *166*, 106685.
- (70) Nikolaev, E. N.; Ovchinnikov, K. V.; Semenov, G. A. *Zhurnal Obshchej Khimii* **1984**, *54*, 977–978.
- (71) Kunkel, K.; Milke, E.; Binnewies, M. *International Journal of Mass Spectrometry* **2014**, *374*, 12–19.
- (72) Belyaev, I. N.; Smolyaninov, N. P. *Russian Journal of Inorganic Chemistry* **1962**, *5*, 579–581.
- (73) Kunev, D. K.; Belyaevskaya, L. V.; Zelikman, A. N. *Russian Journal of Inorganic Chemistry* **1966**, *11*, 1063–1064.
- (74) Bukhalova, G. A.; Manakov, V. M.; Maltsev, V. T. *Russian Journal of Inorganic Chemistry* **1971**, *16*, 280–281.
- (75) Eissa, M. A.; Elmasry, M. A. A.; Younis, S. S. *Thermochimica Acta* **1996**, *288*, 169–178.
- (76) Nihtianova, D. D.; Shumov, D. P.; Angelova, S. S.; Dimitriev, Y. B.; Petrov, L. L. *Journal of Crystal Growth* **1997**, *179*, 161–167.
- (77) Suryanarayana, S. V.; Deshpande, V. T. *Current Science* **1972**, *41*, 837–839.
- (78) Achary, S. N.; Patwe, S. J.; Vishwanath, A.; Wajhal, S.; Krishna, P. S. R.; Tyagi, A. K. *Materials Chemistry and Physics* **2021**, *260*, 124111.
- (79) Argyle, J. F.; Hummel, F. A. *Journal of the American Ceramic Society* **1963**, *46*, 10–14.
- (80) Mentzen, B. F.; Latrach, A.; Bouix, J.; Hewat, A. W. *Materials Research Bulletin* **1984**, *19*, 549–554.
- (81) Aritani, H.; Tanaka, T.; Funabiki, T.; Yoshida, S.; Kudo, M.; Hasegawa, S. *The Journal of Physical Chemistry* **1996**, *100*, 5440–5446.

- (82) Freitas, A. P.; André, R. E.; Poucin, C.; Le, T. K.-C.; Imbao, J.; Lassalle-Kaiser, B.; Carencio, S. *The Journal of Physical Chemistry C* **2021**, *125*, 17761–17773.
- (83) Smith, A. L.; Thi, T. N. P.; Guéneau, C.; Dumas, J.-C.; Epifano, E.; van Burik, W.; Dupin, N. *Calphad* **2021**, *75*, 102350.
- (84) Hillert, M.; Jansson, B.; Sundman, B.; Ågren, J. *Metallurgical Transactions A* **1985**, *16*, 261–266.
- (85) Sundman, B.; Jansson, B.; Andersson, J.-O. *Calphad* **1985**, *9*, 153–190.
- (86) Andersson, J.-O.; Helander, T.; Höglund, L.; Shi, P.; Sundman, B. *Calphad* **2002**, *26*, 273–312.
- (87) Rothe, J.; Butorin, S.; Dardenne, K.; Denecke, M. A.; Kienzler, B.; Löble, M.; Metz, V.; Seibert, A.; Steppert, M.; Vitova, T., et al. *Review of Scientific Instruments* **2012**, *83*, 043105.
- (88) Javorský, P.; Wastin, F.; Colineau, E.; Rebizant, J.; Boulet, P.; Stewart, G. *Journal of Nuclear Materials* **2005**, *344*, 50–55.



# 4

## THE PB-CS-MO-O SYSTEM

*The quaternary compound  $\text{Cs}_2\text{Pb}(\text{MoO}_4)_2$  was synthesised and its structure was characterised using X-ray and neutron diffraction from 298 K to 773 K, while thermal expansion was studied from 298 K to 723 K. The crystal structure of the high-temperature phase  $\beta\text{-Cs}_2\text{Pb}(\text{MoO}_4)_2$  was elucidated and it was found to crystallise in space group  $R\bar{3}m$  (166), i.e. with a palmierite structure. In addition, the oxidation state of Mo in the low-temperature phase  $\alpha\text{-Cs}_2\text{Pb}(\text{MoO}_4)_2$  was studied using X-ray Absorption Near Edge Structure spectroscopy. Phase diagram equilibria measurements in the  $\text{Cs}_2\text{MoO}_4\text{-PbMoO}_4$  system were performed, revisiting a previously reported phase diagram. The equilibrium phase diagram proposed here includes a different composition of the intermediate compound in this system. The obtained data can serve as relevant information for thermodynamic modelling in view of the safety assessment of next generation Lead-cooled Fast Reactors.*

---

This chapter is based on: A. van Hattem, J. Vlieland, R. Dankelman, M. Thijs, G. Wallez, K. Dardenne, J. Röthe, R.J.M. Konings and A.L. Smith, *Structural Studies and Thermal Analysis in the  $\text{Cs}_2\text{MoO}_4\text{-PbMoO}_4$  System with Elucidation of  $\beta\text{-Cs}_2\text{Pb}(\text{MoO}_4)_2$* , *Inorganic Chemistry* **62**, 18 (2023): 6981-6992 and A. van Hattem, J. Vlieland, E. Colineau, J.-C. Griveau, R.J.M. Konings and A.L. Smith *Thermodynamic Study of  $\alpha\text{-Cs}_2\text{Pb}(\text{MoO}_4)_2$  and Safety Assessment of the Pb-JOG Interaction in Lead-cooled Fast Reactors* *Journal of Nuclear Materials* (under review)

## 4.1. INTRODUCTION

In the accidental scenario of failure of the cladding material during reactor operation in lead-cooled fast reactors [1], the coolant will come into contact with the irradiated fuel, starting with the JOG-phase for a burn-up higher than 7-8 at%. During irradiation, numerous fission products are generated within the fuel matrix, including gases, metallic precipitates, oxide precipitates and fission products soluble inside the fuel matrix [2, 3]. Of particular interest in this research is the class of volatile and semi-volatile elements (Cs, Mo, I, Te) that migrate from the centre of the (U,Pu)O<sub>2</sub> fuel pellet towards the fuel periphery because of the expected very high temperatures and thermal gradient (over 2273 K in the centre and 873 K in the pellet rim with a gradient of over 1000 K·cm<sup>-1</sup>) [2]. Those fission products accumulate with time in the space between fuel and cladding and form above 7-8 at% burn-up the so-called JOG (Joint Oxyde Gaine) layer of a few hundred micrometer, with mostly Cs<sub>2</sub>MoO<sub>4</sub> in combination with CsI and Cs<sub>2</sub>Te according to post irradiation examinations (PIE) and thermochemical calculations [4–6].

One of the possible chemical interactions that requires investigation is the interaction of Pb-coolant with Cs<sub>2</sub>MoO<sub>4</sub>, a major JOG-phase constituent. With this scenario in mind, the chemistry of the Pb-Cs-Mo-O system is investigated, building on the chemistry of the Pb-Mo-O system addressed in the previous chapter. In this study, the emphasis is on the pseudo-binary section Cs<sub>2</sub>MoO<sub>4</sub>-PbMoO<sub>4</sub> of the ternary system PbO-Cs<sub>2</sub>O-MoO<sub>3</sub> which includes the quaternary phase Cs<sub>2</sub>Pb(MoO<sub>4</sub>)<sub>2</sub>.

The literature on the phase diagram Cs<sub>2</sub>MoO<sub>4</sub>-PbMoO<sub>4</sub> is, to the best of our knowledge, limited to a study by Belyaev and Chikova published in 1964 [7]. Their published phase diagram is reproduced in Figure 4.1. Their interpretation of the measured phase equilibria can be related to their experimental approach, but their claim of the existence of Cs<sub>2</sub>Pb<sub>2</sub>(MoO<sub>4</sub>)<sub>3</sub>, which they report to decompose at 935 K, is found to be incorrect. They also suggest solid solubility domains near the end-members, which we will discuss in light of our new investigations.

In 1977, Dudnik and Mnushkina investigated K<sub>2</sub>Pb(MoO<sub>4</sub>)<sub>2</sub> and isomorphous compounds, among which Cs<sub>2</sub>Pb(MoO<sub>4</sub>)<sub>2</sub> [8]. They have grown crystals in this series, without studying complete crystallographic details. They made the specific composition, and, using polarised light, determined that a domain structure disappears above a certain temperature. Based on this, they reported a phase transition at (626 ± 10) K for Cs<sub>2</sub>Pb(MoO<sub>4</sub>)<sub>2</sub>. The compound is also mentioned in a review paper on binary molybdates by Solodovnikov *et al.* in 1994 [9]. In a later review on molybdates and tungstates of monovalent and bivalent elements by Isupov [10], both transition temperatures are mentioned, *i.e.* that at (626 ± 10) K (phase transition), and that at 935 K (decomposition) for the Cs<sub>2</sub>Pb(MoO<sub>4</sub>)<sub>2</sub> stoichiometry. The compound Cs<sub>2</sub>Pb(MoO<sub>4</sub>)<sub>2</sub> was also found in a study by Tsyrenova *et al.* in 1987 [11]. The first dedicated crystallographic study on Cs<sub>2</sub>Pb(MoO<sub>4</sub>)<sub>2</sub> was published by Solodovnikov *et al.* in 2017, based on single crystal data [12]. The authors elucidated the crystal structure and performed differential scanning calorimetry to study the thermal behaviour. Moreover, they investigated electronic properties of the compound, which is out of the scope of the current research.

This work brings new insights in the phase equilibria in the Cs<sub>2</sub>MoO<sub>4</sub>-PbMoO<sub>4</sub> system, solves discrepancies noticed in the literature, and explores in more detail the structural and thermal properties of the quaternary phase Cs<sub>2</sub>Pb(MoO<sub>4</sub>)<sub>2</sub>, by using X-ray and

neutron diffraction at ambient and high temperatures, differential scanning calorimetry, solution calorimetry, thermal-relaxation calorimetry and X-ray absorption spectroscopy. Thereby, it positions the compound  $\text{Cs}_2\text{Pb}(\text{MoO}_4)_2$  in the updated phase diagram section  $\text{Cs}_2\text{MoO}_4$ - $\text{PbMoO}_4$  and explores properties of relevance of  $\text{Cs}_2\text{Pb}(\text{MoO}_4)_2$  for Lead-cooled Fast Reactor safety assessment.

Next to the applicability for LFRs, the results obtained are wider applicable, as the structural family of binary molybdates and tungstates shows appealing properties in for instance their ferro-elastic and ferro-electric behaviour [10, 13]. Among these complex compounds is the group of the binary molybdates and tungstates with mono- and bivalent elements, *i.e.* the  $(\text{A}_2^+\text{B}^{2+}(\text{X}^{6+}\text{O}_4)_2)$  structural type, with  $\text{A}=(\text{K}, \text{Rb} \text{ or } \text{Cs})$ ,  $\text{B}=(\text{Ba}, \text{Pb})$  and  $\text{X}=(\text{Mo}, \text{W})$  [8–10, 12, 14–16]. Moreover, binary molybdates and tungstates are also versatile as host material for phosphors [17, 18].

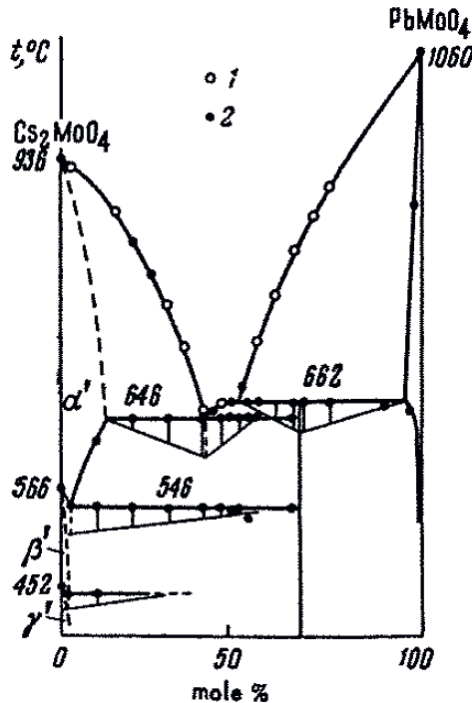


Figure 4.1: The  $\text{Cs}_2\text{MoO}_4$ - $\text{PbMoO}_4$  phase diagram as reported by Belyaev and Chikova [7]. The open circles correspond to visual polythermal results; the closed circles correspond to thermographic results. Reproduced with permission from Reference 21 (Belyaev, I.; Chikova, N. *Zhurnal Neorganicheskoi Khimii*, 9, 2754–2760). Copyright 1964 Springer.

## 4.2. STRUCTURAL CHARACTERISATION OF $\alpha$ - $\text{Cs}_2\text{Pb}(\text{MoO}_4)_2$

$\text{Cs}_2\text{Pb}(\text{MoO}_4)_2$  was synthesised via solid state synthesis and analysed using X-ray and neutron diffraction. The diffraction patterns obtained with X-rays and neutrons are shown in Figures 4.2 and 4.3, respectively.  $\alpha$ - $\text{Cs}_2\text{Pb}(\text{MoO}_4)_2$  crystallises with monoclinic

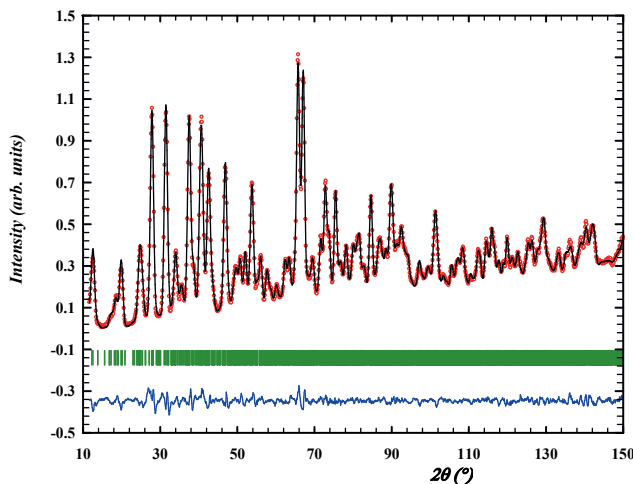


Figure 4.2: Experimental ( $Y_{obs}$ , in red) and calculated ( $Y_{calc}$ , in black) ND patterns of  $\alpha$ - $\text{Cs}_2\text{Pb}(\text{MoO}_4)_2$  at room temperature. The difference between the calculated and the experimental intensities  $Y_{obs} - Y_{calc}$  is shown in blue. The angular positions of the Bragg reflections are shown in green. Measurement at  $\lambda = 1.66718$  Å.

symmetry in space group  $C2/m$  (12); the atomic coordinates as reported by Solodovnikov *et al.* were used as a starting point for the refinement [12]. The cell parameters obtained after refinement of the model against the data from both diffraction methods are listed in Table 4.1. To refine the model against the neutron diffraction data, soft constraints on the Mo-O distances (fixed at  $1.79 \text{ Å} \pm 0.02\%$ ) and atomic displacement parameters (one  $B$  value per chemical element) were imposed. The values obtained for the atomic displacement parameters are high, but rather realistic considering that Cs-based structures are soft and subject to thermal displacement. A refinement without any constraints was first attempted but would lead to unphysical Mo-O bond lengths (scattering between 1.41 and 2.07 Å) considering the covalency of the bond. The quality of the refinement is considered satisfactory given that it is performed on powders for a large unit cell with low symmetry, meaning there are many atomic positions (35 in total) and substantial peaks overlap. The crystal structure (see Figure 4.4) can be described as consisting of two types of layers: layers of corner-sharing caesium polyhedra and layers of alternating lead polyhedra and molybdate tetrahedra that are corner-sharing. The coordination number for Cs cations is 10; the Pb cations have an irregular six-fold coordination.

The atomic positions found in the refinement against the neutron diffraction data were used as input for the refinement of the model against the X-ray diffraction data. It is observed that the obtained cell parameters for ND are slightly smaller than those obtained by XRD. The same effect was observed in the XRD and ND refined profile parameters of  $\text{Cs}_2\text{Ba}(\text{MoO}_4)_2$  by Smith *et al.* [16]. The discrepancy, which is about the same

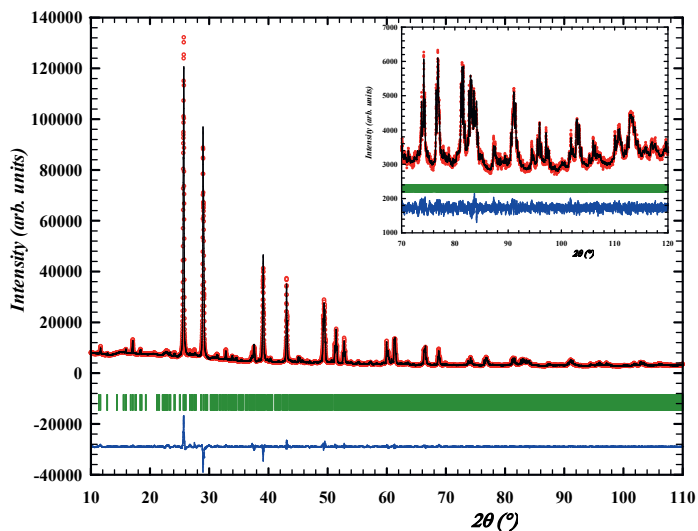


Figure 4.3: Experimental ( $Y_{obs}$ , in red) and calculated ( $Y_{calc}$ , in black) XRD patterns of  $\alpha$ - $\text{Cs}_2\text{Pb}(\text{MoO}_4)_2$  at 298 K. The difference between calculated and experimental intensities  $Y_{obs} - Y_{calc}$  is shown in blue. The angular positions of Bragg reflections are shown in green. Measurement at  $\lambda = \text{Cu } K\alpha$ .

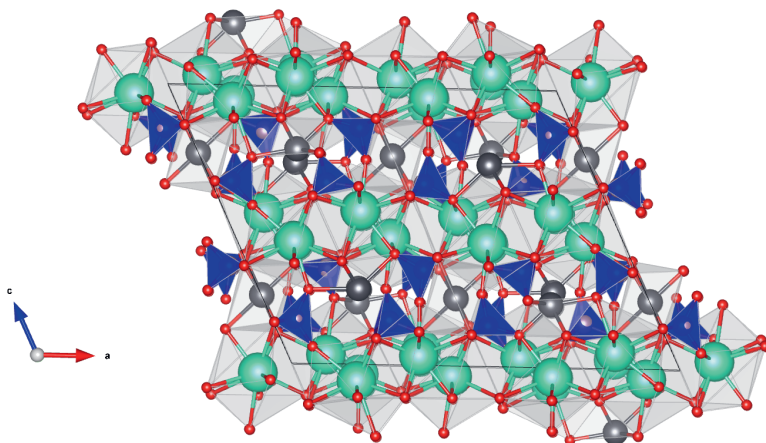


Figure 4.4: The room temperature crystal structure of  $\alpha$ - $\text{Cs}_2\text{Pb}(\text{MoO}_4)_2$  as refined in this work using the neutron diffraction data. In blue, the  $\text{MoO}_4^{2-}$ -tetrahedra; in grey the Pb-atoms; in green the Cs-atoms and in red the O-atoms. The visualisation was made using Vesta [19].

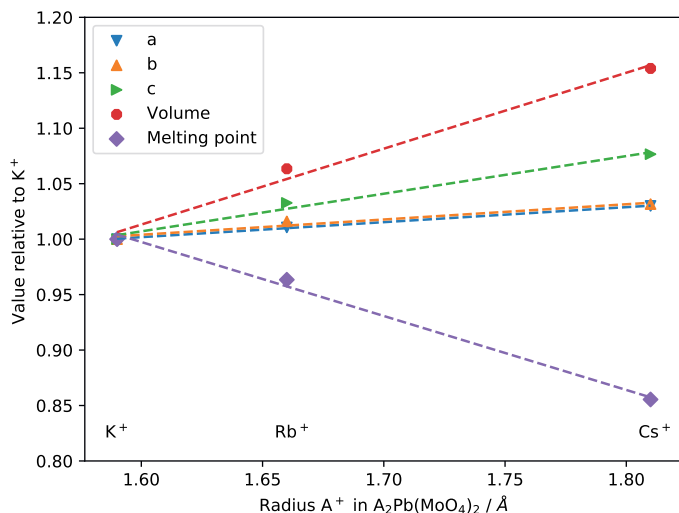


Figure 4.5: Trends of cell parameters  $a$ ,  $b$ ,  $c$ , volume and melting point against the ionic radius of the alkali metal ion with coordination number 10 for  $A_2Pb(MoO_4)_2$  ( $A = K, Rb, Cs$ ) using crystal data from [7, 14, 15] and ionic radii from [20]. The  $K^+$ -values are used as normalisation factor.

on the three axes, might be explained by a slight deviation in neutron wavelength or from a refinement artefact. A temperature difference during the measurement cannot account for the order of magnitude of this observation. The volume at 298 K we find here from XRD data deviates only 0.23% from the one reported by Solodovnikov *et al.* [12]. The choice of the synthesis gas (oxygen vs argon) seems to have no significant effect on the unit cell parameters. With these diffraction studies at 298 K, the recent results of Solodovnikov *et al.* [9] with regard to the composition of the compound in the phase diagram  $Cs_2MoO_4$ - $PbMoO_4$  are confirmed and further substantiated. It is interesting to note that Isupov [13] silently corrected the composition of Belyaev and Chikova [7] and/or used the one reported by Dudnik and Mnushkina [8], since the author did no experimental investigations by that time and Dudnik and Mnushkina do not comment on the composition given by Belyaev and Chikova.

The recent literature on  $A_2Pb(MO_4)_2$  with  $A=(Cs, Rb, K)$  states that all three compounds crystallise in a large palmieriete-related superstructure [14, 15]. Unfortunately, the atomic positions for  $K_2Pb(MoO_4)_2$  have not been reported, so neither are the specific average alkali metal-oxygen distances in the coordination in the actual compound. However, using the ionic radii of the alkali metal ion with a specific coordination number taken from the Shannon database [20], the unit cell parameters can be plotted against ionic radius, as is done in Figure 4.5. For the Cs-variant, the Cs coordination number is reported to be 10 [12], while for Rb, the coordination number is equal to 10-12. For K, we do not have the data. The cell parameters increase approximately linearly, while the melting point decreases with increasing ionic radius of the alkali metal ion [7, 14, 15].

Synthesis atmosphere	Method	$a^a / \text{\AA}$	$b^a / \text{\AA}$	$c^a / \text{\AA}$	$\beta^a / ^\circ$	$V / \text{\AA}^3$
O <sub>2</sub>	XRD	21.3860(19)	12.2784(11)	16.7944(16)	114.994(5)	3997.3(6)
Ar	XRD	21.3752(23)	12.2879(13)	16.7916(19)	114.998(8)	3997.3(8)
O <sub>2</sub>	ND	21.345(14)	12.257(7)	16.760(10)	114.98(6)	3975(4)
not reported	XRD[12]	21.3755(13)	12.3123(8)	16.8024(10)	115.037 (2)	4006.6(3)

Table 4.1: Cell parameters of  $\alpha$ -Cs<sub>2</sub>Pb(MoO<sub>4</sub>)<sub>2</sub> as determined in this research with X-ray Diffraction (XRD) and Neutron Diffraction (ND) and as reported in the literature [12] as measured at ambient conditions. The compound crystallises in the monoclinic space group  $C2/m$  (12).

<sup>a</sup> Note that the statistically derived s.u.'s obtained from the refinement are underestimated by about one order of magnitude, and were thus multiplied by 10 as listed in this table.

### 4.3. STRUCTURAL CHARACTERISATION OF $\beta$ -Cs<sub>2</sub>Pb(MoO<sub>4</sub>)<sub>2</sub>

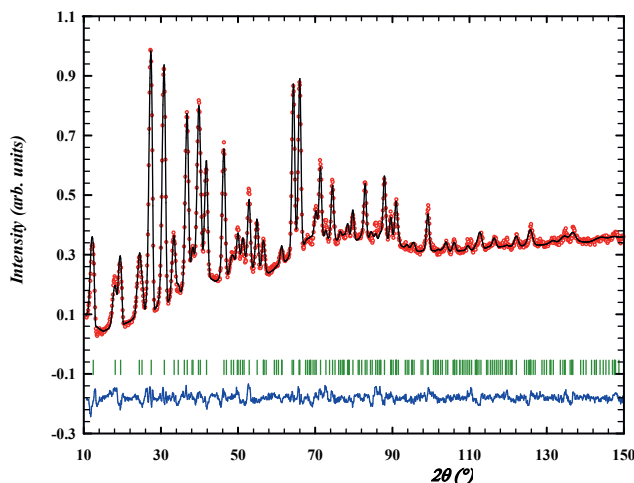


Figure 4.6: Experimental ( $Y_{obs}$ , in red) and calculated ( $Y_{calc}$ , in black) ND patterns of  $\beta$ -Cs<sub>2</sub>Pb(MoO<sub>4</sub>)<sub>2</sub> at 773 K. The difference between calculated and experimental intensities  $Y_{obs} - Y_{calc}$  is shown in blue. The angular positions of Bragg reflections are shown in green. Measurement at  $\lambda = 1.66718 \text{ \AA}$ .

The diffraction patterns obtained with neutrons at 773 K and X-rays at 723 K are shown in Figures 4.6 and 4.7, respectively, while the cell parameters obtained after refinement of the model using the data from both methods are listed in Table 4.2. For the refinement at high temperature, soft constraints on the Mo-O distances still had to be applied; the atomic displacements, however, are high, thus lowering the reliability of the intensities at high angles. Anisotropic displacement parameters were refined for each atom; the rather high values are justified by the high temperature, combined with the weakness of the Cs-O bonds. The position of the O1 atom splits into three po-

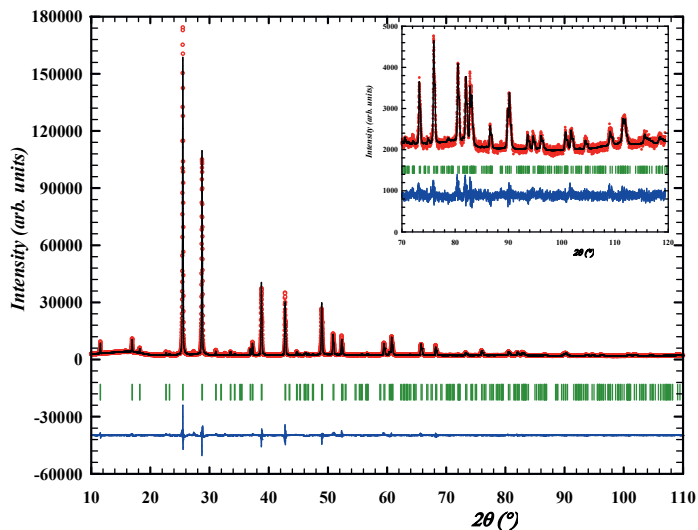


Figure 4.7: Experimental ( $Y_{obs}$ , in red) and calculated ( $Y_{calc}$ , in black) XRD patterns of  $\beta$ - $\text{Cs}_2\text{Pb}(\text{MoO}_4)_2$  at 723 K. The difference between calculated and experimental intensities  $Y_{obs} - Y_{calc}$  is shown in blue. The angular positions of Bragg reflections are shown in green. Measurement at  $\lambda = \text{Cu } K\alpha$ .

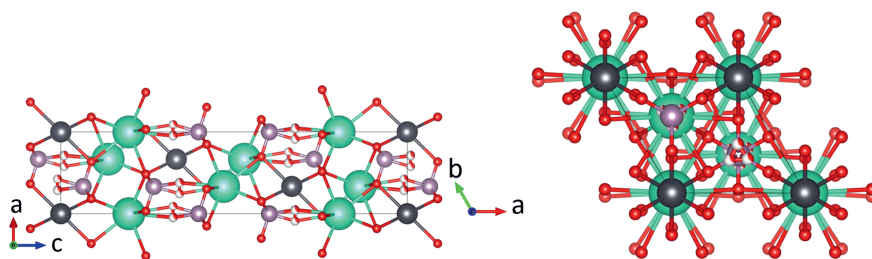


Figure 4.8: The crystal structure of  $\beta$ - $\text{Cs}_2\text{Pb}(\text{MoO}_4)_2$  as obtained in this work from refinement of the model against neutron diffraction data collected at 773 K. In grey the Pb-atoms, in green the Cs-atoms, in purple the Mo-atoms and in red the O-atoms. Partially white O-atoms correspond to partial occupancy. Left: visualisation along the  $b$ -axis. Right: visualisation along the  $c$ -axis. The visualisation was made using Vesta [19].

sitions around the axial site due to the thermal disorder. The atomic coordinates, as based on neutron diffraction at 773 K, are given in Table 4.3, along with the occupancy factors and atomic displacement parameters. Visualisations along the  $b$  and  $c$  axes of  $\beta\text{-Cs}_2\text{Pb}(\text{MoO}_4)_2$  are given in Figure 4.8. In the diffraction patterns obtained above the transition temperature, the reflections with at least one odd Miller index ( $h$ ,  $k$ , or  $l = 2n + 1$  with  $n$  a positive integer) disappear. This disappearance of the superstructure led us to refine  $\beta\text{-Cs}_2\text{Pb}(\text{MoO}_4)_2$  in the same space group (*viz.*  $C2/m$  (12)) with halved cell parameters. In this way, the 2 and  $m$  symmetries are preserved as expected for a second order phase transition; their number is even multiplied due to the shortening of the cell parameters. The  $C$ -mode still applies, as is evident from the systematic extinctions. However, this new unit cell of  $\beta\text{-Cs}_2\text{Pb}(\text{MoO}_4)_2$  actually has a higher symmetry element and it crystallises in space group  $R\bar{3}m$  (166). Thus, the transition from  $\alpha\text{-Cs}_2\text{Pb}(\text{MoO}_4)_2$  to  $\beta\text{-Cs}_2\text{Pb}(\text{MoO}_4)_2$  is the transition of the palmierite-related room temperature phase to the actual palmierite structure at high temperature. In the Fourier difference map, some residuals were found that are believed not to correspond to the mother structure of  $\beta\text{-Cs}_2\text{Pb}(\text{MoO}_4)_2$ . These residuals at a few percent level, that are ascribed to defects, together with the thermal displacement of the atoms, are reflected in the average quality of the refinements. A dedicated high resolution single crystal study would be desirable, but it is out of scope of the current research.

T / K	Method	$a^a$ / Å	$c^a$ / Å	$V$ / Å <sup>3</sup>
673	XRD	6.2057(8)	22.968(3)	766.0(2)
723	XRD	6.2126(8)	22.977(3)	768.02(17)
773	ND	6.26(4)	23.00(25)	781(11)

Table 4.2: Cell parameters of  $\beta\text{-Cs}_2\text{Pb}(\text{MoO}_4)_2$  as determined in this research with X-ray Diffraction (XRD) at 673 and 723 K and Neutron Diffraction (ND) at 773 K. The compound crystallises in the space group  $R\bar{3}m$  (166). Here,  $a = b, \gamma = 120^\circ$ .

<sup>a</sup> Note that the statistically derived s.u.'s obtained from the refinement are underestimated by about one order of magnitude, and were thus multiplied by 10 as listed in this table.

#### 4.4. THERMAL EXPANSION OF $\text{Cs}_2\text{Pb}(\text{MoO}_4)_2$

The thermal expansion of  $\text{Cs}_2\text{Pb}(\text{MoO}_4)_2$  was measured using high-temperature X-ray and neutron diffraction. For nuclear reactor applications, the thermal expansion behaviour is of paramount significance to assess mechanical interaction of the possible product of JOG-coolant interaction with the nuclear fuel and cladding. The cell pa-

Atom	Wyckoff	$x$	$y$	$z$	Occupancy factor	$B_{eq}$ (Å <sup>2</sup> )
Pb	3a	0	0	0	1	6.3(4)
Cs	6c	0	0	0.198(4)	1	3(4)
Mo	6c	0	0	0.398(4)	1	4(4)
O1	18h	0.10(2)	0.05(2)	0.324(6)	0.3333	10(10)
O2	18h	0.302(6)	0.151(3)	0.4212(18)	1	9(2)

Table 4.3: Atomic positions in  $\beta\text{-Cs}_2\text{Pb}(\text{MoO}_4)_2$  obtained after refinement using the neutron diffraction data collected at 773 K.  $B_{eq} = 8\pi^2 U_{eq}$  with  $U_{eq}$  as refined by FullProf.

parameters of  $\text{Cs}_2\text{Pb}(\text{MoO}_4)_2$  as evolving with temperature are given in Table 4.4. As can be concluded from this table,  $\text{Cs}_2\text{Pb}(\text{MoO}_4)_2$  shows a positive thermal expansion in the measured temperature range. The expansion is high due to the weakness of the Cs-O bonds, though the overall expansion is not as high as in  $\text{Cs}_2\text{MoO}_4$  because of the lower Cs-content (for comparison, see Figure 4.9). The relative thermal expansion as calculated using  $f(T) = (x_T - x_{298K})/x_{298K}$  with  $x = \{a, b, c\}$ , is shown in Figure 4.9 for the whole temperature range 298 till 723 K, refining XRD data in space group 12 ( $C2/m$ ). A correction was applied for the fact that the high-temperature structure has halved cell parameters and contains only 1/8 of the atoms of the room-temperature structure. Linear relative expansion coefficients of the axes for  $a$ ,  $b$  and  $c$  for the temperature range from 298 to 723 K are  $16 \cdot 10^{-6} \text{ K}^{-1}$ ,  $26 \cdot 10^{-6} \text{ K}^{-1}$  and  $18 \cdot 10^{-6} \text{ K}^{-1}$ , respectively. The mean relative thermal expansion  $dl/l_0$ , taking  $l_0 = (V_0)^{1/3}$  at room temperature as reference is given by:

$$dl/l_0 = -4.5 \cdot 10^{-3} + 1.3 \cdot 10^{-5} \cdot T + 5.8 \cdot 10^{-9} \cdot T^2 \quad (4.1)$$

for the temperature range from 298 to 723 K. The volumetric thermal expansion is defined as:  $\alpha_V = \frac{1}{V_{298K}} \frac{\partial V}{\partial T}$ . Neglecting the phase transition, the volumetric thermal expansion is found to be  $58.4 \cdot 10^{-6} \text{ K}^{-1}$  over the range of 298-723 K. Besides the high temperature XRD, neutron diffraction data collected at 573 K and 773 K also showed positive thermal expansion coefficients. The cell parameters at 298 K, 573 K and 773 K are given in Tables 4.2 and 4.4.

As reported earlier, the phase transition in  $\text{Cs}_2\text{Pb}(\text{MoO}_4)_2$  is of second order: based on ferroelastic response, the transition temperature is reported to be  $(626 \pm 10) \text{ K}$  [8]; based on DSC the temperature is reported to be  $(635 \pm 2) \text{ K}$  [12]; based on crystal optical observations on a polarising microscope it is reported to be  $(640 \pm 2) \text{ K}$  [12]. In the high temperature XRD measurements, a change was observed in the diffraction pattern by a change of relative intensity in specific Bragg reflections, *vide supra*. The high-temperature diffraction studies confirm the phase transition, as up to 623 K, the diffraction pattern can best be explained by  $\alpha$ - $\text{Cs}_2\text{Pb}(\text{MoO}_4)_2$ , while the patterns at higher temperature are best explained by  $\beta$ - $\text{Cs}_2\text{Pb}(\text{MoO}_4)_2$ , as judged from  $\chi^2$ -values. Close inspection of the evolution of the cell parameters seem to hint to a change of linear response around 573 K. When the cell parameter  $a$  is plotted against temperature (Figure 4.9), the points from 298 K up to 523 K show an almost perfect linear increase; the correlation coefficient decreases slightly when the higher temperature points are included. The mean linear expansion evolves continuously at the transition point, which corresponds with the classification of a second order phenomenon.

The mean relative thermal expansion is compared with  $\text{Cs}_2\text{MoO}_4$  as a model for the JOG-phase and  $\text{UO}_2$  as model for the fuel. For  $\text{Cs}_2\text{MoO}_4$ , the data were taken from Wallez *et al.* [21]. The recommended value for the thermal expansion of  $\text{UO}_2$  [22, 23] was plotted in Figure 4.9. For Pu contents up to 30%, the thermal expansion of  $\text{UO}_2$  is representative for the mixed oxide fuel thermal expansion [22]. As can be concluded from the plotted lines, the thermal expansion of  $\text{Cs}_2\text{Pb}(\text{MoO}_4)_2$  is approximately half of the expansion of the JOG-phase but about twice as high as the fuel expansion. Thus, a potential formation of this quaternary phase in accidental conditions should not aggravate the mechanical interaction with the cladding compared to  $\text{Cs}_2\text{MoO}_4$ .

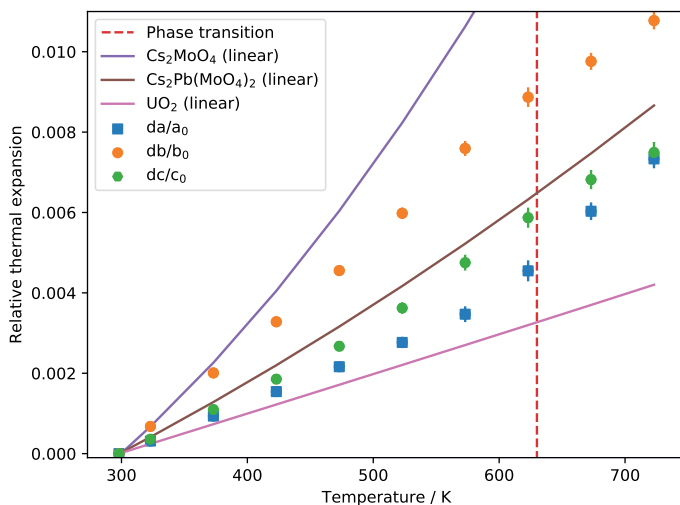


Figure 4.9: Relative thermal expansion of  $\text{Cs}_2\text{Pb}(\text{MoO}_4)_2$  based on XRD at various temperatures. The vertical dashed line is the second order transition temperature, calculated as the average of refs. [8, 12], *i.e.* 630 K. If not visible, error bars are smaller than symbols. The relative figures are calculated using  $f(T) = (x_T - x_{298K})/x_{298K}$  with  $x = \{a, b, c\}$ .

XRD					
T / K	$a^a / \text{\AA}$	$b^a / \text{\AA}$	$c^a / \text{\AA}$	$\beta^a / ^\circ$	$V / \text{\AA}^3$
298	21.3860(18)	12.2791(10)	16.7929(15)	114.990(5)	3997.0(6)
323	21.3928(18)	12.2874(11)	16.7989(15)	114.991(5)	4002.4(6)
373	21.4060(19)	12.3038(11)	16.8113(16)	114.993(5)	4013.1(6)
423	21.4191(21)	12.3194(13)	16.8240(17)	114.998(6)	4023.5(7)
473	21.4323(23)	12.3351(14)	16.8377(19)	115.007(8)	4034.1(8)
523	21.445(3)	12.3526(17)	16.8537(24)	115.023(10)	4045.6(10)
573	21.460(4)	12.3724(23)	16.873(3)	115.045(18)	4058.7(14)
623	21.483(6)	12.388(3)	16.891(4)	115.072(26)	4071.9(18)
ND					
T / K	$a^a / \text{\AA}$	$b^a / \text{\AA}$	$c^a / \text{\AA}$	$\beta^a / ^\circ$	$V / \text{\AA}^3$
298	21.345(14)	12.257(7)	16.760(10)	114.98(6)	3975(4)
573	21.4(2)	12.39(13)	16.86(12)	115.1(8)	4053(70)

Table 4.4: Cell parameters and unit cell volume for  $\alpha$ - $\text{Cs}_2\text{Pb}(\text{MoO}_4)_2$  as measured by ht-XRD and ht-ND.

<sup>a</sup> Note that the statistically derived s.u.'s obtained from the refinements are underestimated by about one order of magnitude, and were thus multiplied by 10 as listed in this table.

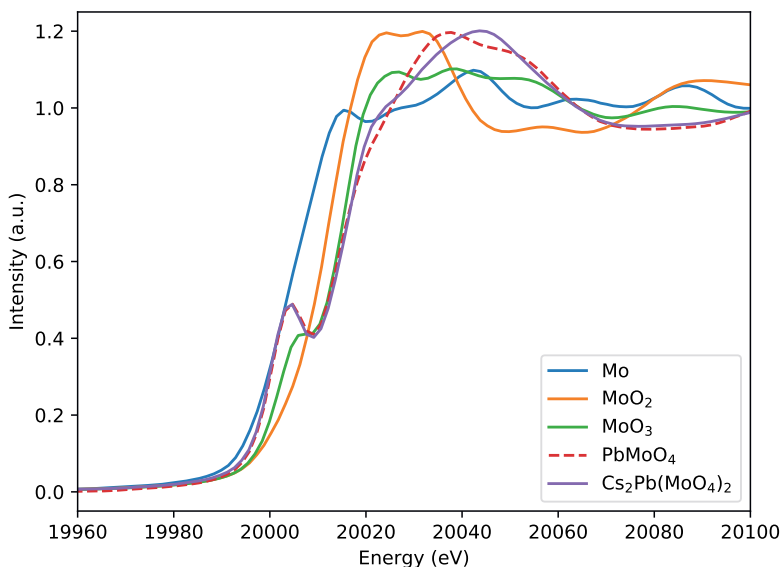


Figure 4.10: X-ray absorption near-edge structure (XANES) spectra around the Mo K-edge.

#### 4.5. X-RAY ABSORPTION SPECTROSCOPY AT THE MO K-EDGE

In a Lead-cooled Fast Reactor, the formation of  $\text{Cs}_2\text{Pb}(\text{MoO}_4)_2$  depends on the oxygen chemical potential of the fuel and the amount of oxygen dissolved in the lead coolant. The oxidation state of Mo is key to this understanding and can be studied using X-ray absorption near-edge structure (XANES) spectroscopy. In Figure 4.10, the collected XANES spectra around the Mo K-edge are shown. The derived absorption edge threshold and pre-peak features are listed in Table 4.5. The intrinsic features of Mo(0), Mo(IV) in  $\text{MoO}_2$  and Mo(VI) in  $\text{MoO}_3$  (reference materials) can be seen in the increase in  $E_0$ -position with increasing Mo valence state. Moreover, while the former two have a simple edge, Mo(VI) in  $\text{MoO}_3$  has a characteristic pre-edge feature, which is explained below. The absorption at the K-edge involves a transition originating from the  $1s$  orbital. Molybdenum metal has the electronic configuration  $[\text{Kr}]5s^14d^55p^0$ . The transitions  $1s \rightarrow 4d$  and  $1s \rightarrow 5s$  are parity forbidden. The transition of  $1s \rightarrow 5p$  is parity allowed, since, using the dipole approximation for the interaction of the X-rays with one electron,  $\langle \Psi(5p) | \hat{\epsilon} \cdot \vec{r} | \Psi(1s) \rangle$  is non-zero. If the centre of inversion on Mo is lost by distortion of an octahedron or switching to tetrahedral symmetry, hybridisation of  $4d$  with  $5p$  causes a pre-edge to appear [24]. In the molybdates, this extra edge feature is more pronounced than in  $\text{MoO}_3$ . In  $\text{MoO}_3$ , this is observed as a shoulder due to core hole broadening; the broadening comes from the hybridisation of  $\text{O}(2p)$  with  $\text{Mo}(4d)$  and  $\text{Mo}(5p)$  [25]. The measured  $E_0$  values (Table 4.5) for  $\text{PbMoO}_4$  and  $\text{Cs}_2\text{Pb}(\text{MoO}_4)_2$  are very close to that of  $\text{MoO}_3$ , indicating a valence state Mo(VI).

Compound	Pre-peak (eV)	Edge $E_0$ (eV)
Mo(0)	-	20000
MoO <sub>2</sub>	-	20012.3
MoO <sub>3</sub>	20007.6	20015.8
PbMoO <sub>4</sub>	20004.5	20014.4
Cs <sub>2</sub> Pb(MoO <sub>4</sub> ) <sub>2</sub>	20004.2	20016.4
MoO <sub>2</sub> [26]	-	20012.0
MoO <sub>3</sub> [26]	20007.6	20015.7
BaMoO <sub>4</sub> [26]	20006.1	20015.1

Table 4.5: Energies of the pre-peak and edge in the normalized XANES spectra. The edges are determined based on the inflection points in the normalised XANES spectra at the Mo K-edge. The pre-peaks are determined via the maximum. The estimated expanded uncertainty (with a coverage factor  $k=2$ ) on the energies is 1.0 eV.

## 4.6. PHASE EQUILIBRIA IN THE $\text{Cs}_2\text{MoO}_4$ - $\text{PbMoO}_4$ PHASE DIAGRAM

### 4.6.1. TRANSITION TEMPERATURES OF THE END-MEMBERS AND INTERMEDIATE COMPOUND $\text{Cs}_2\text{Pb}(\text{MoO}_4)_2$

Combined thermogravimetric-differential scanning calorimetry (TG-DSC) was used to measure phase transition temperatures. The transition temperatures measured in this work for the end-member compounds  $\text{Cs}_2\text{MoO}_4$ ,  $\text{PbMoO}_4$  and intermediate compound  $\text{Cs}_2\text{Pb}(\text{MoO}_4)_2$  are tabulated in Table 4.6 and compared to literature.

$\text{Cs}_2\text{MoO}_4$  was investigated many times and a thermodynamic assessment in combination with a CALPHAD model was published by Smith *et al.* in 2021 [27]. The temperatures corresponding to the phase transition  $\alpha$ - $\text{Cs}_2\text{MoO}_4 \rightarrow \beta$ - $\text{Cs}_2\text{MoO}_4$  and the melting point found during the current investigations ( $(837 \pm 5)$  K and  $(1222 \pm 5)$  K) match the values in the Cs-Mo-O CALPHAD model (841.3 K and 1223 K) well. For comparison, experimentally measured values of Belyaev and Chikova [7] and Smith *et al.* are added in Table 4.6 too [28].

The melting point of  $\text{PbMoO}_4$  as measured in this work ( $(1340 \pm 5)$  K and  $(1338 \pm 5)$  K as measured by TG-DSC and DSC) is in good agreement with the literature data [29–32]. No polymorphism was observed for  $\text{PbMoO}_4$ .

For  $\text{Cs}_2\text{Pb}(\text{MoO}_4)_2$  only a single event was detected upon heating, *viz.* the incongruent melting of the compound. The second order transition, that was detected using DSC by Solodovnikov *et al.*, is only present as a very small feature (see Figure 4.11) in the current measurement with a 100 mg sample. Given the nature of the transition, no significant heat effect is expected. As a result, DSC is not the most appropriate technique for studying this transition. The derived temperature for the transition is  $(626 \pm 5)$  K. Upon heating above the temperature of the large event in the DSC curve of  $\text{Cs}_2\text{Pb}(\text{MoO}_4)_2$ , decomposition starts. This is evident from the cooling curve (also added in Figure 4.11), which shows two peaks close together and a third peak appearing. During the next heating cycle, it turns out the temperature of the lower transition appears close to the polymorphism of  $\text{Cs}_2\text{MoO}_4$  (it is actually somewhat lowered because of the solid solution,

Compound	T / K	Transition type	Method	Reference
Cs <sub>2</sub> MoO <sub>4</sub>	837±10	Polymorphism	TG-DSC	This work
	839	Polymorphism	TG	[7]
	841.3	Polymorphism	CALPHAD model	[27]
	839±5	Polymorphism	TG-DSC	[28]
	1222±5	Congruent melting	TG-DSC	This work
	1209	-	TG	[7]
	1223	Congruent melting	CALPHAD model	[27]
	1225±5	Congruent melting	TG-DSC	[28]
Cs <sub>2</sub> Pb(MoO <sub>4</sub> ) <sub>2</sub>	626±5	Polymorphism	TG-DSC	This work
	626±10	Polymorphism	Optical	[8]
	635±2	Polymorphism	DSC	[12]
	640±2	Polymorphism	Optical	[12]
	923	Melting	DTA	[11]
	933±5	Incongruent melting	TG-DSC	This work
	935	Incongruent melting	TG	[7]
	926±3	Incongruent melting	DSC	[12]
PbMoO <sub>4</sub>	1340±5	Congruent melting	TG-DSC	This work
	1338±5	Congruent melting	DSC	This work
	1338	Congruent melting	-	[29]
	1336	Congruent melting	TG	[30]
	1343	Congruent melting	DTA	[31]
	1336±5	Congruent melting	TG	[32]

Table 4.6: Phase transition temperatures of the compounds in the pseudo-binary section Cs<sub>2</sub>MoO<sub>4</sub>-PbMoO<sub>4</sub> measured in this research as compared to literature. (TG-)DSC = thermogravimetric differential scanning calorimetry; TG = thermogravimetry; DTA = differential thermal analysis; optical = optical microscope.

*vide infra*), while the splitting of the main peak is interpreted as the eutectic signal towards the Cs<sub>2</sub>MoO<sub>4</sub>-rich side and the peritectic towards the PbMoO<sub>4</sub>-rich side.

The presence of other compounds was excluded by synthesis attempts; every time, a mixture of Cs<sub>2</sub>Pb(MoO<sub>4</sub>)<sub>2</sub> with either Cs<sub>2</sub>MoO<sub>4</sub> or PbMoO<sub>4</sub> was found by XRD. Therefore, the number of compounds in this section is limited to the end-members and the 1:1 compound.

#### 4.6.2. SOLID SOLUBILITY

Following the notation of Belyaev and Chikova for a moment [7], (see Figure 4.1), the solid solubility of PbMoO<sub>4</sub> in Cs<sub>2</sub>MoO<sub>4</sub> is 13% in the high-temperature phase ( $\alpha'$ ), 1.5% in the medium-temperature phase ( $\beta'$ ) and 0.5% in the room-temperature phase ( $\gamma'$ ). Their distinction between the medium- and room-temperature phase is not supported in the more recent literature [10, 21], so the  $\gamma'$  can be neglected. Recent literature describes the room-temperature phase as  $\alpha$ -Cs<sub>2</sub>MoO<sub>4</sub>, while the single high-temperature phase is denoted as  $\beta$ -Cs<sub>2</sub>MoO<sub>4</sub> [27]. As described in the experimental section, the solubility of PbMoO<sub>4</sub> in Cs<sub>2</sub>MoO<sub>4</sub> was tested at mole fraction  $x(\text{PbMoO}_4) = 0.03$  and the solubility of Cs<sub>2</sub>MoO<sub>4</sub> in PbMoO<sub>4</sub> at mole fraction  $x(\text{PbMoO}_4) = 0.97$ .

During the cycling (*vide supra*) at  $x = 0.03$  (Figure 4.12), it was found that the temperature of the polymorphic transition of Cs<sub>2</sub>MoO<sub>4</sub> dropped from (833 ± 10) K to (819 ± 10)

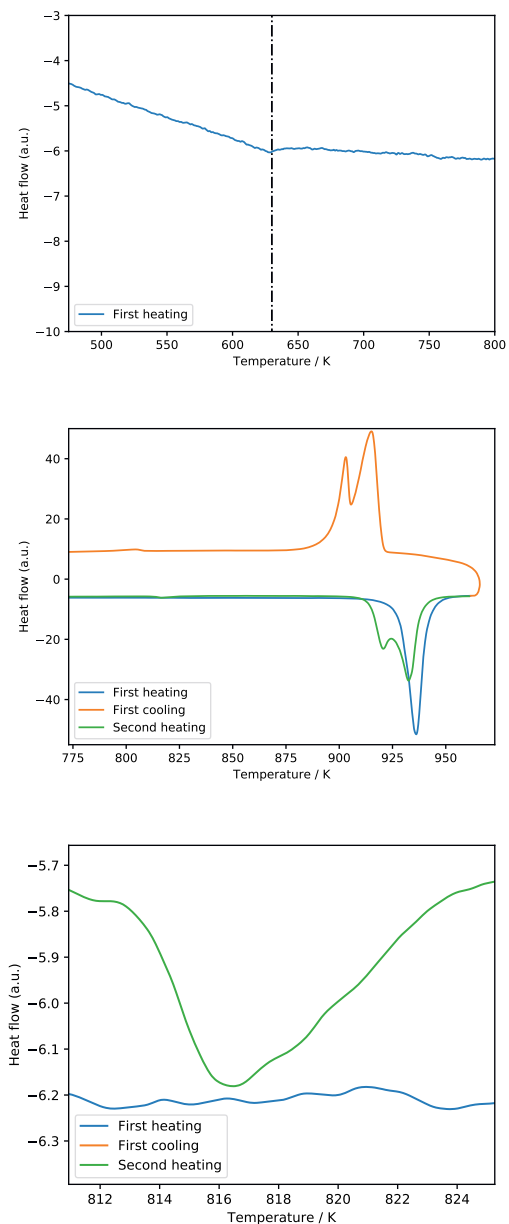


Figure 4.11: DSC curves of  $\text{Cs}_2\text{Pb}(\text{MoO}_4)_2$ . Top: the temperature region in which a polymorphic transition of  $\text{Cs}_2\text{Pb}(\text{MoO}_4)_2$  is reported. The vertical dashed line is drawn at 630 K. Middle: the temperature region of the polymorphic transition of  $\text{Cs}_2\text{MoO}_4$ , together with the decomposition peak of  $\text{Cs}_2\text{Pb}(\text{MoO}_4)_2$ . Bottom: the presence of the solid solution of Pb in  $\text{Cs}_2\text{MoO}_4$  formed after the first heating. For explanation, see text.

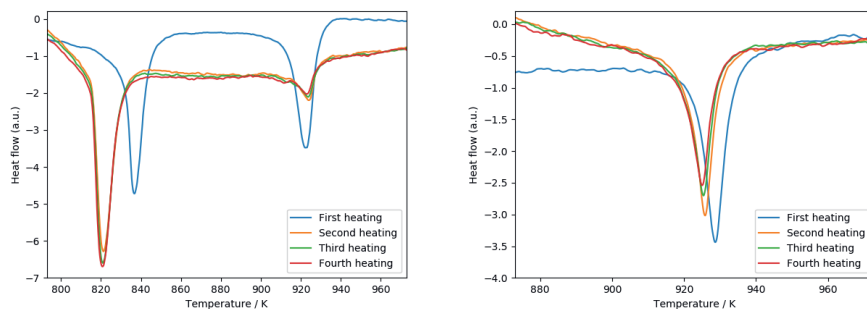


Figure 4.12: Heat flow curves of mixtures of  $\text{Cs}_2\text{MoO}_4$  or  $\text{PbMoO}_4$  with a slight amount of  $\text{Cs}_2\text{Pb}(\text{MoO}_4)_2$  for the study of solid solubility at mole fractions  $x(\text{PbMoO}_4) = 0.03$  (left) and  $x(\text{PbMoO}_4) = 0.97$  (right).

4

K, which is in line with the temperature reported by Belyaev and Chikova [7] for the eutectoid temperature belonging to  $\beta'$  (819 K). The extent of solubility found here is lower than 3%, which is also in line with ref. [7]. At the eutectic temperature, no change in temperature was found, contradicting the reported 13% solubility reported in the phase diagram by [7].

For the solid solubility at  $x = 0.97$ , no significant drop in temperature was found in the present experiments, see Figure 4.12. The analysed onset temperatures decrease slightly, but within the experimental error. The solubility of 5%  $\text{Cs}_2\text{MoO}_4$  in  $\text{PbMoO}_4$  claimed by [7] is thus not substantiated by the present data.

#### 4.6.3. PHASE DIAGRAM EQUILIBRIA IN THE $\text{Cs}_2\text{MoO}_4$ - $\text{PbMoO}_4$ SECTION

The collected TG-DSC data in the pseudo-binary section  $\text{Cs}_2\text{MoO}_4$ - $\text{PbMoO}_4$  are listed in Table 4.7 with the associated invariant reactions. Based on the latter, a sketch of the phase diagram is proposed in Figure 4.13.

The shape of the liquidus is in fair agreement with the data by Belyaev and Chikova, though their results tend to deviate towards the melting point of  $\text{PbMoO}_4$ . Since in the present results, a regular liquidus line near pure  $\text{PbMoO}_4$  was found, they are considered superior to the older results. Moreover, the melting points of the pure end-members as measured in this work agree with the literature data.

The eutectic temperature reported here is  $(919 \pm 10)$  K, in agreement with ref. [7]. The eutectic composition is proposed to be  $0.40 < x < 0.45$ , aligning with  $x = 0.41$  as proposed by Belyaev and Chikova [7].

The peritectic temperature is  $(933 \pm 5)$  K, within error the same as ref [7]. The second order phase transition in  $\text{Cs}_2\text{Pb}(\text{MoO}_4)_2$  is drawn at 630 K. As can be seen from the absence of data points, the behaviour of this transition close to  $\text{Cs}_2\text{MoO}_4$  is still unknown.

Since the liquidus data were collected on the first heating cycle because of decomposition of  $\text{Cs}_2\text{Pb}(\text{MoO}_4)_2$ , data for the eutectoid line were collected in separate multiple cycle measurements; the found temperature matches with [7].

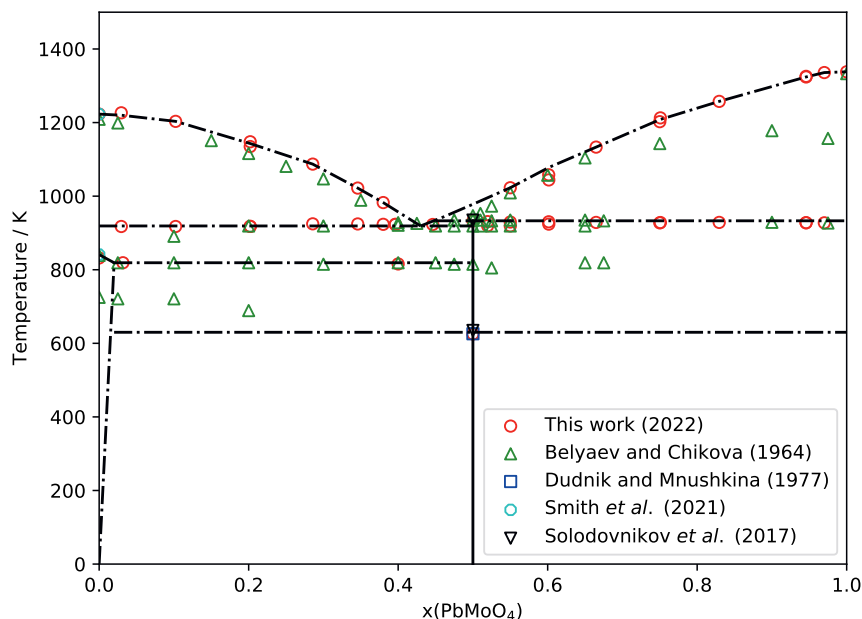


Figure 4.13: A sketch of the  $\text{Cs}_2\text{MoO}_4$ - $\text{PbMoO}_4$  phase diagram as measured experimentally and compared with literature [7, 8, 12, 27]. The lines drawn here depict the suggested phase equilibria.

## 4.7. THERMODYNAMIC PROPERTIES OF $\alpha$ - $\text{Cs}_2\text{Pb}(\text{MoO}_4)_2$

### 4.7.1. ENTHALPY OF FORMATION AT 298.15 K

To derive the enthalpy of formation of  $\alpha$ - $\text{Cs}_2\text{Pb}(\text{MoO}_4)_2$  at 298.15 K, solution calorimetry via the thermochemical cycle listed in Table 4.8 was employed. The enthalpies of dissolution in 2 M NaOH of  $\alpha$ - $\text{Cs}_2\text{Pb}(\text{MoO}_4)_2$  and the  $\text{Cs}_2\text{MoO}_4$ : $\text{PbMoO}_4$  mixture were measured and are given in Table 4.9. The dissolutions were instantaneous in all cases and a minor but significant difference in dissolution enthalpy is observed, meaning the formation of the double molybdate from the two molybdates is slightly exothermic. Using the thermochemical cycle as given in Table 4.8, the enthalpy of formation from the elements was calculated to be  $-(2570.7 \pm 2.3) \text{ kJ} \cdot \text{mol}^{-1}$ .

The formation enthalpy, entropy and Gibbs energy at ambient conditions from elements, simple oxides and simple molybdates were calculated and are given in Table 4.10.

Recent thermodynamic studies on  $\text{Cs}_2\text{Ba}(\text{MoO}_4)_2$  [16] and  $\text{Cs}_3\text{Na}(\text{MoO}_4)_2$  [33] also yielded Gibbs energies of formation of the complex molybdate from the simple molybdates close to zero (resp.  $0.8 \pm 4.9$  and  $2.3 \pm 4.2 \text{ kJ} \cdot \text{mol}^{-1}$ ).

x(PbMoO <sub>4</sub> )	T / K	Equilibrium	Equilibrium reaction
0.000	837	Polymorphism	$\alpha\text{-Cs}_2\text{MoO}_4 = \beta\text{-Cs}_2\text{MoO}_4$
0.000	1222	Congruent melting	$\beta\text{-Cs}_2\text{MoO}_4 = \text{L}$
0.030	819	Eutectoid	$\text{Sol. sol.} = \beta\text{-Cs}_2\text{MoO}_4 + \text{Cs}_2\text{Pb}(\text{MoO}_4)_2$
0.030	918	Eutectic	$\beta\text{-Cs}_2\text{MoO}_4 + \text{Cs}_2\text{Pb}(\text{MoO}_4)_2 = \text{L}'$
0.030	1227	Liquidus	$\beta\text{-Cs}_2\text{MoO}_4 + \text{L}' = \text{L}$
0.102	918	Eutectic	$\beta\text{-Cs}_2\text{MoO}_4 + \text{Cs}_2\text{Pb}(\text{MoO}_4)_2 = \text{L}'$
0.102	1203	Liquidus	$\beta\text{-Cs}_2\text{MoO}_4 + \text{L}' = \text{L}$
0.202	918	Eutectic	$\beta\text{-Cs}_2\text{MoO}_4 + \text{Cs}_2\text{Pb}(\text{MoO}_4)_2 = \text{L}'$
0.202	1141	Liquidus	$\beta\text{-Cs}_2\text{MoO}_4 + \text{L}' = \text{L}$
0.286	925	Eutectic	$\beta\text{-Cs}_2\text{MoO}_4 + \text{Cs}_2\text{Pb}(\text{MoO}_4)_2 = \text{L}'$
0.286	1087	Liquidus	$\beta\text{-Cs}_2\text{MoO}_4 + \text{L}' = \text{L}$
0.346	925	Eutectic	$\beta\text{-Cs}_2\text{MoO}_4 + \text{Cs}_2\text{Pb}(\text{MoO}_4)_2 = \text{L}'$
0.346	1022	Liquidus	$\beta\text{-Cs}_2\text{MoO}_4 + \text{L}' = \text{L}$
0.380	923	Eutectic	$\beta\text{-Cs}_2\text{MoO}_4 + \text{Cs}_2\text{Pb}(\text{MoO}_4)_2 = \text{L}'$
0.380	983	Liquidus	$\beta\text{-Cs}_2\text{MoO}_4 + \text{L}' = \text{L}$
0.396	923	Eutectic	$\beta\text{-Cs}_2\text{MoO}_4 + \text{Cs}_2\text{Pb}(\text{MoO}_4)_2 = \text{L}'$
0.400	816	Eutectoid	$\text{Sol. sol.} = \beta\text{-Cs}_2\text{MoO}_4 + \text{Cs}_2\text{Pb}(\text{MoO}_4)_2$
0.446	923	Eutectic	$\beta\text{-Cs}_2\text{MoO}_4 + \text{Cs}_2\text{Pb}(\text{MoO}_4)_2 = \text{L}'$
0.500	933	Peritectic decomposition	$\text{Cs}_2\text{Pb}(\text{MoO}_4)_2 = \text{PbMoO}_4 + \text{L}''$
0.520	930	Peritectic	$\text{Cs}_2\text{Pb}(\text{MoO}_4)_2 = \text{PbMoO}_4 + \text{L}''$
0.550	930	Peritectic	$\text{Cs}_2\text{Pb}(\text{MoO}_4)_2 = \text{PbMoO}_4 + \text{L}''$
0.550	1023	Liquidus	$\text{PbMoO}_4 + \text{L}'' = \text{L}$
0.601	930	Peritectic	$\text{Cs}_2\text{Pb}(\text{MoO}_4)_2 = \text{PbMoO}_4 + \text{L}''$
0.601	1051	Liquidus	$\text{PbMoO}_4 + \text{L}'' = \text{L}$
0.665	929	Peritectic	$\text{Cs}_2\text{Pb}(\text{MoO}_4)_2 = \text{PbMoO}_4 + \text{L}''$
0.665	1133	Liquidus	$\text{PbMoO}_4 + \text{L}'' = \text{L}$
0.750	928	Peritectic	$\text{Cs}_2\text{Pb}(\text{MoO}_4)_2 = \text{PbMoO}_4 + \text{L}''$
0.750	1208	Liquidus	$\text{PbMoO}_4 + \text{L}'' = \text{L}$
0.830	929	Peritectic	$\text{Cs}_2\text{Pb}(\text{MoO}_4)_2 = \text{PbMoO}_4 + \text{L}''$
0.830	1258	Liquidus	$\text{PbMoO}_4 + \text{L}'' = \text{L}$
0.950	928	Peritectic	$\text{Cs}_2\text{Pb}(\text{MoO}_4)_2 = \text{PbMoO}_4 + \text{L}''$
0.950	1324	Liquidus	$\text{PbMoO}_4 + \text{L}'' = \text{L}$
0.970	928	Peritectic	$\text{Cs}_2\text{Pb}(\text{MoO}_4)_2 = \text{PbMoO}_4 + \text{L}''$
0.970	1336	Liquidus	$\text{PbMoO}_4 + \text{L}'' = \text{L}$
1.000	1338	Congruent melting	$\text{PbMoO}_4 = \text{L}$

Table 4.7: Equilibrium data in the Cs<sub>2</sub>MoO<sub>4</sub>-PbMoO<sub>4</sub> system as measured in this work by DSC. Standard uncertainties on composition are  $u(x(\text{PbMoO}_4)) = 0.005$ ; standard uncertainties on temperature  $T$  are 5 K for pure compounds and 10 K for mixtures. The compositions with  $0 < x < 0.5$  and  $0.5 < x < 1.0$  are prepared by mixing Cs<sub>2</sub>Pb(MoO<sub>4</sub>)<sub>2</sub> with respectively Cs<sub>2</sub>MoO<sub>4</sub> and PbMoO<sub>4</sub>. No distinction is made between the room-temperature and high-temperature phase of Cs<sub>2</sub>Pb(MoO<sub>4</sub>)<sub>2</sub>. Sol. sol. = solid solution at the Cs<sub>2</sub>MoO<sub>4</sub> rich side.

entry	reaction	$\Delta H(298.15\text{ K})$ (kJ·mol <sup>-1</sup> )	ref.
1	$\alpha\text{-Cs}_2\text{Pb}(\text{MoO}_4)_2(\text{cr}) + (\text{sln}) = \text{Cs}_2\text{MoO}_4(\text{sln}) + \text{PbMoO}_4(\text{sln})$	24.4±1.5 <sup>a</sup>	this work
2	$\text{Cs}_2\text{MoO}_4(\text{cr}) + \text{PbMoO}_4(\text{cr}) + (\text{sln}) = \text{Cs}_2\text{MoO}_4(\text{sln}) + \text{PbMoO}_4(\text{sln})$	20.8±1.8 <sup>a</sup>	this work
3	$2\text{Cs}(\text{cr}) + \text{Mo}(\text{cr}) + 2\text{O}_2(\text{g}) = \text{Cs}_2\text{MoO}_4(\text{cr})$	-1514.2±4.3	[27]
4	$\text{Pb}(\text{cr}) + \text{Mo}(\text{cr}) + 2\text{O}_2(\text{g}) = \text{PbMoO}_4(\text{cr})$	-1052.9±0.5	[34]
5	$2\text{Cs}(\text{cr}) + \text{Pb}(\text{cr}) + 2\text{Mo}(\text{cr}) + 4\text{O}_2(\text{g}) = \alpha\text{-Cs}_2\text{Pb}(\text{MoO}_4)_2(\text{cr})$	-2570.7±2.3	this work

Table 4.8: Thermochemical cycle used to determine the standard enthalpy of formation of  $\alpha$ -Cs<sub>2</sub>Pb(MoO<sub>4</sub>)<sub>2</sub>. Measurements performed in the temperature interval T = 298.15±0.2 K. The enthalpy of formation of  $\alpha$ -Cs<sub>2</sub>Pb(MoO<sub>4</sub>)<sub>2</sub> was calculated using the relation  $\Delta_f H_m^o(5) = \Delta_{\text{sln}} H(2) - \Delta_{\text{sln}} H(1) + \Delta_f H_m(3) + \Delta_f H_m(4)$ . <sup>a</sup> Uncertainty with coverage factor k=2.

entry	$m(\text{Cs}_2\text{Pb}(\text{MoO}_4)_2)$ (mg)	$\Delta T$ (mK)	$C_p$ (J·K <sup>-1</sup> )	Q (J)	$\Delta_r H_m^o(298.15\text{ K})$ (kJ·mol <sup>-1</sup> )
1	99.30	-26.513	117.381	3.112	24.85
2	99.70	-24.757	117.413	2.907	23.12
3	100.18	-26.938	116.810	3.147	24.92
4	100.57	-26.382	117.916	3.111	24.53
Average					24.4±1.5 <sup>a</sup>
entry	$m(\text{Cs}_2\text{MoO}_4:\text{PbMoO}_4)$ (mg)	$\Delta T$ (mK)	$C_p$ (J·K <sup>-1</sup> )	Q (J)	$\Delta_r H_m^o(298.15\text{ K})$ (kJ·mol <sup>-1</sup> )
1	99.15	-20.838	117.247	2.443	19.54
2	99.77	-24.122	115.514	2.786	22.14
3	100.20	-22.412	117.530	2.634	20.84
4	100.59	-22.385	117.250	2.625	20.69
Average					20.8±1.8 <sup>a</sup>

Table 4.9: Measured dissolution enthalpies at 298.15 K in 2 M NaOH for  $\alpha$ -Cs<sub>2</sub>Pb(MoO<sub>4</sub>)<sub>2</sub>(cr) (M = 792.92 g·mol<sup>-1</sup>) and the mixture Cs<sub>2</sub>MoO<sub>4</sub>(cr):PbMoO<sub>4</sub>(cr). <sup>a</sup> Uncertainty with coverage factor k=2.

reaction	$\Delta_r H_m^o(298.15\text{ K})$ (kJ·mol <sup>-1</sup> )	$\Delta_r S_m^o(298.15\text{ K})$ (J·K <sup>-1</sup> ·mol <sup>-1</sup> )	$\Delta_r G_m^o(298.15\text{ K})$ (kJ·mol <sup>-1</sup> )
$2\text{Cs}(\text{cr}) + \text{Pb}(\text{cr}) + 2\text{Mo}(\text{cr}) + 4\text{O}_2(\text{g}) = \alpha\text{-Cs}_2\text{Pb}(\text{MoO}_4)_2(\text{cr})$	-2570.7±2.3	-714±12	-2357.8±4.3
$\text{Cs}_2\text{O}(\text{cr}) + \text{PbO}(\text{cr}) + 2\text{MoO}_3(\text{cr}) = \alpha\text{-Cs}_2\text{Pb}(\text{MoO}_4)_2(\text{cr})$	-515.0±2.7	30±12	-524.0±4.5
$\text{Cs}_2\text{MoO}_4(\text{cr}) + \text{PbMoO}_4(\text{cr}) = \alpha\text{-Cs}_2\text{Pb}(\text{MoO}_4)_2(\text{cr})$	-3.6±4.9	-10±12	-0.5±6.1

Table 4.10: Thermodynamic data for  $\alpha$ -Cs<sub>2</sub>Pb(MoO<sub>4</sub>) at ambient conditions. For the elements Cs, Mo and Pb, the  $S_m^o$  were taken from ref. [35]. The NIST-JANAF tables were used for Mo, PbO and MoO<sub>3</sub> [36], while for Cs<sub>2</sub>O values were taken from refs. [37, 38] as recommended by Cordfunke and Konings [39]. For Cs<sub>2</sub>MoO<sub>4</sub> and PbMoO<sub>4</sub>, the selected enthalpy and entropy data from Smith *et al.* and Van Hattem *et al.* have been used [27, 34].

### 4.7.2. LOW-TEMPERATURE HEAT CAPACITY AND STANDARD ENTROPY

The low-temperature heat capacity of  $\alpha$ -Cs<sub>2</sub>Pb(MoO<sub>4</sub>)<sub>2</sub> is shown in Figure 4.14. The heat capacity does not show any anomaly in the measured temperature window. At room temperature, the heat capacity is close to the value estimated by the Neumann-Kopp rule as applied on Cs<sub>2</sub>MoO<sub>4</sub> and PbMoO<sub>4</sub> [40, 41]. The data has been fitted to a sum of one Debye function ( $D(\Theta_D, T)$ ) and three Einstein functions ( $E(\Theta_{E_i}, T)$ ) in the temperature range 10-298.5 K, which was found sufficient to fit the experimental data. The formula used for fitting in this work reads thus, where  $C_p \approx C_v$  in the fitted temperature range.

$$C_v(T) = n_D \cdot D(\Theta_D, T) + \sum_{i=1,2,3} n_{E_i} \cdot E(\Theta_{E_i}, T) \quad (4.2)$$

The polynomial fit made at the lower temperature limit ( $T < 10$  K) is shown in the inset in Figure 4.14, using  $\gamma = 0 \text{ mJ}\cdot\text{mol}^{-1}\cdot\text{K}^{-2}$ . The fitting parameters are given in Table 4.11. The differences between the fit at low temperature and the combined Debye-Einstein fits ( $10 < T < 298.15$  K) are shown in Figure 4.14. As can be seen in the figure, the difference between the fit and experimentally measured data is smaller than the experimental error.

In Figure 4.14, the heat capacity is plotted in  $C_p/T$  vs  $T$  to determine the entropy. The shaded area denotes the integrated area. The entropy was both calculated using a linear spline interpolation of the raw data, and an integration of the combined Debye-Einstein model. In both cases,  $S_m^\circ(298.15 \text{ K}, \alpha\text{-Cs}_2\text{Pb}(\text{MoO}_4)_2, \text{cr}) = (399 \pm 12) \text{ J}\cdot\text{K}^{-1}\cdot\text{mol}^{-1}$  was obtained, using a total error estimation of 3 % on the experimentally determined heat capacity. The heat capacity  $C_p(298.15 \text{ K}, \alpha\text{-Cs}_2\text{Pb}(\text{MoO}_4)_2, \text{cr}) = (264 \pm 8) \text{ J}\cdot\text{K}^{-1}\cdot\text{mol}^{-1}$ .

Temp. range / K	2-10
$\gamma / \text{mJ}\cdot\text{mol}^{-1}\cdot\text{K}^{-2}$	0
$B_3 / \text{mJ}\cdot\text{mol}^{-1}\cdot\text{K}^{-4}$	$3.18 \cdot 10^{-3} \pm 6 \cdot 10^{-5}$
$B_5 / \text{mJ}\cdot\text{mol}^{-1}\cdot\text{K}^{-6}$	$8.84 \cdot 10^{-5} \pm 3 \cdot 10^{-6}$
$B_7 / \text{mJ}\cdot\text{mol}^{-1}\cdot\text{K}^{-8}$	$-9.46 \cdot 10^{-7} \pm 6 \cdot 10^{-8}$
$B_9 / \text{mJ}\cdot\text{mol}^{-1}\cdot\text{K}^{-10}$	$3.30 \cdot 10^{-9} \pm 3 \cdot 10^{-10}$
Temp. range / K	10-298.5
$n_D / \text{mol}$	$4.9 \pm 0.3$
$n_{E1} / \text{mol}$	$1.26 \pm 0.2$
$n_{E2} / \text{mol}$	$3.66 \pm 0.4$
$n_{E3} / \text{mol}$	$2.32 \pm 0.2$
$\Theta_D / \text{K}$	$809 \pm 35$
$\Theta_{E1} / \text{K}$	$49.5 \pm 10$
$\Theta_{E2} / \text{K}$	$111.0 \pm 5$
$\Theta_{E3} / \text{K}$	$261.4 \pm 32$

Table 4.11: Fitting parameters low temperature heat capacity  $\alpha$ -Cs<sub>2</sub>Pb(MoO<sub>4</sub>)<sub>2</sub>

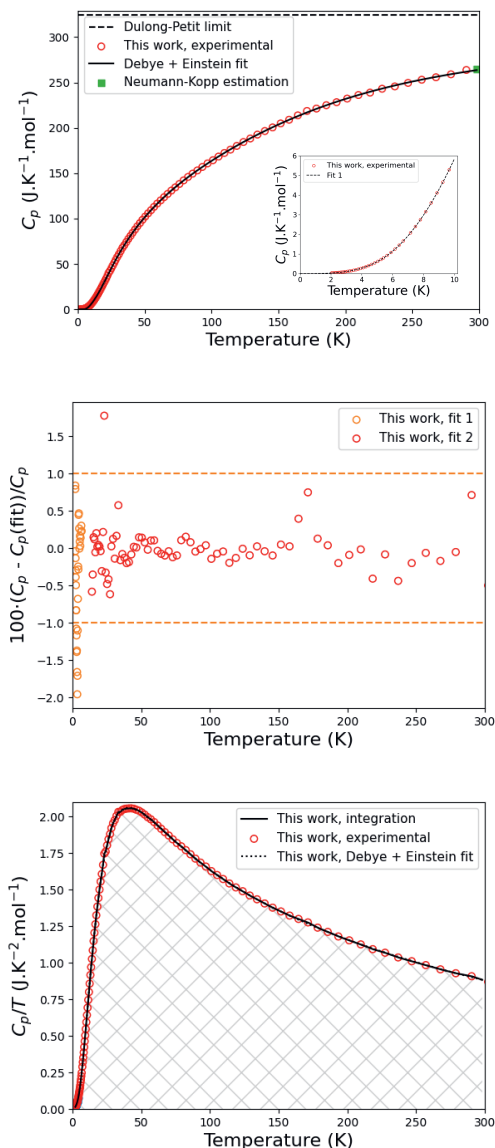


Figure 4.14: Top: The heat capacity of  $\alpha$ -Cs<sub>2</sub>Pb(MoO<sub>4</sub>)<sub>2</sub> as measured and fitted in this work and comparison with Dulong-Petit limit and Neumann-Kopp approximation. Top Inset: The fit to the heat capacity of  $\alpha$ -Cs<sub>2</sub>Pb(MoO<sub>4</sub>)<sub>2</sub> below 10 K. See for explanation of the fits the main text. Middle: The difference between the fits as based on the polynomial and the combined Debye-Einstein model and the experimentally determined low temperature heat capacity of  $\alpha$ -Cs<sub>2</sub>Pb(MoO<sub>4</sub>)<sub>2</sub>. Bottom: The low temperature heat capacity of  $\alpha$ -Cs<sub>2</sub>Pb(MoO<sub>4</sub>)<sub>2</sub> as plotted in  $C_p/T$  vs  $T$  to determine the entropy.

## 4.8. CONCLUSIONS

The phase diagram  $\text{Cs}_2\text{MoO}_4$ - $\text{PbMoO}_4$  and the compound  $\text{Cs}_2\text{Pb}(\text{MoO}_4)_2$  were subjected to (renewed) research. Neutron and X-ray diffraction gave insight into the behaviour of the cell parameters at room temperature and above, up to 773 K. The crystal structure of  $\beta$ - $\text{Cs}_2\text{Pb}(\text{MoO}_4)_2$ , the high temperature phase, was elucidated.  $\beta$ - $\text{Cs}_2\text{Pb}(\text{MoO}_4)_2$  was found to crystallise in the palmierite space group 166. For the first time, the thermal expansion of  $\text{Cs}_2\text{Pb}(\text{MoO}_4)_2$  was measured. The thermal expansion parameters were found to be larger than the thermal expansion parameters of the fuel pin, but smaller than those of the JOG-phase. The X-ray Absorption Near Edge Structure (XANES) spectrum was measured around the Mo K-edge. It was found that the oxidation state of Mo is +6. The phase diagram section  $\text{Cs}_2\text{MoO}_4$ - $\text{PbMoO}_4$  was investigated using a combination of XRD and TG-DSC. The existence of other compounds besides  $\text{Cs}_2\text{Pb}(\text{MoO}_4)_2$  in the investigated temperature-composition-pressure window was excluded. The phase diagram was found to be qualitatively similar to the phase diagram by Belyaev and Chikova [7], but several features were changed or refined. The liquidus line was improved towards the  $\text{PbMoO}_4$ -rich side of the phase diagram. The compound was found to decompose peritectically, but not at the previously suggested mole fraction. Furthermore, the solid solubility near the end-members was investigated. It was found that the extend of solid solubility at the  $\text{Cs}_2\text{MoO}_4$  side as reported earlier is exaggerated and at maximum 3%. The solid solubility at the  $\text{PbMoO}_4$  side was excluded. Last, the enthalpy of formation and standard entropy of the quaternary compound  $\alpha$ - $\text{Cs}_2\text{Pb}(\text{MoO}_4)_2$  have been measured using solution and thermal-relaxation calorimetry.

## EXPERIMENTAL DETAILS

**Synthesis**  $\text{Cs}_2\text{MoO}_4$  was synthesised from  $\text{Cs}_2\text{CO}_3$  (99.99%, Alfa Aesar) and  $\text{MoO}_3$  (99.5%, Alfa Aesar) by means of solid state reaction for 2 times 12 h at 773 K in an alumina crucible under oxygen atmosphere with intermittent grinding.  $\text{Cs}_2\text{Pb}(\text{MoO}_4)_2$  was synthesised from  $\text{Cs}_2\text{MoO}_4$  and  $\text{PbMoO}_4$  (Merck Sigma, 99.9%) via solid state synthesis in an alumina crucible for 12 h at 773 K and for 12 h at 873 K. Several batches were prepared; in general, the synthesis was performed under oxygen atmosphere; one synthesis was done under argon flow. The purity is estimated to be higher than 99%; only some faint peaks ( $I/I_{\text{max}} < 0.1\%$ ) were found on XRD. The presence of other intermediate compounds in the  $\text{Cs}_2\text{MoO}_4$ - $\text{PbMoO}_4$  system was investigated by synthesis attempts as used for  $\text{Cs}_2\text{Pb}(\text{MoO}_4)_2$  at various molar fractions between  $x(\text{PbMoO}_4) = 0.0$  and 0.5 and 0.5 and 1.0. Typically, the samples were heated to 773 K and 873 K for 12 h each.

**X-ray Diffraction** Purity of the synthesised end-members and  $\text{Cs}_2\text{Pb}(\text{MoO}_4)_2$  was confirmed by X-ray powder diffraction (XRD). For  $\text{Cs}_2\text{Pb}(\text{MoO}_4)_2$  refinements, the parameters as given by Solodovnikov *et al.* [12] were taken as a starting point. High-temperature X-ray diffraction was done using the same XRD instrument equipped with an Anton Paar TTK450 sample holder.

**Neutron Diffraction** Neutron diffraction (ND) was performed on  $\text{Cs}_2\text{Pb}(\text{MoO}_4)_2$  at the PEARL beam line [42] at the Hoger Onderwijs Reactor (HOR) at TU Delft. The data were collected at room temperature, 573 K and 773 K with a fixed wavelength of 0.166718 nm.

**X-ray Absorption Near Edge Structure spectroscopy** X-ray Absorption Near Edge Structure spectroscopy measurements were performed for  $\text{Cs}_2\text{MoO}_4$ ,  $\text{PbMoO}_4$  and  $\text{Cs}_2\text{Pb}(\text{MoO}_4)_2$  at the INE-Beamline [43] of the KIT Light Source (Karlsruhe, Germany). Samples were probed around the K-edge of Mo (20 keV). XAS samples were prepared by mixing some of the compound with boron nitride (BN). The samples mixed with BN were pressed into a circular pellet of 8 mm diameter and enclosed in Kapton foil.

**Differential Scanning Calorimetry** Phase diagram measurements in the  $\text{Cs}_2\text{MoO}_4$ - $\text{PbMoO}_4$  system were performed using simultaneous thermogravimetry analysis with differential scanning calorimetry using the TG-DSC module of a Setaram Multi HTC 96 Line with plate type sensors. In general, (mixtures of) the compounds  $\text{Cs}_2\text{Pb}(\text{MoO}_4)_2$ ,  $\text{Cs}_2\text{MoO}_4$  and  $\text{PbMoO}_4$  were measured with a sample size of about 100 mg of powder in an open alumina cup under oxygen atmosphere. The heating ramp used was  $10 \text{ K}\cdot\text{min}^{-1}$ .

The solid solubility near the end-members was studied by mixing  $\text{Cs}_2\text{MoO}_4$  or  $\text{PbMoO}_4$  with  $\text{Cs}_2\text{Pb}(\text{MoO}_4)_2$  to mole fractions  $x(\text{PbMoO}_4) = 0.03$  and  $x = 0.97$ , respectively. At  $x(\text{PbMoO}_4) = 0.03$ , the mixture was heated till 1023 K with  $10 \text{ K}\cdot\text{min}^{-1}$ , stabilised at that temperature for 30 min, cooled down to 773 K, and three times heated and cooled down between 773 K and 1023 K with stabilisation of 30 min after each heating and cooling. At  $x(\text{PbMoO}_4) = 0.97$ , a similar procedure was carried out, with 823 K and 1023 K as set temperatures. In this way, the samples were cycled around the phase transitions in the region of interest without crossing the liquidus line.

The melting point of  $\text{PbMoO}_4$  was also measured using a Setaram Multi-Detector HTC Module of the 96 Line calorimeter with 3D heat flux detection. Open alumina cups were used under oxygen flow around ambient pressure.

**Solution Calorimetry** A mixture of  $\text{Cs}_2\text{MoO}_4$  and  $\text{PbMoO}_4$  was prepared by weighing the compounds in a 1.000:1.000 ratio and grinding for 5 minutes. The dissolution enthalpies of this mixture and  $\text{Cs}_2\text{Pb}(\text{MoO}_4)_2$  in 2 M NaOH were measured using a Precision Solution Calorimeter from TA Instruments with a TAM IV thermostat. The dissolution experiments were performed in a 25 mL Pyrex glass reaction vessel with a golden stirrer holding a glass ampoule. The 1 mL glass ampoule contained about 100 mg sample per measurement and was sealed with beeswax. Stabilisation of the baseline and calibration before and after the break were performed using an electrical heater.

**Thermal Relaxation Calorimetry** Low-temperature heat capacity data of a  $7.024 \pm 0.05 \text{ mg } \alpha\text{-Cs}_2\text{Pb}(\text{MoO}_4)_2$  sample was collected with a Quantum Design Physical Property Measurement System (QD-PPMS 14 T) at zero field in the temperature range 2 - 300 K.

**Accession codes** The neutron diffraction data is available from the CCDC deposition service under deposition numbers 2239227 and 2239228 for the structures at respectively 298 and 773 K.



## BIBLIOGRAPHY

- (1) US DOE Nuclear Energy Research Advisory Committee with Generation IV International Forum [https://www.gen-4.org/gif/jcms/sc\\_40481/technology-roadmap](https://www.gen-4.org/gif/jcms/sc_40481/technology-roadmap) **2002**.
- (2) Pelletier, M.; Guérin, Y. In *Comprehensive Nuclear Materials*, 2nd edition, Konings, R. J. M., Stoller, R. E., Eds.; Elsevier: 2020; Chapter 2.03, pp 72–105.
- (3) Kleykamp, H. *Journal of Nuclear Materials* **1985**, 131, 221–246.
- (4) Imoto, S. *Journal of Nuclear Materials* **1986**, 140, 19–27.
- (5) Tourasse, M.; Boidron, M.; Pasquet, B. *Journal of Nuclear Materials* **1992**, 188, 49–57.
- (6) Cappia, F.; Miller, B. D.; Aguiar, J. A.; He, L.; Murray, D. J.; Frickey, B. J.; Stanek, J. D.; Harp, J. M. *Journal of Nuclear Materials* **2020**, 531, 151964.
- (7) Belyaev, I. N.; Chikova, N. N. *Zhurnal Neorganicheskoi Khimii* **1964**, 9, 2754–2760.
- (8) Dudnik, E. F.; Mnushkina, I. E. *Ukrainian Journal of Physics* **1977**, 22, 1737–1738.
- (9) Solodovnikov, S. F.; Klevtsova, R. E.; Klevtsov, P. V. *Journal of Structural Chemistry* **1994**, 35, 879–889.
- (10) Isupov, V. A. *Ferroelectrics* **2005**, 322, 83–114.
- (11) Tsyrenova, G. D.; Bazarova, Z. G.; Mokhosoev, M. V. *Doklady Akademii Nauk SSSR* **1987**, 294, 387–389.
- (12) Solodovnikov, S. F.; Atuchin, V. V.; Solodovnikova, Z. A.; Khyzhun, O. Y.; Danylenko, M. I.; Pishchur, D. P.; Plyusnin, P. E.; Pugachev, A. M.; GavriloVA, T. A.; Yelisseyev, A. P.; Reshak, A. H.; Alahmed, Z. A.; Habubi, N. F. *Inorganic Chemistry* **2017**, 56, 3276–3286.
- (13) Isupov, V. A. *Ferroelectrics* **2005**, 321, 63–90.
- (14) Gudkova, I. A.; Solodovnikova, Z. A.; Solodovnikov, S. F.; Zolotova, E. S.; Kurat'eva, N. V. *Russian Journal of Inorganic Chemistry* **2011**, 56, 1443–1452.
- (15) Gudkova, I. A.; Solodovnikova, Z. A.; Solodovnikov, S. F.; Zolotova, E. S.; Kuratieva, N. V. *Journal of Structural Chemistry* **2011**, 52, 1063–1069.
- (16) Smith, A. L.; de Zoete, N.; Rutten, M.; van Eijck, L.; Griveau, J.-C.; Colineau, E. *Inorganic Chemistry* **2020**, 59, 13162–13173.
- (17) Sani, E.; Brugioni, A.; Mercatelli, L.; Parisi, D.; Zharikov, E. V.; Lis, D. A.; Subbotin, K. A. *Optical Materials* **2019**, 94, 415–422.
- (18) Song, F. *Journal of Luminescence* **2021**, 239, 118324.
- (19) Momma, K.; Izumi, F. *Journal of Applied Crystallography* **2011**, 44, 1272–1276.

- (20) Shannon, R. D. *Acta crystallographica section A* **1976**, 32, 751–767.
- (21) Wallez, G.; Raison, P. E.; Smith, A. L.; Clavier, N.; Dacheux, N. *Journal of Solid State Chemistry* **2014**, 215, 225–230.
- (22) Martin, D. G. *Journal of Nuclear Materials* **1988**, 152, 94–101.
- (23) Carbajo, J. J.; Yoder, G. L.; Popov, S. G.; Ivanov, V. K. *Journal of Nuclear Materials* **2001**, 299, 181–198.
- (24) Freitas, A. P.; André, R. F.; Poucin, C.; Le, T. K.-C.; Imbao, J.; Lassalle-Kaiser, B.; Carencio, S. *The Journal of Physical Chemistry C* **2021**, 125, 17761–17773.
- (25) Aritani, H.; Tanaka, T.; Funabiki, T.; Yoshida, S.; Kudo, M.; Hasegawa, S. *The Journal of Physical Chemistry* **1996**, 100, 5440–5446.
- (26) Smith, A. L.; Rutten, M.; Herrmann, L.; Epifano, E.; Konings, R. J. M.; Colineau, E.; Griveau, J.-C.; Guéneau, C.; Dupin, N. *Journal of the European Ceramic Society* **2021**, 41, 3664–3686.
- (27) Smith, A. L.; Thi, T. N. P.; Guéneau, C.; Dumas, J.-C.; Epifano, E.; van Burik, W.; Dupin, N. *Calphad* **2021**, 75, 102350.
- (28) Smith, A. L.; Vlieland, J.; Pignié, M.-C.; Abbink, M.; Mikaelian, G.; Benigni, P. *Thermochimica Acta* **2021**, 696, 178825.
- (29) Jaeger, F. M.; Germs, H. C. *Zeitschrift für anorganische und allgemeine Chemie* **1921**, 119, 145–173.
- (30) Kunev, D. K.; Belyaevskaya, L. V.; Zelikman, A. N. *Russian Journal of Inorganic Chemistry* **1966**, 11, 1063–1064.
- (31) Bukhalova, G. A.; Manakov, V. M.; Maltsev, V. T. *Russian Journal of Inorganic Chemistry* **1971**, 16, 280–281.
- (32) Eissa, M. A.; Elmasry, M. A. A.; Younis, S. S. *Thermochimica Acta* **1996**, 288, 169–178.
- (33) Smith, A. L.; Pignié, M.-C.; van Eijck, L.; Griveau, J.-C.; Colineau, E.; Konings, R. J. M. *The Journal of Chemical Thermodynamics* **2018**, 120, 205–216.
- (34) Van Hattem, A.; Dankelman, R.; Colineau, E.; Griveau, J.-C.; Dardenne, K.; Rothe, J.; Couweleers, S.; Konings, R. J. M.; Smith, A. L. *Journal of Alloys and Compounds* **2024**, 1003, 175588.
- (35) Grenthe, I.; Gaona, X.; Rao, L.; Plyasunov, A.; Runde, W.; Grambow, B.; Konings, R. J. M.; Smith, A. L.; Moore, E.; Ragoussi, M.-E., et al. *Second update on the chemical thermodynamics of uranium, neptunium, plutonium, americium and technetium. Chemical Thermodynamics Volume 14*; tech. rep.; Organisation for Economic Co-Operation and Development, 2020.
- (36) Chase, M. W. *Journal of Physical and Chemical Reference Data* **1996**, 25, 1069–1111.
- (37) Settle, J. L.; Johnson, G. K.; Hubbard, W. N. *The Journal of Chemical Thermodynamics* **1974**, 6, 263–269.

- (38) Flotow, H. E.; Osborne, D. W. *The Journal of Chemical Thermodynamics* **1974**, *6*, 135–140.
- (39) *Thermochemical Data for Reactor Materials and Fission Products*; Cordfunke, E. H. P., Konings, R. J. M., Eds.; Elsevier Science Publishers: 1990.
- (40) Osborne, D. W.; Flotow, H. E.; Hoekstra, H. R. *The Journal of Chemical Thermodynamics* **1974**, *6*, 179–183.
- (41) Aiswarya, P. M.; Ganesan, R.; Gnanasekaran, T. *The Journal of Chemical Thermodynamics* **2018**, *116*, 21–31.
- (42) Van Eijck, L.; Cussen, L. D.; Sykora, G. J.; Schooneveld, E. M.; Rhodes, N. J.; Van Well, A. A.; Pappas, C. *Journal of Applied Crystallography* **2016**, *49*, 1398–1401.
- (43) Rothe, J.; Butorin, S.; Dardenne, K.; Denecke, M. A.; Kienzler, B.; Löble, M.; Metz, V.; Seibert, A.; Steppert, M.; Vitova, T., et al. *Review of Scientific Instruments* **2012**, *83*, 043105.



# 5

## THE COMPOUND $\text{CsBi}(\text{MoO}_4)_2$

*In the interaction between LBE and the JOG-phase,  $\text{CsBi}(\text{MoO}_4)_2$  might be formed. The antiferroelectric compound  $\text{CsBi}(\text{MoO}_4)_2$  has been known for a long time, but the mechanism underlying its physical properties remains poorly understood. No temperature-dependent crystallographic investigation was performed to solve this. In this work, X-ray absorption spectroscopy at the Mo K-edge confirms the oxidation state and local environment around Mo at room temperature. The crystal structure change with temperature is elucidated using neutron and X-ray diffraction studies at ambient and non-ambient temperature. It is shown that  $\text{Bi}^{3+}$   $6s^2$  lone pairs are causing an antiferroelectric lattice and the crystallographic unit cell is doubled along b. Upon increasing temperature, Bi-cations move towards an ideal position, yielding the earlier reported paraelectric archetype crystal structure. With this work, the antiferroelectricity mechanism of  $\text{CsBi}(\text{MoO}_4)_2$  is revealed to be driven by the temperature-dependent Bi-displacement caused by the  $6s^2$  lone pair, solving a long-standing question into its origin.*

---

This chapter is based on: A. van Hattem, G. Wallez, N.T.H ter Veer, I. Dhiman, K. Dardenne, J. Rothe, R.J.M. Konings and A.L. Smith. *Elucidation of the Antiferroelectricity Mechanism in  $\text{CsBi}(\text{MoO}_4)_2$*  (submitted)

## 5.1. INTRODUCTION

The two compounds CsBi(MoO<sub>4</sub>)<sub>2</sub> and Cs<sub>5</sub>Bi(MoO<sub>4</sub>)<sub>4</sub> have been reported [1–3], and they can be located on the pseudo-binary section Cs<sub>2</sub>MoO<sub>4</sub>-Bi<sub>2</sub>(MoO<sub>4</sub>)<sub>3</sub>. The understanding of these compounds is important for lead-bismuth eutectic (LBE) cooled systems in a similar way as outlined at the beginning of Chapter 4 for lead-cooled systems. Despite the systematic studies into double molybdates over multiple decades [4–9], the double molybdate CsBi(MoO<sub>4</sub>)<sub>2</sub> has some structural mysteries to unravel, both at ambient and at non-ambient temperatures. A crystal of CsBi(MoO<sub>4</sub>)<sub>2</sub> was first grown by Klevtsov, Vinokurov and Klevtsova in 1973, who stated that the compound is isostructural to CsPr(MoO<sub>4</sub>)<sub>2</sub> and crystallises in space group *Pccm* (*D*<sub>2h</sub><sup>3</sup>, 49) [1, 2, 4]. They did not observe polymorphic transitions using differential thermal analysis and measured the melting point to be 945 ± 15 K [1]. Pelikh and Zvyagin, on the other hand, reported two phase transitions in CsBi(MoO<sub>4</sub>)<sub>2</sub>, observed while studying the temperature-dependent permittivity in a single crystal [10]. They observed a discontinuity at 135 K as well as an inflection point at 330 K, and interpreted the low-temperature anomaly as an improper antiferroelectric transition. A few years later they reported on the effect of uniaxial pressure on CsBi(MoO<sub>4</sub>)<sub>2</sub> and concluded that the transition at 135 K is accompanied by a remarkable volume change [11]. In 1980, Brilingas *et al.* [12] investigated the dielectric properties of CsBi(MoO<sub>4</sub>)<sub>2</sub> crystals at microwave frequencies, observing transitions at the same temperatures. They classified the transition at 135 K as a first-order ferroelastic transition and the transition at 330 K as antiferroelectric. Other studies into the phase transitions of CsBi(MoO<sub>4</sub>)<sub>2</sub> included the sample size effect (Pelikh [13]), specific heat (Stokka and Samulionis [14]), infrared and Raman studies (Zvyagin and Kutko [15], Hanuza and Maczka [16], Maczka, Hanuza and coworkers [17–20]).

Zvyagin and Kut'ko were the first authors to conjecture that the actual room temperature structure may have a doubled cell parameter, and they proposed that the crystal structure evolves according to  $D_{2h}^3 \xrightarrow{330\text{K}} D_{2h}^8 \xrightarrow{135\text{K}} C_i^1$  [15]. Similar to the later spectroscopic studies of Maczka, Hanuza and several co-workers [16–20], the physics of the compound was interpreted in analogy to other double molybdate compounds. Although the  $D_{2h}^3 \xrightarrow{330\text{K}} D_{2h}^8$  transition will turn out to be the proper assignment, it is not caused by the molybdate-moiety but by the Bi(III) 6s<sup>2</sup> lone pair activity. Important to note is that the spectroscopic studies were interpreted with isolated tetrahedral molybdate moieties. Moreover, Maczka *et al.* claimed that at the second order transition, the point group symmetry for the molybdate ions changes from *C*<sub>s</sub> to *C*<sub>1</sub> and the phase transition seems of a displacive nature [17]. The doubling of the *a* lattice parameter is hypothesised by them to be caused by an anti-phase displacement of the Cs<sup>+</sup>-ions or a [Bi(MoO<sub>4</sub>)<sub>2</sub>]<sup>-</sup>-layer. They reject this hypothesis and propose a monoclinic space group instead of *Pcca*, even though they rejected the monoclinic option themselves earlier based on the available diffraction data [17, 19]. In their latest article (2005), Maczka, Hanuza and co-workers wrote that the room-temperature phase has an unknown symmetry. In this high-pressure Raman study two phases next to the antiferroelectric and paraelectric phases were found [20].

No X-ray or neutron diffraction studies at non-ambient pressure or temperature have been reported to this date and according to several of the discussed studies, the original

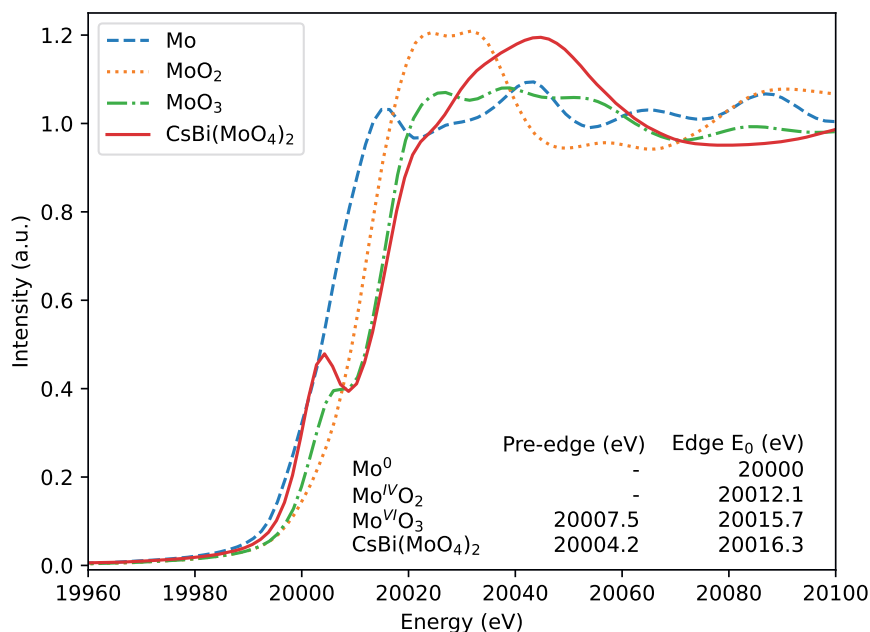


Figure 5.1: XANES spectra obtained on CsBi(MoO<sub>4</sub>)<sub>2</sub> and Mo, MoO<sub>2</sub> and MoO<sub>3</sub> reference materials at room temperature.

space group assigned to the room-temperature phase of CsBi(MoO<sub>4</sub>)<sub>2</sub> is incorrect. In this chapter, we describe the antiferroelectric ( $135 < T < 330$  K) structure of CsBi(MoO<sub>4</sub>)<sub>2</sub> as determined using X-ray and neutron diffraction at various temperatures, together with the phase transition mechanism at 330 K. The analysis is supported by X-ray absorption near edge structure (XANES) measurement analysis at ambient temperature. The neutron diffraction, especially at low temperature, is key to measure the displacive phase transition reported below. The XAS spectroscopy confirms the local Mo environment, in line with expectations based on older literature.

## 5.2. X-RAY ABSORPTION SPECTROSCOPY AT THE MO K-EDGE

The X-ray absorption near-edge structure (XANES) spectrum collected at the Mo K-edge is shown in Figure 5.1. The absorption energies are also listed in the same figure and compared to Mo, MoO<sub>2</sub> and MoO<sub>3</sub>. The edge position aligns with MoO<sub>3</sub>, confirming the expected hexavalent oxidation state of Mo. Moreover, the pre-edge feature in the CsBi(MoO<sub>4</sub>)<sub>2</sub> spectrum is characteristic for MoO<sub>4</sub><sup>2-</sup> tetrahedra [21, 22], which aligns with the earlier reported crystal structure. The origin of the pre-edge feature is explained in Chapter 4.

### 5.3. SOLVING THE ROOM-TEMPERATURE CRYSTAL STRUCTURE

#### 5.3.1. TOWARDS UNDERSTANDING THE ANTIFERROELECTRIC PHASE

A yellow material was obtained after the synthesis performed as described at the end of this chapter. Laboratory X-ray, synchrotron X-ray and neutron diffraction measurements have been performed on this material. A refinement of the model for CsBi(MoO<sub>4</sub>)<sub>2</sub> in space group *Pccm* (49) against the X-ray diffraction patterns at non-ambient temperatures for the determination of the thermal expansion indicates a non-linearity in cell parameters when crossing 330 K. However, atomic shifts for a second-order phase transition of displacive nature between 298 K and 330 K are expected to be very small, stimulating us to collect neutron diffraction data at a temperature where the displacement should be most pronounced, *i.e.* at around 150 K. For the initial refinement against the synchrotron X-ray diffraction data, the *Pccm* (49) space group model was taken as well. In the Fourier difference map, the Bi-atom was found to split between two symmetric positions, which hinted at a lone pair effect, but the extent of the effect was too small to conclusively assign it to a doubled cell.

The space group search was initiated based on the following criteria:

1. The symmetry should remain orthorhombic according to the absence of peak splitting or broadening of the synchrotron diffraction pattern recorded at room temperature;
2. The space group should be a subgroup of that of the high-temperature form owing to the second order character of the transition;
3. A polar space group was hypothesised considering the dielectric anomaly [12] as a hint for an (anti)ferroelectric to paraelectric phenomenon.

The *Pccm* space group is centrosymmetric, and thus in contradiction with a dielectric effect, but it is a proper description for the paraelectric phase ( $T > 330$  K).

A neutron diffraction pattern was recorded at 150 K. As previous research suggested [15], the peak of the dielectric permittivity at 330 K implies a doubled cell parameter or superstructure. This led us to consider the three *mm2*-type subgroups of *Pccm*, namely: *P2cm*, *Pc2m* and *Pcc2* with unchanged axes orientation. In the *Pccm* phase, Cs and Bi occupy independent *222*-positions, implying doubling of the *b*-parameter which induces the loss of half of these special positions in the *P2cm* and *Pcc2* forms. In these symmetries, only one of Cs or Bi can remain on a special position (2.. and ..2), while in *Pc2m*, both can keep occupying a .2. position. The five most likely options were tested (*P2cm* with Cs in .2. or Bi in 2.. or Cs and Bi in ..2.; *Pcc2* with Cs in ..2 or Bi in ..2) against the neutron diffraction pattern obtained at 150 K using split pseudo-Voigt peaks profile function with Caglioti polynomial width. Independent isotropic atomic displacement factors (ADPs) were refined for all atoms, while the background was modelled by interpolation of selected points that were refined.

The refinement of the five tested models led to an unambiguous outcome: four of them resulted in unrealistic MoO<sub>4</sub> tetrahedra deformations, thus requiring distance constraints in order to comply with spectroscopic interpretation of molybdate tetrahedra in

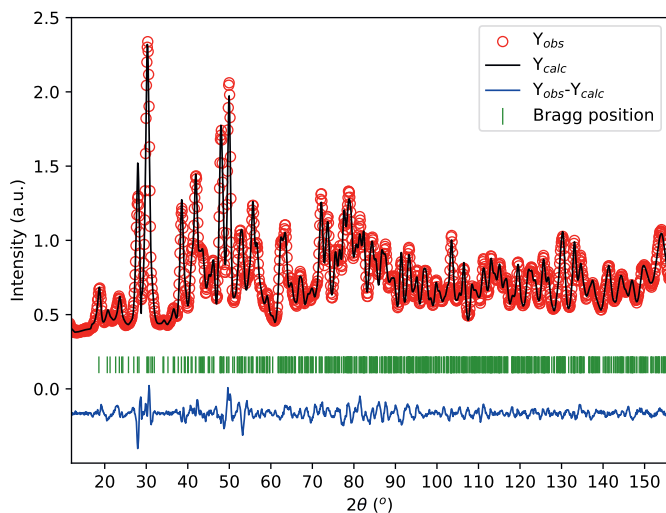


Figure 5.2: Experimental ( $Y_{obs}$ , in red) and calculated ( $Y_{calc}$ , in black) neutron diffraction patterns at 150 K. The difference between the calculated and the experimental intensities  $Y_{calc} - Y_{obs}$  is shown in blue. The angular positions of the Bragg reflections are shown in green. Measurement at  $\lambda = 1.667 \text{ \AA}$ .

earlier studies and our XANES-results (see below). Distance constraints still yielded unrealistic models, with highly divergent O-Mo-O angles, high or negative ADPs and high  $R_{Bragg}$  factors. On the opposite, the model in space group  $Pcc2$  (27) with Bi in ..2 was satisfactory in every aspect (positive definite ADPs, regular-shaped  $\text{MoO}_4$ -tetrahedra without constraints). However, the so-obtained atomic positions turned out to match with the centric  $Pccb$  symmetry (space group 54).

### 5.3.2. CRYSTAL STRUCTURE AND ANTIFERROELECTRICITY MECHANISM

Refinement of the model in space group  $Pccb$  against the neutron diffraction data obtained at 150 K is shown in Figure 5.2, while the cell parameters are given in Table 5.1. The choice of space group  $Pccb$  allows a drastic reduction of the number of variable atomic coordinates (17 in  $Pccb$  instead of 34 in  $Pcc2$ ) whereas the fit quality remains reasonable with only a slight degradation. In view of parsimony, this  $Pccb$  symmetry is henceforth preferred. The geometry of the unconstrained, now unique  $\text{MoO}_4$ -tetrahedrons as well as the atomic displacement parameters are satisfactory. The refined parameters are listed in Table 5.2. The cumulated bond valence values using Brese and O'Keeffe's model [23] are 1.05 for Cs(I), 3.21 for Bi(III) and 5.44 for Mo(VI).

The crystal structure at 150 K as shown in Figure 5.4 reveals the mechanism of the antiferroelectric-paraelectric phase transition at 330 K. First, the antiferroelectric phase exhibits a highly asymmetric environment around Bi(III), with an 'umbrella-shaped' coordination polyhedron due to the stereochemical activity of the  $6s^2$  lone pair. The Bi-O distances range from 2.33 Å (opposite) to 2.74 Å (in front), see Figure 5.5. This configura-

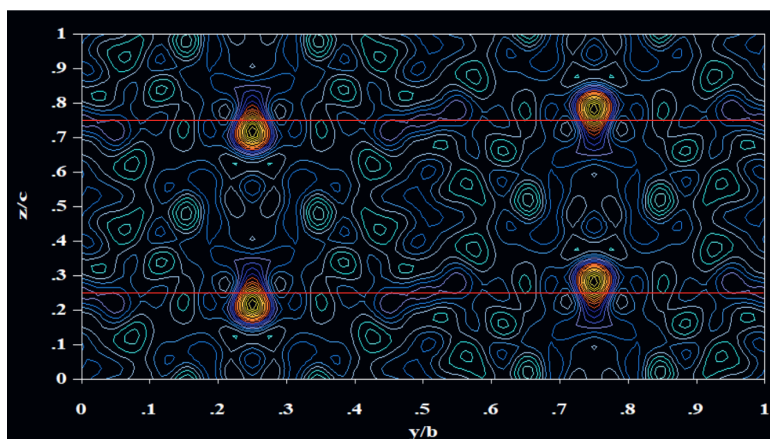


Figure 5.3: Fourier plot at 150 K, showing the most pronounced Bi shift from its ideal position.

## 5

tion is probably responsible for the apparent discrepancy between the expected and the calculated valence of Bi(III). A similar excess in bond valence sum is observed in isoelectronic structures like  $\alpha$ -PbO [24]. Second, the doubling of the  $b$ -parameter appears to be driven by the alternation of the Bi  $6s^2$ -dipoles following the  $b$ -axis. The alternation of these opposite-oriented dipoles (and to a lesser extent, of those formed by the more regular  $\text{CsO}_8$  and  $\text{MoO}_4$  polyhedra) makes the structure an antiferroelectric array, a rather common property amongst oxides containing cations with lone pairs [25–27].

Profile refinement was applied using the neutron diffraction patterns obtained at 200 K and 298 K, the synchrotron diffraction pattern at 298 K and the neutron diffraction pattern at 423 K as well, as shown in Figures 5.6, 5.7, 5.8 and 5.9. Cell parameters at various temperatures are reported in Table 5.1. The optimised atomic parameters are presented in Tables 5.3, 5.4, 5.5 and 5.6.

High-temperature XRD data ( $T > 330$  K) were refined against the archetype  $Pccm$  model and the relation between the  $Pccb$  superstructure at 150 K and the  $Pccm$  archetype structure at 773 K is visualised in Figure 5.5.

Technique	Space group	Temp. (K)	a (Å)	b (Å)	c (Å)	Volume (Å <sup>3</sup> )
ND	$Pccb$	150	5.1592(2)	18.6361(7)	8.1790(3)	786.4
ND	$Pccb$	200	5.1528(3)	18.6999(9)	8.1909(4)	789.3
ND	$Pccb$	298	5.1211(2)	18.9272(6)	8.2265(3)	797.4
ND	$Pccm$	423	5.1297(4)	9.5210(7)	8.2574(6)	403.3
sXRD	$Pccb$	298	5.12536(1)	18.98122(3)	8.23987(1)	801.7
XRD[1]	$Pccm$	298	5.14(3)	9.44(1)	8.20(9)	397.9

Table 5.1: Cell parameters of  $\text{CsBi}(\text{MoO}_4)_2$ . Uncertainties as given by FullProf.

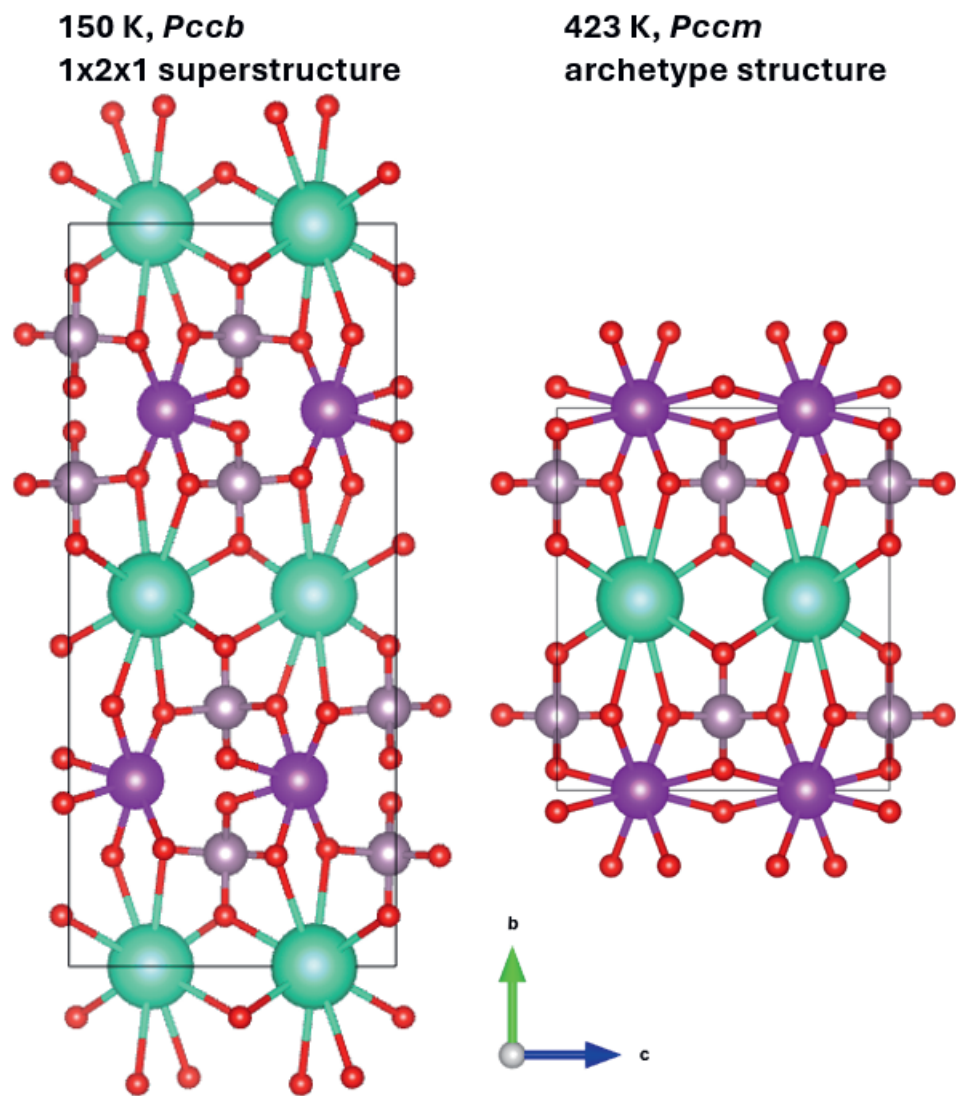


Figure 5.4: The *Pccb* superstructure of antiferroelectric  $\text{CsBi}(\text{MoO}_4)_2$  (stable between 135 and 330 K) compared to the high-temperature archetype *Pccm* structure (stable from 330 K up to the melting point).

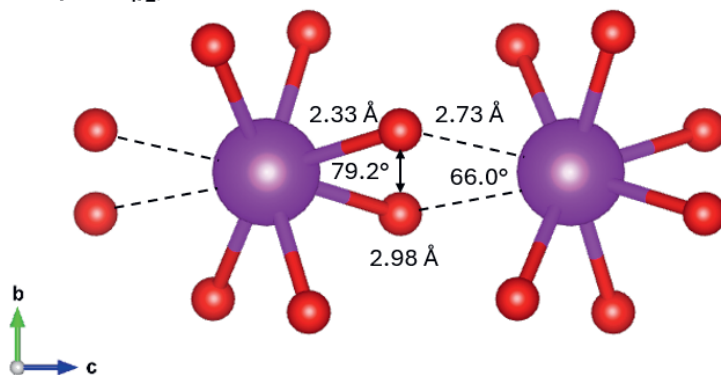
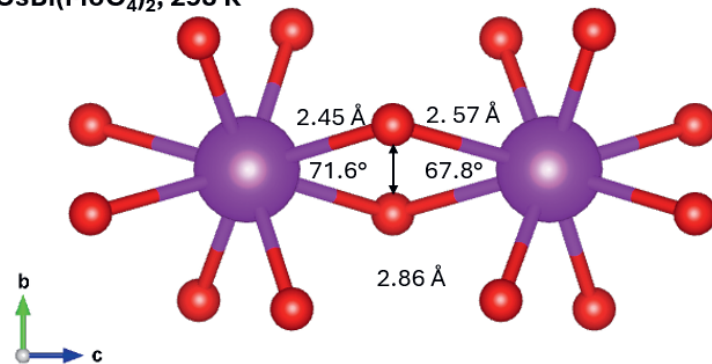
**$\text{CsBi}(\text{MoO}_4)_2$ , 150 K** **$\text{CsBi}(\text{MoO}_4)_2$ , 298 K**

Figure 5.5: Close view of the Bi-coordination at 150 K and 298 K, showing the lone-pair effect is much more pronounced at lower temperatures.

Atom	Wyckoff	x/a	y/b	z/c	B (Å <sup>2</sup> )
Bi	4d	0	0.25	0.2020(6)	0.33(6)
Cs	4c	0.040(19)	0.5	0.25	1.66(13)
Mo	8f	0.5209(8)	0.34863(19)	-0.0206(5)	0.60(5)
O1	8f	0.7760(9)	0.3510(3)	0.1317(6)	1.39(9)
O2	8f	0.6965(8)	0.3415(2)	-0.2112(6)	0.99(7)
O3	8f	0.2669(7)	0.2802(2)	-0.0160(6)	0.46(7)
O4	8f	0.3853(8)	0.4316(2)	-0.0203(7)	0.76(7)

<sup>a</sup>  $R_p = 7.29$ ,  $R_{wp} = 8.85$ ,  $R_{exp} = 2.21$ ,  $\chi^2 = 16.0$ .

Table 5.2: Atomic positions and isotropic atomic displacement parameters based on refinement using neutron diffraction data at 150 K in space group  $Pccb$  (54).<sup>a</sup>

Atom	Wyckoff	x/a	y/b	z/c	B (Å <sup>2</sup> )
Bi	4d	0	0.25	0.2051(7)	0.31(9)
Cs	4c	0.025(3)	0.5	0.25	2.0(2)
Mo	8f	0.521(10)	0.3477(3)	-0.0195(7)	0.75(9)
O1	8f	0.7708(12)	0.3519(4)	0.1373(8)	1.30(12)
O2	8f	0.7039(11)	0.3424(4)	-0.2061(7)	0.97(13)
O3	8f	0.2685(11)	0.2810(3)	-0.0149(9)	0.92(12)
O4	8f	0.3853(11)	0.4316(4)	-0.01592(10)	1.28(11)

<sup>a</sup>  $R_p = 9.16$ ,  $R_{wp} = 10.8$ ,  $R_{exp} = 2.43$ ,  $\chi^2 = 19.8$ .

Table 5.3: Atomic positions and isotropic atomic displacement parameters based on refinement using neutron diffraction data at 200 K in space group  $Pccb$  (54).<sup>a</sup>

Atom	Wyckoff	x/a	y/b	z/c	B (Å <sup>2</sup> )
Bi	4d	0	0.25	0.2313(7)	1.60(6)
Cs	4c	0.000(3)	0.5	0.25	1.80(9)
Mo	8f	0.5259(5)	0.34856(13)	-0.0090(6)	1.56(4)
O1	8f	0.7445(11)	0.3501(3)	0.1569(5)	2.04(9)
O2	8f	0.7241(11)	0.3440(3)	-0.1889(5)	1.74(9)
O3	8f	0.2532(5)	0.2820(16)	-0.0100(7)	1.40(5)
O4	8f	0.3745(6)	0.4310(16)	-0.0164(7)	2.18(8)

<sup>a</sup>  $R_p = 5.74$ ,  $R_{wp} = 6.73$ ,  $R_{exp} = 2.70$ ,  $\chi^2 = 6.20$ .

Table 5.4: Atomic positions and isotropic atomic displacement parameters based on refinement using neutron diffraction data at  $298 \pm 5$  K in space group  $Pccb$  (54).<sup>a</sup>

Atom	Wyckoff	x/a	y/b	z/c	B ( $\text{\AA}^2$ )
Bi	4d	0	0.25	0.2461(2)	1.360(8)
Cs	4c	0.0082(6)	0.5	0.25	3.025(19)
Mo	8f	0.5179(2)	0.34935(3)	-0.0005(3)	1.242(15)
O1	8f	0.7266(17)	0.3472(5)	0.1476(9)	0.7(2)
O2	8f	0.7359(15)	0.3401(5)	-0.1885(9)	0.03(17)
O3	8f	0.2812(8)	0.2818(3)	-0.002(2)	0.42(10)
O4	8f	0.3665(8)	0.4231(3)	0.001(2)	0.71(11)

$$^a R_p = 11.9, R_{wp} = 13.9, R_{exp} = 2.43, \chi^2 = 32.7$$

Table 5.5: Atomic positions and isotropic atomic displacement parameters based on refinement using synchrotron diffraction data at 298 K in space group  $Pccb$  (54).<sup>a</sup>

Atom	Wyckoff	x/a	y/b	z/c	B ( $\text{\AA}^2$ )
Bi	2e	0	0	0.25	1.08(11)
Cs	2g	0	0.5	0.25	1.8(2)
Mo	4q	0.5478(13)	0.1931(7)	0	0.89(10)
O1	8r	0.2663(8)	0.1973(5)	0.3365(5)	0.68(7)
O2	4q	0.2420(16)	0.0553(8)	0	1.65(15)
O3	4q	0.3461(17)	0.3575(8)	0	1.65(16)

$$^a R_p = 13.7, R_{wp} = 15.2, R_{exp} = 5.76, \chi^2 = 6.99.$$

Table 5.6: Atomic positions and isotropic atomic displacement parameters based on refinement using neutron diffraction data at 423 K in space group  $Pccm$  (49).<sup>a</sup>

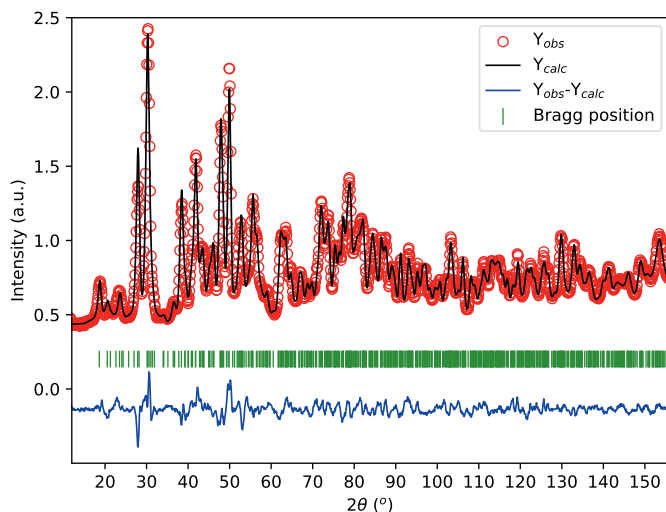


Figure 5.6: Experimental ( $Y_{obs}$ , in red) and calculated ( $Y_{calc}$ , in black) neutron diffraction patterns at 200 K. The difference between calculated and experimental intensities  $Y_{calc} - Y_{obs}$  is shown in blue. The angular positions of Bragg reflections are shown in green. Measurement at  $\lambda = 1.667 \text{ \AA}$ .

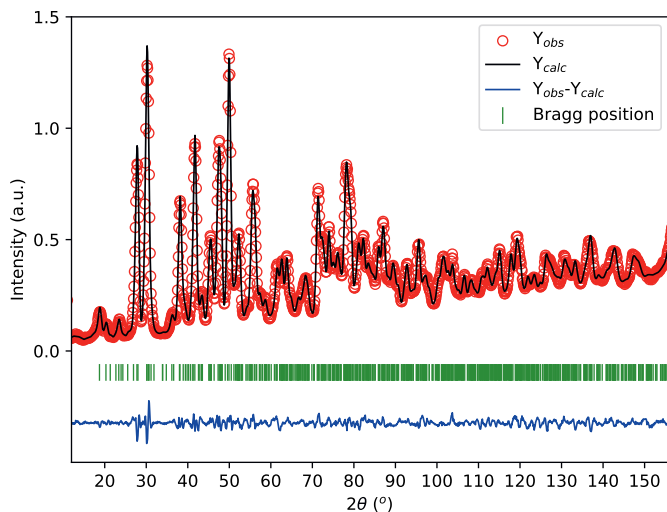


Figure 5.7: Experimental ( $Y_{obs}$ , in red) and calculated ( $Y_{calc}$ , in black) neutron diffraction patterns at 298 K. The difference between calculated and experimental intensities  $Y_{calc} - Y_{obs}$  is shown in blue. The angular positions of Bragg reflections are shown in green. Measurement at  $\lambda = 1.667 \text{ \AA}$ .

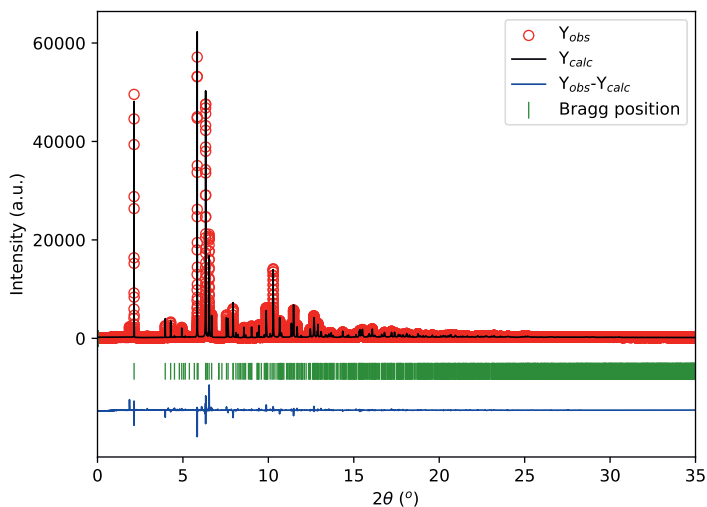


Figure 5.8: Experimental ( $Y_{obs}$ , in red) and calculated ( $Y_{calc}$ , in black) synchrotron diffraction patterns at 298 K. The difference between calculated and experimental intensities  $Y_{calc} - Y_{obs}$  is shown in blue. The angular positions of Bragg reflections are shown in green. Measurement at  $\lambda = 0.35451 \text{ \AA}$ .

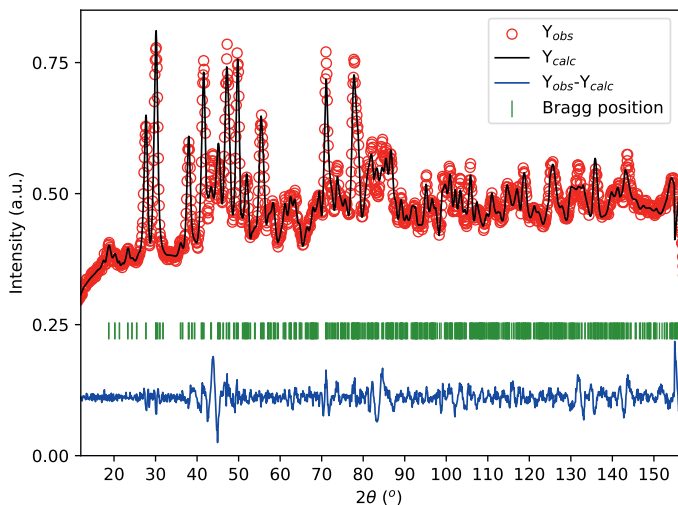


Figure 5.9: Experimental ( $Y_{obs}$ , in red) and calculated ( $Y_{calc}$ , in black) neutron diffraction patterns at 423 K. The difference between calculated and experimental intensities  $Y_{calc} - Y_{obs}$  is shown in blue. The angular positions of Bragg reflections are shown in green. Measurement at  $\lambda = 1.667 \text{ \AA}$ .

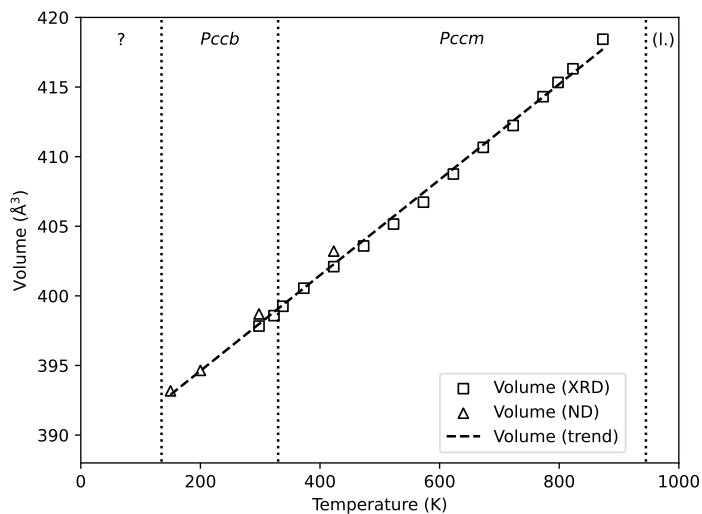


Figure 5.10: Change of unit cell volume, as rescaled to the archetype structure. The dotted lines indicate the phase transition temperatures of  $\text{CsBi}(\text{MoO}_4)_2$ . The dashed line is a guide for the eye.

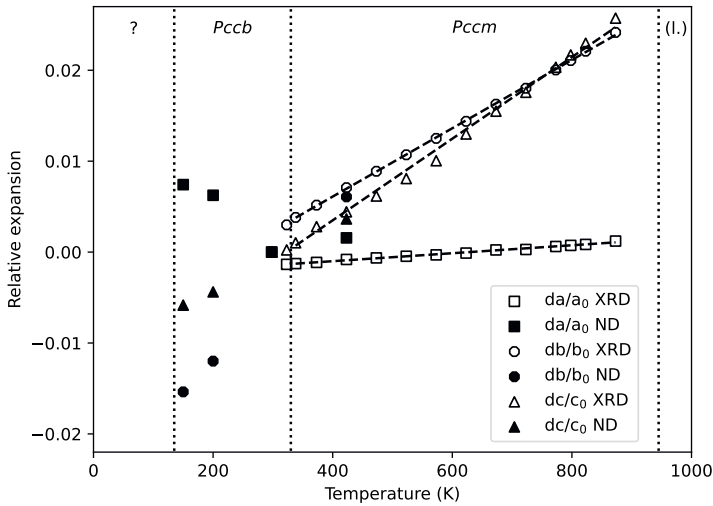


Figure 5.11: Relative thermal expansion following the  $a$ ,  $b$  and  $c$  axes as measured by low-temperature neutron and high-temperature X-ray diffraction. The dotted lines indicate the phase transition temperatures of  $\text{CsBi}(\text{MoO}_4)_2$ . The dashed lines are a guide for the eye.

## 5.4. TEMPERATURE DEPENDENCE OF CRYSTAL PROPERTIES

The cell parameters obtained using neutron diffraction were combined with those obtained in the high-temperature X-ray diffraction measurement. The  $b$ -axis was rescaled to the archetype (high temperature) phase and the resulting cell volume with increasing temperature is shown in Figure 5.10. The resulting volumetric thermal expansion  $\alpha_V = 87 \cdot 10^{-6} \text{ K}^{-1}$  using all data from both X-ray and neutron diffraction. Effectively,  $\text{CsBi}(\text{MoO}_4)_2$  shows a continuous volumetric expansion over the phase transition around 330 K, which is in agreement with a second-order transition.

The cell parameters obtained from neutron and X-ray diffraction were all rescaled to room temperature; the resulting relative thermal expansion along the three axes is shown in Figure 5.11.

A change of expansion appears near the temperature of the anomaly observed by dielectric measurements (330 K) [12]. This confirms the existence of a second-order phase transition. The phenomenon is particularly visible on the  $a = f(T)$  and  $b = f(T)$  plots, and to a lesser extent on the  $c = f(T)$  plot. The strong contraction along  $a$  below the Curie temperature becomes much smaller above the Curie temperature. The  $a$ -axis contracts, because of the new bond formation between  $\text{MoO}_4$  and Bi, as the O-atom is less repelled by the Bi  $6s^2$  lone pair with temperature increasing from 150 to 298 K.

Beyond the Curie temperature, the coefficients of thermal expansion are:  $\alpha_a = 4.4 \cdot 10^{-6} \text{ K}^{-1}$ ,  $\alpha_b = 38 \cdot 10^{-6} \text{ K}^{-1}$  and  $\alpha_c = 45 \cdot 10^{-6} \text{ K}^{-1}$  for the temperature range 338-873 K. The strong expansion along  $b$  can be ascribed to the weakness of the Cs-O bonds that link the (010) slabs, while the strong expansion along  $c$  is due to repulsive Coulombic

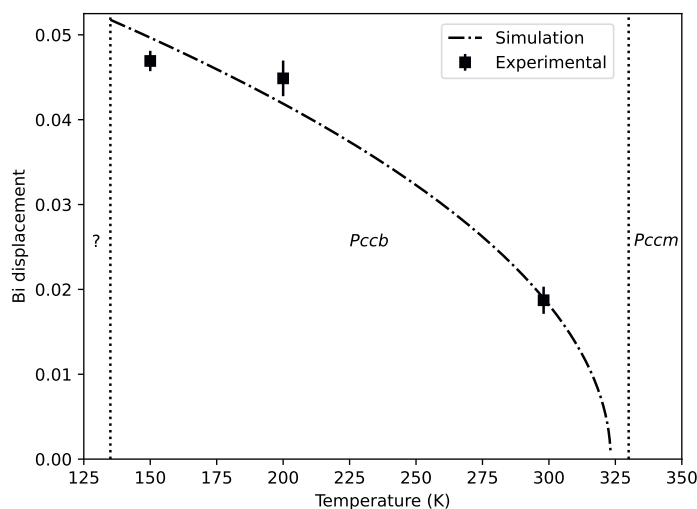


Figure 5.12: Landau model using the Bi-displacement as order parameter.  $T_C = 323.2$  K. The dotted lines indicate literature values of 135 and 330 K for the phase transitions, respectively. The error bars are the standard deviations of FullProf multiplied by the score of Bérar and Lennan [28]

interactions between edge-sharing  $\text{Bi}^{3+}$  cations. The moderate expansion following  $a$  is a consequence of the latter mechanism, that induces a contraction of the shared O-O edges.

To assess whether the Bi-displacement is the driving force of the second-order phase transition, a phenomenological Landau model has been developed. As order parameter, the Bi-displacement is calculated via its  $z$ -coordinate, *i.e.*  $z_{\text{displacement}} = 0.25 - z(T)$  using the values in Tables 5.2, 5.3 and 5.4. The Curie-temperature and constant factor are optimised such that the model follows  $\sqrt{(T_C - T)}$ , yielding  $T_C = 323.2$  K. The result is shown in Figure 5.12. The optimised  $T_C$  value is in line with literature values of 325 and 330 K [10, 14].

With the herein obtained diffraction data, the earlier conjecture of  $D_{2h}^8$  symmetry is proven correct [15], although the cell is obtained by a doubling of the  $b$ -parameter and the mechanism is not driven by the molybdate-ions but by the  $\text{Bi}^{3+} 6s^2$  lone pair.

## 5.5. CONCLUSIONS

The crystal structure of  $\text{CsBi}(\text{MoO}_4)_2$  has been investigated using neutron and X-ray diffraction in the temperature range 150-873 K. X-ray absorption near-edge structure spectroscopy at room temperature confirmed the presence of  $\text{MoO}_4^{2-}$  ions and the hexavalent oxidation state of Mo. The mechanism of the antiferroelectric to paraelectric state has been derived from the comparison of the structures obtained by neutron diffraction at  $T = 150$  K and  $T = 298$  K. The  $6s^2$  lone pairs of the Bi-atoms form an antiferroelec-

tric arrangement at low and ambient temperature, and via a displacive mechanism, the archetype symmetry is restored above 330 K.

## EXPERIMENTAL DETAILS

**Synthesis** CsBi(MoO<sub>4</sub>)<sub>2</sub> was synthesised using a two-stage solid state synthesis process. All samples were handled in Ar-filled gloveboxes. First, Cs<sub>2</sub>MoO<sub>4</sub> was synthesised from Cs<sub>2</sub>CO<sub>3</sub> (99.99%, Alfa Aesar) and MoO<sub>3</sub> (99.5%, Alfa Aesar). The precursors were mixed in stoichiometric quantities, ground thoroughly and heated twice for 12 h at 973 K in an alumina crucible under oxygen atmosphere. The sample was reground intermittently. Second, Bi<sub>2</sub>(MoO<sub>4</sub>)<sub>3</sub> was synthesised from Bi<sub>2</sub>O<sub>3</sub> (99.99%, Sigma Aldrich) and MoO<sub>3</sub> at 875 K for 12 h under oxygen flow twice with intermittent regrinding. Finally, CsBi(MoO<sub>4</sub>)<sub>2</sub> was synthesised by mixing Cs<sub>2</sub>MoO<sub>4</sub> and Bi<sub>2</sub>(MoO<sub>4</sub>)<sub>3</sub>. After thorough grinding, the mixtures were heated in an alumina crucible for 12 h at 750 K. After cooling, the mixture was reground and again heated for 12 h at 750 K. No unaccounted Bragg reflections were found. Alternatively, Cs<sub>2</sub>CO<sub>3</sub>, MoO<sub>3</sub> and Bi<sub>2</sub>O<sub>3</sub> were directly mixed in the 1:4:1 molar ratio and heated to obtain CsBi(MoO<sub>4</sub>)<sub>2</sub>.

**X-ray diffraction** For the high-temperature studies (298 to 873 K), an Panalytical X'Pert Pro diffractometer was used in Bragg-Brentano geometry ( $U=45$  kV,  $I=40$  mA) with Cu  $K_{\alpha 1}$  radiation, a Ge(111) fore monochromator and a PIXcel detector equipped with an Anton Paar furnace. Synchrotron diffraction measurements were performed at ID22 at the ESRF in Grenoble [29]. Data analysis was performed using the profile refinement method [30, 31] in the FullProf suite [32]. The synchrotron diffraction data was refined using the Thompson-Cox-Hastings function with spherical harmonics expansion.

**Neutron diffraction** Neutron diffraction (ND) was measured at the PEARL beam line at the Hoger Onderwijs Reactor (HOR) at TU Delft [33]. The sample was encapsulated in a vanadium Null-alloy can. For the measurements at room temperature and below, the can was hermetically closed with an In-seal. For the measurement at 423 K, the rubber o-ring was substituted for a copper ring.

**X-ray absorption near-edge structure (XANES) spectroscopy** XANES samples were prepared by pressing pellets of 8 mm diameter consisting of a mixture of the compound and boron nitride (BN). These pellets were enclosed in Kapton foil. X-ray Absorption Spectroscopy measurements were performed at the INE beamline [34] of the Karlsruhe Research Accelerator (KARA) synchrotron facility (Karlsruhe, Germany). Samples were probed around the K-edge of Mo (20 keV).



## BIBLIOGRAPHY

- (1) Klevtsov, P. V.; Vinokurov, V. A. *Neorganicheskie Materialy* **1973**, 9, 156.
- (2) Klevtsov, P. V.; Vinokurov, V. A.; Klevtsova, R. F. *Kristallografiya* **1973**, 18, 1192–1197.
- (3) Klevtsov, P. V.; Vinokurov, V. A.; Klevtsova, R. F. *Neorganicheskie Materialy* **1975**, 11, 1467–1468.
- (4) Klevtsov, P. V.; Klevtsova, R. F. *Journal of Structural Chemistry* **1977**, 18, 339–355.
- (5) Trunov, V. K.; Efremov, V. A.; Velikodnyj, Y. A., *Crystal chemistry and properties of double molybdates and tungstates*; Science. Leningrad. department: 1986.
- (6) Serezhkin, V. N. *Journal of Structural Chemistry* **1986**, 26.
- (7) Isupov, V. A. *Ferroelectrics* **2005**, 321, 63–90.
- (8) Isupov, V. A. *Ferroelectrics* **2005**, 322, 83–114.
- (9) Solodovnikov, S. F.; Gulyaeva, O. A.; Savina, A. A.; Yudin, V. N.; Buzlukov, A. L.; Solodovnikova, Z. A.; Zolotova, E. S.; Spiridonova, T. S.; Khaikina, E. G.; Stefanovich, S. Y., et al. *Journal of Structural Chemistry* **2022**, 63, 1101–1133.
- (10) Pelikh, L. N.; Zvyagin, A. I. *Fizika Tverdogo Tela* **1978**, 20, 1912–1914.
- (11) Pelikh, L. N.; Zvyagin, A. I.; Gurskas, A. A. *Fizika Tverdogo Tela* **1982**, 24, 297–299.
- (12) Brilingas, A.; Grigas, I.; Gurskas, A.; Zvyagin, A. I.; Kalesinskas, V.; Pelikh, L. N. *Fizika Tverdogo Tela* **1980**, 22, 3477–3479.
- (13) Pelikh, L. N. *Fizika Tverdogo Tela* **1983**, 25, 3467–3468.
- (14) Stokka, S.; Samulionis, V. *physica status solidi a* **1981**, 67, K89–K92.
- (15) Zvyagin, A. I.; Kut'ko, V. I. *Fizika Nizkikh Temperatur* **1987**, 13, 537–540.
- (16) Hanuza, J.; Maczka, M. *Vibrational spectroscopy* **1994**, 7, 85–96.
- (17) Maczka, M.; Kojima, S.; Hanuza, J. *Journal of Physics: Condensed Matter* **1998**, 10, 8093.
- (18) Maczka, M.; Kojima, S.; Hanuza, J. *Journal of Physics and Chemistry of Solids* **2000**, 61, 735–742.
- (19) Maczka, M.; Hanuza, J.; Ko, J.-H.; Kojima, S. *Physical Review B* **2003**, 68, 174101.
- (20) Maczka, M.; Paraguassu, W.; Souza Filho, A. G.; Freire, P. T. C.; Melo, F. E. A.; Mendes Filho, J.; Hanuza, J. *Journal of Raman Spectroscopy* **2005**, 36, 56–62.
- (21) Smith, A. L.; Rutten, M.; Herrmann, L.; Epifano, E.; Konings, R. J. M.; Colineau, E.; Griveau, J.-C.; Guéneau, C.; Dupin, N. *Journal of the European Ceramic Society* **2021**, 41, 3664–3686.

- (22) Van Hattem, A.; Dankelman, R.; Colineau, E.; Griveau, J.-C.; Dardenne, K.; Rothe, J.; Couweleers, S.; Konings, R. J. M.; Smith, A. L. *Journal of Alloys and Compounds* **2024**, *1003*, 175588.
- (23) Brese, N. E.; O’Keeffe, M. *Acta Crystallographica Section B* **1991**, *47*, 192–197.
- (24) Dickinson, R. G.; Friauf, J. B. *Journal of the American Chemical Society* **1924**, *46*, 2457–2463.
- (25) Smolensky, G. A.; Isupov, V. A. *Le Journal de Physique Colloques* **1972**, *33*, C2–25.
- (26) Subbarao, E. C. *Ferroelectrics* **1973**, *5*, 267–280.
- (27) Rabe, K. M. *Functional metal oxides: new science and novel applications* **2013**, 221–244.
- (28) Bérrar, J.-F.; Lelann, P. *Journal of Applied Crystallography* **1991**, *24*, 1–5.
- (29) Fitch, A.; Dejoie, C.; Covacci, E.; Confalonieri, G.; Grendal, O.; Claustre, L.; Guillo, P.; Kieffer, J.; Nolf, W. d.; Petitdemange, S., et al. *Synchrotron Radiation* **2023**, *30*, 1003–1012.
- (30) Rietveld, H. M. *Journal of Applied Crystallography* **1969**, *2*, 65–71.
- (31) Van Laar, B.; Schenk, H. *Acta Crystallographica Section A* **2018**, *74*, 88–92.
- (32) Rodríguez-Carvajal, J. *Physica B: Condensed Matter* **1993**, *192*, 55–69.
- (33) Van Eijck, L.; Cussen, L. D.; Sykora, G. J.; Schooneveld, E. M.; Rhodes, N. J.; Van Well, A. A.; Pappas, C. *Journal of Applied Crystallography* **2016**, *49*, 1398–1401.
- (34) Rothe, J.; Butorin, S.; Dardenne, K.; Denecke, M. A.; Kienzler, B.; Löble, M.; Metz, V.; Seibert, A.; Steppert, M.; Vitova, T., et al. *Review of Scientific Instruments* **2012**, *83*, 043105.

# 6

## THE CsI-PbI<sub>2</sub>-BiI<sub>3</sub> SYSTEM

*The thermochemistry of the ternary system CsI-PbI<sub>2</sub>-BiI<sub>3</sub>, investigated in this work, is of interest in the nuclear field, but also for applications in photovoltaics, memory devices and nuclear applications. The compounds CsPbI<sub>3</sub>, Cs<sub>4</sub>PbI<sub>6</sub> and Cs<sub>3</sub>Bi<sub>2</sub>I<sub>9</sub> were found to be the only stable phases in the investigated temperature window. The heat capacities of CsPbI<sub>3</sub>, Cs<sub>4</sub>PbI<sub>6</sub> and Cs<sub>3</sub>Bi<sub>2</sub>I<sub>9</sub> were studied using low-temperature thermal-relaxation calorimetry in the temperature range of 1.9-300 K. The three compounds are insulators, with no electronic contribution to the heat capacity. None of them show detectable anomalies in the studied temperature window. Thermodynamic properties at standard conditions are derived. Previously reported results on Cs<sub>3</sub>Bi<sub>2</sub>I<sub>9</sub> are not fully consistent with the present findings. Moreover, the magnetic susceptibilities of the three compounds were measured.*

*The binary phase diagrams CsI-PbI<sub>2</sub> and CsI-BiI<sub>3</sub> were subjected to renewed experimental investigation, and the liquidus lines and invariant equilibria were determined. The phase equilibria in the BiI<sub>3</sub>-PbI<sub>2</sub> system were measured for the first time using Differential Scanning Calorimetry (DSC). The end-members form a solid solution over the entire composition range. The pseudo-binary section CsPbI<sub>3</sub>-Cs<sub>3</sub>Bi<sub>2</sub>I<sub>9</sub> of the CsI-PbI<sub>2</sub>-BiI<sub>3</sub> ternary system was furthermore measured by DSC, as well as the ternary eutectic points. A thermodynamic model of the complete CsI-PbI<sub>2</sub>-BiI<sub>3</sub> system was developed using the Compound Energy Formalism (CEF) for the solid phases and the Modified Quasichemical Model in the Quadruplet Approximation (MQMQA) for the liquid phase. The binary systems were modelled first and no ternary interaction parameters were found necessary to accurately reproduce the phase equilibria in the ternary system. With our model, the whole liquidus surface of the field CsI-PbI<sub>2</sub>-BiI<sub>3</sub> is described for the first time.*

---

This chapter is based on the publications: A. van Hattem, J.-C. Griveau, E. Colineau, A.J.E. Lefering, R.J.M. Konings and A.L. Smith, *Low-Temperature Heat Capacity of CsPbI<sub>3</sub>, Cs<sub>4</sub>PbI<sub>6</sub>, and Cs<sub>3</sub>Bi<sub>2</sub>I<sub>9</sub>*, The Journal of Physical Chemistry C **127**, 46 (2023): 22808-22816 and A. van Hattem, D. Alders, R.J.M. Konings and A.L. Smith *Ternary System CsI-PbI<sub>2</sub>-BiI<sub>3</sub> and Thermodynamic Stability of Cesium Metal Halide Perovskites*, The Journal of Physical Chemistry C **127**, 35 (2023): 17482-17496.

## 6.1. INTRODUCTION

The CsI-PbI<sub>2</sub>-BiI<sub>3</sub> system is relevant for lead-cooled fast reactors [1–9], as it is part of the Pb-Bi-Cs-I system, the representative for coolant-volatile fission product interaction in this work. For the safety assessment of the lead-cooled fast reactor, it is important to know how the coolant elements Pb and Bi will interact with radiotoxic and volatile fission products such as caesium (Cs) and iodine (I) in case the cladding around a nuclear fuel pin would break [10, 11]. Because of the very high temperature and thermal gradient inside a mixed oxide (U,Pu)O<sub>2</sub> fuel pellet, volatile fission products like Cs and I tend to migrate to the periphery of the fuel pin [10, 12], meaning they will be among the most likely elements to come in contact with the coolant upon clad breach.

The ternary salt system CsI-PbI<sub>2</sub>-BiI<sub>3</sub> with the phases CsPbI<sub>3</sub>, Cs<sub>4</sub>PbI<sub>6</sub> and Cs<sub>3</sub>Bi<sub>2</sub>I<sub>9</sub>, is relevant for many other applications, ranging from X-ray detection and scintillation purposes [13–16], memory devices [17–19] and LEDs [20, 21] to photovoltaic solar cells [22–25]. In their review of metal halide perovskites, Kovalenko *et al.* describe the huge increase in publications in the field in the past decade [26]. Especially the compounds Cs<sub>3</sub>Bi<sub>2</sub>I<sub>9</sub> and CsPbI<sub>3</sub> were subjected to in-depth physical and chemical studies in fields varying from photovoltaics [26, 27] and scintillation [28, 29] to thermoelectrics [30, 31] because of the existence of a perovskite-related phase. Cs<sub>4</sub>PbI<sub>6</sub> is the lesser investigated salt in the CsI-PbI<sub>2</sub> system [15, 32, 33].

One of the reasons for the keen interest is the fact that the halide perovskite phases that occur in the CsI-PbI<sub>2</sub>-BiI<sub>3</sub> system have favourable optoelectronic properties. They are applied in a variety of forms in devices, thin films, nano-crystalline materials or single crystals. The latter, used in X-ray detection and scintillation techniques, are grown from the molten state by the Czochralski or Bridgman methods using slow pulling and cooling. This is a quasi-equilibrium process, governed by kinetics and thermodynamics. Thin films are generally produced by physical or chemical vapour deposition (resp. PVD and CVD) [34, 35], in which the crystalline layers are deposited on a substrate from a vapour phase composed of the individual precursors. Although it is a non-equilibrium process, chemical thermodynamic considerations are highly useful in predicting the stable materials at the temperature, (gas) pressure and concentrations in a CVD reactor. All these applications have in common that high-temperature processes are involved, so the development of thermodynamic models is extremely helpful to describe synthesis and operating conditions of the envisaged materials.

Despite the attention materials in the CsI-PbI<sub>2</sub>-BiI<sub>3</sub> system are getting, studies of their low-temperature behaviour seem to be rather limited and originate mainly from luminescence and scintillation related studies [32, 36, 37]. Other works include the investigation of thermal transport properties, reporting (ultra-)low thermal conductivity for Cs<sub>3</sub>Bi<sub>2</sub>I<sub>9</sub> and CsPbI<sub>3</sub> [38–42], but the standard entropy at 298.15 K as can be determined from low-temperature heat capacity has not been reported. To fill this knowledge gap, the low-temperature heat capacity up to room temperature of CsPbI<sub>3</sub>, Cs<sub>4</sub>PbI<sub>6</sub> and Cs<sub>3</sub>Bi<sub>2</sub>I<sub>9</sub> is reported in the first part of this chapter, providing insight into the physics and thermodynamics (heat capacity, standard entropy) of the complex metal iodides in the CsI-PbI<sub>2</sub>-BiI<sub>3</sub> system.

Knowledge of the equilibrium phase diagrams in the CsI-PbI<sub>2</sub>-BiI<sub>3</sub> system is very limited or the available data are not recent [43–51]. CsI-PbI<sub>2</sub> and CsI-BiI<sub>3</sub> were investigated

for the last time in 1972 and 1988, respectively. To the best of our knowledge, no phase diagrams of the binary  $\text{BiI}_3\text{-PbI}_2$  or the ternary  $\text{CsI-PbI}_2\text{-BiI}_3$  systems were ever reported in literature. For that reason we have made a systematic study of this ternary iodide salt system, with experimental investigations of the binary systems, of selected compositions in the ternary system, and a CALPHAD-based assessment, to provide a sound chemical thermodynamic description of the phase equilibria in the ternary system.

## 6.2. LITERATURE REVIEW

### 6.2.1. THE $\text{CSI-BiI}_3$ SYSTEM

Three phase diagram investigations into the  $\text{CsI-BiI}_3$  system were found in literature: a study from Plyushev *et al.* from 1970 [47], a study from Dzeranova *et al.* from 1984 [48] and a study from Kun *et al.* from 1988 [46]. The three phase diagrams agree on the fact that there is only one compound, that forms eutectic systems with the end members  $\text{CsI}$  and  $\text{BiI}_3$ . However, there is some confusion about the exact composition of the compound: Plyushev *et al.* report it as  $\text{Cs}_3\text{Bi}_2\text{I}_9$ , while Dzeranova *et al.* report it to be “ $\text{Cs}_3\text{BiI}_6$ ”, with the strange remark that this compound corresponds to 57%  $\text{CsI}$ . Kun *et al.* later report  $\text{Cs}_3\text{Bi}_2\text{I}_9$ . Upon analysis of the  $d$ -spacing that is reported for “ $\text{Cs}_3\text{BiI}_6$ ” by Dzeranova *et al.*, we consider it is actually a mixture of  $\text{CsI}$  and  $\text{Cs}_3\text{Bi}_2\text{I}_9$ . This observation undermines the paper by Kaloev *et al.* [52] that analyses the phase diagram based on the wrong composition. Kun *et al.* also report a homogeneity range up to 4.7 mol-% for  $\text{Cs}_3\text{Bi}_2\text{I}_9$ , hence  $\text{Cs}_3\text{Bi}_2\text{I}_9$  is actually the non-stoichiometric compound  $\text{Cs}_{3-x}\text{Bi}_{2+x}\text{I}_{9+2x}$  with  $x$  either positive or negative. To increase the legibility in this work, however, the notation  $\text{Cs}_3\text{Bi}_2\text{I}_9$  will be used for this non-stoichiometric compound. The data points reported by [46–48] are reproduced in the phase diagram optimisation, see Figure 6.9. The melting temperature of  $\text{Cs}_3\text{Bi}_2\text{I}_9$  reported by [46, 47] is also listed in Table 6.5. The crystal structure of  $\text{Cs}_3\text{Bi}_2\text{I}_9$  was already elucidated in 1968 by Lindqvist [53]. More recently, it was found by Johansson *et al.* that between  $\text{Cs}_3\text{Bi}_2\text{I}_9$  and  $\text{BiI}_3$ , only mixtures of these two compounds are formed [25]. When assessing other claims, it is necessary to clearly discriminate between compounds that form as bulk powder and thin films. In studies on thin films, *e.g.* reports on  $\text{CsBi}_3\text{I}_{10}$  are found [24], though it also claimed to form as freestanding material [54]. The latter authors propose a degradation mechanism in which the decomposition temperature of  $\text{CsBi}_3\text{I}_{10}$  would be 428 K. Polymorphism for  $\text{Cs}_3\text{Bi}_2\text{I}_9$  was investigated below room temperature [55–58]. Kun *et al.* [46] claim a transition to a high-temperature polymorph of  $\text{Cs}_3\text{Bi}_2\text{I}_9$  at 605 K; to the best of our knowledge, they are the only ones.

In the phase diagram optimisation, the congruent melting point of  $\text{Cs}_3\text{Bi}_2\text{I}_9$  was derived to be 874 K (*vide infra*). However, thermal degradation of a single crystal was reported to already occur at 823 K [16]. Thermo-Gravimetric Analysis (TGA) measurements of  $\text{Cs}_3\text{Bi}_2\text{I}_9$  by Gu *et al.* report a large weight loss at 698 K and another at 923 K [59]. Thermal expansion of  $\text{Cs}_3\text{Bi}_2\text{I}_9$  was determined using *in situ* synchrotron X-ray Diffraction by McCall *et al.* in 2017 [60]. The authors measured the X-ray diffraction patterns starting at 298 K up to 873 K with intervals of 6–10 K. They report Bragg peaks to remain from room temperature to decomposition at 775 K, after which  $\text{Cs}_3\text{Bi}_2\text{I}_9$  starts to dissociate. A discontinuity in lattice parameter is observed at 682 K. In their Differential

Thermal Analysis (DTA), they observe events at 815 K, which they assigned to BiI<sub>3</sub> boiling, and at 883 K, which they state to nearly coincide with the melting point of CsI (905 K). This interpretation does not agree with dedicated phase diagram investigations.

Regarding thermodynamic data on the ternary compound, the melting enthalpy was measured by Kun *et al.* [46]. They found the value of  $(148 \pm 2.2)$  kJ·mol<sup>-1</sup> at  $T = (905 \pm 5)$  K. To the best of our knowledge, no experimental data on the enthalpy of formation, entropy or heat capacity at  $T \geq 300$  K of Cs<sub>3</sub>Bi<sub>2</sub>I<sub>9</sub> are available in the literature. A recent experimental measurement [61] of the low-temperature heat capacity of Cs<sub>3</sub>Bi<sub>2</sub>I<sub>9</sub> is not in agreement with our measurements (see below), while another article only presents a partial heat capacity curve [42]. A computational study reports the enthalpy of formation of Cs<sub>3</sub>Bi<sub>2</sub>I<sub>9</sub> at 0 K to be -1345 kJ·mol<sup>-1</sup> [62].

### 6.2.2. THE CSI-PBI<sub>2</sub> SYSTEM

Two phase diagram investigations were performed for the system CsI-PbI<sub>2</sub>. Firstly, the liquidus line was published by Ilyasov *et al.* in 1967 [44]. They reported Cs<sub>4</sub>PbI<sub>6</sub> to melt with peritectic decomposition and CsPbI<sub>3</sub> to melt congruently. Secondly, a complete phase diagram was published in 1969 by Belyaev *et al.* [43]. The data points reported by [43, 44] are reproduced in the phase diagram optimisation in Figure 6.10. The two intermediate compounds are well-established in the scientific literature: CsPbI<sub>3</sub> since 1893 [49] and Cs<sub>4</sub>PbI<sub>6</sub> since 1960 [51]. Several polymorphs of CsPbI<sub>3</sub> exist, but the stable states are limited to  $\delta$ -CsPbI<sub>3</sub> at room temperature and  $\alpha$ -CsPbI<sub>3</sub> at high temperature till melting.

Thermodynamic data are mostly limited to the study of enthalpic properties of CsPbI<sub>3</sub>: the enthalpy of formation and the enthalpy of transition were studied several times. Wang *et al.* measured the enthalpy of formation from binary iodides using solution calorimetry with DMSO as solvent [63, 64]. Tsvetkov *et al.* also used solution calorimetry with a DMSO-water mixture as solvent [65]. Sereda *et al.* [66] derived the enthalpy of reaction from the iodides using high temperature heat flux inverse drop calorimetry. They found within error the same value, though the error is quite larger than that reported by the other publications. The results are in excellent agreement, as shown in Table 6.1. The enthalpy of the phase transition in CsPbI<sub>3</sub> was studied by Dastidar *et al.* [67] and by Wang *et al.* [63]. Their results are included in Table 6.5. Using Density Functional Theory (DFT), Kye *et al.* also found  $\alpha$ -CsPbI<sub>3</sub> to have a negative enthalpy of formation, though it was less negative than  $\delta$ -CsPbI<sub>3</sub>, *i.e.* the  $\alpha$ -polymorph is only metastable with respect to the  $\delta$ -phase [68]. The low-temperature heat capacity of CsPbI<sub>3</sub> was only reported from 0.4 up to 150 K by Evarestov *et al.* [69].

$\Delta_f H^\circ(298.15 \text{ K}) / \text{kJ}\cdot\text{mol}^{-1}$	Method	Reference
-539.0±0.9	Solution calorimetry	[63]
-539.1±0.4	Solution calorimetry	[65]
-537.5±6.0	Drop calorimetry	[66]

Table 6.1: Reported experimentally determined enthalpy of formation of  $\delta$ -CsPbI<sub>3</sub>.

As a side-note: the Cs<sub>2</sub>PbX<sub>4</sub> and CsPb<sub>2</sub>X<sub>5</sub> compounds, which were studied using Time Dependent Density Functional Theory (TD-DFT), do not exist as bulk compound for X=I

[70], though there can be two-dimensional materials formed via non-ambient pressure routes [71].

### 6.2.3. THE $\text{BiI}_3$ - $\text{PbI}_2$ SYSTEM

Compared to the two systems discussed *supra*, practically nothing is known on the  $\text{BiI}_3$ - $\text{PbI}_2$  system. No compounds have been reported. To the best of our knowledge, no phase diagram was ever reported on this system, neither is any thermodynamic property known. The phases that occur in the system have not been identified clearly. In 1999, a paper describing the  $(\text{PbI}_2)_x$ - $(\text{BiI}_3)_{1-x}$  structure was reported, but the study is inconclusive with respect to the solid solution phases, their structural ordering and their thermal stability [72]. From an application point of view, a study by Neuhausen and Eichler from 2006 on the thermal release of iodine from liquid eutectic lead bismuth alloy is of interest [73]. Although this study is important in the practical assessment of the evaporation of radio-iodine, it does not explain the nature of the solid behaviour of mixtures of  $\text{PbI}_2$  and  $\text{BiI}_3$  at the atomic scale. A single DSC measurement at  $x = 0.50$  is known, reporting a single thermal event at 654 K [19]. Alexander *et al.* studied the structure of this system at a composition  $x_{\text{BiI}_3} = 0.5$  [18], using among other techniques single-crystal XRD, Transmission Electron Microscopy (TEM), Scanning Electron Microscopy with Energy Dispersive Scattering (SEM/EDS) and powder XRD. Their XRD and EDS data indicate that  $\text{Pb}^{2+}$ ,  $\text{Bi}^{3+}$  and vacancies share the same site, while iodine has a fully occupied position. The TEM and electron diffraction data indicate micro-structured composites with two phases with mixed occupancies.

### 6.2.4. THE TERNARY PHASE FIELD $\text{CsI}$ - $\text{PbI}_2$ - $\text{BiI}_3$

No complete thermodynamic investigations into the ternary phase diagram are known to us. However, bismuth doping into  $\text{CsPbI}_3$  was studied. Papers on  $\text{CsPb}_{1-x}\text{Bi}_x\text{I}_3$  can be interpreted as study of the subsolidus field of the section  $\text{CsPbI}_3$ -“ $\text{CsBiI}_4$ ”. In 2017, Hu and coworkers [22] investigated the bismuth incorporation into  $\alpha$ - $\text{CsPbI}_3$ . Initially, this stabilises the  $\alpha$ -polymorph. According to the authors, above 10% bismuth incorporation, the  $\delta$ -polymorph is again the most stable crystal structure at room temperature. Computational research using DFT by Zhang *et al.* contradicts the attribution of this effect to incorporation of  $\text{Bi}^{3+}$ , though stating that incorporation of  $\text{Bi}(0)$  would stabilise the high-temperature structure [74]. In a following publication, Zhang *et al.* state that the perovskite-stabilising due to the B-site doping is only valid for  $\text{Sn}^{2+}$ -doping. The authors claim that if the effect is found experimentally, this probably depends on the synthesis route and it is not due to the inherent physics of  $\text{CsPb}_{1-x}\text{Bi}_x\text{I}_3$  [75]. Kye *et al.* found similar results [68]. For thin films, the metastability of  $\alpha$ - $\text{CsPbI}_3$  with respect to  $\delta$ - $\text{CsPbI}_3$  upon  $\text{Bi}^{3+}$ -doping was also experimentally proven: above 393 K, the films turn into the  $\delta$ - $\text{CsPbI}_3$  variant [76].

### 6.2.5. DATA USED FOR THERMODYNAMIC MODELLING

The thermodynamic functions selected in this work to describe the end-members and intermediate compounds in the  $\text{CsI}$ - $\text{PbI}_2$ - $\text{BiI}_3$  system are given in Table 6.2. The thermodynamic functions for  $\text{CsI}$  are taken from Capelli *et al.* [77]. For  $\text{PbI}_2$ (s), the enthalpy of formation and entropy are taken from JANAF [78]. A fit for the heat capacity of the solid

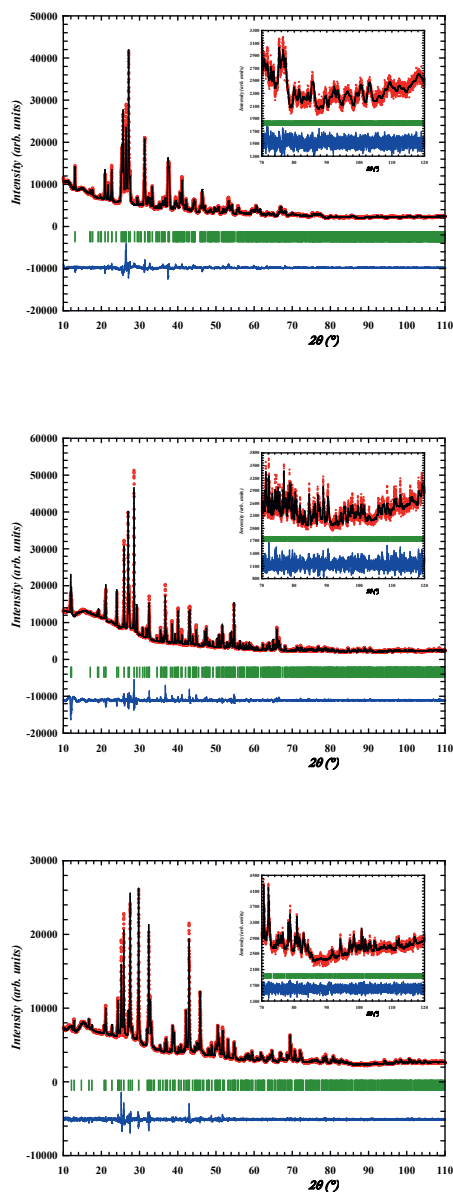


Figure 6.1: Experimental ( $Y_{obs}$ , in red) and calculated ( $Y_{calc}$ , in black) XRD patterns of  $\delta\text{-CsPbI}_3$  (top),  $\text{Cs}_4\text{PbI}_6$  (middle) and  $\text{Cs}_3\text{Bi}_2\text{I}_9$  (bottom) at ambient conditions. The difference between the calculated and the experimental intensities  $Y_{obs} - Y_{calc}$  is shown in blue. The angular positions of the Bragg reflections are shown in green. Measurement at  $\lambda = \text{Cu } K\alpha$ .

phase was made to the heat capacity values listed by JANAF [78]. The enthalpy of transition ( $\text{PbI}_2(\text{s})=\text{PbI}_2(\text{l})$ ) as reported by Konings *et al.* [79] ( $23.5 \text{ kJ}\cdot\text{mol}^{-1}$ ) is used, which is close to the value reported in JANAF ( $23.4 \text{ kJ}\cdot\text{mol}^{-1}$ ). The heat capacity for the liquid phase is also taken from JANAF [78]. The standard enthalpy of formation and entropy of  $\text{BiI}_3(\text{s})$  are taken from Cubicciotti [80]. The heat capacity for the solid phase and enthalpy of melting are taken from Barin *et al.* [81]. The heat capacity for  $\text{BiI}_3(\text{l})$  is taken from Cubicciotti and Eding [82]. The enthalpy of formation of  $\delta\text{-CsPbI}_3$  is based on the measurements of Wang *et al.* and Tsvetkov *et al.* [63, 65]. The standard enthalpy of formation and entropy of  $\alpha\text{-CsPbI}_3$  are correlated to those of  $\delta\text{-CsPbI}_3$  via the enthalpy of the phase transition as measured by Dastidar *et al.* [67] and Wang *et al.* [63]. The standard entropy of  $\delta\text{-CsPbI}_3$  was optimised in this work, as well as the standard enthalpy of formation and entropy of  $\text{Cs}_4\text{PbI}_6$  and  $\text{Cs}_3\text{Bi}_2\text{I}_9$ . The heat capacities of  $\text{CsPbI}_3$ ,  $\text{Cs}_4\text{PbI}_6$  and  $\text{Cs}_3\text{Bi}_2\text{I}_9$  were estimated using the Neumann-Kopp rule [83, 84].

Compound	$\Delta_f H_m^\circ(298.15 \text{ K})$ ( $\text{kJ}\cdot\text{mol}^{-1}$ )	$S_m^\circ(298.15 \text{ K})$ ( $\text{J}\cdot\text{K}^{-1}\cdot\text{mol}^{-1}$ )	$C_{p,m}(T)(\text{J}\cdot\text{K}^{-1}\cdot\text{mol}^{-1}) = A + BT + CT^{-2} + DT^2$				Temperature range (K)	Source
			A	B	C	D		
CsI(s)	-348.100	122.2	43.815	0.0218422	200,247.7	$2.495766\cdot 10^{-6}$	[298-905]	[77]
CsI(l)	-331.912	131.90	74.268	-	-	-	[905-1500]	[77]
$\text{PbI}_2(\text{s})$	-175.3933	174.837	114.6362	-0.12982	-942,533.9	$1.377482\cdot 10^{-4}$	[298-683]	[78]
$\text{PbI}_2(\text{l})$	-162.509	185.92	108.5748	-	-	-	[683-1500]	[78, 79]
$\text{BiI}_3(\text{s})$	-150.624	224.681	40.95	0.1086732	288,972.0	$-3.519\cdot 10^{-8}$	[298-682]	[80, 81]
$\text{BiI}_3(\text{l})$	-127.7018	246.17	150.624	-	-	-	[682-1000]	[82]
$\delta\text{-CsPbI}_3$	<b>-543.000</b>	<b>294.8</b>	158.4512	-0.10798	-742,286	$1.4\cdot 10^{-4}$	[298-594]	[63, 65], This work
$\alpha\text{-CsPbI}_3$	<b>-528.800</b>	<b>318.71</b>	158.4512	-0.10798	-742,286	$1.4\cdot 10^{-4}$	[594-763]	[67], This work
$\text{Cs}_4\text{PbI}_6$	<b>-1,598.000</b>	<b>658.3</b>	289.896	-0.04245	-141,543	$1.5\cdot 10^{-4}$	[298-764]	This work
$\text{Cs}_3\text{Bi}_2\text{I}_9$	<b>-1,478.243</b>	<b>819.2</b>	213.345	0.28287	1,178,687	$7.42\cdot 10^{-6}$	[298-905]	This work

Table 6.2: Thermodynamic functions used in the CALPHAD model in this work for the end-member functions and stoichiometric compounds. The heat capacity is expressed as the following polynomial:  $C_{p,m}(T) = A + BT + CT^{-2} + DT^2$ . Optimised values are marked in **bold**.

### 6.3. CHARACTERISATION OF SYNTHESISED TERNARY SALTS

$\delta\text{-CsPbI}_3$ ,  $\text{Cs}_4\text{PbI}_6$  and  $\text{Cs}_3\text{Bi}_2\text{I}_9$  were synthesized as described in detail at the end of this chapter. They were found to be respectively yellow/green, white and red/deep orange, in line with literature [25, 49, 51]. The X-ray diffraction patterns of  $\delta\text{-CsPbI}_3$ ,  $\text{Cs}_4\text{PbI}_6$  and  $\text{Cs}_3\text{Bi}_2\text{I}_9$  are shown in Figure 6.1. Rietveld refinement was used against the diffraction patterns of  $\delta\text{-CsPbI}_3$  and  $\text{Cs}_4\text{PbI}_6$ , while LeBail refinement was used against the pattern of  $\text{Cs}_3\text{Bi}_2\text{I}_9$ . No peaks remained unexplained meaning that there are no secondary phases within detection limit. The obtained lattice parameters are listed in Table 6.3, along with a comparison to literature values [51, 53, 85].

The calculated densities are also given in Table 6.3. The density of the salts as compared to liquid Pb or LBE is of practical importance. The density of Pb and LBE at various temperatures is given in the Handbook [86]; till 1100 K, it stays above  $10 \text{ g}\cdot\text{cm}^{-3}$ . Based on the density at room temperature, it means that if these ternary compounds are formed in the coolant vessel, they will float on top of the coolant.

Compound	#	a / Å	b / Å	c / Å	$\gamma / ^\circ$	Volume / Å <sup>3</sup>	$\rho / \text{g}\cdot\text{cm}^{-3}$	Source
$\delta$ -CsPbI <sub>3</sub>	62	10.455(2)	4.8015(6)	17.773(2)	90	892.2(2)	5.366(1)	This work
	62	10.4581(3)	4.8017(1)	17.7761(5)	120	892.66	5.36	[85]
Cs <sub>4</sub> PbI <sub>6</sub>	167	14.5578(7)	14.5578(7)	18.300(1)	120	3348.7(3)	4.4500(4)	This work
	167	14.528	14.528	18.313	120	3347.35	4.47	[51]
Cs <sub>3</sub> Bi <sub>2</sub> I <sub>9</sub>	194	8.4134(4)	8.4134(4)	21.196(1)	120	1299.4(1)	5.0066(4)	This work
	194	8.4116	8.4116	21.182	120	1297.94	5.01	[53]

Table 6.3: Crystallographic information for synthesised  $\delta$ -CsPbI<sub>3</sub>, Cs<sub>4</sub>PbI<sub>6</sub> and Cs<sub>3</sub>Bi<sub>2</sub>I<sub>9</sub> as used and obtained in this work, compared with literature values [51, 53, 85]. # = number of crystallographic space group. Densities calculated based on crystal structure. Standard uncertainties given by FullProf are multiplied by 10.

## 6.4. LOW-TEMPERATURE HEAT CAPACITY

Thermal-relaxation calorimetry using PPMS was employed to measure the low-temperature heat capacity of  $\delta$ -CsPbI<sub>3</sub>, Cs<sub>4</sub>PbI<sub>6</sub> and Cs<sub>3</sub>Bi<sub>2</sub>I<sub>9</sub>

### 6.4.1. LOW-TEMPERATURE HEAT CAPACITY OF $\delta$ -CSPI<sub>3</sub>

The experimentally measured heat capacity of  $\delta$ -CsPbI<sub>3</sub> is shown in Figure 6.2, together with the Dulong-Petit limit, a Neumann-Kopp estimation from CsI and PbI<sub>2</sub> at 298.15 K, the data of Evarestov *et al.* [69] using QD-PPMS, a calculation estimating the anharmonicity and a fit obtained using one Debye and one Einstein function. The data obtained herein with the QD-PPMS and QD-Versalab instruments agree well.

The heat capacity rises fast; around 200 K, it already exceeds the Dulong-Petit limit. At 298.15 K, the experimentally measured value agrees with the value calculated using the Neumann-Kopp estimation rule (130 J·K<sup>-1</sup>·mol<sup>-1</sup>). In the lower temperature region, the heat capacity obtained in this work and the heat capacity obtained by Evarestov *et al.* [69] agree perfectly, except for the last points measured between 90 to 100 K. In contrast to our results, the latter points seem to stabilise at a lower constant value.

For  $\delta$ -CsPbI<sub>3</sub>, a correction using the Grüneisen parameter and thermal expansion coefficient (Equation 2.6) is able to reproduce the heat capacity beyond Dulong-Petit fairly well. The Grüneisen parameter for this compound is reported to be 0.86 [87] and 1.03 [88]. Volumetric thermal expansion coefficients for  $\delta$ -CsPbI<sub>3</sub> of (132·10<sup>-6</sup> K<sup>-1</sup>) [89] and (118·10<sup>-6</sup> K<sup>-1</sup>) [85] have been determined based on cell parameters in the temperature region 298 to 609 K as determined using synchrotron-based powder diffraction. Using the average value and Equation 2.6, a heat capacity value of 129.4 J·K<sup>-1</sup>·mol<sup>-1</sup> is derived at 298.15 K, in agreement with the experimentally determined value and the Neumann-Kopp estimation. The calculation in the region 200 to 400 K using  $\gamma = 0.86$  as shown in Figure 6.2 indicates that Equation 2.6 models the heat capacity quite accurately. A calculation with  $\gamma=1.03$  is shown in Figure B.4. Analysis of the heat capacity towards 0 K shows there is no electronic contribution to the heat capacity.

Fittings according to Equation 2.2 and 2.5 were made for  $\delta$ -CsPbI<sub>3</sub>; the combined Debye-Einstein fit is shown in Figure 6.2, while the difference between both fits and the measured data is shown in Figure 6.3. The fitting parameters and temperature windows are listed in Table 6.4. In Figure 6.3, the dashed line indicates a 3% deviation [90]; it can be seen that the error stays mostly within this margin; the extra deviation towards room temperature can be ascribed to anharmonic effects related to thermal expansion. In principle, the used technique can achieve a higher precision and accuracy [91], so a

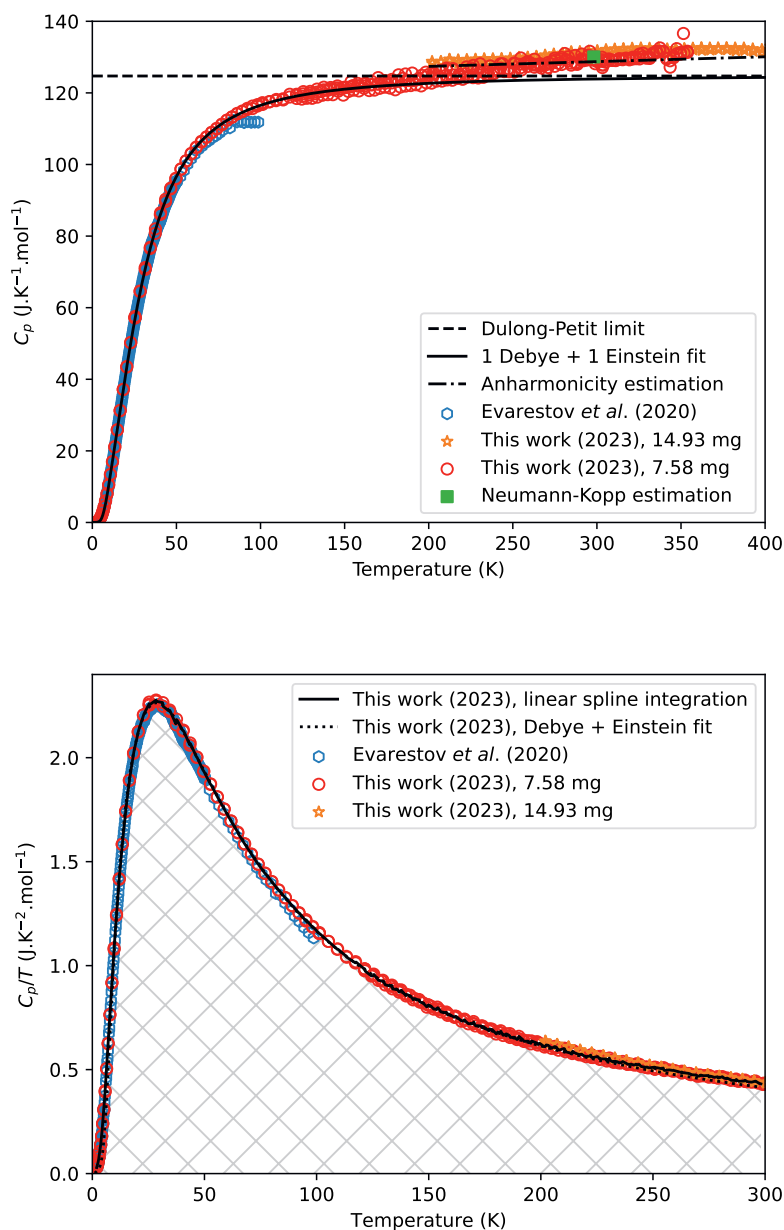


Figure 6.2: Experimentally measured heat capacity of  $\delta$ -CsPbI<sub>3</sub> as measured in this work and compared with the Dulong-Petit law, the Neumann-Kopp estimation at 298.15 K, the data of Evarestov *et al.* [69], a calculation estimating the anharmonicity and a fit of one Debye and one Einstein function as plotted in  $C_p$  vs.  $T$  (top) and  $C_p/T$  vs  $T$  (bottom). The marked area in the right figure corresponds to the entropy as determined using linear spline (see main text).

Harmonic lattice model			
	CsPbI <sub>3</sub>	Cs <sub>4</sub> PbI <sub>6</sub>	Cs <sub>3</sub> Bi <sub>2</sub> I <sub>9</sub>
temp. range (K)	2-8.5	2-9.5	2-14
$\gamma$ (mJ·K <sup>-2</sup> ·mol <sup>-1</sup> )	0	0	0
$B_3$ (mJ·K <sup>-2</sup> ·mol <sup>-1</sup> )	$6.59 \cdot 10^{-3}$	$2.09 \cdot 10^{-2}$	$8.87 \cdot 10^{-2}$
$B_5$ (mJ·K <sup>-4</sup> ·mol <sup>-1</sup> )	$3.21 \cdot 10^{-4}$	$3.96 \cdot 10^{-4}$	$-6.63 \cdot 10^{-4}$
$B_7$ (mJ·K <sup>-6</sup> ·mol <sup>-1</sup> )	$-5.51 \cdot 10^{-6}$	$-6.64 \cdot 10^{-6}$	$2.89 \cdot 10^{-6}$
$B_9$ (mJ·K <sup>-8</sup> ·mol <sup>-1</sup> )	$3.00 \cdot 10^{-8}$	$3.19 \cdot 10^{-8}$	$-5.26 \cdot 10^{-9}$
Debye and Einstein fit			
temp. range (K)	8.5-135	14-275	14-298
$n_D$ (mol)	3.583	9.39	6.75
$\Theta_D$ (K)	135.9	112.9	166.2
$n_E$ (mol)	1.423	1.55	6.71
$\Theta_E$ (K)	44.6	38.0	44.8
$n_D + n_E$ (mol)	5.006	10.94	13.46

Table 6.4: Fitting parameters. For explanation, see the main text.

3% uncertainty is used as a conservative error estimation.

The entropy and heat capacity at 298.15 K are calculated using linear spline interpolation in the measured region and extrapolation towards 0 K using the fitted Equation 2.5. The obtained values are  $S_m^o(298.15 \text{ K}) = (294.8 \pm 8.9) \text{ J} \cdot \text{K}^{-1} \cdot \text{mol}^{-1}$  and  $C_{p,m}(298.15 \text{ K}) = (128.6 \pm 3.9) \text{ J} \cdot \text{K}^{-1} \cdot \text{mol}^{-1}$  as listed in Table 6.9. The obtained entropy value is around the lower limit given by Tsvetkov *et al.* [65]; they estimate the entropy of CsPbI<sub>3</sub> to lie in between 297.90 and 347.90  $\text{J} \cdot \text{K}^{-1} \cdot \text{mol}^{-1}$ . The obtained heat capacity at 298.15 K is well in line with the Neumann-Kopp estimation.

For CsPbI<sub>3</sub>, several anharmonic features were reported in the recent literature. In 2020, Straus *et al.* reported single crystal X-ray diffraction and X-ray pair distribution function measurements on CsPbI<sub>3</sub> in the temperature range 100 to 295 K [92]. They found that the Cs atom occupies a single site from 100 to 150 K, above which thermal disorder results in two different Cs sites in the structure, one of which exhibits lower coordination by iodine anions. No phase transformation is associated with this. This implies that an anharmonic oscillator model would be more physically realistic above 150 K for CsPbI<sub>3</sub>. However, rattling effects occur usually at far lower temperatures, where they can be described with an Einstein type model (single atom frequency vibrations) in a host lattice. Also crystal-liquid duality or phonon glass-electron crystal (PGEC) phenomena, as discussed in relation to metal halide perovskites, seem to have no influence on the overall heat capacity [93]. These theories describe the phonon behaviour as a glass-like crystal, *i.e.* they are disordered, have no long range correlation and the atoms are not able to move well as compared to a liquid; this in contrast to a phonon liquid, which has a correlated movement of vibrational motion. Similar theories have been applied to CsPbBr<sub>3</sub> [94, 95]; the heat capacity of this compound also looks ‘classical’ [69]. Electron-phonon coupling is reported for CsPbI<sub>3</sub> and explained by the 6s<sup>2</sup>-lone pair effect of Pb<sup>2+</sup> by Huang *et al.* [96]. It is concluded that the reported anharmonic effects do not result in an anomaly in the heat capacity in the studied temperature range, though

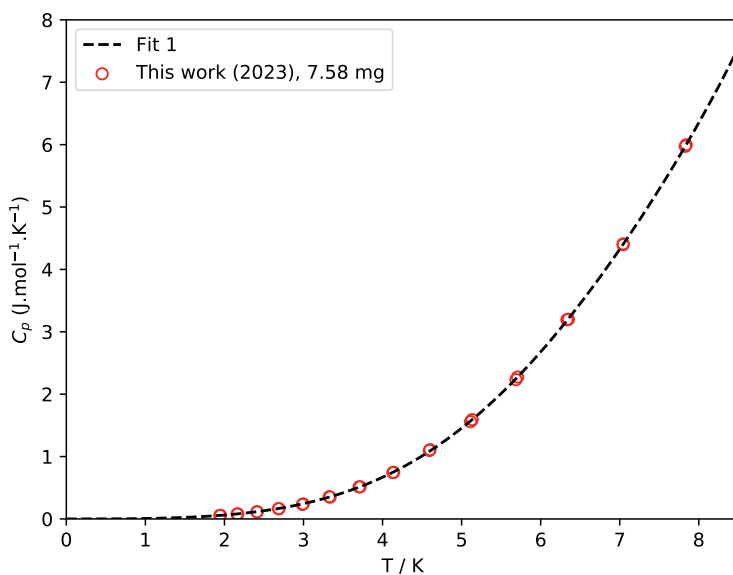
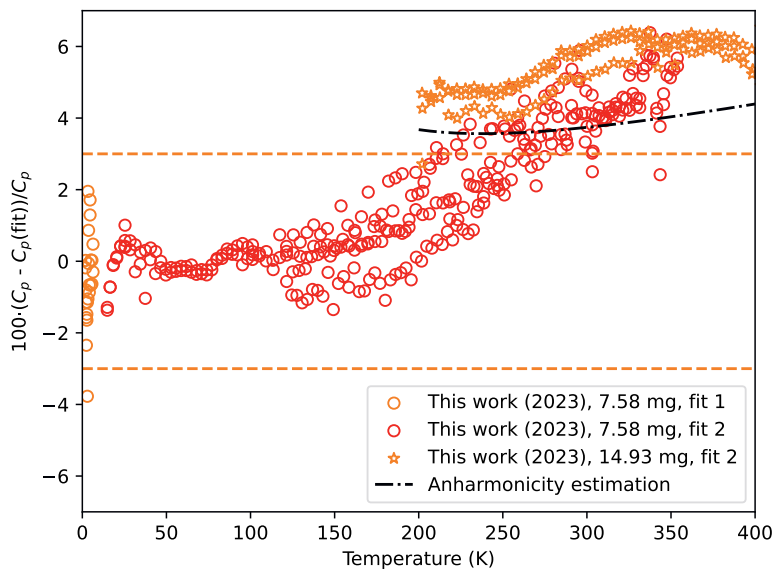


Figure 6.3: Top: Relative difference between experimentally measured heat capacity of  $\delta$ -CsPbI<sub>3</sub> as measured in this work and fitting functions. Fit 1 is a fit by a polynomial equation at low-temperature (Equation 2.5); Fit 2 is the fit of one Debye and one Einstein function. The dashed orange lines are a guide to the eye and are drawn at 3% deviation from the fit. Bottom: the low-temperature part fitted using Equation 2.5 (fit 1).

they do contribute to the increase of the heat capacity beyond the Dulong-Petit limit.

The magnetic susceptibility of CsPbI<sub>3</sub> is perfectly diamagnetic and low in absolute value. It did not show any anomaly in the temperature range studied supporting heat capacity measurement results (Figure B.1). Interestingly, we obtained a much smaller value of magnetization than reported by Qiao *et al.* [97], suggesting the presence of magnetic impurities in their compound.

#### 6.4.2. LOW-TEMPERATURE HEAT CAPACITY OF Cs<sub>4</sub>PbI<sub>6</sub>

The experimentally measured data are shown in Figure 6.4, together with the Dulong-Petit limit, the Neumann-Kopp estimation, and a fit of one Debye and one Einstein function. For Cs<sub>4</sub>PbI<sub>6</sub>, the Dulong-Petit limit is reached at a higher temperature (around 270 K) than for CsPbI<sub>3</sub>. The data obtained with the QD-PPMS and QD-Versalab instruments are close, though the heat capacity obtained with the QD-Versalab is a bit higher. The Neumann-Kopp estimation is close to the measured values and in between both results. Towards the low-temperature part, a polynomial fit was used. The difference between the measured data and the combined polynomial and Debye-Einstein fit is shown in Figure 6.5. The fitting parameters are listed in Table 6.4. There is no electronic contribution to the heat capacity.

The entropy and heat capacity at 298.15 K are calculated using linear interpolation in the measured region and extrapolation towards 0 K. The obtained values are  $S_m^\circ(298.15 \text{ K}) = (659.5 \pm 19.8) \text{ J} \cdot \text{K}^{-1} \cdot \text{mol}^{-1}$  and  $C_{p,m}(298.15 \text{ K}) = (272.9 \pm 8.2) \text{ J} \cdot \text{K}^{-1} \cdot \text{mol}^{-1}$  as listed in Table 6.9. The error was again calculated using a 3% uncertainty on the heat capacity. To the best of our knowledge, no other investigations into the low-temperature heat capacity of Cs<sub>4</sub>PbI<sub>6</sub> have ever been reported.

Here also, the heat capacity of Cs<sub>4</sub>PbI<sub>6</sub> is in line with a diamagnetic, low in value and quasi temperature independent magnetic susceptibility, showing no anomaly as shown in Figure B.2.

#### 6.4.3. LOW-TEMPERATURE HEAT CAPACITY OF Cs<sub>3</sub>Bi<sub>2</sub>I<sub>9</sub>

The experimentally measured heat capacity is shown in Figure 6.6, together with the Dulong-Petit limit, the Neumann-Kopp estimation at 298.15 K, the data of Tailor and Satapathi [61] using QD-PPMS, Acharyya *et al.* [42] (using QD-PPMS too) and a fit of 1 Debye and 1 Einstein function. Again, the heat capacity increases quickly, though it does not exceed the Dulong-Petit limit in the studied temperature window. For the lower temperature part (till 50 K), the current data agrees well with literature data. At higher temperatures, the data in this work obtained with the QD-PPMS and QD-Versalab agree fairly well. Both measurements gave a heat capacity that slightly exceeds the value obtained using the Neumann-Kopp estimation rule.

The fits to Equations 2.2 and 2.5 are shown in Figure 6.6 and 6.7; the difference between the fits and the measured data is shown in Figure 6.7. In this figure, the dashed lines indicate a 3% deviation; it can be seen that the error stays mostly within this margin. The fitting parameters are given in Table 6.4.

There is no electronic contribution to the heat capacity, as can easily be concluded from Figure 6.8. This is in contrast with Tailor and Satapathi [61], who published a Sommerfeld coefficient  $\gamma = 0.762 \text{ J} \cdot \text{K}^{-2} \cdot \text{mol}^{-1}$ . Clearly, this would be atypical for an insu-

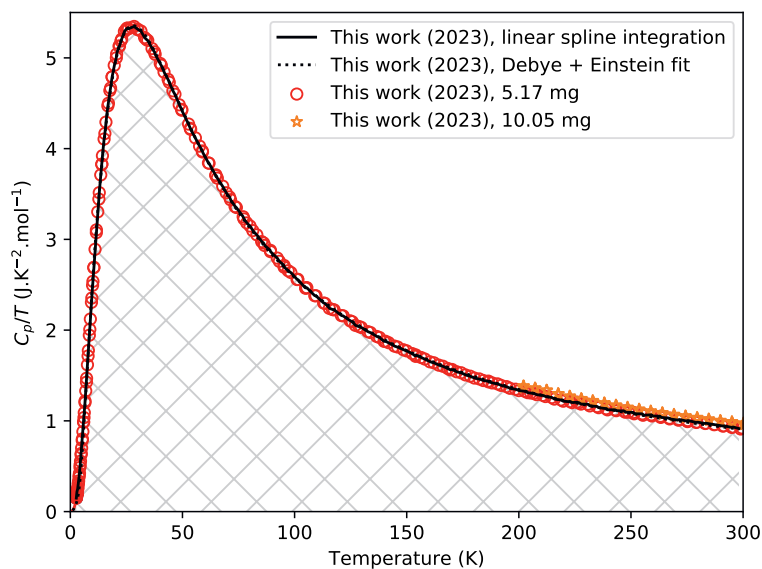
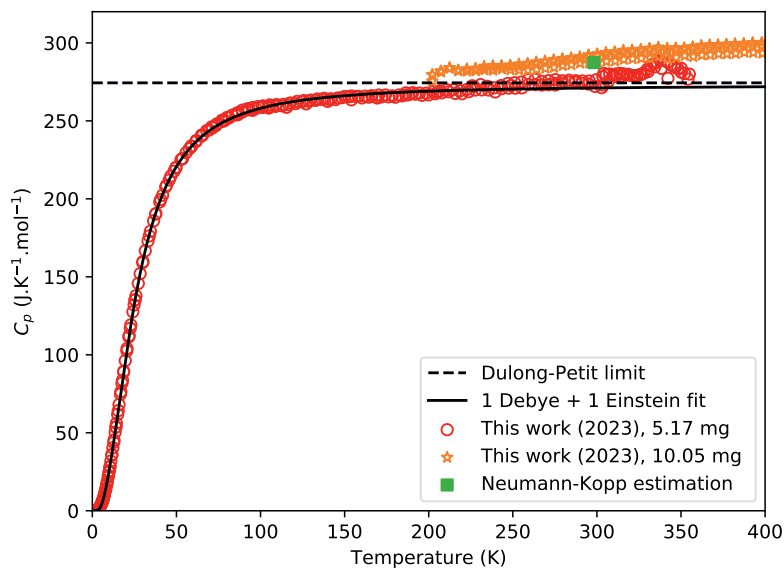
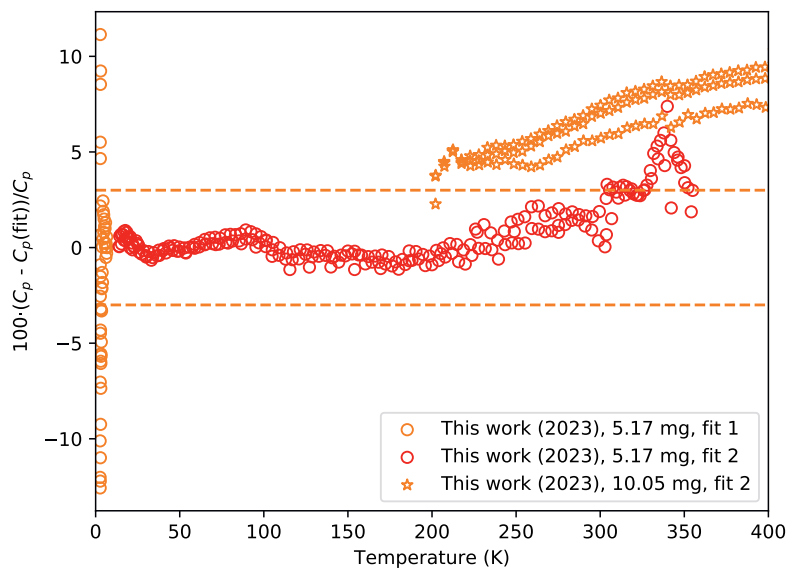


Figure 6.4: Experimentally measured heat capacity of  $\text{Cs}_4\text{PbI}_6$  as measured in this work and compared with the Dulong-Petit law, the Neumann-Kopp estimation at 298.15 K and a fit of one Debye and one Einstein function as plotted in  $C_p$  vs  $T$  (Top) and  $C_p/T$  vs  $T$  (Bottom). The marked area in the right figure corresponds to the entropy as determined using linear spline (see main text).



6

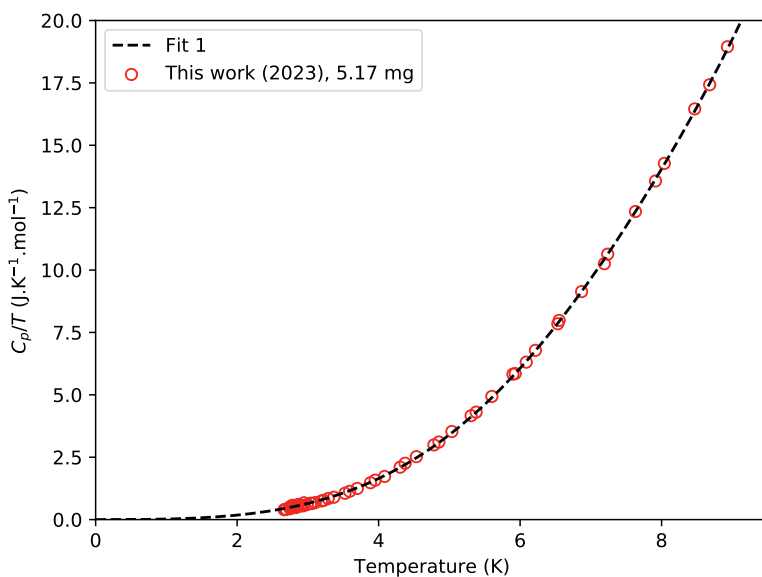


Figure 6.5: Top: Relative difference between experimentally measured heat capacity of  $\text{Cs}_4\text{PbI}_6$  as measured in this work and fitting functions. Fit 1 is a fit by a polynomial equation at low-temperature (Equation 2.5); Fit 2 is the fit of one Debye and one Einstein function. The dashed orange lines are a guide to the eye and are drawn at 3% deviation from the fit. Bottom: the low-temperature part, using Equation 2.5 (fit 1).

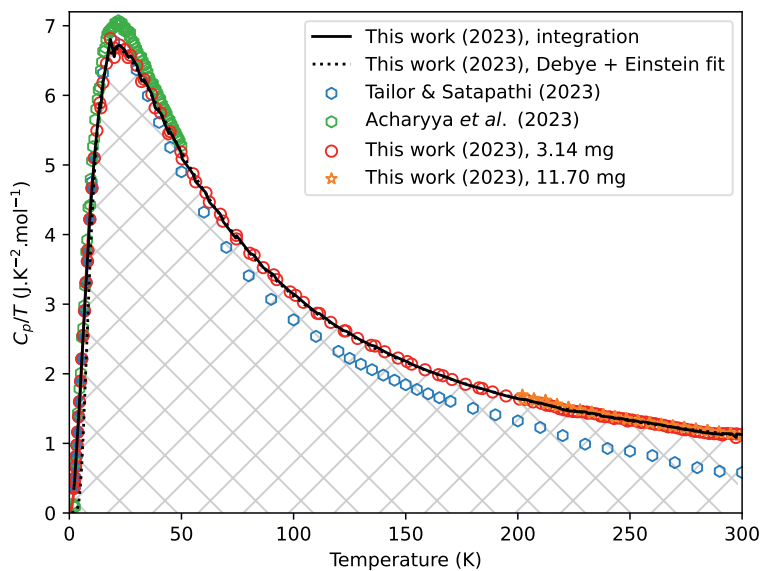
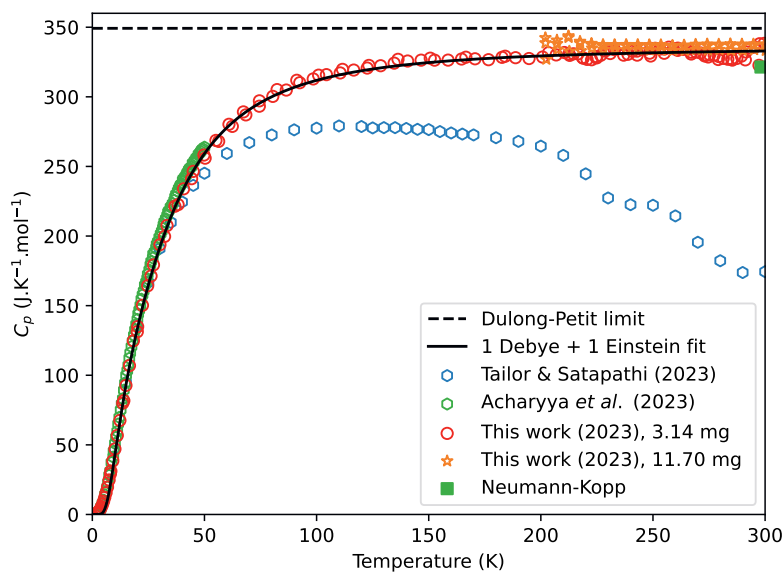
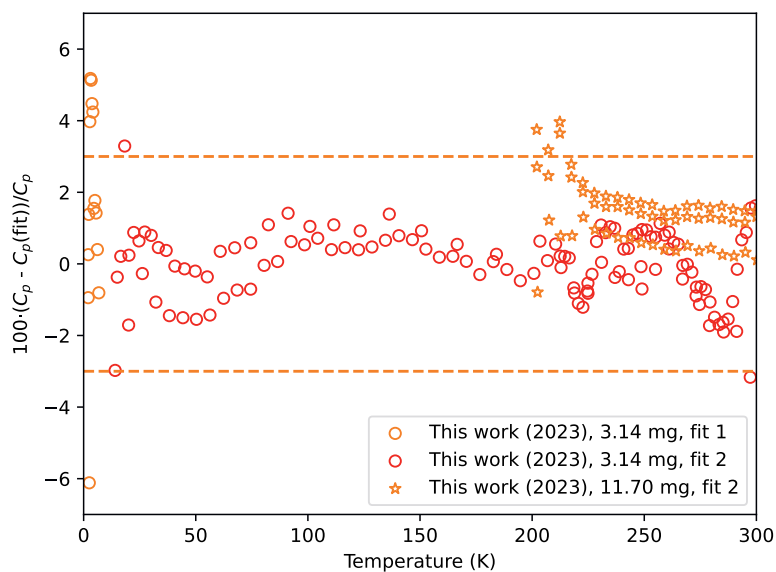


Figure 6.6: Experimentally measured heat capacity of  $\text{Cs}_3\text{Bi}_2\text{I}_9$  as measured in this work and compared with the data from Taylor and Satapathi [61], Acharyya *et al.* [42], the Dulong-Petit law, the Neumann-Kopp estimation at 298.15 K and a fit of one Debye and one Einstein function as plotted in  $C_p$  vs.  $T$  (Top) and  $C_p/T$  vs  $T$  (Bottom). The marked area in the right figure corresponds to the entropy as determined using linear spline (see main text).



6

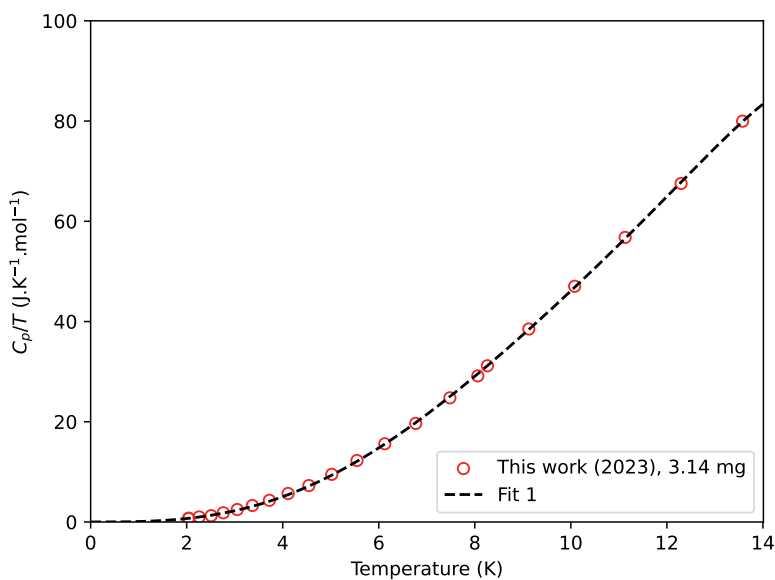


Figure 6.7: Top: relative difference between experimentally measured heat capacity of  $\text{Cs}_3\text{Bi}_2\text{I}_9$  as measured in this work and fitting functions. Fit 1 is a fit by a polynomial equation at low-temperature (Equation 2.5); Fit 2 is the fit of one Debye and one Einstein function. The dashed orange lines are a guide to the eye and are drawn at 3% deviation from the fit. Bottom: the low-temperature part, which shows a slight mismatch between the fitted and measured data.

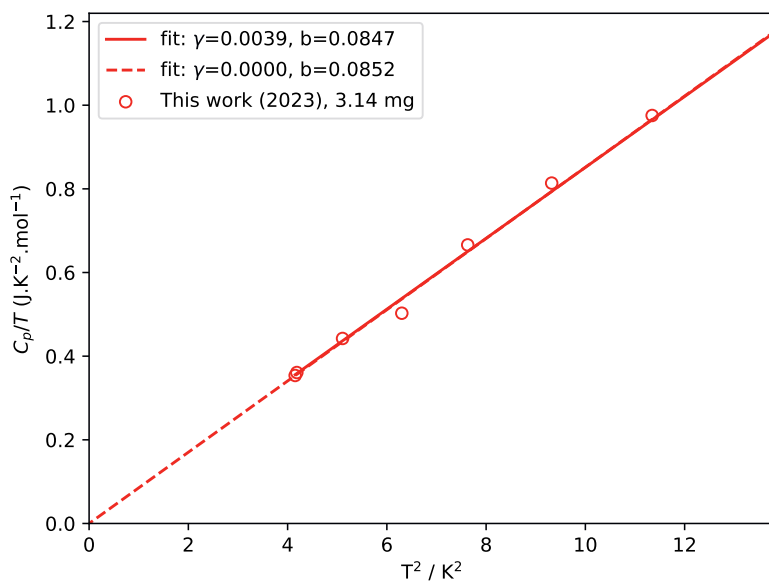


Figure 6.8:  $C_p/T$  vs  $T^2$  in the lower temperature limit for  $\text{Cs}_3\text{Bi}_2\text{I}_9$  as fitted to  $y = \gamma + b \cdot x$ , with an  $\gamma = 0$  constraint for the second fit. The  $\gamma$ -term in the equation is the Sommerfeld coefficient.

lating material. The Sommerfeld coefficient as published by Acharyya *et al.* [42] ( $0.22 \text{ J}\cdot\text{K}^{-2}\cdot\text{mol}^{-1}$ ) is also unexpectedly high. In the first study, this is due to the low number of data points below 10 K, thus missing the typical curvature at low temperature. In both studies, the mathematical fitting procedure involves a combination of Sommerfeld, Debye and Einstein equations, in which case the derived coefficients lose their physical meaning. This resulted in very high reported coefficients and improper comparison with other materials.

Before the results of Tailor and Satapathi [61] are further considered, a short overview of low-temperature studies is necessary for a thorough understanding of the physics of  $\text{Cs}_3\text{Bi}_2\text{I}_9$  at low temperature. Its structure at 298 K was first solved in 1968 [53]. The low-temperature properties of this compound were studied for the first time by Melnikova *et al.* in 1996 [56]. They studied the optical birefringence, the dielectric and elastic constants and performed differential scanning calorimetry (DSC), besides nuclear quadrupole resonance (NQR). They observed a phase transition at 223 K based on the temperature dependence of the birefringence and the elastic constant, but an associated heat anomaly was too small to be detected with their DSC-unit. They classify the phase transition as ferroelastic. Aleksandrov *et al.* [98] continued the studies with  $^{127}\text{I}$ -NQR and reported an incommensurate phase in  $\text{Cs}_3\text{Bi}_2\text{I}_9$ . They found that the second order normal phase-incommensurate phase transition occurs at 220 K and reported the associated symmetry change. Another report by Melnikova and Zaitsev [99] is a bit more elaborate and, besides reporting the same information, reports thermal expansion studies that lead to the conclusion that the phase transition is located at  $(220.0\pm 0.6)$  K. The next report is by Aleksandrova *et al.* [100]. They provide 224 K as the phase transition temperature, based on  $^{127}\text{I}$ -NQR measurements. In 1999, Arakcheeva *et al.* reported a first attempt to solve the low-temperature phase using X-ray diffraction studies. This study was followed by a neutron diffraction study of Jorio *et al.* [101]. It needed another report by Arakcheeva *et al.* before the low-temperature structure was finally elucidated [58]. It is stressed here that to solve the structure at room temperature down to the phase transition, anharmonic displacement parameters were necessary, while below the phase transition temperature, no anharmonic parameters were needed for a satisfying profile refinement. The anharmonic displacement parameters were especially useful in explaining residual electronic densities close to the Cs(1) and I(1) atoms. The authors hypothesise that the anharmonic displacements of these atoms, which are in highly symmetric positions, may be the driving force for symmetry breaking upon phase transition. Ivanov *et al.* further investigated  $\text{Cs}_3\text{Bi}_2\text{I}_9$  using  $^{133}\text{Cs}$ -NMR in 2001 [102]. In 2003, Girnyk *et al.* [103] studied  $\text{Cs}_3\text{Bi}_2\text{I}_9$  in several ways: dilatometry, ultrasonic velocity and domain structure, concluding to a first order type phase transition. Based on thermal expansion studies, they calculated a latent heat associated by the phase transition around 220 K of  $0.15 \text{ kJ}\cdot\text{mol}^{-1}$ . Moreover, they found a thermal hysteresis of 5 K and identified the region from 183 till 221 K at cooling as heterophase, *i.e.* where coexistence of the ferroelastic and paraelastic phases is claimed.

Between 2004 and 2010, a series of studies into the optical behaviour of the low-temperature phase of  $\text{Cs}_3\text{Bi}_2\text{I}_9$  were furthermore reported by Motsnyi *et al.* [104–108]. Electron-phonon coupling was studied [60], as well as exciton-phonon coupling [107, 109]. Exciton-phonon interaction [107] resulted in disappearance of the layered struc-

ture below the transition temperature. Phonon calculations using VASP were performed by Geng *et al.* [38]. Until recently, no report on the low-temperature heat capacity of  $\text{Cs}_3\text{Bi}_2\text{I}_9$  had been published, apart from statements on an undetectable anomaly or very small latent heat by Melnikova *et al.* [56]. The recent work by Tailor and Satapathi [61] is the first report of a heat capacity curve. The even more recent work of Acharyya *et al.* [42] measured the heat capacity only up to 50 K. The discrepancy with respect to our own results for the electronic contribution was already discussed *supra*. Below, the contradictions between our results and the results of Tailor and Satapathi [61] towards room temperature will be discussed.

Towards room temperature, the results are quite striking, as one can observe in Figure 6.6. The authors attributed this to crystalline-liquid duality in the material, but it is not clear to us how this could explain their results. Starting from low temperature, their results show a typical evolution for a heat capacity curve, in agreement with our data. However, a drastic deviation is observed starting above 50 K, ending via two steps at a value far below what is expected from classical limits. Their reference to disorder and anharmonicity would, in our view, result primarily in an increase in the heat capacity above the classical limit instead of a decrease. Given the literature on a phase transition around 220 K, a heat effect might be expected. However, no detectable heat effect was found, neither by Melnikova *et al.* [56] nor in our work. Moreover, this could only explain a single anomaly in the heat capacity, and not the shape of the heat capacity as reported by Tailor and Satapathi, which flattens already below 220 K and drops via two steps. Their attempt to explain their results refers to research into thermal conductivity.  $\text{Cs}_3\text{Bi}_2\text{I}_9$  is known to have a very low thermal conductivity ( $0.15 \text{ W}\cdot\text{m}^{-1}\cdot\text{K}^{-1}$  as measured on thin films) [38] and cautiousness is necessary in measuring the heat capacity of insulating materials [110]. When performing QD-PPMS measurements by the thermal-relaxation technique, caution should be taken with regards to the sample mass. For materials with a very low thermal conductivity, lower mass results in more accurate measurements, while sample mass can affect the results already above quantities as small as 15 mg [91]. No mass of the crystal is given in the work of Tailor and Satapathi [61], but based on the picture in their Supporting Information, the sample is estimated to be between 7 and 30 mg, so it is not clear to us whether the mass might play a role.

On top of the difference between the results on  $\text{Cs}_3\text{Bi}_2\text{I}_9$ , it was also noted that the heat capacity for  $\text{Cs}_3\text{Bi}_2\text{Br}_9$ , which also decreases unexpectedly in the report by Tailor and Satapathi, is not in line with previous measurements reported in literature. Aleksandrova *et al.* [111] measured the low-temperature heat capacity of  $\text{Cs}_3\text{Bi}_2\text{Br}_9$  and found a result in line with physical theory. To our surprise, Tailor and Satapathi even cite this paper, but do not discuss the difference between their results and those of Aleksandrova *et al.* For all these reasons, we trust the results of Tailor and Satapathi on  $\text{Cs}_3\text{Bi}_2\text{I}_9$  only in the temperature window from 5 to 50 K and we have more confidence in the present results above that temperature.

As for the slight difference with the data as measured by Acharyya *et al.* [42]: their data have been extracted from a figure, thus introducing some error. In general, all data reported in literature and measured in this work agree below 50 K, though the interpretation may differ (see discussion Sommerfeld coefficient above). Finally, the heat capacity of  $\text{Cs}_3\text{Bi}_2\text{I}_9$  does not show any anomaly, which is in line with its magnetic susceptibility

from 2 to 300 K (Figure B.3).

Based on the current results, the entropy and heat capacity at 298.15 K are calculated using linear interpolation in the measured region and extrapolation towards 0 K. Using again an absolute error of 3% on the heat capacity, the obtained thermodynamic values are  $S_m^\circ(298.15 \text{ K}) = (819.2 \pm 24.6) \text{ J} \cdot \text{K}^{-1} \cdot \text{mol}^{-1}$  and  $C_{p,m}(298.15 \text{ K}) = (338.2 \pm 10.1) \text{ J} \cdot \text{K}^{-1} \cdot \text{mol}^{-1}$ . These values are also listed in Table 6.9.

## 6.5. PHASE TRANSITION DETERMINATIONS OF THE END MEMBERS AND COMPOUNDS

The DSC results of the purchased compounds CsI, PbI<sub>2</sub> and BiI<sub>3</sub> were compared to literature values. The measured melting points for CsI (904±5) K, PbI<sub>2</sub> (687±5) K and BiI<sub>3</sub> (665±5) K are compared with literature values in Table 6.5. The melting point for CsI was found to agree very well, while those for PbI<sub>2</sub> and BiI<sub>3</sub> are respectively a bit higher and lower than found in literature. The compounds CsI and BiI<sub>3</sub> do not have polymorphs. PbI<sub>2</sub> has a CdI<sub>2</sub>-like structure and exhibits polytypism. However, polytype 2H is by far the most abundant and the polytypic transition does not come with a large enthalpy change [79]. Therefore, the polytypism of PbI<sub>2</sub> is further neglected in this work. The phase transition and melting point of CsPbI<sub>3</sub> were found to agree well with literature. For the peritectically decomposing compound Cs<sub>4</sub>PbI<sub>6</sub>, the heat effect on the first cycle of the synthesised compound was taken and found to be some 20 K higher than the values reported in literature [43, 44]. The melting temperature of freshly synthesised Cs<sub>3</sub>Bi<sub>2</sub>I<sub>9</sub> on the first DSC cycle was found to be (870±5) K, which drops by approximately 10 degrees upon subsequent cycles with a small pre-peak appearing. This might be attributed to the homogeneity range as described by Kun *et al.* [46]; in this work, the temperature on the first heating ramp was taken as the melting point of Cs<sub>3</sub>Bi<sub>2</sub>I<sub>9</sub>. Values as determined in this work and in the literature for all six compounds are collected in Table 6.5, alongside known melting enthalpies (*e.g.* CsI, PbI<sub>2</sub> and BiI<sub>3</sub>). There is, to the best of our knowledge, no experimental data available on the melting enthalpy of intermediates CsPbI<sub>3</sub> and Cs<sub>4</sub>PbI<sub>6</sub>. There is, however, data on the melting enthalpy of Cs<sub>3</sub>Bi<sub>2</sub>I<sub>9</sub>, reported by Kun *et al.* [46].

## 6.6. BINARY PHASE DIAGRAMS: CALORIMETRIC MEASUREMENTS AND MODELLING

Phase transition equilibria were determined in the binary systems using DSC on mixtures of the end-members mixed in stoichiometric ratios, as detailed at the end of this chapter. Thermodynamic models were then developed for each system based on the measured experimental and literature data. The quasi-chemical formalism in the quadruplet approximation was used for the liquid solution, while the solid solutions were modelled as detailed in Appendix C.

Species	T / K	Transition type	$\Delta_{tr}H_m^o(T_{tr}) /$ kJ·mol <sup>-1</sup>	Reference
CsI	904±5	Congr. melting	-	This work, exp.
	905		25.7	This work, mod.
	914		-	[43]
	903.8±0.2		24.0±0.2	[112]
	905±2		25.65±0.4	[113]
PbI <sub>2</sub>	902.4±5	Polytypism	-	[77]
	580		0.339	[79]
	687±5		-	This work, exp.
	682.9		23.5	This work, mod.
	677		-	[43]
BiI <sub>3</sub>	679	Congr. melting	23.344	[79]
	665±5		-	This work, exp.
	681.8		39.1	This work, mod.
CsPbI <sub>3</sub>	681.7	Polymorphism	39.1±0.3	[82]
	599±5		-	This work, exp.
	594		14.2	This work, mod.
	600		-	[43]
	594.8-599		14.2±0.5	[67]
	595		-	[89]
	593		14.1±0.24	[63]
	758±5		Congr. melting	-
757	26.78	This work, mod.		
Cs <sub>4</sub> PbI <sub>6</sub>	754	Peritectic	-	[44]
	753		71.31	This work, mod.
	737		-	[44]
	741		-	[43]
	757		-	[89]
Cs <sub>3</sub> Bi <sub>2</sub> I <sub>9</sub>	754±5	Congr. melting	-	This work, exp.
	870±5		-	This work, exp.
	872		177	This work, mod.
	907		-	[47]
	905±5		148±2.2	[46]

Table 6.5: Phase transition temperatures and melting enthalpies of the compounds as measured in this research compared to literature. The values referred to as "This work" are the experimentally determined (exp.) values and the values used in the modelling (mod.).

### 6.6.1. THE BINARY SYSTEM CSI-BII<sub>3</sub>

The experimentally measured thermal transitions in the CsI-BiI<sub>3</sub> system with their interpretation are given in Table B.2. As shown in Figure 6.9, the DSC results can be interpreted in line with the previously reported phase diagrams of Plyushev *et al.* and Kun *et al.* [46, 47]. This interpretation is further underpinned by post-DSC analysis (see Ta-

ble B.1), in which only binary mixtures of Cs<sub>3</sub>Bi<sub>2</sub>I<sub>9</sub> with one of the end-members CsI or BiI<sub>3</sub> were found. However, for the measurements at  $0.1 \leq x(\text{BiI}_3) \leq 0.4$ , extra thermal arrests were also detected around 724 K. A series of quenching and synthesis experiments with phase analysis (see Table B.1) did not show the presence of any other compound besides Cs<sub>3</sub>Bi<sub>2</sub>I<sub>9</sub> and CsI. The trend in composition versus heat (see Figure B.7) indicates the effect cannot be ascribed to polymorphism in Cs<sub>3</sub>Bi<sub>2</sub>I<sub>9</sub> nor to a compound at  $x(\text{BiI}_3) = 0.25$ , a composition which is known for other cesium bismuth halide phases. A high temperature polymorph was not found upon a quenching experiment (see Table B.1). A further possible explanation would be the existence of a high-temperature phase at  $x(\text{BiI}_3) = 0.2$ , corresponding to the maximum in the heat release of the DSC curves in the composition range, but quenching experiments did not reveal the existence of such a phase either (see Table B.1). In absence of additional evidence on the existence of such a high-temperature phase, this thermal effect was not accounted for in the model.

The calculated phase diagram of the CsI-BiI<sub>3</sub> system is shown in Figure 6.9. The calculated invariant equilibria are listed in Table 6.6. The CALPHAD model agrees well with the data measured in this work. The mixing enthalpy of this system is shown in Figure B.6 at  $T = 1000$  K. The CsI-BiI<sub>3</sub> system is characterised by two eutectic points, formed between Cs<sub>3</sub>Bi<sub>2</sub>I<sub>9</sub> and respectively CsI and BiI<sub>3</sub>. The eutectic composition between Cs<sub>3</sub>Bi<sub>2</sub>I<sub>9</sub> and CsI is well-defined. In the current work, the composition was found to be  $x(\text{BiI}_3) = 0.22 \pm 0.005$ , matching with [46, 47]. The eutectic composition reported by [48] differs, but their figure is judged to be unreliable on the composition axis. The eutectic temperature corresponding to this event varies between  $T = (784 \pm 10)$  K (this work) and  $T = 795$  K ([48]). The eutectic composition between Cs<sub>3</sub>Bi<sub>2</sub>I<sub>9</sub> and BiI<sub>3</sub> is ill-defined, varying between  $x(\text{BiI}_3) = 0.70$  ([47]) and  $x(\text{BiI}_3) = 0.86$  ([46]). Our experimental ( $x(\text{BiI}_3) = 0.77$ ) as well as optimised ( $x(\text{BiI}_3) = 0.80$ ) values are intermediate in the range of reported values. The temperature of the eutectic as reported in literature is slightly higher than modelled and measured in this work. The measured congruent melting temperature of the intermediate Cs<sub>3</sub>Bi<sub>2</sub>I<sub>9</sub> is not entirely in agreement with the data from the aforementioned literature. There is, however, good agreement between the model and the available experimental data for compositions  $x(\text{BiI}_3) \leq 0.8$ . The homogeneity range of Cs<sub>3</sub>Bi<sub>2</sub>I<sub>9</sub> as measured by Kun *et al.* [46] has been included in the model. The model fits well with the available experimental data at temperatures of  $T = 630$  K and above; the homogeneity range is not quite as wide at lower temperatures, as measured by Kun *et al.* at 600 K and 570 K. The value of the melting enthalpy of the non-stoichiometric compound Cs<sub>3</sub>Bi<sub>2</sub>I<sub>9</sub> as predicted using the CALPHAD model presented in this work is slightly higher. The congruent melting point of this compound, however, is predicted to be at  $x(\text{BiI}_3) = 0.39$ , rather than  $x(\text{BiI}_3) = 0.40$  like its stoichiometry suggests at face value. Further investigation into the exact temperature and composition of this congruent melting point is necessary to assess the accuracy of the predicted melting enthalpy. Overall, the current model captures the system well within the sometimes rather wide spread of experimental results.

### 6.6.2. THE BINARY SYSTEM CsI-PbI<sub>2</sub>

The experimentally measured thermal transitions with their interpretation are given in Table B.4. The current results agree well with the liquidus line of Ilyasov *et al.* [44] and

Reaction	Type	$x(\text{BiI}_3)$	T / K	Reference
$\text{Cs}_3\text{Bi}_2\text{I}_9 + \text{CsI} = \text{L}$	Eutectic	0.22	784	This work, exp.
		0.21	790	This work, mod.
		0.22	814	[47]
		0.30	795	[48]
		0.22	790	[46]
$\text{Cs}_3\text{Bi}_2\text{I}_9 = \text{L}$	Congr. Melting	0.40	870	This work, exp
		0.39	872	This work, mod.
		0.40	907	[47]
		0.40	905	[46]
$\text{Cs}_3\text{Bi}_2\text{I}_9 + \text{BiI}_3 = \text{L}$	Eutectic	0.77	636	This work, exp
		0.80	640	This work, mod.
		0.86	638	[47]
		0.75	637	[48]
		0.70	625	[46]

Table 6.6: Invariant points on the CsI-BiI<sub>3</sub> phase diagram. The uncertainties on the experimental results of this work on composition are estimated to be  $\pm 0.005$ ; the uncertainties on temperature for mixtures are estimated to be  $\pm 10$  K.

the phase diagram of Belyaev *et al.* [43]. The peritectic decomposition temperature of Cs<sub>4</sub>PbI<sub>6</sub> varies a bit. The mixing enthalpy of this system is shown in Figure B.6 at T = 1000 K. Post-DSC XRD studies at  $x(\text{PbI}_2) = 0.20$  indicated the presence of three compounds, *viz.* Cs<sub>4</sub>PbI<sub>6</sub>, CsPbI<sub>3</sub> and CsI. Based on the presence of only these three compounds, we can conclude that the compounds on the Cs-rich and Cs-poorer side are respectively CsI and CsPbI<sub>3</sub>. Moreover, the difficulty in obtaining a pure Cs<sub>4</sub>PbI<sub>6</sub> single crystal is consistent with the presence of a peritectic decomposition near a eutectic equilibrium. The XRD pattern of the sample with a mixture at  $x(\text{PbI}_2) = 0.50$  showed the presence of just one compound:  $\delta$ -CsPbI<sub>3</sub>. The XRD pattern of the sample with a mixture at  $x(\text{PbI}_2) = 0.70$  was analysed using HighScore [114] analysis; only CsPbI<sub>3</sub> and PbI<sub>2</sub> were found. From these crystallographic analyses the number of compounds in the pseudo-binary phase diagram CsI-PbI<sub>2</sub> was found to be limited to two: Cs<sub>4</sub>PbI<sub>6</sub> and CsPbI<sub>3</sub>. The post-DSC XRD studies are summarised in Table B.1.

The calculated phase diagram of this system is presented in Figure 6.10. The calculated invariant equilibria are listed in Table 6.7, along with the corresponding experimental data. Calculations performed with the CALPHAD model displayed in Figure 6.10 show good agreement with the measured invariant points obtained in this work. The overall agreement with the data reported in the literature is also good, though there is a slight discrepancy between the calculated liquidus at  $x(\text{PbI}_2) = 0.5$  and 0.79 and the experimental data by Ilyasov *et al.* [44] and Belyaev *et al.* [43].

### 6.6.3. THE BINARY SYSTEM BiI<sub>3</sub>-PbI<sub>2</sub>

The experimentally measured temperatures with their interpretation are given in Table B.3. Upon first inspection, several of the peaks were quite broad. This could indicate solidus and liquidus equilibria overlapping upon measurement. Thus, the data were

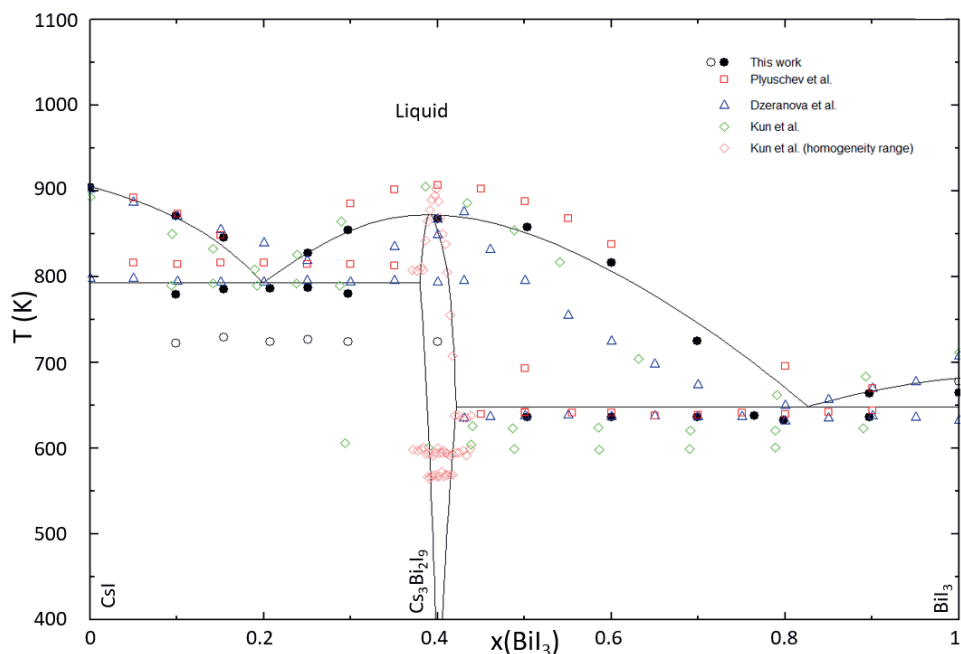


Figure 6.9: Phase diagram of the  $\text{CsI-BiI}_3$  binary system as calculated with the thermodynamic model presented in Table C.2. The experimental data shown on the phase diagram are from Plyushev *et al.* [47] (green squares), Dzeranova *et al.* [48] (blue triangles) and Kun *et al.* [46] (red and orange squares) and this work (black circles).

interpreted by taking the onset temperature of every peak on heating as the *solidus* line and the maximum as the *liquidus* line. In this way, the trend of the measured points indicates the formation of a complete solid solution over the whole composition range. Given the similarities in the crystal structures of  $\text{PbI}_2$  and  $\text{BiI}_3$ , a structure where the positions of  $\text{Pb}^{2+}$  are occupied by  $\text{Bi}^{3+}$  and holes can be hypothesised, as was done by Dmitriev *et al.* [72] and Alexander *et al.* [18, 19]. Alexander [19] also reports the only DSC measurement on a mixture in this system that is known to us; that single point is in line with the current results. The mixing enthalpy of this system is shown in Figure B.6 at  $T = 1000$  K. The post-DSC XRD studies of the  $\text{BiI}_3\text{-PbI}_2$  axis, as summarised in Table B.1, indicated the presence of crystalline material, the structure of which we could not resolve. The X-ray diffraction patterns are shown in Figure B.5. Recently, Alexander *et al.* [18, 19] reported an XRD pattern of a sample at  $x(\text{PbI}_2) = 0.50$  and ascribe the results to a layered structure that is disordered. TEM analysis indicated Pb-rich and Bi-rich “bricks” at the nano-scale.

The calculated phase diagram of this system is presented in Figure 6.11. It shows good agreement between the measured data and the thermodynamic model. The entire composition range between  $\text{PbI}_2$  and  $\text{BiI}_3$  consists of a solid solution with composition  $\text{Pb}_{1-x}\text{Bi}_x\text{I}_{2+x}$ . The only available literature data point of Alexander [19] fits with the current experimentally measured and modelled results. The *solidus* and *liquidus* lines cross

Reaction	Type	$x(\text{PbI}_2)$	T / K	Reference
$\text{Cs}_4\text{PbI}_6 = \text{CsI} + \text{L}$	Peritectic	0.20	754	This work, exp.
		0.20	753	This work, mod.
		0.20	737	[44]
		0.20	741	[43]
$\text{Cs}_4\text{PbI}_6 + \text{CsPbI}_3 = \text{L}$	Eutectic	0.38	718	This work, exp.
		0.36	722	This work, mod.
		0.39	707	[44]
		0.40	705	[43]
$\delta\text{-CsPbI}_3 = \alpha\text{-CsPbI}_3$	Polymorphism	0.50	599	This work, exp.
		0.50	594	This work, mod.
		0.50	600	[43]
		0.50	595	[67]
		0.50	595	[89]
$\alpha\text{-CsPbI}_3 = \text{L}$	Congr. Melting	0.50	593	[63]
		0.50	758	This work, exp.
		0.50	757	This work, mod.
		0.50	754	[44]
		0.50	749	[43]
$\text{PbI}_2 + \text{CsPbI}_3 = \text{L}$	Eutectic	0.50	757	[89]
		0.80	618	This work, exp.
		0.79	623	This work, mod.
		0.80	614	[44]
		0.80	615	[43]

Table 6.7: Invariant points on the pseudo-binary section CsI-PbI<sub>2</sub>. The uncertainties on the experimental results of this work on composition are estimated to be  $\pm 0.005$ ; the uncertainties on temperature for mixtures are estimated to be  $\pm 10$  K.

at  $x(\text{PbI}_2) = 0.41$  at  $T = 634$  K. The atomic scale structure of BiI<sub>3</sub>-PbI<sub>2</sub> mixtures, which we consider here to be a solid solution, deserves a dedicated analysis. Both structures are layered, so the solid solution will be a mixture of Pb, Bi and vacancies. The question is whether this mixing is completely random, or if there is a strong preference of the vacancies and Bi to be together.

## 6.7. TERNARY PHASE DIAGRAM STUDIES: MODELLING AND EXPERIMENTS

The ternary phase diagram CsI-PbI<sub>2</sub>-BiI<sub>3</sub> was calculated using only the binary interaction parameters as described *supra*. The liquidus projection of the ternary phase diagram is shown in Figure 6.12. An isotherm at  $T = 300$  K is given in Figure 6.13, showing the stable phases at room temperature. The ternary eutectic points and the phase equilibria in the pseudo-binary section Cs<sub>3</sub>Bi<sub>2</sub>I<sub>9</sub>-CsPbI<sub>3</sub> are discussed *infra*. Moreover, some miscellaneous points are described.

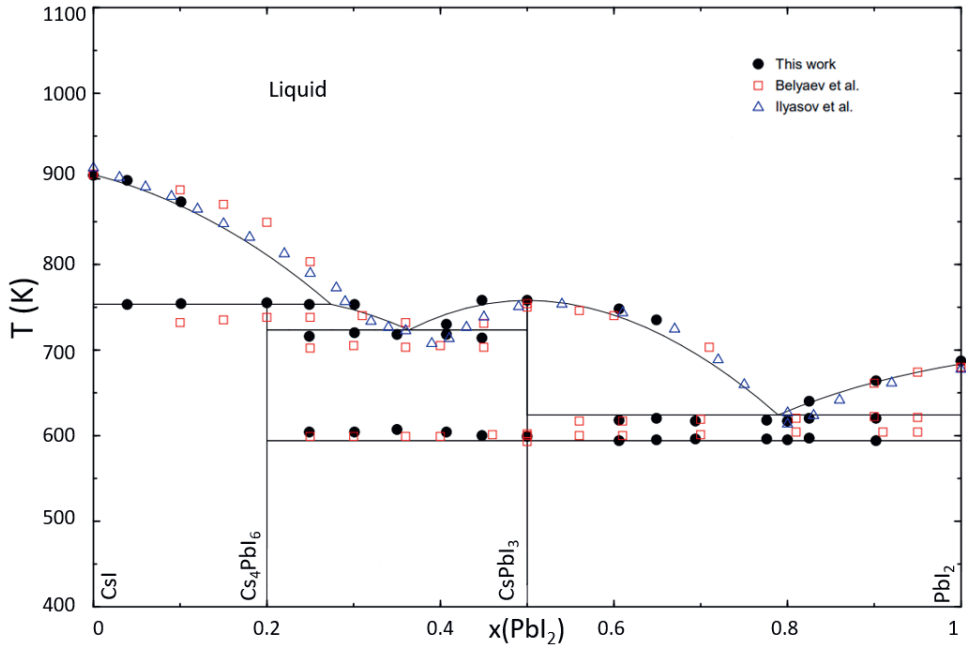


Figure 6.10: Phase diagram of the CsI–PbI<sub>2</sub> binary system as calculated with the thermodynamic model presented in the main text. The experimental data shown on the phase diagram are from Ilyasov *et al.* [44] (blue squares), Belyaev *et al.* [43] (red squares) and this work (black circles).

6

### 6.7.1. TERNARY EUTECTIC EQUILIBRIA

The calculated ternary phase field reveals three ternary eutectic points. The calculated compositions are given alongside the experimentally measured phase transition temperatures in Table 6.8. As can be concluded from the table, the eutectic temperatures are accurately reproduced by the model. It is observed that the ternary eutectic points are all located close to the CsI-PbI<sub>2</sub> side.

$x(\text{CsI})$	$x(\text{PbI}_2)$	$x(\text{BiI}_3)$	$T_c / \text{K}$	$T_e / \text{K}$	Equilibrium	Equilibrium reaction
0.72	0.21	0.07	739	729	Eutectic	$\text{CsI} + \text{Cs}_3\text{Bi}_2\text{I}_9 + \text{Cs}_4\text{PbI}_6 = \text{L}$
0.63	0.33	0.04	715	707	Eutectic	$\text{Cs}_3\text{Bi}_2\text{I}_9 + \text{Cs}_4\text{PbI}_6 + \text{CsPbI}_3 = \text{L}$
0.22	0.76	0.02	621	617	Eutectic	$\text{Cs}_3\text{Bi}_2\text{I}_9 + \text{CsPbI}_3 + \text{Pb}_{1-x}\text{Bi}_x\text{I}_{2+x} = \text{L}$

Table 6.8: Calculated ternary eutectic compositions with the phase transitions experimentally found at those compositions.  $T_c$  = calculated temperature;  $T_e$  = experimentally measured temperature. The uncertainties on the measured temperatures are estimated to be  $\pm 10$  K.

### 6.7.2. THE PSEUDO-BINARY SECTION Cs<sub>3</sub>Bi<sub>2</sub>I<sub>9</sub>-CsPbI<sub>3</sub>

The measured phase transition temperatures as obtained by DSC are given, together with their interpretation, in Table B.5 and drawn on top of the modelled phase diagram in Figure 6.14. The experimentally measured liquidus curve and eutectic events

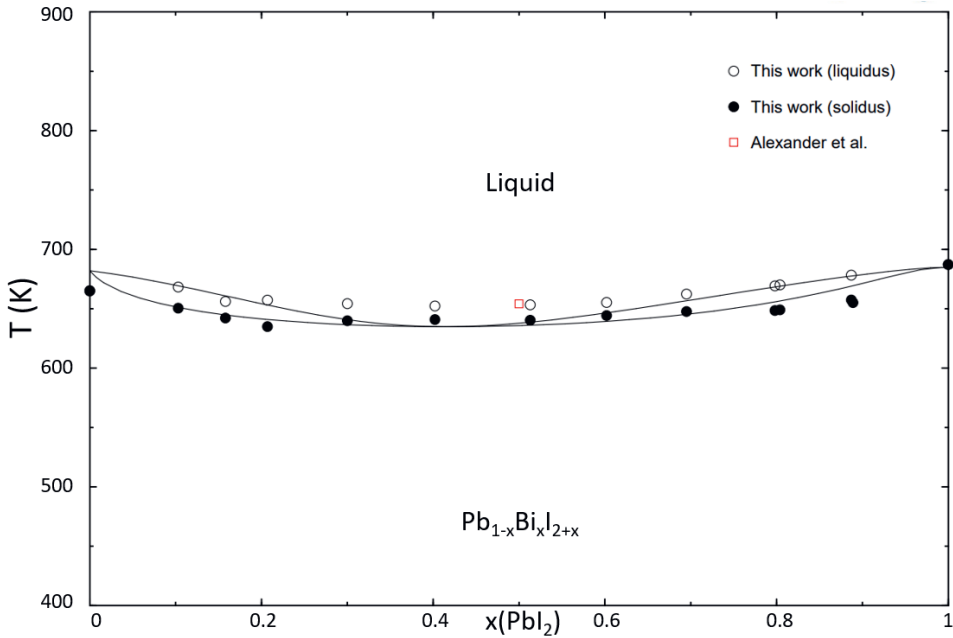


Figure 6.11: Phase diagram of the BiI<sub>3</sub>-PbI<sub>2</sub> binary system as calculated with the thermodynamic model presented in Table C.2. The peak onset temperature was used to determine the solidus data (black solid circles) and the temperature at the peak maximum was used to determine the liquidus data (black open circles).

agree well with the points predicted by the thermodynamic model. The experimental data point at  $x(\text{CsPbI}_3) = 0.7$  and  $T = 680$  K was possibly a measurement error, as it seems to be an outlier compared to similar compositions. The eutectic point on this pseudo-binary section is at  $x(\text{CsPbI}_3) = 0.91$  and  $T = 740$  K. No indication for the existence of quaternary compounds was found.

### 6.7.3. THE TERNARY SYSTEM: MISCELLANEOUS POINTS

Based on the reports by Hu *et al.* [22], a sharp decrease of the transition temperature  $\delta$ -CsPbI<sub>3</sub>→ $\alpha$ -CsPbI<sub>3</sub> was expected when small amounts of BiI<sub>3</sub> were added. However, three attempts on this axis with compositions  $x(\text{CsPbI}_3) = 0.96$  and  $x = 0.98$  did not result in a sharp drop of the temperature. The found temperature values for the  $\delta$ -CsPbI<sub>3</sub>→ $\alpha$ -CsPbI<sub>3</sub> transition are respectively 586 and 589 K, which is just a few degrees below the reported values for the phase transitions as given in Table 6.5, but definitely not stabilising the perovskite phase down to room temperature. The obtained results are consistent with the conclusion of Zhang *et al.* [74, 75] who found computationally that stabilisation of the perovskite phase cannot be ascribed to the physical properties of Bi<sup>3+</sup>. However, the current results also do not support the de-stabilising effect, as suggested in ref. [74]. For thin films, it was also found that  $\alpha$ -CsPbI<sub>3</sub> is not stabilised by the incorporation of Bi-ions [76].

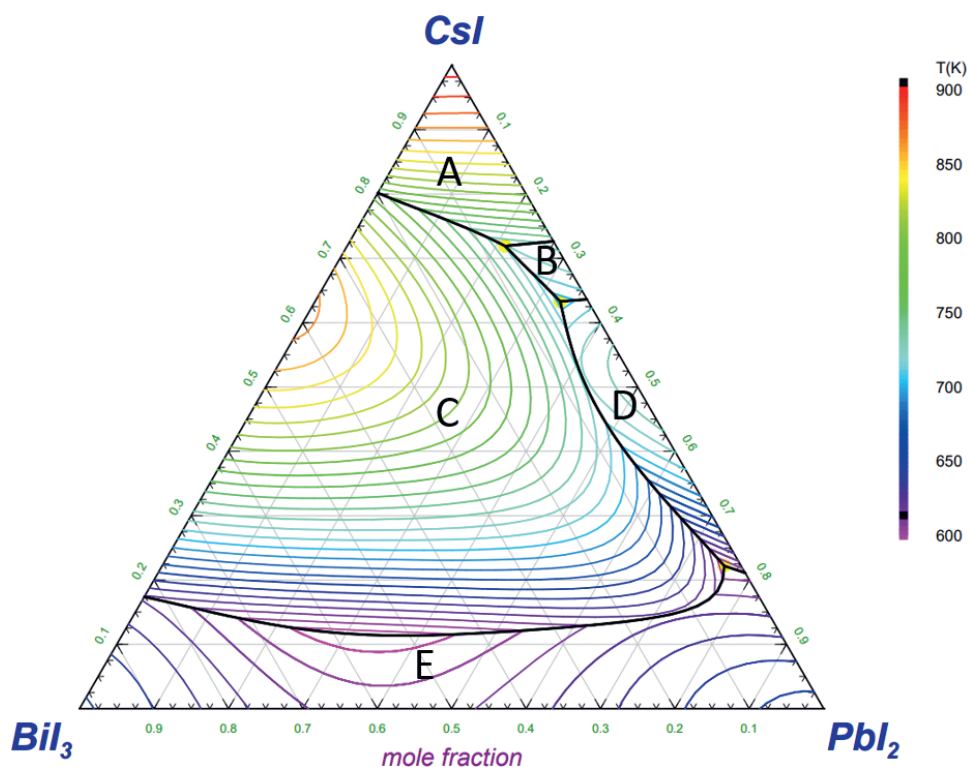


Figure 6.12: Liquidus surface of the  $\text{CsI-PbI}_2\text{-BiI}_3$  ternary system as calculated with the thermodynamic model presented in Table C.2. The precipitate target phases labelled A-E are as follows:  $\text{CsI}$  (A),  $\text{Cs}_4\text{PbI}_6$  (B),  $\text{Cs}_3\text{Bi}_2\text{I}_9$  (C),  $\text{CsPbI}_3$  (D) and  $\text{Pb}_{1-x}\text{Bi}_x\text{I}_{2+x}$  (E).

Other compositions in the ternary field that have been investigated with DSC are reported in Table 6.10, along with the temperatures calculated with the CALPHAD model. The measured points show a slight deviation from the calculated values, but are close enough that further optimisation of the ternary field was deemed unnecessary.

Compound	$C_{p,m}(298.15\text{ K})$ ( $\text{J}\cdot\text{K}^{-1}\cdot\text{mol}^{-1}$ )	$S_m^o(298.15\text{ K})$ ( $\text{J}\cdot\text{K}^{-1}\cdot\text{mol}^{-1}$ )	
		Experimental work	CALPHAD model
$\delta\text{-CsPbI}_3$	$128.6\pm 3.9$	$294.8\pm 8.9$	294.8
$\text{Cs}_4\text{PbI}_6$	$272.9\pm 8.2$	$659.5\pm 19.8$	658.3
$\text{Cs}_3\text{Bi}_2\text{I}_9$	$338.2\pm 10.1$	$819.2\pm 24.6$	819.2

Table 6.9: Thermodynamic properties at 298.15 K.

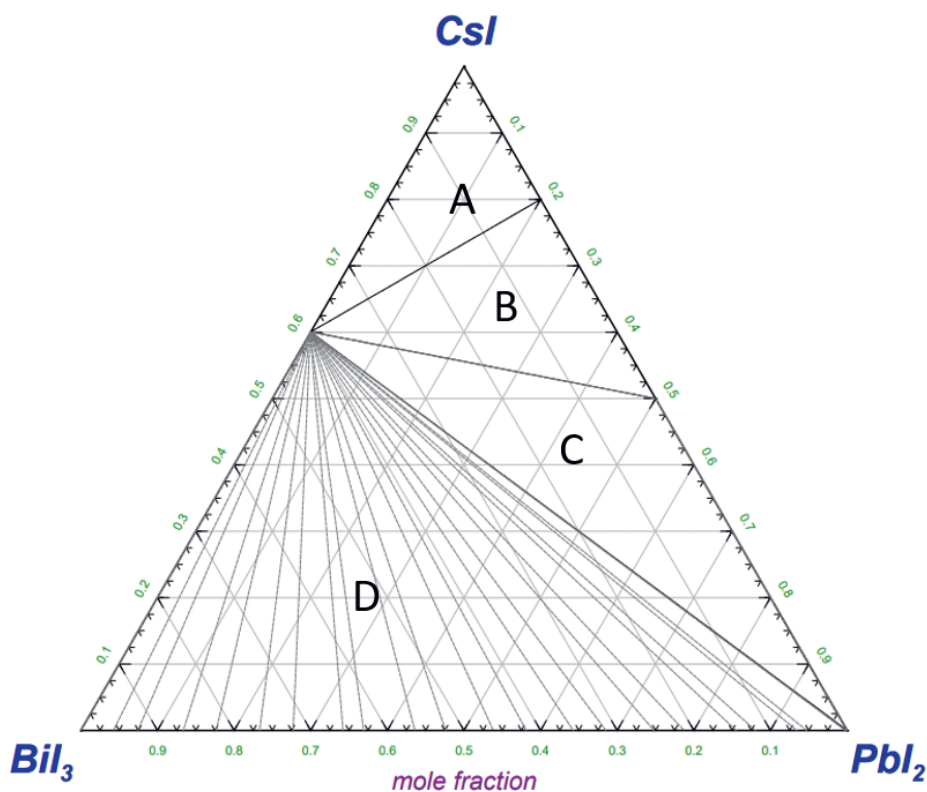


Figure 6.13: Isothermal section of the CsI–PbI<sub>2</sub>–BiI<sub>3</sub> ternary system at  $T = 300$  K as calculated with the thermodynamic model presented in Table C.2. The phases on the diagram labelled A–D are as follows: CsI + Cs<sub>3</sub>Bi<sub>2</sub>I<sub>9</sub> + Cs<sub>4</sub>PbI<sub>6</sub> (A), Cs<sub>3</sub>Bi<sub>2</sub>I<sub>9</sub> + CsPbI<sub>3</sub> + Cs<sub>4</sub>PbI<sub>6</sub> (B), Cs<sub>3</sub>Bi<sub>2</sub>I<sub>9</sub> + CsPbI<sub>3</sub> + PbI<sub>2</sub> (C), Pb<sub>1-x</sub>Bi<sub>x</sub>I<sub>2+x</sub> + Cs<sub>3</sub>Bi<sub>2</sub>I<sub>9</sub> (D).

## 6.8. CONCLUSIONS

The low-temperature heat capacities of  $\delta$ -CsPbI<sub>3</sub>, Cs<sub>4</sub>PbI<sub>6</sub> and Cs<sub>3</sub>Bi<sub>2</sub>I<sub>9</sub> were measured using a thermal-relaxation technique on two different instruments. These insulating materials showed no detectable anomalies in the studied temperature window. The standard entropy and heat capacity of the three compounds at 298.15 K have been derived, as listed in Table 6.9.

The obtained thermodynamic data were used to constrain the standard entropies of the ternary compounds in the model of the ternary salt system CsI–PbI<sub>2</sub>–BiI<sub>3</sub>. The thermodynamic model optimization required only very slight to no deviation compared to the measured entropy data, as is shown in Table 6.9. Moreover, the magnetic susceptibility of the three compounds has been measured.

To study the liquidus surface of the ternary system CsI–PbI<sub>2</sub>–BiI<sub>3</sub>, the constituting binary salt systems were investigated for the first time (BiI<sub>3</sub>–PbI<sub>2</sub>) or subjected to renewed investigation (CsI–PbI<sub>2</sub> and CsI–BiI<sub>3</sub>). Based on our DSC results, the BiI<sub>3</sub>–PbI<sub>2</sub> system seems to form a continuous solid solution over the whole composition range. In gen-

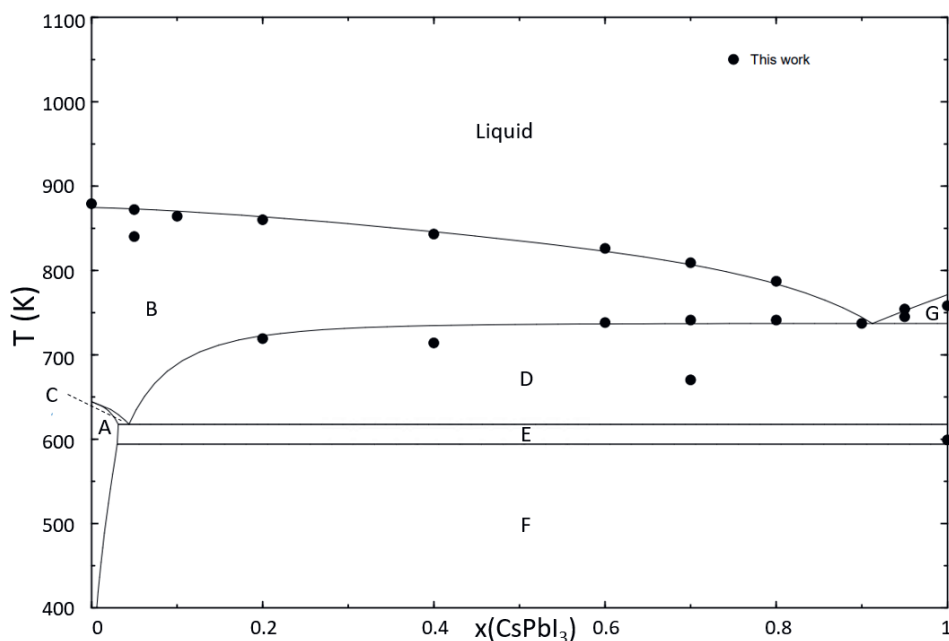


Figure 6.14: Phase diagram of the  $\text{Cs}_3\text{Bi}_2\text{I}_9$ - $\text{CsPbI}_3$  pseudo-binary system as calculated with the thermodynamic model presented in Table C.2. The experimental data shown on the phase diagram have been obtained in this work. The phases on the diagram labelled A-G are as follows:  $\text{Cs}_3\text{Bi}_2\text{I}_9 + \text{Pb}_{1-x}\text{Bi}_x\text{I}_{2+x}$  (A),  $\text{Cs}_3\text{Bi}_2\text{I}_9 + \text{L}$  (B),  $\text{Cs}_3\text{Bi}_2\text{I}_9 + \text{Pb}_{1-x}\text{Bi}_x\text{I}_{2+x} + \text{L}$  (C),  $\alpha$ - $\text{CsPbI}_3 + \text{Cs}_3\text{Bi}_2\text{I}_9 + \text{L}$  (D),  $\alpha$ - $\text{CsPbI}_3 + \text{Cs}_3\text{Bi}_2\text{I}_9 + \text{Pb}_{1-x}\text{Bi}_x\text{I}_{2+x}$  (E),  $\delta$ - $\text{CsPbI}_3 + \text{Cs}_3\text{Bi}_2\text{I}_9 + \text{Pb}_{1-x}\text{Bi}_x\text{I}_{2+x}$  (F),  $\alpha$ - $\text{CsPbI}_3 + \text{L}$  (G).

6

eral, the CsI-PbI<sub>2</sub> and CsI-BiI<sub>3</sub> systems behave as reported previously in literature. The three binary systems were modelled and extrapolated to the ternary phase field. The predicted ternary eutectic points and the section  $\text{Cs}_3\text{Bi}_2\text{I}_9$ - $\text{CsPbI}_3$  were experimentally measured. They agree well with the predictions by the CALPHAD model. Using the obtained liquidus surface, the state (solid, liquid) of any mixture of CsI-PbI<sub>2</sub>-BiI<sub>3</sub> can easily be determined at any given temperature and composition. Depending on the temperature of interest, this model predicts which phases will be thermodynamically stable.

Two limitations of our current study for the safety assessment of the LFRs and LBE-cooled reactors are given by the fact that we only studied the ternary salt field, mainly focusing on the determination of the liquidus surface. Since most of the Pb and Bi will be present as liquid metal, thermodynamic studies into the Pb-Bi-Cs-I system are also necessary. Moreover, under high operating temperatures or severe accident conditions, the gas phase properties are relevant and important to consider too. The temperature window of applicability of the current model can however be bound to the maximum temperature in the coolant vessel, which is around 1115 K as given *supra*.

## EXPERIMENTAL DETAILS

**Synthesis** The chemicals CsI (Merck, 99.999%), PbI<sub>2</sub> (Merck, 99.999%) and BiI<sub>3</sub> (Alfa Aesar, 99.998%) were purchased. All samples were handled inside an Ar-filled glove box with low oxygen and water content (< 5 ppm)

$x(\text{CsI})$	$x(\text{PbI}_2)$	$x(\text{BiI}_3)$	$T_c / \text{K}$	$T_e / \text{K}$	Equilibrium	Equilibrium reaction
0.36	0.36	0.28	772	752	Liquidus	$\text{Cs}_3\text{Bi}_2\text{I}_9 + \text{L}' = \text{L}$
			649	621		$\text{Cs}_3\text{Bi}_2\text{I}_9 + \text{CsPb}_{1-x}\text{Bi}_x\text{I}_{3+x} + \text{L}' = \text{Cs}_3\text{Bi}_2\text{I}_9 + \text{L}'$
			618	608		$\delta\text{-CsPbI}_3 + \text{Cs}_3\text{Bi}_2\text{I}_9 + \text{CsPb}_{1-x}\text{Bi}_x\text{I}_{3+x}$ $= \text{Cs}_3\text{Bi}_2\text{I}_9 + \text{CsPb}_{1-x}\text{Bi}_x\text{I}_{3+x} + \text{L}'$
0.57	0.37	0.06	736	751	Liquidus	$\alpha\text{-CsPbI}_3 + \text{Cs}_3\text{Bi}_2\text{I}_9 + \text{L}' = \text{L}$
			708	686	Eutectic	$\alpha\text{-CsPbI}_3 + \text{Cs}_4\text{PbI}_6 + \text{Cs}_3\text{Bi}_2\text{I}_9$ $= \alpha\text{-CsPbI}_3 + \text{Cs}_3\text{Bi}_2\text{I}_9 + \text{L}'$
			-	667	-	-
			-	608	-	-
			594	584	Polymorphism	$\delta\text{-CsPbI}_3 + \text{Cs}_4\text{PbI}_6 + \text{Cs}_3\text{Bi}_2\text{I}_9$ $= \alpha\text{-CsPbI}_3 + \text{Cs}_4\text{PbI}_6 + \text{Cs}_3\text{Bi}_2\text{I}_9$
0.50	0.48	0.02	758	759	Liquidus	$\alpha\text{-CsPbI}_3 = \text{L}$
			594	587	Polymorphism	$\delta\text{-CsPbI}_3 + \text{Cs}_3\text{Bi}_2\text{I}_9 + \text{CsPb}_{1-x}\text{Bi}_x\text{I}_{3+x}$ $= \alpha\text{-CsPbI}_3 + \text{Cs}_3\text{Bi}_2\text{I}_9 + \text{CsPb}_{1-x}\text{Bi}_x\text{I}_{3+x}$
0.50	0.49	0.01	756	762	Liquidus	$\alpha\text{-CsPbI}_3 = \text{L}$
			594	584	Polymorphism	$\delta\text{-CsPbI}_3 + \text{Cs}_3\text{Bi}_2\text{I}_9 + \text{CsPb}_{1-x}\text{Bi}_x\text{I}_{3+x}$ $= \alpha\text{-CsPbI}_3 + \text{Cs}_3\text{Bi}_2\text{I}_9 + \text{CsPb}_{1-x}\text{Bi}_x\text{I}_{3+x}$

Table 6.10: Measured and calculated invariant equilibria in the ternary phase field  $\text{CsI}-\text{PbI}_2-\text{BiI}_3$ .  $T_c$  = calculated temperature;  $T_e$  = experimentally measured temperature. The uncertainties on the measured temperatures are estimated to be  $\pm 10$  K.

and not exposed to air in any stage of the experiments.  $\text{CsPbI}_3$  was synthesised by mixing  $\text{CsI}$  and  $\text{PbI}_2$  in a 1:1 ratio. The mixture was ground and heated to the melt (823 K) in a nickel liner in an air tight stainless steel container. It was kept for 30 min in the melt, after which it was cooled down to 723 K. This temperature was maintained for 1 h.  $\text{Cs}_4\text{PbI}_6$  was synthesised via solid state reaction.  $\text{CsI}$  and  $\text{PbI}_2$  were mixed in a 4:1 ratio, ground and put in a nickel liner in an air tight stainless steel container. It was heated to 673 K for 48 h.  $\text{Cs}_3\text{Bi}_2\text{I}_9$  was synthesised by mixing  $\text{CsI}$  and  $\text{BiI}_3$  in a 3:2 ratio, thorough grinding and heating twice in the aforementioned containment for 12 h at 723 K with intermittent regrinding.

**X-ray Diffraction** Formation and purity of the compounds were confirmed by X-ray powder diffraction (XRD) as described in Chapter 2.

**Low-temperature heat capacity measurements** Samples were prepared by pressing the synthesised powders into pellets of 3 mm diameter. The pellets used weighed 7.58(5) mg and 14.93(10) mg for  $\text{CsPbI}_3$ , 5.17(5) mg and 10.05(10) mg for  $\text{Cs}_4\text{PbI}_6$ , and 3.14(5) mg and 11.70(10) mg for  $\text{Cs}_3\text{Bi}_2\text{I}_9$ , respectively. For  $\text{CsPbI}_3$ , the polymorph stable at room temperature and below, *viz.*  $\delta\text{-CsPbI}_3$  was studied. The low-temperature heat capacity was measured on two instruments, namely a QD-PPMS and a QD-Versalab equipment system from Quantum Design. Data treatment is explained in Chapter 2.

**Magnetic susceptibility measurements** The static magnetic susceptibilities  $M/H$  of the three title compounds,  $\text{CsPbI}_3$ ,  $\text{Cs}_4\text{PbI}_6$  and  $\text{Cs}_3\text{Bi}_2\text{I}_9$ , respectively, were also measured on the MPMS-3 Quantum Design [115] instrument by magnetic SQUID technique, achieving DC magnetization  $M$  from 2 to 300 K under constant magnetic field  $H$  up to 70 kOe. The samples used were identical to the heat capacity samples measured on the QD-PPMS instrument. The corresponding pellets had masses 6.61(5), 5.02(6) and 3.19(4) mg, respectively. Magnetization  $M(T)$  measurements were performed by thermalizing each piece of material using an exchange gas (6N helium) at a partial pressure of 9 Torr. First, cooling was performed without magnetic field applied (Zero Field Cooled = ZFC). After application of static DC magnetic field  $H = 70$  kOe, each measurement point was then obtained by stabilizing the temperature  $T$  and subsequent extraction of  $M(T)$  signal by mechanical oscillation.

**Differential Scanning Calorimetry** Phase diagram measurements were performed using differential scanning calorimetry (DSC) on a Setaram Multi-Detector HTC Module of the 96 Line calorimeter with 3D heat flux detection. Typically,  $\text{CsI}$ ,  $\text{PbI}_2$  and  $\text{BiI}_3$  and their binary and ternary mixtures were measured. Samples were prepared inside the glove-box under purified Ar-atmosphere, in which the powders were mixed and loaded in closed stainless steel containers with liners made of nickel [116]. Data analysis is explained in Chapter 2.



# BIBLIOGRAPHY

- (1) US DOE Nuclear Energy Research Advisory Committee with Generation IV International Forum [https://www.gen-4.org/gif/jcms/c\\_40481/technology-roadmap](https://www.gen-4.org/gif/jcms/c_40481/technology-roadmap) **2002**.
- (2) Weeks, J. R. *Nuclear Engineering and Design* **1971**, *15*, 363–372.
- (3) Zhang, J. *Advanced Engineering Materials* **2014**, *16*, 349–356.
- (4) Zverev, D. L.; Neevin, S. M.; Doronkov, D. L.; Sokolova, L. B. *Atomic Energy* **2020**, *129*, 1–7.
- (5) Troyanov, V. M.; Toshinsky, G. I.; Stepanov, V. S.; Petrochenko, V. V. *Nuclear Energy and Technology* **2022**, *8*, 187–195.
- (6) Abderrahim, H. A.; Kupschus, P.; Malambu, E.; Benoit, P.; Van Tichelen, K.; Arien, B.; Vermeersch, F.; D'hondt, P.; Jongen, Y.; Ternier, S., et al. *Nuclear Instruments and Methods in Physics Research Section A* **2001**, *463*, 487–494.
- (7) Abderrahim, H. A.; Baeten, P.; De Bruyn, D.; Fernandez, R. *Energy Conversion and Management* **2012**, *63*, 4–10.
- (8) Bandini, G.; Bubelis, E.; Schikorr, M.; Stempnievicz, M.; Tucek, K.; Lázaro, A.; Kudinov, P.; Kööp, K.; Jeltsov, M.; Mansani, L. Safety analysis results of representative DEC accidental transients for the ALFRED reactor, 2013.
- (9) Alemberti, A.; Caramello, M.; Frignani, M.; Grasso, G.; Merli, E.; Morresi, G.; Tarantino, M. *Nuclear Engineering and Design* **2020**, *370*, 110884.
- (10) Pelletier, M.; Guérin, Y. In *Comprehensive Nuclear Materials, 2nd edition*, Konings, R. J. M., Stoller, R. E., Eds.; Elsevier: 2020; Chapter 2.03, pp 72–105.
- (11) Kleykamp, H. *Journal of Nuclear Materials* **1985**, *131*, 221–246.
- (12) Cappia, F.; Miller, B. D.; Aguiar, J. A.; He, L.; Murray, D. J.; Frickey, B. J.; Stanek, J. D.; Harp, J. M. *Journal of Nuclear Materials* **2020**, *531*, 151964.
- (13) Xu, Q.; Li, C.; Nie, J.; Guo, Y.; Wang, X.; Zhang, B.; Ouyang, X. *The Journal of Physical Chemistry Letters* **2020**, *12*, 287–293.
- (14) Li, Y.; Chen, L.; Gao, R.; Liu, B.; Zheng, W.; Zhu, Y.; Ruan, J.; Ouyang, X.; Xu, Q. *ACS Applied Materials & Interfaces* **2021**, *14*, 1489–1495.
- (15) Li, Y.; Chen, L.; Ouyang, X.; Zhao, K.; Xu, Q. *Inorganic Chemistry* **2022**, *61*, 7553–7559.
- (16) Zhang, J.; Li, A.; Li, B.; Yang, M.; Hao, X.; Wu, L.; Zhao, D.; Xia, G.; Ren, Z.; Tian, W., et al. *ACS Photonics* **2022**, *9*, 641–651.
- (17) Ge, S.; Wang, Y.; Xiang, Z.; Cui, Y. *ACS Applied Materials & Interfaces* **2018**, *10*, 24620–24626.

- (18) Alexander, G. C.; Krantz, P. W.; Jung, H. J.; Davis, S. K.; Xu, Y.; Dravid, V. P.; Chandrasekhar, V.; Kanatzidis, M. G. *Advanced Materials* **2021**, *33*, 2103098.
- (19) Alexander, G. C. B. Exploratory synthesis and characterization of heavy metal halide semiconductors: unveiling new properties and structures, Ph.D. Thesis, Northwestern University, 2020.
- (20) Wang, Y.-K.; Yuan, F.; Dong, Y.; Li, J.-Y.; Johnston, A.; Chen, B.; Saidaminov, M. I.; Zhou, C.; Zheng, X.; Hou, Y., et al. *Angewandte Chemie International Edition* **2021**, *60*, 16164–16170.
- (21) Fakhruddin, A.; Gangishetty, M. K.; Abdi-Jalebi, M.; Chin, S.-H.; bin Mohd Yusoff, A. R.; Congreve, D. N.; Tress, W.; Deschler, E.; Vasilopoulou, M.; Bolink, H. J. *Nature Electronics* **2022**, *5*, 203–216.
- (22) Hu, Y.; Bai, F.; Liu, X.; Ji, Q.; Miao, X.; Qiu, T.; Zhang, S. *ACS Energy Letters* **2017**, *2*, 2219–2227.
- (23) Hutter, E. M.; Savenije, T. J. *ACS Energy Letters* **2018**, *3*, 2068–2069.
- (24) Johansson, M. B.; Zhu, H.; Johansson, E. M. J. *The Journal of Physical Chemistry Letters* **2016**, *7*, 3467–3471.
- (25) Johansson, M. B.; Philippe, B.; Banerjee, A.; Phuyal, D.; Mukherjee, S.; Chakraborty, S.; Cameau, M.; Zhu, H.; Ahuja, R.; Boschloo, G., et al. *Inorganic Chemistry* **2019**, *58*, 12040–12052.
- (26) Kovalenko, M. V.; Protesescu, L.; Bodnarchuk, M. I. *Science* **2017**, *358*, 745–750.
- (27) Ghosh, B.; Wu, B.; Mulmudi, H. K.; Guet, C.; Weber, K.; Sum, T. C.; Mhaisalkar, S.; Mathews, N. *ACS Applied Materials & Interfaces* **2018**, *10*, 35000–35007.
- (28) Zhang, Y.; Liu, Y.; Xu, Z.; Ye, H.; Yang, Z.; You, J.; Liu, M.; He, Y.; Kanatzidis, M. G.; Liu, S. F. *Nature Communications* **2020**, *11*, 1–11.
- (29) Wu, H.; Ge, Y.; Niu, G.; Tang, J. *Matter* **2021**, *4*, 144–163.
- (30) Jong, U.-G.; Kim, Y.-S.; Ri, C.-H.; Kye, Y.-H.; Yu, C.-J. *The Journal of Physical Chemistry C* **2021**, *125*, 6013–6019.
- (31) Dutta, M.; Sarkar, D.; Biswas, K. *Chemical Communications* **2021**, *57*, 4751–4767.
- (32) Kondo, S.; Masaki, A.; Saito, T.; Asada, H. *Solid State Communications* **2002**, *124*, 211–214.
- (33) Yunakova, O. N.; Miloslavskii, V. K.; Kovalenko, E. N. *Optics and Spectroscopy* **2012**, *112*, 91–96.
- (34) Wang, Y.; Guan, X.; Li, D.; Cheng, H.-C.; Duan, X.; Lin, Z.; Duan, X. *Nano Research* **2017**, *10*, 1223–1233.
- (35) Bonomi, S.; Malavasi, L. *Journal of Vacuum Science & Technology A: Vacuum, Surfaces, and Films* **2020**, *38*, 060803.
- (36) Babin, V.; Fabeni, P.; Nikl, M.; Nitsch, K.; Pazzi, G. P.; Zazubovich, S. *physica status solidi (b)* **2001**, *226*, 419–428.
- (37) Kondo, S.; Amaya, K.; Saito, T. *Journal of Physics: Condensed Matter* **2003**, *15*, 971.

- (38) Geng, H.; Yao, X.; Tu, X.; Wang, Z.; Gu, Y.; Cui, H.; Guan, G.; Han, M. *ACS Applied Electronic Materials* **2021**, *4*, 217–224.
- (39) Kovalsky, A.; Wang, L.; Marek, G. T.; Burda, C.; Dyck, J. S. *The Journal of Physical Chemistry C* **2017**, *121*, 3228–3233.
- (40) Lee, W.; Li, H.; Wong, A. B.; Zhang, D.; Lai, M.; Yu, Y.; Kong, Q.; Lin, E.; Urban, J. J.; Grossman, J. C., et al. *Proceedings of the National Academy of Sciences* **2017**, *114*, 8693–8697.
- (41) Kawano, S.; Tadano, T.; Iikubo, S. *The Journal of Physical Chemistry C* **2021**, *125*, 91–97.
- (42) Acharyya, P.; Pal, K.; Ahad, A.; Sarkar, D.; Rana, K. S.; Dutta, M.; Soni, A.; Waghmare, U. V.; Biswas, K. *Advanced Functional Materials* **2023**, 2304607.
- (43) Belyaev, I. N.; Shurginov, E. A.; Kudryashov, N. S. *Russian Journal of Inorganic Chemistry* **1972**, *17*, 1473–1475.
- (44) Ilyasov, I. I.; Chaurskii, N. I.; Barsegov, D. G.; Bergman, A. G. *Russian Journal of Inorganic Chemistry* **1967**, *12*, 1163–1165.
- (45) Ilyasov, I. I.; Barsegov, D. G.; Berikashvili, I. G.; Danilenko, L. P. *Russian Journal of Inorganic Chemistry* **1969**, *14*, 776–778.
- (46) Kun, S. V.; Peresh, E. Y.; Lazarev, V. B.; Orinchai, A. V.; Gorvat, M. I. *Neorganicheskie Materialy* **1988**, 1899–1903.
- (47) Plyushev, B. E.; Stepina, S. B.; Zimina, G. V.; Molchanova, O. P.; Savelyeva, L. V.; Yashkov, D. A. *Non-ferrous Metallurgy* **1970**, *1*, 65–67.
- (48) Dzeranova, K. B.; Kaloev, N. I.; Egerev, O. I.; Bukhalova, G. A. *Zhurnal Neorganicheskoy Khimii* **1984**, *29*, 3171–3172.
- (49) Wells, H. L. *Zeitschrift für anorganische Chemie* **1893**, *3*, 195–210.
- (50) Møller, C. K., *The structure of caesium plumbo iodide CsPbI<sub>3</sub>*; 1; Munksgaard: 1959; Vol. 32.
- (51) Møller, C. K., *On the structure of caesium hexahalogeno-plumbates (II)*; Munksgaard Copenhagen, Denmark: 1960; Vol. 32.
- (52) Kaloev, N. I.; Kubalova, L. M.; Dzeranova, K. B.; Toporovskaya, E. A.; Paramazova, S. E. *Russian Journal of Inorganic Chemistry* **1998**, *43*, 125–127.
- (53) Lindqvist, O.; Johansson, G.; Sandberg, E.; Norin, T. *Acta Chemica Scandinavica* **1968**, *22*, 2943–2952.
- (54) Sebastia-Luna, P.; Gélvez-Rueda, M. C.; Dreessen, C.; Sessolo, M.; Grozema, F. C.; Palazon, F.; Bolink, H. J. *Journal of Materials Chemistry A* **2020**, *8*, 15670–15674.
- (55) Mel'Nikova, S. V.; Zaitsev, A. I. *Physics of the Solid State* **1997**, *39*, 1652–1654.
- (56) Melnikova, S. V.; Shabanova, L. A.; Zaitsev, A. I.; Parshikov, S. A.; Ageev, O. A.; Aleksandrov, K. S. *Ferroelectrics Letters Section* **1996**, *20*, 163–167.
- (57) Arakcheeva, A. V.; Bonin, M.; Chapuis, G.; Zaitsev, A. I. *Zeitschrift für Kristallographie-Crystalline Materials* **1999**, *214*, 279–283.

- (58) Arakcheeva, A. V.; Chapuis, G.; Meyer, M. *Zeitschrift für Kristallographie-Crystalline Materials* **2001**, *216*, 199–205.
- (59) Gu, J.; Yan, G.; Lian, Y.; Mu, Q.; Jin, H.; Zhang, Z.; Deng, Z.; Peng, Y. *RSC Advances* **2018**, *8*, 25802–25807.
- (60) McCall, K. M.; Stoumpos, C. C.; Kostina, S. S.; Kanatzidis, M. G.; Wessels, B. W. *Chemistry of Materials* **2017**, *29*, 4129–4145.
- (61) Tailor, N. K.; Satapathi, S. *Scripta Materialia* **2023**, *223*, 115061.
- (62) Filip, M. R.; Liu, X.; Miglio, A.; Hautier, G.; Giustino, F. *The Journal of Physical Chemistry C* **2018**, *122*, 158–170.
- (63) Wang, B.; Novendra, N.; Navrotsky, A. *Journal of the American Chemical Society* **2019**, *141*, 14501–14504.
- (64) Wang, B.; Navrotsky, A. *Thermochimica Acta* **2021**, *695*, 178813.
- (65) Tsvetkov, D. S.; Mazurin, M. O.; Sereda, V. V.; Ivanov, I. L.; Malyshkin, D. A.; Zuev, A. Y. *The Journal of Physical Chemistry C* **2020**, *124*, 4252–4260.
- (66) Sereda, V. V.; Sednev-Lugovets, A. L.; Malyshkin, D. A.; Tsvetkov, D. S.; Zuev, A. Y. *Thermochimica Acta* **2020**, *694*, 178802.
- (67) Dastidar, S.; Hawley, C. J.; Dillon, A. D.; Gutierrez-Perez, A. D.; Spanier, J. E.; Fafarman, A. T. *The Journal of Physical Chemistry Letters* **2017**, *8*, 1278–1282.
- (68) Kye, Y.-H.; Yu, C.-J.; Kim, C.-H.; Kim, Y.-S.; Jong, U.-G. *The Journal of Physical Chemistry C* **2021**, *125*, 13195–13211.
- (69) Evarestov, R. A.; Kotomin, E. A.; Senocrate, A.; Kremer, R. K.; Maier, J. *Physical Chemistry Chemical Physics* **2020**, *22*, 3914–3920.
- (70) Zhang, B.; Zhang, H.; Lin, J.; Cheng, X. *International Journal of Quantum Chemistry* **2020**, *120*, e26232.
- (71) Li, M.; Peng, S.; Fang, S.; Gong, Y.; Yang, D.; Bu, K.; Liu, B.; Luo, H.; Guo, S.; Li, J., et al. *The Journal of Physical Chemistry Letters* **2022**, *13*, 2555–2562.
- (72) Dmitriev, Y. N.; Bennett, P. R.; Cirignano, L. J.; Gupta, T. K.; Klugerman, M.; Shah, K. S. *MRS Online Proceedings Library (OPL)* **1999**, *580*, 99–104.
- (73) Neuhausen, J.; Eichler, B. *Radiochimica Acta* **2006**, *94*, 239–242.
- (74) Zhang, J.; Yang, L.; Liu, R.; Chen, L. *Materials Research Express* **2019**, *6*, 105529.
- (75) Zhang, J.; Zhong, Y.; Chen, L.; Yang, L. *Chemical Physics Letters* **2020**, *752*, 137572.
- (76) Kajal, S.; Kim, J.; Shin, Y. S.; Singh, A. N.; Myung, C. W.; Kim, J. Y.; Kim, K. S. *Small Methods* **2020**, *4*, 2000296.
- (77) Capelli, E.; Beneš, O.; Konings, R. J. M. *Journal of Nuclear Materials* **2018**, *501*, 238–252.
- (78) Chase, M. W.; National Information Standards Organization, U. S., *NIST-JANAF thermochemical tables*; American Chemical Society Washington, DC: 1998; Vol. 9.
- (79) Konings, R. J. M.; Cordfunke, E. H. P.; van der Laan, R. R. *Journal of Alloys and Compounds* **1995**, *230*, 85–88.

- (80) Cubicciotti, D. *Inorganic Chemistry* **1968**, *7*, 211–213.
- (81) Barin, I.; Knacke, O.; Kubaschewski, O. In *Thermochemical properties of inorganic substances*; Springer: 1977, pp 1–861.
- (82) Cubicciotti, D.; Eding, H. *The Journal of Physical Chemistry* **1965**, *69*, 3621–3625.
- (83) Neumann, F. E. *Annalen der Physik und Chemie* **1831**, *23*, 1–39.
- (84) Kopp, H. *Philosophical Transactions of the Royal Society of London* **1865**, 71–202.
- (85) Trots, D. M.; Myagkota, S. V. *Journal of Physics and Chemistry of Solids* **2008**, *69*, 2520–2526.
- (86) OECD–NEA, *Handbook on lead-bismuth eutectic alloy and lead properties, materials compatibility, thermalhydraulics and technologies*; Organisation for Economic Co-Operation and Development: 2015.
- (87) Mu, H.; Zhang, Y.; Zou, H.; Tian, F.; Fu, Y.; Zhang, L. *The Journal of Physical Chemistry Letters* **2022**, *14*, 190–198.
- (88) Kurt, A. *Journal of Applied Physics* **2020**, *128*.
- (89) Marronnier, A.; Roma, G.; Boyer-Richard, S.; Pedesseau, L.; Jancu, J.-M.; Bonnassieux, Y.; Katan, C.; Stoumpos, C. C.; Kanatzidis, M. G.; Even, J. *ACS Nano* **2018**, *12*, 3477–3486.
- (90) Lashley, J. C.; Hundley, M. F.; Migliori, A.; Sarrao, J. L.; Pagliuso, P. G.; Darling, T. W.; Jaime, M.; Cooley, J. C.; Hults, W. L.; Morales, L., et al. *Cryogenics* **2003**, *43*, 369–378.
- (91) Kennedy, C. A.; Stancescu, M.; Marriott, R. A.; White, M. A. *Cryogenics* **2007**, *47*, 107–112.
- (92) Straus, D. B.; Guo, S.; Abeykoon, A. M.; Cava, R. J. *Advanced Materials* **2020**, *32*, 2001069.
- (93) Miyata, K.; Atallah, T. L.; Zhu, X.-Y. *Science Advances* **2017**, *3*, e1701469.
- (94) Tadano, T.; Saidi, W. A. *Physical Review Letters* **2022**, *129*, 185901.
- (95) Lahnsteiner, J.; Bokdam, M. *Physical Review B* **2022**, *105*, 024302.
- (96) Huang, X.; Li, X.; Tao, Y.; Guo, S.; Gu, J.; Hong, H.; Yao, Y.; Guan, Y.; Gao, Y.; Li, C., et al. *Journal of the American Chemical Society* **2022**, *144*, 12247–12260.
- (97) Qiao, T.; Liu, X.; Rossi, D.; Khurana, M.; Lin, Y.; Wen, J.; Cheon, J.; Akimov, A. V.; Son, D. H. *Nano Letters* **2021**, *21*, 9543–9550.
- (98) Aleksandrov, I. P.; Bovina, A. F.; Ageev, O. A.; Sukhovskii, A. A. *Physics of the Solid State* **1997**, *39*, 991–994.
- (99) Mel’Nikova, S. V.; Zaitsev, A. I. *Physics of the Solid State* **1997**, *39*, 1652–1654.
- (100) Aleksandrova, I. P.; Sukhovskiy, A. A.; Aleksandrov, K. S. *Solid State Communications* **1998**, *105*, 323–326.
- (101) Jorio, A.; Currat, R.; Myles, D. A. A.; McIntyre, G. J.; Aleksandrova, I. P.; Kiat, J. M.; Saint-Grégoire, P. *Physical Review B* **2000**, *61*, 3857.

- (102) Ivanov, Y. N.; Sukhovskii, A. A.; Lisin, V. V.; Aleksandrova, I. P. *Inorganic Materials* **2001**, *37*, 623–627.
- (103) Girnyk, I.; Krupych, O.; Martunyk-Lototska, I.; Motsnyi, F.; Vlokh, R. *Ukrainian Journal of Physical Optics* **2003**, *4*, 165–169.
- (104) Motsnyi, F. V.; Peresh, E. Y.; Smolanka, O. M. *Solid State Communications* **2004**, *131*, 469–471.
- (105) Machulin, V. F.; Motsnyi, F. V.; Smolanka, O. M.; Svechnikov, G. S.; Peresh, E. Y. *Low Temperature Physics* **2004**, *30*, 964–967.
- (106) Motsnyi, F. V.; Smolanka, O. M.; Sugakov, V. I.; Peresh, E. Y. *Solid state communications* **2006**, *137*, 221–224.
- (107) Motsnyi, F. V.; Smolanka, O. M.; Peresh, E. Y.; Virko, S. V.; Dorogan, V. G. *Physica B: Condensed Matter* **2008**, *403*, 2838–2841.
- (108) Motsnyi, F. V. In *2010 International Conference on Advanced Optoelectronics and Lasers*, 2010, pp 185–187.
- (109) Nilä, A.; Baibarac, M.; Matea, A.; Mitran, R.; Baltog, I. *physica status solidi b* **2017**, *254*, 1552805.
- (110) Rosen, P. F.; Woodfield, B. F. *The Journal of Chemical Thermodynamics* **2020**, *141*, 105974.
- (111) Aleksandrova, I. P.; Burriel, R.; Bartolome, J.; Bagautdinov, B. S.; Blasco, J.; Sukhovskiy, A. A.; Torres, J. M.; Vasiljev, A. D.; Solovjev, L. A. *Phase Transitions* **2002**, *75*, 607–620.
- (112) Cordfunke, E. H. P.; Prins, G. *Thermochimica Acta* **1985**, *90*, 169–176.
- (113) Roki, F.-Z.; Ohnet, M.-N.; Fillet, S.; Chatillon, C.; Nuta, I. *The Journal of Chemical Thermodynamics* **2014**, *70*, 46–72.
- (114) Degen, T.; Sadki, M.; Bron, E.; König, U.; Nénert, G. *Powder Diffraction* **2014**, *29*, S13–S18.
- (115) QuantumDesign <https://www.qdusa.com/products/mpms3.html>, SQUID Magnetometer Quantum Design MPMS3, Date of last access: 2023-08-15, 2023.
- (116) Beneš, O.; Konings, R. J. M.; Wurzer, S.; Sierig, M.; Dockendorf, A. *Thermochimica Acta* **2010**, *509*, 62–66.

# 7

## THE BAO-DEFICIENT $Ba_3PuO_6$ COMPOUND

*A BaO-deficient plutonium-containing perovskite with a composition close to  $Ba_3PuO_6$  has been obtained via solid state synthesis. The compound was characterised using X-Ray Diffraction from room temperature up to 1473 K, revealing two phase transitions and ordered Ba-deficiency. X-ray Absorption Spectroscopy was performed at the Pu  $L_3$ - and  $M_5$ -edges. The XANES spectrum at the Pu  $L_3$ -edge and the XANES in HERFD mode at the Pu  $M_5$ -edge both indicate a Pu(VI) oxidation state. Despite the rather complex crystallographic unit cell, Extended X-ray Absorption Fine Structure (EXAFS) spectroscopy at the Pu  $L_3$ -edge yields Pu-O distances of 2.01(1) and 2.4(3) Å. The low-temperature heat capacity of  $Ba_{2.875}PuO_{5.875}$  was measured between 5 and 270 K. The heat capacity and standard entropy at 298.15 K were found to be  $C_p(298.15K) = (251 \pm 8) J \cdot K^{-1} \cdot mol^{-1}$  and  $S_m^0(298.15K) = (318 \pm 8) J \cdot K^{-1} \cdot mol^{-1}$ , respectively. The magnetic susceptibility was measured from 2 to 320 K and shows a temperature-independent paramagnetism, consistent with the hexavalent oxidation state of Pu. This article reports the first extended low-temperature heat capacity curve and a temperature-dependent magnetic susceptibility measurement in a  $[Rn]5f^2$  Pu-based system.*

---

This chapter is based on the publication: A. van Hattem, K. Popa, G. Wallez, J. Boshoven, E. Colineau, E. Dahms, J-C. Griveau, H. Hein, O. Walter, B. Schacherl, T. Vitova, K. Dardenne, T. Pruessmann, J. Rothe, A.L.Smith, and R.J.M. Konings *Structural and Physical Investigation of Ordered BaO-deficient  $Ba_3PuO_6$* , Communications Chemistry **8** (2025): 270

## 7.1. INTRODUCTION

The initial attempt to study the Pb-Ba-An-O (An=U,Pu) system as part of the coolant-grey phase interaction resulted in an in-depth study of a compound in the Ba-Pu-O system, as this system posed several questions. The oxide precipitates in irradiated fuel are compounds of the type (Ba,Sr,Cs)(Zr,U,Pu,Mo,RE) $\text{O}_3$  [1]. For  $\text{BaPuO}_3$ , a formal average oxidation state of Pu(IV) is expected, but for the reported  $\text{Ba}_2\text{PbPuO}_6$  [2], a rather unique Pu(VI) oxidation state might be expected, depending on the use of Pb(II) or Pb(IV) in the calculation. Data on Pu(VI) solid state compounds are rather scarce, and it was found necessary to investigate the ternary  $\text{Ba}_3\text{PuO}_6$  before studying  $\text{Ba}_2\text{PbPuO}_6$ . In fast-neutron reactor MOX fuel, Pu(III) and Pu(IV) are found [3], but, in analogy to U [4], the oxide precipitates might show other Pu oxidation states. This is especially the case if a higher oxygen potential is expected, *i.e.* in the scenario of higher burn-up typical for fast-neutron reactors. The fact that Pu(VI) seems to be able to crystallise in the perovskite phase makes the question on its existence and thermodynamic stability even more intriguing.

In general, the actinide elements (An) at the bottom of the periodic table allow for a wide range of oxidation states and a concomitant rich chemistry. Throughout the actinide group, the  $5f$  electron-shell is gradually filled, but the exact nature of the electronic occupation of the valence shells remains a matter of debate, especially for the transuranium elements like plutonium (Pu). In recent years, a surprising feature was reported for the well-known material  $\text{PuO}_2$ : Tobin and Wu obtained a  $[\text{Rn}]5f^5$  occupation using a  $N_{4,5}$  branching ratio analysis [5], which is however contrary to the  $[\text{Rn}]5f^4$  occupancy that Bagus, Schacherl and Vitova reported [6]. In a very recent study by Bajaj, Ramanantoanina *et al.*, a clear distinction was made between  $5f^4$  open shell electrons that do not participate in bonding and  $5f$  electrons transferred from O to Pu, which do participate in covalent Pu-O interaction [7]. Another surprising case is the long-range magnetic order in the perovskite compounds  $\text{BaPuO}_3$  and  $\text{SrPuO}_3$  below 164(1) and 76(1) K, respectively [8], that one would not expect for a  $[\text{Rn}]5f^4$  system without unpaired electrons. Moreover, although the shortest Pu-Pu distance is smaller than 4.5 Å, the transition temperature is high [9]. Systematic studies into the solid state chemistry of systems of Pu-O with alkali (Li, Na, K, Rb, Cs) or alkaline-earth (Be, Mg, Ca, Sr, Ba) metals are very rare and often date back to the last century, except for Na-Pu-O [10–12]. The Na-Pu(VI)-O phases that were reported therein are claimed to be impossible in a recent DFT study because calculations predict Pu(V) is the maximum physical oxidation state in solid state actinide compounds [13].

As evidenced by the cited cases  $\text{BaPuO}_3$  and  $\text{SrPuO}_3$ , alkaline-earth actinide oxides crystallize in perovskite phases. In addition to these compounds,  $\text{BaAn}^{\text{IV}}\text{O}_3$  with An = Th, Pa, U, Np, Am, Cm and Cf have been studied experimentally by at least one technique [14–17]. More rare double perovskites with barium and actinides have been reported to exist:  $\text{Ba}_3\text{PaO}_{5.5}$  [14] and  $\text{Ba}_3\text{An}^{\text{VI}}\text{O}_6$  with An = U, Np, Pu [18, 19], but the understanding of any of these compounds is rather poor and the literature raises questions starting very basically at the stoichiometry of the compounds. A generalized overview of the phases reported in the Ba-An-O system [18–25] was made with respect to the Ba / An ratio and the average formal oxidation state, and is shown in Figure 7.1, in which the perovskite-related phases are presented by open squares.

The plutonium-containing double perovskite  $\text{Ba}_3\text{PuO}_6$  was synthesized and reported for the first time by Keller in 1962 [18]. The compound was synthesised by heating  $\text{BaO}_2$  and  $\text{PuO}_2$  in a 3:1 ratio in oxygen-flow at 1423 and 1523 K. Keller found the dark brown  $\text{Ba}_3\text{PuO}_6$  to have a cubic structure ( $Fm\bar{3}m$ ) with cell parameter  $a = 8.844(6)$  Å and Pu-O distances of 2.211 Å. The Pu(VI) oxidation state was derived from the absorption spectrum in 1 n HCl, where only  $\text{PuO}_2^{2+}(\text{aq.})$  was found. In experiments of equimolar ratio  $\text{BaO}_2$  and  $\text{PuO}_2$  in oxygen flow,  $\text{Ba}_3\text{PuO}_6$  and  $\text{PuO}_2$  were found up to 1073 K, above which Keller proposed the ordered perovskite-structure  $\text{Ba}(\text{Pu}_x^{4+}, \text{Pu}_{0.5(1-x)}^{6+}, \text{Ba}_{0.5(1-x)})\text{O}_3$  to form based on a non-linear trend in lattice parameter. Next to this dark brown  $\text{Ba}_3\text{PuO}_6$ , Keller tried to produce a Pu(V)-based Ba-Pu-O compound. For a deep black reaction mixture of  $\text{Ba}_3\text{PuO}_6$ ,  $\text{PuO}_2$  and 3 BaO in Ar-flow at 1273 to 1473 K,  $\text{Ba}(\text{Pu}_x^{4+}, \text{Pu}_{0.5(1-x)}^{6+}, \text{Ba}_{0.5(1-x)})\text{O}_3$  was found again. Absorption spectrometry in 0.5 n HCl showed only  $\text{Pu}^{4+}$  and  $\text{PuO}_2^{2+}(\text{aq.})$  and he concluded the constitution to be  $\text{Ba}_3\text{PuO}_{5.5}$ . Gens *et al.* reported the standard enthalpy of formation at 298.15 K of  $\text{Ba}_3\text{PuO}_6$ , but unlike Keller, they did not find an ideal perovskite-type structure [26]. They prepared  $\text{Ba}_3\text{PuO}_6$  from  $\text{BaCO}_3$  and  $\text{PuO}_2$  via heat-treatment at 900, 1000, 1100 and 1200 K with intermittent grinding. They also described that the thermal history of  $\text{PuO}_2$  dictates the reactivity towards BaO and they used slow temperature increases to avoid Ba loss. Four successful syntheses gave identical diffraction patterns, that indicated a distorted perovskite structure, while the Pu was found to be hexavalent by spectrophotometry.  $\text{Ba}_3\text{PuO}_6$  stock from Argonne National Laboratory is mentioned as Pu(VI) stock for X-ray absorption experiments in some studies [27, 28], but data on this stock is not available in open literature to our knowledge.

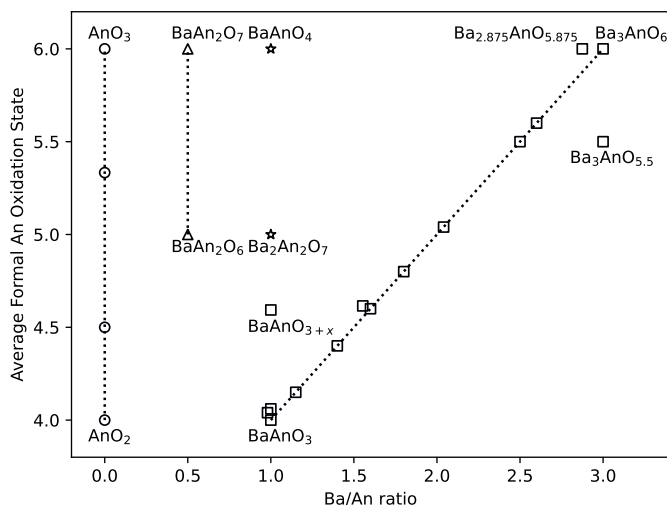


Figure 7.1: Non-exhaustive overview of reported phases in the Ba-An-O systems [18–25]. The phases are organised based on their Ba/An ratio and the average formal An oxidation state. Note that not all An (mainly U, Np, Pu) crystallise in all depicted stoichiometries. The dotted lines are guides for the eye.

Investigations on the U-containing double perovskite compound  $\text{Ba}_3\text{UO}_6$  showed an analogous development: a first indication of an ordered perovskite-type structure [29, 30] was later indexed in space groups of lower symmetry. Rietveld indexed all lines but three to a rather small tetragonal cell [31]. Kemmler-Sack and Seemann reported a much larger rhombohedral cell for  $\text{Ba}_3\text{UO}_6$  [32]. Griffiths, Kemmler-Sack and Treiber reported that (next to triclinic  $\text{Ba}_3\text{UO}_6$ ), a tetragonal BaO-deficient phase is formed, *viz.*  $\text{Ba}_{2.875}\text{UO}_{5.875}$  [20–22]. Rietveld's solution is listed in the Pearsons Crystal Database as similar to  $\text{Ba}_{2.875}\text{UO}_{5.875}$ . De Blicke *et al.* used electron diffraction to determine the lattice of  $\text{Ba}_3\text{UO}_6$  [33]. They interpreted the structure to be a 531 oriented superlattice.

Thus,  $\text{Ba}_3\text{PuO}_6$  in particular and the Ba-Pu-O system in general deserve attention and the solid state chemistry of the Ba-U-O system may serve as a more investigated analogy. Three main hypotheses can be formulated after studying the literature about the perovskite-related structures in the Ba-An-O systems: First, the BaO-deficient phase  $\text{Ba}_{2.875}\text{AnO}_{5.875}$  should be understood as a stoichiometric compound or as a member of solid solutions on the pseudo-binary BaO-AnO<sub>3</sub> axis, *i.e.* as a (end-)member of a purely An(VI)-solid solution series. More precisely, a solid solution  $\text{Ba}_{3-x}\text{AnO}_{6-x}$  exists with a maximum  $x = 0.125$ . Second, the perovskite phases are related via the pseudo-binary system  $\text{BaAnO}_3\text{-Ba}_{1+y}\text{AnO}_{3+x}\text{-Ba}_3\text{AnO}_6$ , *i.e.* with increasing average formal oxidation state of the actinide ion, following the dotted line in Figure 7.1 [18, 25]. The conjecture by Keller from 1964 that an ordered perovskite structure exists of composition  $\text{Ba}(\text{Pu}_x^{4+}, \text{Pu}_{0.5(1-x)}^{6+}, \text{Ba}_{0.5(1-x)})\text{O}_3$  is an equivalent proposal [18] to the proposal of Cordfunke *et al.*, although according to the latter, uranium oxidises via U(V) to U(VI), while Keller proposes a mixture between Pu(IV) and Pu(VI) [18, 25]. Third, the actual chemistry is given by a ternary phase field enclosed by (at least)  $\text{BaAnO}_3\text{-Ba}_3\text{AnO}_6\text{-Ba}_{2.875}\text{AnO}_{5.875}$ .

The crystallography of  $\text{Ba}_3\text{PuO}_6$  needs to be revisited in light of the complexity found in the Ba-U-O system [25, 32], while the recent findings for nominally  $5f^4$   $\text{PuO}_2$  and  $\text{BaPuO}_3$  raise the question on the nature of the nominally closed-shell (no unpaired electrons)  $[\text{Rn}]5f^2$   $\text{Ba}_3\text{PuO}_6$  compound as well [5, 8]. The goal of this Chapter is to unravel the chemistry and the related impact on the physical properties of  $\text{Ba}_3\text{PuO}_6$ , but we found particularly its BaO-deficient related phase, and report on crystal structure, oxidation state, Pu-coordination and electronic structure, thermal expansion, low-temperature heat capacity, standard entropy and magnetic susceptibility. The analysis will follow the paradigm for this class of materials as set out in Figure 7.1. Figure 7.1 implies that proper analysis needs to account for the (average) formal An oxidation state and for the Ba/An ratio. Once these properties are established, physical and thermodynamic properties of well-defined compounds can be studied.

## 7.2. RESULTS AND DISCUSSION

The results and discussion are organised in line with the paradigm set out in Figure 7.1. After a short description of the synthesis, the average Pu formal oxidation state investigations using X-ray Absorption Spectroscopy are presented. Next, the results that led to the Ba/Pu quantification and crystal structure (XRD, EXAFS) are described. Last, study of various physical and thermodynamic properties (thermal expansion, low-temperature heat capacity, magnetic susceptibility) is discussed.

### 7.2.1. THE OXIDATION STATE OF PU

The black reaction mixture of synthesis 1 did not change colour upon the subsequent thermal treatments. A gradual mass loss was observed, as is expected with the loss of  $\text{CO}_2$  from the reactant  $\text{BaCO}_3$ . The diffraction pattern collected after the heat treatment at 900 K, showed peaks that could be attributed to  $\text{BaCO}_3$  and  $\text{PuO}_2$ . After the heat treatment at 1000 K, a new phase was found on the diffraction pattern.  $\text{BaCO}_3$  is still partially visible, but disappeared after the heat treatment at 1100 K. At 1100, 1200 and 1270 K, the diffraction patterns showed the new phase and the reagents were not visible any more. The black reaction mixture of synthesis 2 did not change colour. As noted in the introduction, Keller reported a dark brown colour for  $\text{Ba}_3\text{PuO}_6$  obtained in oxygen flow, and a deep black colour for the decomposition product  $\text{Ba}_3\text{PuO}_{5.5}$  in Ar-flow [18]. The thermogravimetric-differential thermal analysis (TG-DTA) result on a reaction mixture of  $3\text{BaCO}_3$  and  $\text{PuO}_2$  in air is shown and discussed in Appendix D.

To study the average Pu oxidation state, X-ray absorption spectra at the Pu  $L_3$  and  $M_5$ -edge were recorded. The recorded X-ray Absorption Near Edge Structure (XANES) spectrum at the Pu  $L_3$ -edge of  $\text{Ba}_{2.875}\text{PuO}_{5.875}$  is shown in Figure 7.2. The edge threshold is compared to  $\text{PuO}_2$  measured at the same beamline [34]. A shift towards higher energy with respect to  $\text{PuO}_2$  measured at the same beamline is clearly observed while the white line aligns well with  $\text{Na}_4\text{Pu(VI)O}_5$  collected at ROBL as shown in Figure 7.2 as well. This indicates a solid state Pu(VI) compound, contradicting claims from theory that Pu(V) is the highest possible oxidation state for solid state samples [13], as was also found by Pidchenko *et al.* on  $\text{K}_4\text{PuO}_2(\text{CO}_3)_3$  [35]. Since Pu(V) always shows a characteristic energy shift towards low energies at the  $L_3$ -edge compared to both Pu(IV) and Pu(VI), it can be excluded from this data as well [36]. The white line is rather broad and an additional shoulder-like feature in between the edge-position and the primary white line is visible. Comparison with solid state uranate and neptunite species shows that the shoulder is common for ‘-ate’ geometry and solid state samples tend to give a broad white line [12, 37–40]. Moreover, the calculated Pu  $L_3$ -edge spectra of  $\text{Ba}_{2.875}\text{PuO}_{5.875}$  and  $\text{BaPuO}_3$  (space group  $Pnma$ ) using FDMNES are shown in Figure 7.2, and a similar shoulder-like feature is visible at the low-energy side of the white line. The calculated near-edge structure is very similar to the experimentally observed spectrum, underpinning the proposed structural model.

The high-resolution XANES spectrum collected around the Pu  $M_5$ -edge in scattering angle of  $142^\circ$  relative to the incident beam is shown in Figure 7.3, together with a  $\text{PuO}_2$  reference sample measured in the same geometry. A shift in the peak position of the sample compared to  $\text{PuO}_2$  is clearly visible, indicating a higher oxidation state than the starting material of the reaction. To the best of our knowledge, no Pu(VI)  $M_5$  plutonate spectrum of a solid state sample has been reported before; compared to aqueous plutonyl species, the peak reported here for  $\text{Ba}_{2.875}\text{PuO}_{5.875}$  starts at the same energy, but the spectral feature labelled A is a bit broader [41]. The energy shift between A and B spectral features is with almost 4 eV similar to aqueous species. The Pu  $M_5$ -edge and  $L_3$ -edge spectra both indicate a pure Pu(VI) character for  $\text{Ba}_{2.875}\text{PuO}_{5.875}$ , supporting the first scenario formulated in the introduction (*vide supra*). The herein reported material should thus be understood as a stoichiometric compound  $\text{Ba}_{2.875}\text{PuO}_{5.875}$  or as an end member on the  $\text{BaO-An(VI)O}_3$  axis. If the actual stoichiometry would be a member of

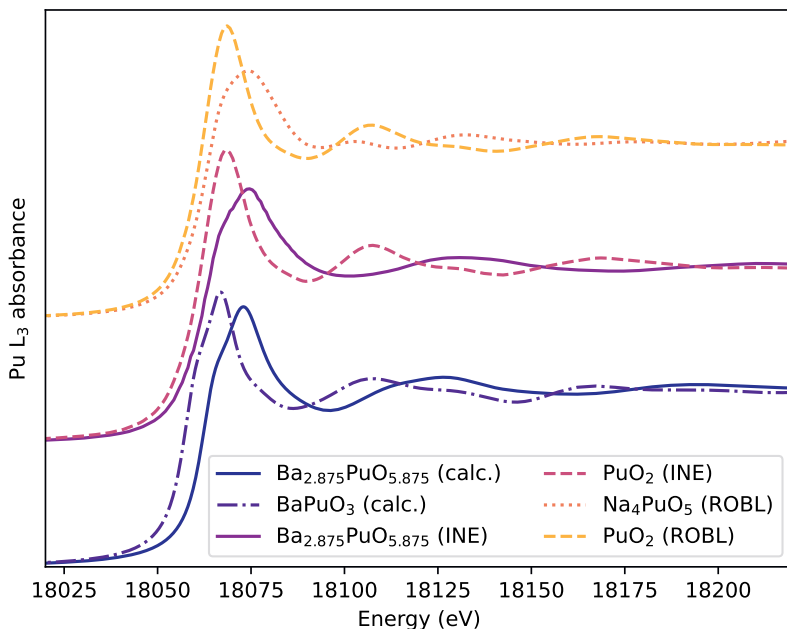


Figure 7.2: Pu  $L_3$ -edge spectra of  $\text{Ba}_{2.875}\text{PuO}_{5.875}$ . The XAS spectrum collected at the INE beamline of the KIT Light Source is compared to  $\text{PuO}_2$  measured at the same beamline [34], FDMNES calculations (calc.) of  $\text{Ba}_{2.875}\text{PuO}_{5.875}$  and  $\text{BaPuO}_3$ , and to Pu(IV) and Pu(VI) spectra from literature [12].

7

the line  $\text{BaAnO}_3\text{-Ba}_3\text{AnO}_6$  in Figure 7.1, like in scenario 2, the true compound would be  $\text{Ba}_2(\text{Pu}_{0.0625}^{4+}, \text{Pu}_{0.9375}^{6+}, \text{Ba}_{0.875})\text{O}_{5.8125}$  or  $\text{Ba}_2(\text{Pu}_{0.125}^{5+}, \text{Pu}_{0.875}^{6+}, \text{Ba}_{0.875})\text{O}_{5.8125}$ , meaning 6.25% Pu(IV) or 12.5% Pu(V) in the crystal structure instead of Pu(VI) only. The HR-XANES at the  $M_5$ -edge excludes scenario 2, as mixed oxidation states of over 5% should be clearly discernible. As scenario 3 includes scenario 1, it can neither be excluded nor confirmed. A further analysis of the Ba/Pu ratio has to be undertaken.

### 7.2.2. THE BA:PU RATIO

The X-Ray Diffraction pattern obtained after the last heat treatment at 1273 K of synthesis 1 is shown in Appendix D. The split main diffraction peak and the presence of multiple other minor peaks indicates that the cubic symmetry reported by Keller for  $\text{Ba}_3\text{PuO}_6$  [18], will not be able to explain the diffraction pattern found in this work. Gens *et al.* [26] reported a table with visually estimated relative intensities on a scale from 1 to 10, meaning all peaks with a relative intensity higher than 5% in our work should be compared. The early models proposed by Keller [18] and Gens *et al.* [26] consisted in a cubic cell corresponding to a 32-fold superstructure of the perovskite, but the latter authors mentioned peaks that cannot be indexed by this model. In spite of slight discrepancies in Bragg po-

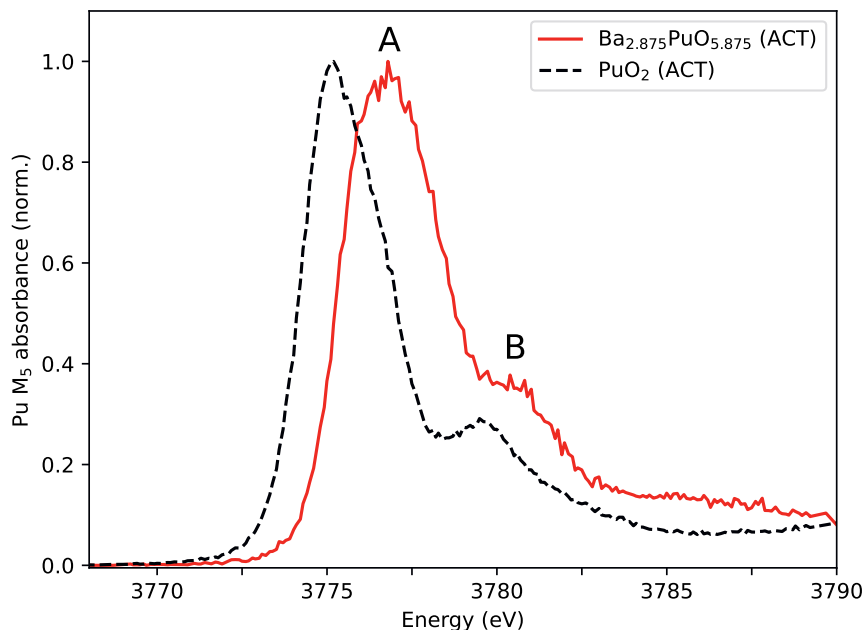


Figure 7.3: Pu  $M_5$ -edge spectrum of  $\text{Ba}_{2.875}\text{PuO}_{5.875}$ . The recorded HR-XANES spectrum is compared to the  $\text{PuO}_2$  spectrum measured in the same geometry. Both spectra are measured at the ACT station of the CAT-ACT beamline, KIT Light Source.

sition and intensity ascribable to the experimental conditions (see Appendix D), these peaks were also observed in the present work, along with some extra peaks. Given all reagents reacted to a product that is stable in the temperature window 1000–1270 K, it can be concluded that a pure product was formed that is the same or close to the material Gens *et al.* obtained. However, in-depth structural characterisation of the material is required to explain all peaks in the obtained diffraction pattern. As mentioned in the introduction, the crystal structure of  $\text{Ba}_3\text{UO}_6$  initially proposed to be cubic was later assigned lower symmetry. As a starting point to elucidate the crystal structure of the material obtained in this work, it was found, however, that all peaks could be matched using the tetragonal model of Treiber *et al.* [22] for BaO-deficient  $\text{Ba}_3\text{UO}_6$  in space group  $I4/mmm$  (139). Compared to the archetype perovskite structure  $\text{ABO}_3$  in Kröger-Vink notation, this model can be written as  $(\text{Ba}_A^x)(\text{Pu}_{B\ 8/16}\text{Ba}_{B\ 7/16}''\text{Va}_{B\ 1/16}'''')(\text{O}_{O\ 47/16}\text{Va}_{O\ 1/16}'''')$ . In this model, the cation vacancies ( $\text{Va}$ ) are located in the  $\text{Ba}_B$ -sublattice, while the anion vacancies are statistically distributed over the  $\text{O}_O$  sites. The Ba4 atoms shifted position by  $0.55\text{ \AA}$  towards the holes, while the U2 and U3 atoms moved respectively  $0.17$  and  $0.26\text{ \AA}$  in the direction of the holes [22]. Cell parameters for the obtained Pu-material could be successfully derived by a LeBail fit using the U-model in space group  $I4/mmm$ , but an initial Rietveld attempt to refine all atomic distances resulted in unrealistic bond

distances and, in particular, the low weight of the oxygen atoms compared to Pu and Ba resulted in high uncertainty on their positions. The model by Treiber *et al.* poses two problems that need clarification. First, the Ba:Pu ratio does not match our weighed target stoichiometry. Second, no discrimination between unit cells with the same reflection conditions was made using the LeBail fit. The absence of reflection conditions matches with the archetype space group  $I4/mmm$ , but also with numerous hemihedral tetragonal groups. Group-subgroup relationships via octahedral tilting were analysed for ordered double perovskites by Howard, Kennedy and Woodward in 2003 [42]. In their Figure 1, the only space group next to  $I4/mmm$  is  $I4/m$ , in which the loss of the vertical mirrors is due to geared rotations of the corner-connected octahedra along the four-fold axes. The resulting bending of the M-O-M linkages in the (001) planes is correlated to the inter-cations distances. Other types of group-subgroup relationships were found, but none strictly cover the current structure type [43–45].

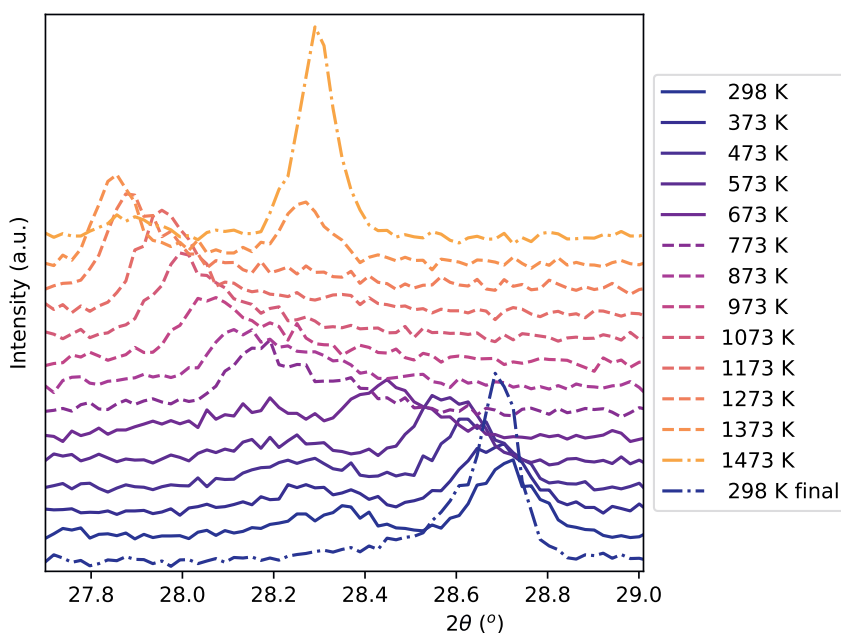
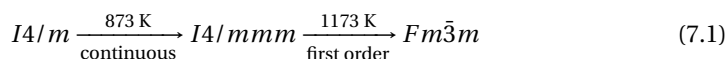


Figure 7.4: Shift of the main diffraction peak of  $\text{Ba}_{2.875}\text{PuO}_{5.875}$ . The material is from synthesis 1 after 1200 K and is measured at various increasing temperatures; the measurement after the heating rate (298 K final) is shown as well. The different line-styles are a guide to the eye to the phase transitions proposed in the main text.

XRD data were collected up to 1473 K with the aim to get more insight in possible phase transitions and the thermal expansion of the material. In Figure 7.4, the shift of the main diffraction peak ((224) reflection) at increasing temperature is shown. Starting at 298 K, the *supra* described pattern was found. The peak at  $28.7^\circ$   $2\theta$  shifted to lower an-

gle upon heating to 673 K. At higher temperatures, the relative intensities of the left and right peak change, up to 1373 K. At 1373 K, the rise of a peak at  $28.3^\circ 2\theta$  was observed, which resulted in a single, more intense peak at 1473 K. After cooling, it was found that the structure changed irreversibly, as only a single intense peak at  $28.7^\circ 2\theta$  was visible. This means that there are at least two phase transitions in the studied temperature window; however, the diffraction data quality does not allow for full elucidation of the crystal pattern, because many low-intensity peaks are not observed with the current signal-to-noise ratio. The group-theoretical considerations explain the possible phase transition pathway, however. As explained, the diffraction pattern obtained at room temperature after heating till 1270 K can be indexed in the space groups  $I4/m$  and  $I4/mmm$ . For the double perovskite  $\text{Sr}_2\text{CuWO}_6$ , the structure was found to evolve as [46]:



The first transition means a change from a space group that allows for both deformations and rotations of the octahedra ( $I4/m$ ) to a space group that allows for only deformations of the octahedra ( $I4/mmm$ ) and it should be a continuous, reversible, second order transition. Symmetry breaking can lower the energy of the electronic state, usually with an odd number of electrons in degenerate states as in the cited example of  $\text{Sr}_2\text{CuWO}_6$  with  $\text{Cu}^{2+}$  in a  $d^9$ -system. The  $\text{Pu}^{6+}$  electron configuration of  $[\text{Rn}]5f^2$  is interpreted as a non-degenerate singlet ground state based on magnetic susceptibility measurements (*vide infra*), so the mechanism is not driven electronically in the current case. The second transition seems a transition to the ideal cubic perovskite structure, although the present data does not allow for full assignment.

Although we propose a slightly different stoichiometry, it can be hypothesised with caution that the cubic crystal structure by Keller may correspond to our material obtained after heat treatment at 1423 K or higher, so the material has passed an irreversible phase transition temperature, as opposed to Gens *et al.* [26] and the initial material obtained in the current work, which were both obtained at lower temperatures. In addition to this, Keller makes the general statement that after the end of reaction, the samples were quenched [18]. Thus, high-temperature X-ray diffraction hints at the assignment of space group  $I4/m$  to the room-temperature crystal structure of  $\text{Ba}_{2.875}\text{PuO}_{5.875}$  and allows to determine the cell parameters of a rather big cell. Smaller cell parameters seem not to be possible because the peaks in between  $20$  and  $30^\circ 2\theta$  have odd Miller indices.

The following model for the room temperature crystal structure of  $\text{Ba}_{2.875}\text{PuO}_{5.875}$  is developed: The crystal structure can be thought of as an array of Pu and Ba1, Ba2 and Ba3 atoms occupying the centres of  $15/16^{\text{th}}$  of the corner-connected oxygen octahedra that build a  $\text{ReO}_3$ -like structure, while Ba4 and Ba5 occupy the so-formed 12-oxygen polyhedra, thus building a perovskite-related structure with structural formula  $(\text{Pu}_{1/2}\text{Ba}_{7/16}\text{Va}_{1/16})\text{BaO}_{47/16}$ . The tetragonal symmetry is subject to the presence of four-fold axes, several of which have Pu and Ba atoms. Following Howard and Carpenter [45], the only tetragonal subgroup of the  $I4/mmm$  archetype form compatible with the preservation of these axes is  $I4/m$  (Table 7.2), in which the  $.m$  and  $..m$  mirrors in particular would disappear, thus allowing the  $\text{PuO}_6$  octahedra to tilt around the  $[001]$  direction. This distortion could be evidenced by localising the oxygen equatorial corners, but the low atomic mass of these atoms compared to plutonium and barium does not allow to

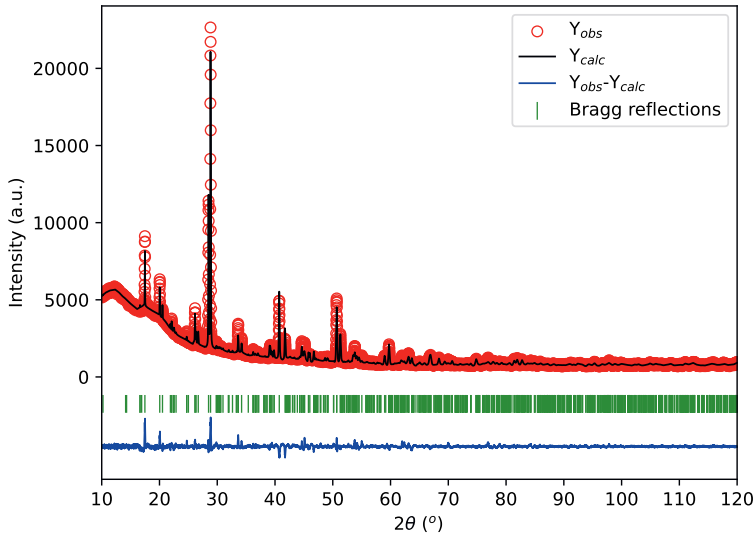


Figure 7.5: XRD pattern of  $\text{Ba}_{2.875}\text{PuO}_{5.875}$  with profile refinement. Experimental ( $Y_{obs}$ , in red) and calculated ( $Y_{calc}$ , in black) powder XRD patterns of  $\text{Ba}_{2.875}\text{PuO}_{5.875}$  at ambient temperature. The sample is taken from the material obtained from synthesis 2 after 1323 K. Measurement at  $\lambda = \text{Cu K}\alpha_1$ . The angular positions of Bragg reflections are shown in green. The difference between calculated and experimental intensities  $Y_{obs} - Y_{calc}$  is shown in blue for the Rietveld refinement in space group  $I4/m$ . The uncertainties on optimised cell parameters and atomic positions are given in Tables 7.1 and 7.2.

Synthesis	a (Å)	c (Å)	V (Å <sup>3</sup> )
Synthesis 1	12.502(3)	17.280(4)	2700.8(1.1)
Synthesis 2	12.5187(15)	17.298(2)	2710.8(6)

Table 7.1: Cell parameters obtained at ambient temperature for synthesis 1 and synthesis 2.

observe them from the present XRD data; in other words, no tilt can be evidenced. On the opposite, heavy plutonium ( $Z = 94$ ) and barium ( $Z = 56$ ) can be located far more precisely, but most of them occupy fixed positions in both space groups, which makes them insensitive to the possible distortion (Table 7.2). The only relevant markers appeared to be Ba<sub>4</sub>, Ba<sub>5</sub> and Pu<sub>3</sub>, which could shift from their ideal  $.m.$  or  $..m$  mirror position in the  $I4/m$  symmetry.

The crystal structure was therefore refined in the latter space group, except for the oxygen atoms, which were fixed on the ideal positions defined by Treiber *et al.* [22]. The diffraction patterns of the materials obtained in synthesis 1 at 1273 K and in synthesis 2 at 1323 K were used and the refinement against the latter is shown in Figure 7.5, while the former is shown in the Appendix D. Cell parameters are given in Table 7.1. The cell volumes between the syntheses differ less than 1 %. The quality of the fit is moderate because of the signal-to-noise ratio that did not allow to observe significant

	Ba1	Ba2	Ba3	Ba4	Ba5	Pu1	Pu2	Pu3
<i>I4/mmm</i>	0 0 0	0 $\frac{1}{2}$ 0	$\frac{1}{4}$ $\frac{1}{4}$ $\frac{1}{4}$	<b>0 y z</b>	<b>0 y z</b>	0 $\frac{1}{2}$ $\frac{1}{4}$	0 0 z	<b>x x 0</b>
	2a	4c	8f	<b>16n</b>	<b>16n</b>	4d	4e	<b>8h</b>
	4/mmm	mmm.	..2/m	<b>.m.</b>	<b>.m.</b>	-4m2	4mm	<b>m.2m</b>
<i>I4/m</i>	0 0 0	0 $\frac{1}{2}$ 0	$\frac{1}{4}$ $\frac{1}{4}$ $\frac{1}{4}$	<b>x y z</b>	<b>x y z</b>	0 $\frac{1}{2}$ $\frac{1}{4}$	0 0 z	<b>x y 0</b>
	2a	4c	8f	<b>16i</b>	<b>16i</b>	4d	4e	<b>8h</b>
	4/m..	2/m..	-1	<b>1</b>	<b>1</b>	-4..	4..	<b>m..</b>
Optimised positions synthesis 1				x = -0.006(5) y = 0.229(3) z = 0.389(2)	x = 0.024(4) y = 0.290(4) z = 0.143(3)		x = 0 y = 0 z = 0.247(2)	x = 0.247(3) y = 0.235(4) z = 0
Optimised positions synthesis 2				x = -0.023(3) y = 0.209(3) z = 0.399(2)	x = 0.002(6) y = 0.270(3) z = 0.132(6)		x = 0 y = 0 z = 0.240(2)	x = 0.234(3) y = 0.240(4) z = 0

Table 7.2: Refined atomic positions, Wyckoff symbol and local symmetry of the heavy atoms in the *I4/mmm* and *I4/m* space groups. Discriminant positions between the two space groups are highlighted in bold characters. Ba6 is completely empty.

reflections beyond  $2\theta \approx 90^\circ$ . Solving the structure, in particular, the determination of the space group, was made difficult by several factors linked to the nature of the sample. On the one hand, the very small amount of material, the unusual geometry and the resin-embedded sample resulted in somewhat imprecise XRD data, with regard to the usual data collection standards. On the other hand, the overwhelming presence of heavy barium and very heavy plutonium atoms resulted in an exceedingly high contrast with lighter oxygen atoms, that hampered the determination of their position. This proved particularly critical when it came to deciding whether the oxygen atoms were located or not on the special positions corresponding to the vertical mirrors of the *I4/mmm* space group. For these reasons, the oxygen atoms were assigned to these fixed ‘ideal’ positions. According to the estimated standard uncertainties on atomic positions, the Ba and Pu atoms were rather correctly located this way, but secondary parameters like their atomic displacement parameters obviously suffered of this non-ideal procedure. The refined atomic positions for the Ba and Pu ions are given in Table 7.2; all the standard uncertainties given by FullProf were multiplied by Bérar and Lelann’s statistic factor for the sake of realism [47]. The difference between *I4/mmm* and *I4/m* for the Ba3, Ba4 and Pu3 atoms is small but measurable. Pu3 is almost on its ideal position ( $y \approx x$ ), while the difference for Ba4 and Ba5 ( $y - x - 0.25$ ) is more significant. Typical metal-metal bond distances are given in Table 7.3, where they are compared with the EXAFS refinement. Although these results tend to support the *I4/m* symmetry for the room-temperature form, this hypothesis cannot be considered a certainty due to the relatively high standard deviations in regard to the measured atoms shifts. Visualisations of the crystal structure are shown in Figure 7.6.

This model gives a rather good fit to the experimentally measured diffraction pattern, but the Ba:Pu ratio does not correspond to the weighed amounts of material and proper composition and molar mass are important for the (thermo)physical properties. Therefore, it was attempted to refine the model in such a way that the B-site of the perovskite contains vacancies, but the Ba:Pu ratio remains 3:1 overall, i.e. change the occupancy factors to  $\text{Ba}_2(\text{Ba}_{\frac{29}{32}}\text{Pu}_{\frac{31}{32}}\text{Va}_{\frac{4}{32}})\text{O}_{5\frac{26}{32}}$  instead of  $\text{Ba}_2(\text{Ba}_{\frac{28}{32}}\text{Pu}_{\frac{32}{32}}\text{Va}_{\frac{4}{32}})\text{O}_{5\frac{28}{32}}$  as refined by Treiber *et al.* for the U-analog. Since the Ba and Pu atoms are both heavy but still differ

a lot in atomic number, this effect may be measurable by refining the occupancy factors of the respective lattice positions. Technically, this means refining the 3 Pu sites with a  $Pu_{1-x}Ba_x$  mix. This attempt did not result in an improvement of the fit. Moreover, the empty Ba-site was tested for excess electron density but it turned out to be completely empty.

BaO-deficiency is thus justifiable by the XRD pattern, and a number of possible explanations for the concomitant BaO-loss during the synthesis have been suggested. First of all, Keller wrote that  $Ba_3PuO_6$  is stable under Ar until 1673 K, above which temperature oxygen loss takes place with formation of  $BaPuO_3$ . In our case, the material does not even reach this temperature. The vaporisation behaviour of the related compound  $BaPuO_3$  was studied by Nakajima *et al.* [48], who observed  $Ba(g)$  and  $BaO(g)$  vapour species. At 1673 K, the total vapor pressure is still lower than 1 Pa. Interaction with the alumina crucible is highly unlikely, even if the phase diagram gives possible  $Al_2O_3$ -BaO phases [49], because the crucibles are high-fired ceramic materials. Thirdly, the formation of an amorphous phase was considered but judged unlikely. Next to this, the Ba:Pu ratio was analysed by Gens *et al.* during their synthesis and they found a 3:1 ratio [26]. Recently, in the synthesis of  $BaPuO_3$  and  $SrPuO_3$ , stoichiometric excesses of 7.5 and 10% of the respective earth alkali oxalates were added to obtain a stoichiometric compound [8]. Similarly, an excess  $BaCO_3$  was added during the synthesis of  $BaThO_3$  [17]. Gens *et al.* write about slow heating to avoid Ba-losses, which they seem to confirm with their elemental analysis [26]. A close look at the crystal structure proposed in this work for  $Ba_{2.875}PuO_{5.875}$  reveals that the large Ba-atoms move towards the empty Ba-sites. Therefore, we conjecture that the empty Ba-sites are necessary to allow for a stable structure and the material obtained in this work for both syntheses should be treated as a stoichiometric compound with a Ba:Pu ratio of 2.875:1. From electrostatic considerations, disappearance of 1 Ba is accompanied by 1 oxygen, for which statistical distribution should be assumed with the current data.

As Pu-O distances are inherently difficult to study using XRD, the EXAFS signal at the Pu  $L_3$ -edge was analysed to obtain insights into the local Pu environment. The EXAFS and Fourier-transformed spectra at the Pu  $L_3$ -edge are shown in Figure 7.7, together with the fit to the data. Bond lengths are reported in Table 7.3 and compared to refined interatomic distances from XRD if possible. The scattering paths for Pu1, Pu2 and Pu3 contribute 25%, 25% and 50%, respectively, to the total EXAFS signal. Only an average Pu-O distance was refined in each case for the first coordination shell, given the complexity of the structure, the lack of information from XRD on the oxygen positions, and the expected similar distances. The Pu sites are in all cases six-fold coordinated. A common Debye-Waller factor was imposed for all oxygen atoms. This resulted in a fit with indistinguishable distances for Pu1-O and Pu3-O at 2.01(1) Å, and a Pu2-O distance of 2.4(3) Å. Using Shannon's ionic radii, the Pu-O distance is expected to be about 2.11 Å [50], which means that the Pu-O distances obtained for  $Ba_{2.875}PuO_{5.875}$  are in a physically realistic range. In addition, Pu-Ba distances in the second coordination shell could also be captured with the fit. Here again, some simplifications were made to account for indistinguishable distances. Pu1 is surrounded by 14 Ba atoms: 2 Ba2 + 4 Ba3 at a distance of 4.51(9) Å, 4 Ba4 at 3.9(5) Å and 4 Ba5 at 3.43(9) Å. Similarly, for Pu2 the Ba4 and Ba5 distances were merged, yielding 3.8320(8) Å, while the Pu1-Ba3 distance equals 4.28(15)

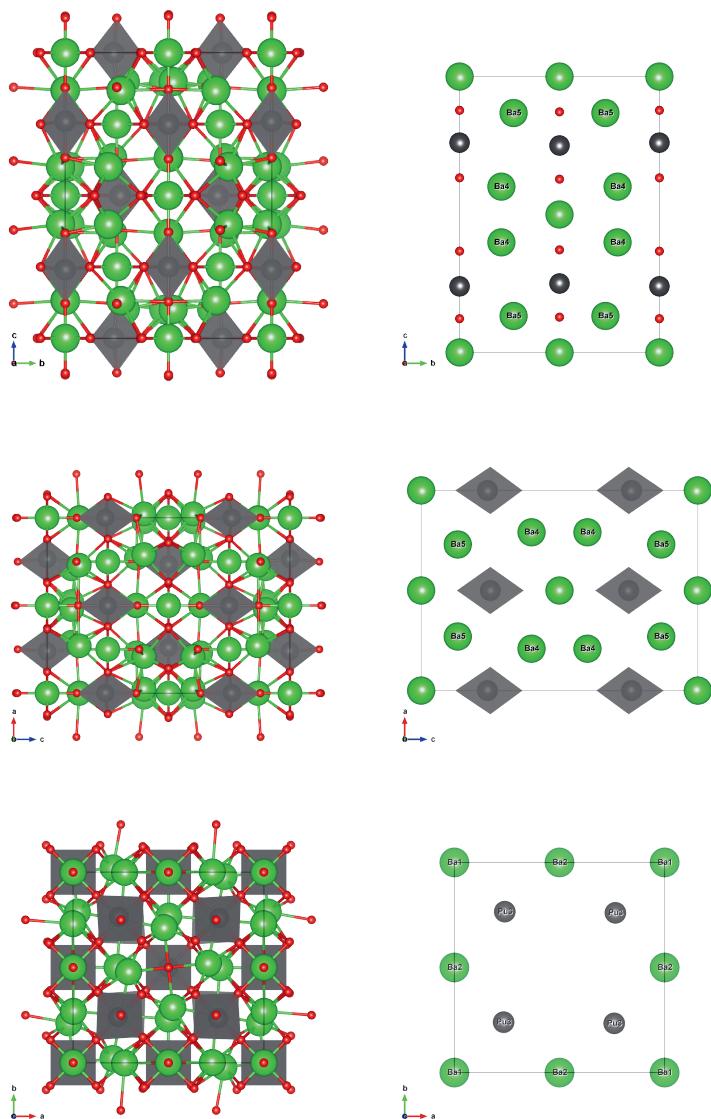


Figure 7.6: Crystal structure of  $\text{Ba}_{2.875}\text{PuO}_{5.875}$  obtained after refinement in space group  $I4/m$ . Left, from top to bottom: views along the  $a$ ,  $b$ , and  $c$  axes. Right, from top to bottom: visualisation of the 100, 010 and 001 faces. Ba4 and Ba5 are the atoms shifted with respect to space group with extra symmetry elements  $I4/mmm$ .

Scattering Pathway		CN	Distance EXAFS (Å)	Debye-Waller factor (Å <sup>2</sup> )	Distance XRD	
					synthesis 1	synthesis 2
Pu1+Pu3	O	2x6	2.014(10)	0.0045(12)	not refined	
Pu2	O	6	2.4(3)	0.0045(12)	not refined	
Pu1	2Ba2+4Ba3	6	4.51(9)	0.015(15)	4.42016(11)	4.42605(6)
	Ba4	4	3.9(5)	0.002(15)	4.161(11)	4.469(10)
	Ba5	4	3.43(9)	0.008(7)	3.229(13)	3.524(11)
Pu2	Ba3	4	4.28(6)	0.008(11)	4.42044(16)	4.4296(4)
	4Ba4+4Ba5	2x4	3.82(7)	0.002(15)	3.770(13)	3.812(12)
	Ba5	-	-	-	4.057(14)	3.859(12)
Pu3	Ba3	2	3.9(5)	0.008(12)	4.3242(6)	4.3307(7)
	Ba4	2	3.53(9)	0.002(15)	3.77(3)	3.520(16)
	Ba5	4	3.68(10)	0.0029(10)	3.780(17)	3.72(2)

Table 7.3: Bond lengths and Debye-Waller Factors obtained from the fit to the EXAFS data.  $\Delta E_0 = -2.93$  eV. The R-factor for this data set equals 0.02180.

Å. The distances Pu3-Ba3, Pu3-Ba4 and Pu3-Ba5 equal 3.9(5), 3.531(12) and 3.67(5) Å, respectively. Comparison between distances obtained via XRD data refinement and EXAFS data refinement yields the same distances within error in most cases. Combining the determination of the average Pu oxidation state with the Ba/Pu ratio locates the obtained material thus on a unique position in Figure 7.1 and allows to further study its physical properties. In the remainder of the article, the stoichiometry and molar mass of net  $\text{Ba}_{2.875}\text{PuO}_{5.875}$  is used for all analyses.

7

### 7.2.3. PHYSICAL PROPERTY MEASUREMENTS

The high-temperature XRD was further analysed in order to obtain the thermal expansion coefficient of the material. Because of the large unit cell and the two phase transitions that seem to occur, it was not trivial to establish the thermal expansion coefficients. The data from room temperature up to 673 K was refined using space group  $I4/m$ , while the data up to 1273 K was refined using  $I4/mmm$ . The pattern at 1373 K was multiphase. The pattern at 1473 K was indexable using DICVOL as cubic with cell parameter 4.4327 Å, with 1 peak unaccounted for ( $2\theta = 27.8^\circ$ ) [51]. The pattern obtained after cooling was not indexable as cubic, but as tetragonal with cell parameters  $a = 4.3865$  Å and  $c = 17.6094$  Å. The obtained volume as function of temperature and relative expansion of the  $a$ - and  $c$ -axes are shown in Figure 7.8. Towards the first phase transition, the volume increases non-linear, mainly caused by the  $c$ -axis expansion, while after the phase transition, the axes expand linearly. A single volumetric thermal expansion coefficient of  $\alpha_V = 7 \cdot 10^{-5} \text{K}^{-1}$  fits the data rather well. This is about twice as high as  $\text{BaThO}_3$ ,  $\text{BaUO}_3$ ,  $\text{BaZrO}_3$  and  $\text{BaCeO}_3$ , with linear thermal expansion values of  $11.9 \cdot 10^{-6} \text{K}^{-1}$ ,  $11.01 \cdot 10^{-6} \text{K}^{-1}$ ,  $7.13 \cdot 10^{-6} \text{K}^{-1}$  and  $11.2 \cdot 10^{-6} \text{K}^{-1}$ , respectively [52–54]. These values are close to the thermal expansion coefficients of the actinide dioxides [55], and rather high when compared to uranium-containing double perovskites [56, 57]. The most interesting comparison is with high-temperature X-ray diffraction on  $\text{Sr}_3\text{UO}_6$ , measured under both oxygen-rich and reducing atmospheres [58]. This compound has a volumetric thermal

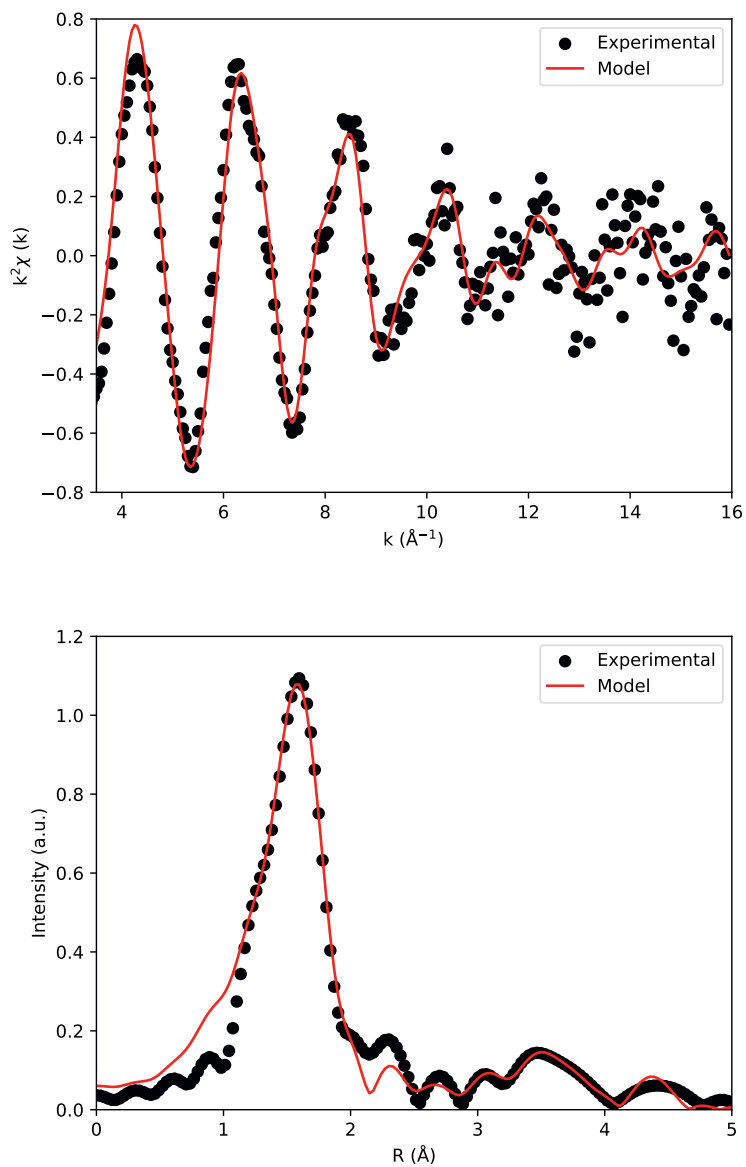


Figure 7.7: The extracted (black dots) and fitted (red line) EXAFS signal of  $\text{Ba}_{2.875}\text{PuO}_{5.875}$ .

expansion of  $33 \cdot 10^{-6} \text{ K}^{-1}$ , but seems also able to lose oxygen under inert or reducing conditions. The high thermal expansion of  $\text{Ba}_{2.875}\text{PuO}_{5.875}$  compared to  $\text{BaMO}_3$  can be explained by the unusual high amount of Ba for a perovskite: half of the medium-size, high-charge M cations are replaced by big, low-charge Ba-ions that make weaker bonds to oxygen and are more prone to thermal expansion. The anisotropic expansion hints at antiferrodistorsive behaviour. A tentative Landau model with the  $c$ -axis distortion as order parameter with  $T_c = 758 \text{ K}$  is proposed (Appendix D). This mechanism supposed the Ba4 and Ba5 atoms to align from their position in  $I4/m$  to the  $I4/mmm$  form. The twisted  $c$ -directed chains straighten, therefore expanding faster than the other axes. Beyond the transition, the chains should be straight along the 3 axes, so the expansion becomes similar.

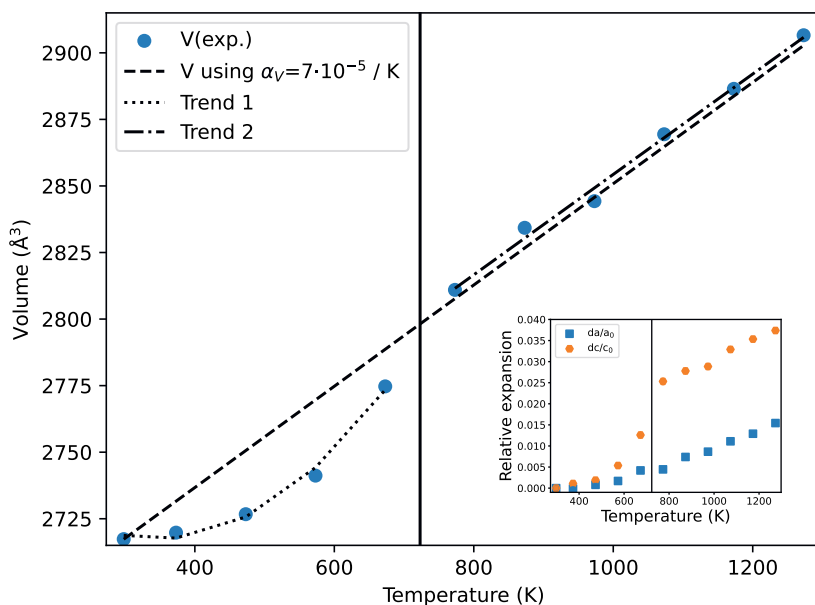


Figure 7.8: The thermal expansion of  $\text{Ba}_{2.875}\text{PuO}_{5.875}$  as measured in this work. See for explanation of the fits in the main text. Inset: Relative expansion of the  $a$ - and  $c$ -axes with temperature. The vertical line in both figures indicates the tentative first transition  $I4/m \rightarrow I4/mmm$ . Trend 1 and Trend 2 are a guide for the eye. If not visible, the standard deviations are smaller than the data points.

The low-temperature heat capacity of  $\text{Ba}_{2.875}\text{PuO}_{5.875}$  obtained using PPMS is shown in Figure 7.9. No anomalies were observed in the measured temperature window, and the  $C_p(T)$  increases with temperature, yielding a value slightly above the classical Dulong-Petit value for  $C_v$  at ambient temperature. There is a small artefact between 47 and 61 K that is ascribed to the machine; these data points are excluded in all fits and calculations. The commonly used strategy to compare the heat capacity of complex oxides to the sum of simple oxides (Neumann-Kopp) cannot be used directly, since  $\text{PuO}_3$  does

not exist. The heat capacity was fit to a polynomial from the lowest measured temperature up to 14 K and to a combination of one Debye and three Einstein fits in the temperature range 14 to 270 K. The difference between the fit and the experimental data is shown in the inset in Figure 7.9. Based on these fits, the heat capacity at 298.15 K  $C_p(T) = (251 \pm 8) \text{ J} \cdot \text{K}^{-1} \cdot \text{mol}^{-1}$ , and the standard entropy  $S_m^0 = (318 \pm 8) \text{ J} \cdot \text{K}^{-1} \cdot \text{mol}^{-1}$  (see Figure 7.10) are derived. Heat capacity data at high temperature for  $\text{Ba}_{2.875}\text{PuO}_{5.875}$  have not been reported. Data for similar alkaline-earth actinide oxide compounds are limited to  $\text{Ba}_3\text{UO}_6$  and  $\text{Ba}_{2.875}\text{UO}_{5.875}$ . Dash and Singh reported the low-temperature heat capacity of these two compounds from 127 to 303 K measured by DSC and joined this to high-temperature heat capacity [59]. As is shown in Figure S.6, the heat capacities of  $\text{Ba}_3\text{UO}_6$  and  $\text{Ba}_{2.875}\text{PuO}_{5.875}$  are almost equal at 125 K, but the reported heat capacity of  $\text{Ba}_3\text{UO}_6$  flattens faster and reaches a point close to the Neumann-Kopp value for  $\text{Ba}_3\text{UO}_6$  of  $222.85 \text{ J} \cdot \text{K}^{-1} \cdot \text{mol}^{-1}$  based on  $\text{BaO}$  and  $\gamma\text{-UO}_3$  [60, 61].

In Figure 7.11 the heat capacity close to 0 K is shown as  $C_p/T$  versus  $T^2$ . In case of a perfectly insulating crystalline material, the signal should intersect the origin, *i.e.*  $\gamma = 0$ . For this freshly annealed  $\text{Ba}_{2.875}\text{PuO}_{5.875}$ , a very minor excess towards lower temperature is found and a linear fit gives  $4.2 \text{ mJ} \cdot \text{K}^{-1} \cdot \text{mol}^{-1}$ , which may be attributed to disorder, the origin of which are structural vacancies of the oxygen sublattice or Frenkel pairs created by radioactive decay of the actinides ( $^{239}\text{Pu}$ ,  $^{241}\text{Am}$ ) [62, 63]. As can be seen in the Figure, however, with an applied field of 14 T the heat capacity shows a very pronounced upturn. The fact that the addendum curve was only collected at 0 T cannot account for such a pronounced effect, indicating some physical explanation should be given for this upturn towards 5 K. This upturn cannot be explained by disorder due to radiation damage, as there is no significant difference between a measurement after a few days after annealing and a week after annealing with no applied field, ruling out this as the main source. The low-temperature upturn may be attributed to a maximum below 5 K at 0 T, shifted to slightly higher temperatures at 14 T. This is reminiscent of behaviour of the Schottky-anomaly in  $\text{CePO}_4$  under magnetic field [64] and atypical for a magnetic transition [65]. If a Schottky anomaly is assumed in  $\text{Ba}_{2.875}\text{PuO}_{5.875}$ , an herein small, unquantified entropy term corresponding to a Schottky anomaly should be added to the supra calculated standard entropy at 298.15 K. This small entropy term depends on the degeneracy of the energy split, most probably of the  $^3H_4$  ground state of the  $[\text{Rn}]5f^2$  ion.

The temperature dependence of the magnetic susceptibility  $\chi_{\text{measured}} - \chi_{\text{diamagnetic}}$  of  $\text{Ba}_{2.875}\text{PuO}_{5.875}$  is shown in Figure 7.12, while a plot of  $1/\chi$  versus temperature is shown in Figure 7.13. The magnetisation curve is shown in the inset in Figure 7.12. The magnetisation curve was obtained by increasing the field up to 70 kOe, decreasing to -70 kOe and increasing to 0 kOe. The curves overlap. The observed magnetic behaviour classifies the studied material best as paramagnetic. The formal oxidation state of Pu(VI) translates to an electron configuration of  $[\text{Rn}]5f^2$ , and with an even number of electrons and singlet ground state, there are no unpaired electrons and therefore there is no reason to assume local magnetic moments and apply the Curie-Weiss law. Nevertheless, as the shape of the susceptibility after subtraction of the diamagnetic contribution is similar in shape to Curie-Weiss behaviour, the data obtained at 70 kOe was fitted to:

$$\chi_M = \frac{C}{T} + \chi_0 \quad (7.2)$$

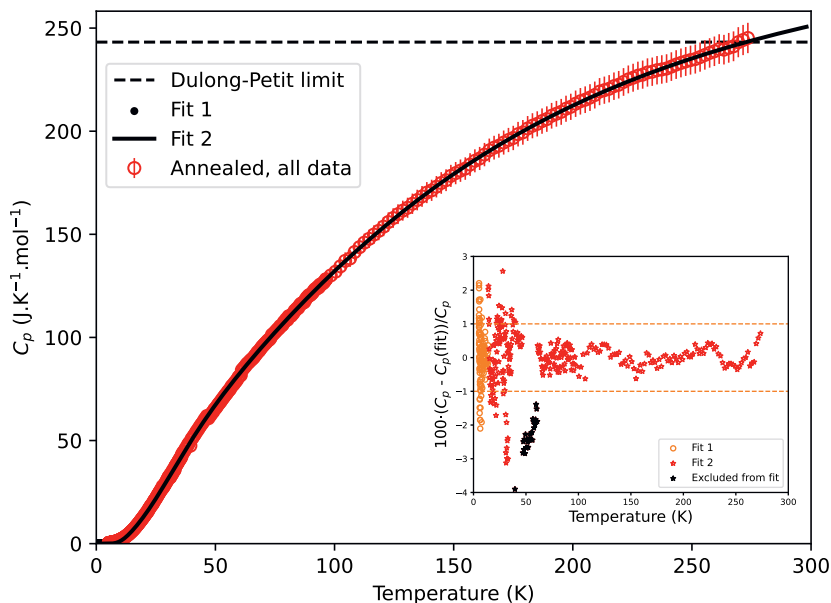


Figure 7.9: Heat capacity of  $\text{Ba}_{2.875}\text{PuO}_{5.875}$ . The heat capacity as measured in this work is shown and fitted to a polynomial fit (fit 1) and a combined Debye-Einstein fit (fit 2) with comparison to the classical Dulong-Petit limit. See for explanation of the fits the main text. The error bar represents a 3% error on the heat capacity as explained in the main text. Inset: Relative difference between the experimental heat capacity data and the polynomial and combined Debye-Einstein fit.

7

The fitting parameters are  $C = 0.0090 \text{ emu}\cdot\text{mol}^{-1}\cdot\text{K}^{-1}$  and a temperature-independent contribution  $\chi_0 = 121\cdot 10^{-6} \text{ emu}\cdot\text{mol}^{-1}$ . The uncertainty on  $\chi_0$  should include the estimation of the estimated  $\chi_{dia}$  as described *supra*. As far as the current authors are aware, no full temperature-dependent magnetic susceptibility curve of a Pu-based  $5f^2$  system has been reported, making good comparison difficult [66, 67]. However,  $5f^2$ -systems based on U have been reported [68]. Moreover, Hinatsu and Edelstein discuss the magnetic susceptibility of (impurity)  $\text{Np}^{5+}$  in their study into  $\text{Ba}_3\text{NpO}_6$  [69]. They write that if a  $5f^2$  ion is octahedrally coordinated by six oxygens, its susceptibility shows a large temperature independent paramagnetism (TIP) over a wide temperature range. To give rise to magnetic ordering in oxide actinide system, the distance An-An should be less than 450 pm, as is summarised for  $[\text{Rn}]5f^1$  and  $[\text{Rn}]5f^3$  configurations by Keller [9]. Therefore,  $\text{Ba}_3\text{NpO}_6$  also has no magnetic ordering because of the too long Np-Np distance. Theoretically, the Pu-Pu distance in the  $\text{Ba}_{2.875}\text{PuO}_{5.875}$  host could be minimised by a non-standard ordering of Pu in octahedral sites, forming chains instead of being in a rock-salt fashion with Ba. Since the distance for fully oxidised Pu(VI) would already result in too long Pu-Pu distances, the magnetic behaviour cannot be explained by diluted Pu(V) contributions ( $[\text{Rn}]5f^3$ ) in the crystal structure.

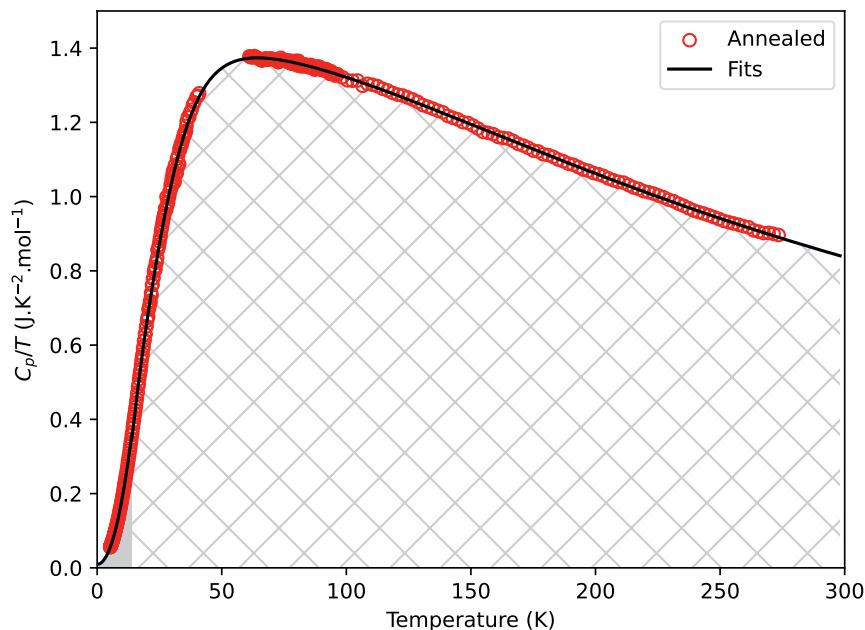


Figure 7.10: Heat capacity of  $\text{Ba}_{2.875}\text{PuO}_{5.875}$  as plotted in  $C_p/T$  vs.  $T$ . The shaded areas represent the contributions to the standard entropy as calculated using the two fits in their respective domains. See main text for explanation of the fits.

### 7.3. CONCLUSIONS

Proper study of Ba-An-O perovskite related phases needs to account for the average formal An oxidation state and the Ba/An ratio. In the attempt to synthesise  $\text{Ba}_3\text{PuO}_6$ , a perovskite-related phase with the actual composition  $\text{Ba}_{2.875}\text{PuO}_{5.875}$  was found. This alkaline-earth plutonium containing perovskite-related phase  $\text{Ba}_{2.875}\text{PuO}_{5.875}$  has been synthesised for the first time using solid state synthesis starting from  $\text{BaCO}_3$  and  $\text{PuO}_2$ . X-ray Absorption Spectroscopy at the Pu  $M_5$  and  $L_3$  edges showed Pu to be present as Pu(VI). The  $\text{Ba}_{2.875}\text{PuO}_{5.875}$  spectra were like '-ate' species and agree well with FDMNES calculations. The Ba/Pu ratio was indirectly deduced from the analysis of the XRD pattern which was best modelled by introducing BaO deficiency. The positions of the heavy metal atoms Ba and Pu in the crystal structure were refined in space group  $I4/m$  instead of  $I4/mmm$  proposed for the U-analog, yielding an overall satisfactory model with ordered empty Ba-sites. The change of the space group with temperature was proposed based on high-temperature X-Ray Diffraction measurements. The EXAFS data are in line with the FDMNES calculations and the local Pu-environments derived from crystallography were found to yield a good model to the EXAFS data. The low-temperature heat capacity was measured, yielding the heat capacity and standard entropy at 298.15

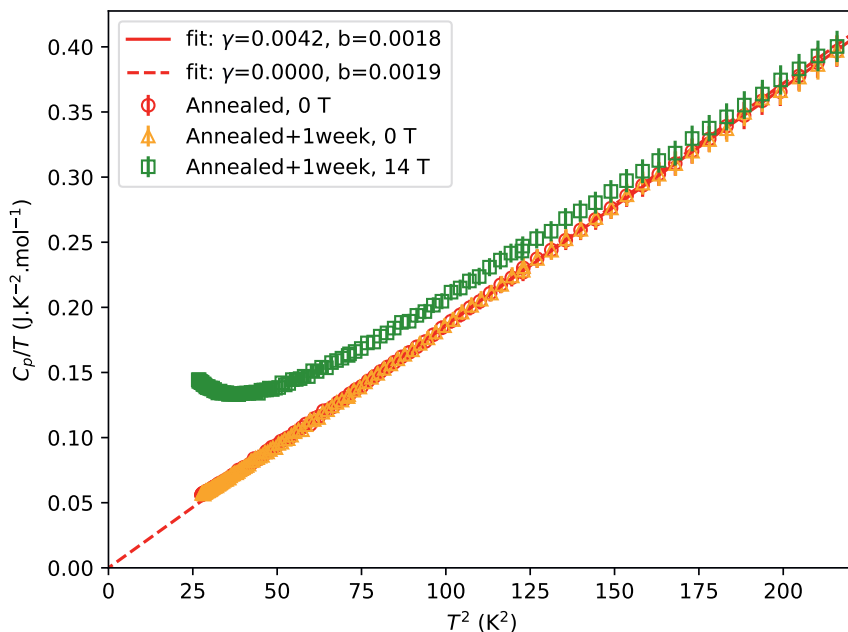


Figure 7.11: Heat capacity of  $\text{Ba}_{2.875}\text{PuO}_{5.875}$  as plotted in  $C_p/T$  vs.  $T^2$  in the low-temperature limit. The error bar is determined based on the 3% error on the heat capacity as explained in the main text.

7

K. Moreover, the magnetic susceptibility was measured, which is the first reported full temperature-dependent curve for a  $[\text{Rn}]5f^2$  Pu-based compound.

## EXPERIMENTAL DETAILS

**Synthesis** 218.7 mg  $\text{BaCO}_3$  (Merck, 99.98% trace metal basis) and 100 mg  $\text{PuO}_2$  (see Appendix D) were weighed and thoroughly mixed to obtain  $\text{Ba}_{3.0}\text{Pu}_{1.0}\text{O}_6$ . The mixture was subsequently heated in simulated air in a furnace at 900, 1000, 1100 and 1200 K for 48 h at each step. After each thermal treatment, XRD analysis was performed. After the thermal treatment at 1200 K, part of the product was separated for an additional thermal treatment at 1273 K for another 48 h. This synthesis will be referred to as synthesis 1. All spectroscopic and physical analyses have been performed on this batch.

38.2 mg of this reaction mixture of 3.0  $\text{BaCO}_3$  and 1.0  $\text{PuO}_2$  was heated in simulated air from room temperature to 1773 K using a Netzsch STA 449C thermogravimetric analysis apparatus to study the thermal behaviour using heating and cooling rates of 10 K/min. Pt-PtRh (10%) was used as thermocouple for temperature control. The experimental error is less than 1 percent on temperature and mass reading.

A second mixture was made using 39.6 mg  $\text{BaCO}_3$  and 18.6 mg  $\text{PuO}_2$ , which corresponds to  $\text{Ba}_{2.9}\text{Pu}_{1.0}\text{O}_6$ . This mixture was thermally treated in simulated air at 1273 K for 48h and at 1323 K for 24 h. After each step, XRD analysis was performed. This second synthesis will be referred to as synthesis 2; material from this synthesis was only used for room-temperature X-ray Diffraction.

**X-Ray Diffraction** Powder X-Ray diffraction (XRD) at ambient temperature was measured using a Bruker D8 X-ray diffractometer mounted in the Bragg-Brentano configuration with the  $\text{Cu K}\alpha_1$  radiation (40 kV, 40 mA,  $\text{Ge}(111)$  monochromator). About 10 mg of the specimen was immobilised in bi-component epoxy resin on a

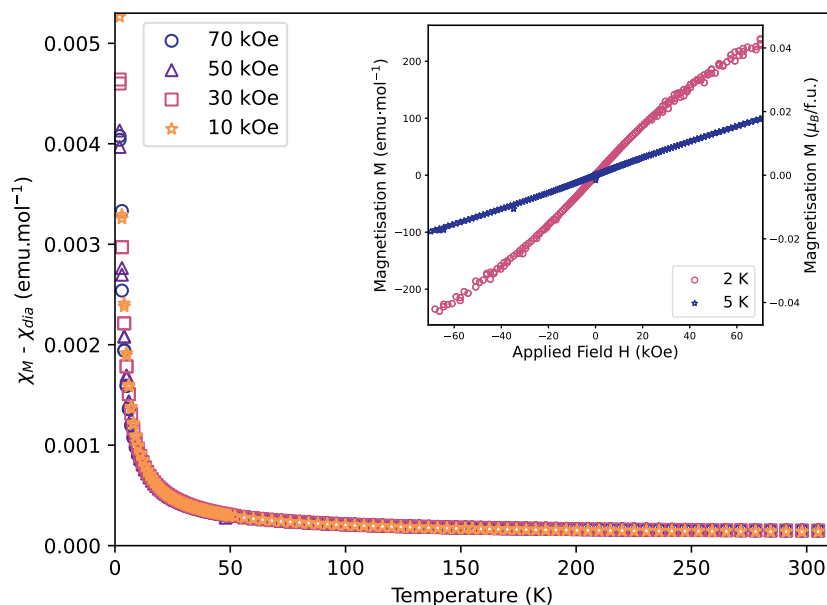


Figure 7.12: Magnetic susceptibility of  $\text{Ba}_{2.875}\text{PuO}_{5.875}$ . The magnetic susceptibility is acquired at various applied magnetic field strengths. Inset: Magnetisation curve of  $\text{Ba}_{2.875}\text{PuO}_{5.875}$  collected at 2 K and at 5 K.

sample holder to prevent spreading of radioactive powder. Data were collected from  $10\text{--}120^\circ 2\theta$  with a step size of  $0.013^\circ 2\theta$  using a LynxEye detector for up to 24 hours per measurement.

A second Bruker D8 X-ray diffractometer was used to collect data at elevated temperatures. The sample was dispersed on the surface of a Pt heating strip using a few drops of alcohol in a  $\text{N}_2$ -filled glove box and measured every 100 K under vacuum ( $10^{-3}$  bar).

Analysis of the diffraction data was performed using the FullProf package [70] using the Rietveld profile refinement method [31, 71]. Visualisations of the crystal structures were made using VESTA [72].

**X-Ray Absorption Spectroscopy** About 1 mg sample was mounted with bicomponent glue on a sample holder and doubly encapsulated with  $12\ \mu$  Kapton. X-ray Absorption Near-Edge Structure (XANES) and Extended X-ray Absorption Fine Structure (EXAFS) spectroscopy at the Pu  $L_3$ -edge were measured at the INE-Beamline [73] and High-Energy Resolution Fluorescence Detected (HERFD) X-ray Absorption Spectroscopy at the Pu  $M_5$ -edge was performed at the ACT station of the CAT-ACT beamline of the KIT Light Source in Karlsruhe, Germany [74, 75]. The storage ring operates at 2.5 GeV and has a maximum stored current of 170 mA.

The Pu  $L_3$  edge (18057 eV) was measured in both transmission and fluorescence mode. For calibration, the K-edge of a metallic Zr foil (17998 eV) was measured between the second and third ionisation chamber. Ge(422) crystals are used in the double-crystal monochromator (DCM). The X-ray beam is collimated and focussed to a spot size of  $500 \times 500$  microns by means of two Rh-coated mirrors, respectively located before (cylindrically bent) and after (toroidal) the DCM. EXAFS spectra were collected at room temperature in fluorescence mode, using a combination of two silicon drift detectors, *viz.* a Vortex- ME4 (4 elements) and a Vortex-60EX (1 element, Hitachi/SHINT). The transmission data was exploited for XANES and the fluorescence signal was used for EXAFS.

The XANES-region of the spectrum was analysed using the ATHENA software and the inflection point of the edge was taken as the threshold position  $E_0$  [76]. The white line position is the maximum of the spectrum. The EXAFS data was collected up to  $16\ \text{\AA}^{-1}$  and Fourier-transformed using the Hanning window over the  $k$ -range

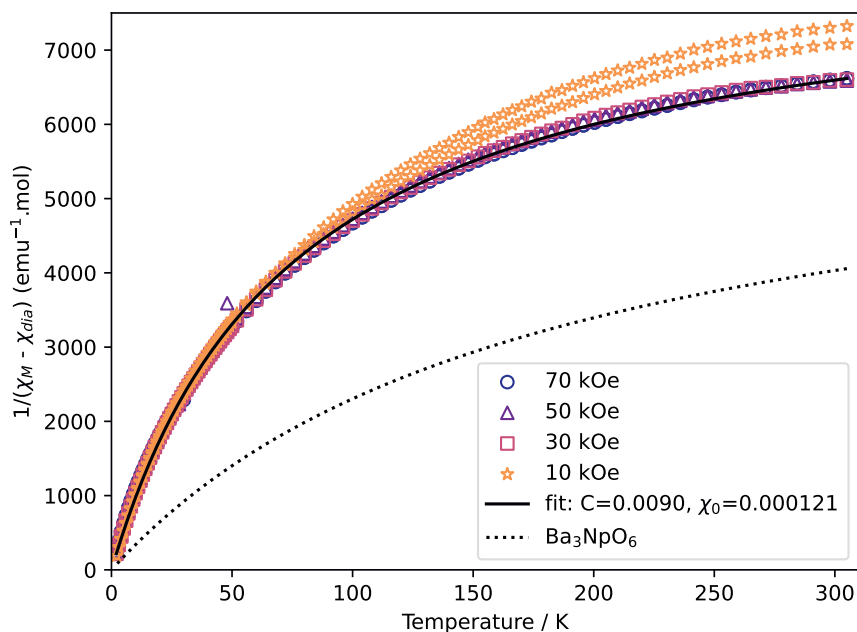


Figure 7.13: Inverse magnetic susceptibility of Ba<sub>2.875</sub>PuO<sub>5.875</sub>. The magnetic susceptibility is acquired at various applied magnetic field strengths. The data obtained at 70 kOe was fitted; see for explanation the main text. Fit for Ba<sub>3</sub>NpO<sub>6</sub> from Hinatsu and Edelstein [69].

3.5 to 14.5 Å<sup>-1</sup> ( $dk = 2$ ). The ARTEMIS software suite was used to fit the data in  $k^2$ -space [76]. The *ab initio* code FEFF8.40 was used to calculate the phases and amplitudes for the interatomic scattering paths. The shift in the threshold energy ( $\Delta E_0$ ) was varied as a global parameter. The bond distances were optimized, but the coordination numbers were kept constant. The amplitude for all paths  $S_0^2$  was fixed to 0.9. A single value of  $\Delta E_0$  for all scattering paths was allowed to vary, while the Debye-Waller parameters  $\sigma^2$  were allowed to vary as well. The distance resolution  $\Delta R$ , i.e. the ability to differentiate neighbouring atom shells in the EXAFS spectrum, is given by  $\Delta R = \pi / (2 \cdot \Delta k)$  where  $\Delta k$  is the  $k$ -range of the spectra, resulting in  $\Delta R = 0.14$  Å for the present  $k$ -range. This means that distances with differences shorter than 0.14 Å cannot be fitted independently. The distances found in the XRD model as listed in Table 7.3 for synthesis 2, which was preferred from XRD perspective over synthesis 1, were used as starting parameters and further optimised. Independent Pu1-O, Pu2-O and Pu3-O scattering pathways were used in the EXAFS fitting procedure, to reflect the fact that three different crystal positions and environments exist in the compound under study.

Pu  $L_3$ -edge XANES spectra have been calculated with the FDMNES code using the herein proposed crystal structure and earlier published BaPuO<sub>3</sub> [77–79]. The simulations were performed with a cluster radius of 6 Å using Greens function, relativistic effect and spin-orbit coupling. The simulated spectra were normalised and shifted by the Pu  $L_3$  edge (18057 eV) for comparison with the experimental spectrum.

The distances found in the XRD model as listed in Table 7.3 for synthesis 2, which was preferred from XRD perspective over synthesis 1, were used as starting parameters in the EXAFS optimisation and further optimised. Independent Pu1-O, Pu2-O and Pu3-O scattering pathways were used in the EXAFS fitting procedure, to reflect the fact that three different crystal positions and environments exist in the compound under study.

HERFD XANES the Pu  $M_5$  edge (3775 eV) was collected at the ACT-station of the CAT-ACT beamline, using the Pu  $M_{\alpha 1}$  emission (3351 eV) with a Si(220) analyzer crystal of 0.5m bending radius. Si collimating and focussing

mirrors and Si(111) DCM crystals were used and the size of the beamspot was decreased to  $500\ \mu\text{m} \times 500\ \mu\text{m}$  using slits to increase the energy resolution of the collected spectra. The analyzer crystal was positioned at  $142^\circ$  scattering angle relative to the incident beam. The spectrophotometer was placed in a He-flushed glovebox to minimize tender X-ray absorption in the beam path [74, 75].

**Low-temperature Heat Capacity** The material obtained after heat treatment at 1200 K in synthesis 1 was pressed in a pellet and given another heat treatment at 1270 K to have a freshly annealed specimen. A piece of 13.67(10) mg was encapsulated in 4.99(10) mg Stycast [80]. The low temperature heat capacity was measured using the Physical Property Measurement System (PPMS) from Quantum Design from 270 K down to 5 K with no applied magnetic field. 1 week after the annealing, an additional measurement below 50 K was done at 0 T and 14 T. The addendum and Stycast 2850 FT contribution were subtracted from the total heat capacity, yielding the sample heat capacity.

**Magnetic Susceptibility** A 22.77(10) mg piece freshly annealed at 1270 K was enclosed in a blank tube. The magnetic susceptibility was measured on a Quantum Design MPMS-3 instrument by the SQUID technique. DC magnetisation  $M(T)$  was achieved from 2 to 320 K under constant magnetic field  $H$  of 10, 30, 50 and 70 kOe. Moreover, the magnetisation  $M$  was measured as function of applied field  $H$  from -70 to 70 kOe. The magnetic contribution of the blank was fitted to a curve. The magnetic susceptibility was obtained by subtracting the susceptibility of the blank from the total measured susceptibility. To correct for the diamagnetic contribution, values for  $\text{Ba}^{2+}$ ,  $\text{U}^{6+}$  and  $\text{O}^{2-}$  were taken from Bain and Berry, yielding  $-170.5 \cdot 10^{-6}\ \text{emu} \cdot \text{mol}^{-1}$  [81].  $\text{U}^{6+}$  was taken as substitute for  $\text{Pu}^{6+}$ , as we are not aware of any tabulated value for the Pascal constant of  $\text{Pu}^{6+}$ .



# BIBLIOGRAPHY

- (1) Pelletier, M.; Guérin, Y. In *Comprehensive Nuclear Materials, 2nd edition*, Konings, R. J. M., Stoller, R. E., Eds.; Elsevier: 2020; Chapter 2.03, pp 72–105.
- (2) Awasthi, S.; Chackraborty, D.; Tondon, V. *Journal of Inorganic and Nuclear Chemistry* **1968**, *30*, 819–821.
- (3) Fouquet-Métivier, P.; Medyk, L.; Lebreton, F.; Guéneau, C.; Hunault, M. O.; Solari, P.-L.; Dardenne, K.; Rothe, J.; Martin, P. M. *Inorganic Chemistry* **2024**, *63*, 20482–20491.
- (4) Fee, D. C.; Johnson, C. E. *Journal of nuclear materials* **1981**, *99*, 107–116.
- (5) Tobin, J. G.; Yu, S.-W. *Inorganic Chemistry* **2023**, *62*, 2592–2598.
- (6) Bagus, P. S.; Schacherl, B.; Vitova, T. *Inorganic Chemistry* **2021**, *60*, 16090–16102.
- (7) Bajaj, A.; Ramanantoanina, H.; Schacherl, B.; Schenk, S.; Pruessmann, T.; Tasi, A.; Fellhauer, D.; Humiston, A.; Terry, J.; Wang, X., et al. *Inorganic Chemistry* **2025**, *64*, 12297–12312.
- (8) Skanthakumar, S.; Yu, X.; Autschbach, J.; Soderholm, L. *Inorganic Chemistry* **2023**, *62*, 15891–15901.
- (9) Keller, C. *Journal of the Less Common Metals* **1986**, *121*, 15–26.
- (10) Bykov, D. M.; Raison, P. E.; Konings, R. J. M.; Apostolidis, C.; Orlova, M. *Journal of Nuclear Materials* **2015**, *457*, 54–62.
- (11) Smith, A. L.; Raison, P. E.; Hen, A.; Bykov, D.; Colineau, E.; Sanchez, J.-P.; Konings, R. J. M.; Cheetham, A. K. *Dalton Transactions* **2015**, *44*, 18370–18377.
- (12) Smith, A. L.; Martin, P.; Prieur, D.; Scheinost, A. C.; Raison, P. E.; Cheetham, A. K.; Konings, R. J. M. *Inorganic Chemistry* **2016**, *55*, 1569–1579.
- (13) Ao, B.; Lu, H.; Yang, Z.; Qiu, R.; Hu, S.-X. *Physical Chemistry Chemical Physics* **2019**, *21*, 4732–4737.
- (14) Keller, C. *Journal of Inorganic and Nuclear Chemistry* **1965**, *27*, 321–327.
- (15) Fuger, J.; Haire, R. G.; Peterson, J. R. *Journal of Alloys and Compounds* **1993**, *200*, 181–185.
- (16) Konings, R. J. M.; Morss, L. R.; Fuger, J. In *The Chemistry of the Actinide and Transactinide Elements*; Springer: 2006, pp 2113–2224.
- (17) Murphy, G. L.; Kennedy, B. J.; Zhang, Z.; Avdeev, M.; Brand, H. E.; Kegler, P.; Alekseev, E. V. *Journal of Alloys and Compounds* **2017**, *727*, 1044–1049.
- (18) Keller, C. *Nukleonik* **1962**, *4*, 271–277.
- (19) Keller, C. *Nukleonik* **1963**, *5*, 89–93.

- (20) Griffiths, A. J.; Kemmler-Sack, S. *Zeitschrift für anorganische und allgemeine Chemie* **1979**, *457*, 161–164.
- (21) Griffiths, A. J.; Kemmler-Sack, S. *Zeitschrift für anorganische und allgemeine Chemie* **1980**, *466*, 116–130.
- (22) Treiber, U.; Griffiths, A. J.; Kemmler-Sack, S. *Zeitschrift für anorganische und allgemeine Chemie* **1981**, *473*.
- (23) Barrett, S. A.; Jacobson, A. J.; Tofield, B. C.; Fender, B. E. F. *Acta Crystallographica Section B* **1982**, *38*, 2775–2781.
- (24) Cordfunke, E. H. P.; Ijdo, D. J. W. *Journal of Physics and Chemistry of Solids* **1988**, *49*, 551–554.
- (25) Cordfunke, E. H. P.; Booi, A. S.; Smit-Groen, V.; van Vlaanderen, P.; Ijdo, D. J. W. *Journal of Solid State Chemistry* **1997**, *131*, 341–349.
- (26) Gens, R.; Fuger, J.; Morss, L. R.; Williams, C. W. *Journal of Chemical Thermodynamics* **1985**, *17*, 561–573.
- (27) Richmann, M. K.; Reed, D. T.; Kropf, A. J.; Aase, S. B.; Lewis, M. A. *Journal of Nuclear Materials* **2001**, *297*, 303–312.
- (28) Reed, D. T.; Aase, S. B.; Kropf, A. J.; Curtiss, L. A.; Zygmunt, S. In *Workshop Proceedings, Tokai-Mura, Ibaraki, Japan, 16-28 october 1999*, 1999.
- (29) Rüdorff, W.; Pfitzer, F. *Zeitschrift für Naturforschung B* **1954**, *9*, 568–569.
- (30) Sleight, A. W.; Ward, R. *Inorganic Chemistry* **1962**, *1*, 790–793.
- (31) Rietveld, H. M. *Acta Crystallographica* **1966**, *20*, 508–513.
- (32) Kemmler-Sack, S.; Seemann, I. *Zeitschrift für anorganische und allgemeine Chemie* **1975**, *411*, 61–78.
- (33) De Blieck, R.; van Cappellen, E.; van Tendeloo, G.; Amelinckx, S.; Gens, R.; Fuger, J. *Journal of Solid State Chemistry* **1987**, *68*, 375–378.
- (34) Böhler, R.; Welland, M. J.; Prieur, D.; Cakir, P.; Vitova, T.; Prüßmann, T.; Pidchenko, I.; Hennig, C.; Guéneau, C.; Konings, R. J. M., et al. *Journal of Nuclear Materials* **2014**, *448*, 330–339.
- (35) Pidchenko, I.; März, J.; Hunault, M. O.; Bauters, S.; Butorin, S. M.; Kvashnina, K. O. *Inorganic Chemistry* **2020**, *59*, 11889–11893.
- (36) Kvashnina, K. O.; Romanchuk, A. Y.; Pidchenko, I.; Amidani, L.; Gerber, E.; Trigub, A.; Rossberg, A.; Weiss, S.; Popa, K.; Walter, O., et al. *Angewandte Chemie* **2019**, *131*, 17722–17726.
- (37) Van den Berghe, S.; Verwerft, M.; Laval, J.-P.; Gaudreau, B.; Allen, P. G.; van Wynn-garden, A. *Journal of Solid State Chemistry* **2002**, *166*, 320–329.
- (38) Prieur, D. B.; Popa, K.; Vigier, J.-E.; Scheinost, A. C.; Martin, P. M. *Journal of Nuclear Materials* **2019**, *516*, 303–308.
- (39) Conradson, S. D.; Abney, K. D.; Begg, B. D.; Brady, E. D.; Clark, D. L.; Den Auwer, C.; Ding, M.; Dorhout, P. K.; Espinosa-Faller, F. J.; Gordon, P. L., et al. *Inorganic Chemistry* **2004**, *43*, 116–131.

- (40) Soldatov, A. V.; Lamoen, D.; Konstantinović, M.; van den Berghe, S.; Scheinost, A. C.; Verwerft, M. *Journal of Solid State Chemistry* **2007**, *180*, 54–61.
- (41) Vitova, T.; Pidchenko, I.; Fellhauer, D.; Bagus, P. S.; Joly, Y.; Pruessmann, T.; Bahl, S.; Gonzalez-Robles, E.; Rothe, J.; Altmaier, M., et al. *Nature Communications* **2017**, *8*, 16053.
- (42) Howard, C. J.; Kennedy, B. J.; Woodward, P. M. *Acta Crystallographica Section B* **2003**, *59*, 463–471.
- (43) Bock, O.; Müller, U. *Acta Crystallographica Section B* **2002**, *58*, 594–606.
- (44) Bock, O.; Müller, U. *Zeitschrift für anorganische und allgemeine Chemie* **2002**, *628*, 987–992.
- (45) Howard, C. J.; Carpenter, M. A. *Acta Crystallographica Section B* **2010**, *66*, 40–50.
- (46) Gateshki, M.; Igartua, J. M. *Journal of Physics: Condensed Matter* **2003**, *15*, 6749.
- (47) Bézar, J.-F.; Lelann, P. *Journal of Applied Crystallography* **1991**, *24*, 1–5.
- (48) Nakajima, K.; Arai, Y.; Suzuki, Y.; Yamawaki, M. *Journal of the Mass Spectrometry Society of Japan* **1999**, *47*, 46–48.
- (49) Ye, X.; Zhuang, W.; Deng, C.; Yuan, W.; Qiao, Z. *Calphad* **2006**, *30*, 349–353.
- (50) Shannon, R. D. *Acta crystallographica section A* **1976**, *32*, 751–767.
- (51) Boultif, A.; Louer, D. *Journal of Applied Crystallography* **2004**, *37*, 724–731.
- (52) Yamanaka, S.; Kurosaki, K.; Matsuda, T.; Uno, M. *Journal of Nuclear Materials* **2001**, *294*, 99–103.
- (53) Yamanaka, S.; Fujikane, M.; Hamaguchi, T.; Muta, H.; Oyama, T.; Matsuda, T.; Kobayashi, S.-i.; Kurosaki, K. *Journal of Alloys and Compounds* **2003**, *359*, 109–113.
- (54) Ohishi, Y.; Yusnitha, E.; Kurosaki, K.; Muta, H.; Yamanaka, S. *Journal of Nuclear Materials* **2014**, *448*, 62–65.
- (55) Yamashita, T.; Nitani, N.; Tsuji, T.; Inagaki, H. *Journal of Nuclear Materials* **1997**, *245*, 72–78.
- (56) Knyazev, A. V.; Chernorukov, N. G.; Zhizhin, M. G.; Sazhina, Y. S.; Ershova, A. V. *Radiochemistry* **2006**, *48*, 568–571.
- (57) Knyazev, A. V.; Chernorukov, N. G.; Dashkina, Z. S.; Bulanov, E. N.; Ladenkov, I. V. *Russian Journal of Inorganic Chemistry* **2011**, *56*, 888–898.
- (58) Pialoux, A.; Touzelin, B. *Canadian Journal of Chemistry* **1999**, *77*, 1384–1393.
- (59) Dash, S.; Singh, Z. *Journal of Nuclear Materials* **2010**, *404*, 9–18.
- (60) Cordfunke, E. H. P.; Westrum Jr, E. F. *Thermochimica Acta* **1988**, *124*, 285–296.
- (61) Cordfunke, E. H. P.; van der Laan, R. R.; van Miltenburg, J. C. *Journal of Physics and Chemistry of Solids* **1994**, *55*, 77–84.
- (62) Válu, S.-O.; De Bona, E.; Popa, K.; Griveau, J.-C.; Colineau, E.; Konings, R. J. M. *Scientific Reports* **2019**, *9*, 15082.

- (63) Griveau, J.-C.; Vigier, J.-F.; Popa, K.; Vălu, S.-O.; Colineau, E.; Konings, R. J. M. *Journal of Applied Physics* **2022**, *132*, 185103.
- (64) Thiriet, C.; Konings, R. J. M.; Javorský, P.; Wastin, F. *Physics and Chemistry of Minerals* **2004**, *31*, 347–352.
- (65) Thiriet, C.; Javorský, P.; Konings, R. J. M. *Solid State Communications* **2005**, *134*, 409–412.
- (66) Dawson, J. *Journal of the Chemical Society (Resumed)* **1952**, 2705–2707.
- (67) Gruen, D. M.; Malm, J. G.; Weinstock, B. *The Journal of Chemical Physics* **1956**, *24*, 905–906.
- (68) Edelstein, N. M.; Lander, G. H. In *The Chemistry of the Actinide and Transactinide Elements*, Morss, L. R., Edelstein, N. M., Fuger, J., Eds.; Springer: 2006; Chapter 20, pp 2225–2306.
- (69) Hinatsu, Y.; Edelstein, N. *Journal of Solid State Chemistry* **1991**, *93*, 173–182.
- (70) Rodríguez-Carvajal, J. *Physica B: Condensed Matter* **1993**, *192*, 55–69.
- (71) Van Laar, B.; Schenk, H. *Acta Crystallographica Section A* **2018**, *74*, 88–92.
- (72) Momma, K.; Izumi, F. *Journal of Applied Crystallography* **2011**, *44*, 1272–1276.
- (73) Rothe, J.; Butorin, S.; Dardenne, K.; Denecke, M. A.; Kienzler, B.; Löble, M.; Metz, V.; Seibert, A.; Steppert, M.; Vitova, T., et al. *Review of Scientific Instruments* **2012**, *83*, 043105.
- (74) Zimina, A.; Dardenne, K.; Denecke, M. A.; Doronkin, D. E.; Huttel, E.; Lichtenberg, H.; Mangold, S.; Pruessmann, T.; Rothe, J.; Spangenberg, T., et al. *Review of Scientific Instruments* **2017**, *88*.
- (75) Schacherl, B.; Prüssmann, T.; Dardenne, K.; Hardock, K.; Krepper, V.; Rothe, J.; Vitova, T.; Geckeis, H. *Synchrotron Radiation* **2022**, *29*, 80–88.
- (76) Ravel, B.; Newville, M. *Journal of Synchrotron Radiation* **2005**, *12*, 537–541.
- (77) Christoph, G. G.; Larson, A. C.; Eller, P. G.; Purson, J. D.; Zahrt, J. D.; Penneman, R. A.; Rinehart, G. H. *Acta Crystallographica Section B* **1988**, *44*, 575–580.
- (78) Bunău, O.; Joly, Y. *Journal of Physics: Condensed Matter* **2009**, *21*, 345501.
- (79) Guda, S. A.; Guda, A. A.; Soldatov, M. A.; Lomachenko, K. A.; Bugaev, A. L.; Lamberti, C.; Gawelda, W.; Bressler, C.; Smolentsev, G.; Soldatov, A. V., et al. *Journal of Chemical Theory and Computation* **2015**, *11*, 4512–4521.
- (80) Javorský, P.; Wastin, F.; Colineau, E.; Rebizant, J.; Boulet, P.; Stewart, G. *Journal of Nuclear Materials* **2005**, *344*, 50–55.
- (81) Bain, G. A.; Berry, J. F. *Journal of Chemical Education* **2008**, *85*, 532.

# 8

## CONCLUSIONS AND OUTLOOK

This dissertation pertains to the chemistry between irradiated fuel and coolant in lead-cooled fast reactors from a structural and thermodynamic perspective. It describes studies between selected fission products and the coolant, and its prime focus is on the chemical interaction of the coolant with the JOG-phase, the volatile fission products and the grey phase after cladding failure in lead-cooled fast reactors. In this concluding chapter, answers to the questions posed in **Chapter 1** will be formulated. For this dissertation, the thermodynamic approach was chosen. This approach yields results that should be combined with post-irradiation examination and kinetic or release studies and the results obtained herein assist in the interpretation of those experiments. The chosen thermodynamic approach entails experimental and modelling methods that are explained in **Chapter 2**. The main findings and implications of this dissertation for lead-cooled fast reactor development will be detailed here from a physical-chemists' perspective and for an engineering perspective. After this, some general implications and an outlook are given.

### 8.1. COOLANT-JOG INTERACTION FOR Pb-COOLED SYSTEMS

The possible chemical interactions between Pb-coolant and JOG-phase (approximated as  $\text{Cs}_2\text{MoO}_4$ ) were investigated.

In **Chapter 3**, studies into the Pb-Mo-O system are described. Several physical properties were experimentally determined: the thermal expansion and low temperature heat capacity of the compounds  $\text{PbMoO}_4$  and  $\text{Pb}_2\text{MoO}_5$ , the melting enthalpy of  $\text{PbMoO}_4$  and the Mo-oxidation state of  $\text{PbMoO}_4$  and  $\text{Pb}_2\text{MoO}_5$ . A thermodynamic model using the CALPHAD approach was developed, featuring the hexavalent molybdates  $\text{PbMoO}_4$ ,  $\text{Pb}_2\text{MoO}_5$  and  $\text{Pb}_5\text{MoO}_8$ . Thus, a comprehensive understanding of the Pb-Mo-O system was obtained by combining experimental studies with thermodynamic modelling of the solid and liquid phases. Given the high melting point and low volatility of

---

Part of this chapter is based on: A. van Hattem, J. Vlieland, E. Colineau, J-C. Griveau, R.J.M. Konings and A.L. Smith *Thermodynamic Study of  $\alpha$ - $\text{Cs}_2\text{Pb}(\text{MoO}_4)_2$  and Safety Assessment of the Pb-JOG Interaction in Lead-cooled Fast Reactors* Journal of Nuclear Materials (under review)

the solids and liquids in this ternary system in the operational temperature window, the gaseous species do not pose a serious safety concern. The Pb-Mo-O system is of interest to the main topic of this thesis (*i.e.* cladding failure), but as many structural materials contain some Mo, it is also relevant in modelling of the corrosion of structural materials in contact with Pb-coolant.

Next, the fission product Cs was added to the studies and the Pb-Cs-Mo-O system was investigated in the oxygen-rich limit, *i.e.* with focus on the system  $\text{Cs}_2\text{MoO}_4$ - $\text{PbMoO}_4$  and the compound  $\text{Cs}_2\text{Pb}(\text{MoO}_4)_2$  as reported in **Chapter 4**. Diffraction techniques gave insight into the behaviour of the cell parameters at room temperature and above, up to 773 K. The crystal structure of  $\beta$ - $\text{Cs}_2\text{Pb}(\text{MoO}_4)_2$ , the high-temperature phase, was elucidated.  $\beta$ - $\text{Cs}_2\text{Pb}(\text{MoO}_4)_2$  was found to crystallise in space group 166, like archetype palmierite. The thermal expansion of  $\text{Cs}_2\text{Pb}(\text{MoO}_4)_2$  was measured and X-ray Absorption Near Edge Structure (XANES) spectroscopy showed that Mo was present as Mo(VI). The pseudo-binary system  $\text{Cs}_2\text{MoO}_4$ - $\text{PbMoO}_4$  was investigated using XRD and TG-DSC. The liquidus line was found to be qualitatively similar to the earlier reported phase diagram, but several other phase diagram features were changed or refined. Finally, the enthalpy of formation and standard entropy of  $\text{Cs}_2\text{Pb}(\text{MoO}_4)_2$  at 298.15 K were measured, yielding the standard Gibbs energy of the compound.

Like the compounds in the Pb-Mo-O system, the compound  $\text{Cs}_2\text{Pb}(\text{MoO}_4)_2$  that can form is solid till quite high temperatures and can mechanically interact in a LFR. The thermal expansion coefficient of  $\text{Cs}_2\text{Pb}(\text{MoO}_4)_2$  is compared to typical values for the fuel and JOG-phase and found to be moderately high, meaning it will not aggravate local stress or pressure build-up.

In general, formation of solid interaction products should be limited to prevent blockage of coolant channels. Even though the density of oxygen-containing phases is typically lower than the density of liquid Pb and the solid interaction products should thus float, a nuclear reactor coolant is not in a static equilibrium. Formation of volatile interaction products is on the other hand limited by the rather high thermal stability of the possible chemical interaction products. The actual formation of the solid interaction products depends on the oxygen potential at the interface of irradiated fuel-coolant, or if the fission products are released into the coolant, on the non-negligible oxygen concentration in liquid metal.

### MARGIN TO FORMATION DURING LFR OPERATION

With the results from Chapter 3 and 4, complete descriptions for the Gibbs energy of  $\text{PbMoO}_4$ ,  $\text{Pb}_2\text{MoO}_5$ ,  $\text{Pb}_5\text{MoO}_8$  and  $\text{Cs}_2\text{Pb}(\text{MoO}_4)_2$  are obtained and the question whether these compounds are actually thermodynamically stable in typical LFR operating conditions can be answered.

In case of cladding failure, the JOG-phase can chemically interact with the coolant and the oxygen dissolved in it. Molybdenum (Mo), that acts in the nuclear fuel as oxygen buffer via the Mo/MoO<sub>2</sub> pair, can be present in multiple oxidation states: as metal Mo(0) in the 5-metal particles (white phase), as tetravalent cation Mo(IV) in the perovskite phase (Ba(Mo,Zr,U)O<sub>3</sub>) or as hexavalent cation Mo(VI) in the scheelite (Ba(Mo,U)O<sub>4</sub>) (grey phase) or JOG-phase ( $\text{Cs}_2\text{MoO}_4$ ). Mo-containing species in the coolant could also originate from structural materials degradation. Here, multiple equilibrium reaction

pathways that can be envisaged towards the formation of  $\text{PbMoO}_4$ ,  $\text{Pb}_2\text{MoO}_5$ ,  $\text{Pb}_5\text{MoO}_8$  and  $\text{Cs}_2\text{Pb}(\text{MoO}_4)_2$  are considered to assess their stability in operating conditions.

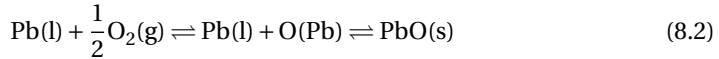
### RELATION BETWEEN OXYGEN POTENTIAL AND OXYGEN CONCENTRATION IN LIQUID Pb

First, a relation between the oxygen potential and oxygen concentration in liquid Pb is derived, following a similar procedure as Sreedharan and Gnanamoorthy [1] and Smith *et al.* [2] took for liquid alkali metals and Müller *et al.* took for liquid Pb and LBE [3, 4].

Molecular gasses like  $\text{O}_2$  dissociate to their atomic counterparts upon dissolution into in liquid metal, known as Sieverts' law [5].



At the oxygen solubility limit in liquid Pb, there is a thermodynamic equilibrium between solid PbO, oxygen dissolved in liquid lead O(Pb) and molecular oxygen ( $\text{O}_2$ ) in the cover gas:



Equating the first and the last term at equilibrium gives, for a saturation oxygen pressure  $p_{\text{O}_2, \text{sat}}$ , and the solvent Pb and solid PbO at unit activity:

$$\Delta_f G_m^o(\text{PbO}(\text{s}), T) = \frac{1}{2}RT \ln(p_{\text{O}_2, \text{sat}}) \quad (8.3)$$

In case of normal operation, the concentration of oxygen dissolved in liquid Pb is below the solubility limit. Below the saturation O(Pb) concentration, the activity of dissolved oxygen is assumed to follow Henry's law and thus to be linear in oxygen (O) concentration:

$$a_{\text{O}} = \gamma_{\text{O}} c_{\text{O}} = \frac{c_{\text{O}}}{c_{\text{O}, \text{sat}}} = \sqrt{\frac{p_{\text{O}_2}}{p_{\text{O}_2, \text{sat}}}} \quad (8.4)$$

This can be rewritten to:

$$p_{\text{O}_2, \text{sat}} = p_{\text{O}_2} \cdot \frac{c_{\text{O}, \text{sat}}^2}{c_{\text{O}}^2} \quad (8.5)$$

and combined with Equation 8.3 to yield:

$$RT \ln(p_{\text{O}_2}) = 2\Delta_f G_m^o(\text{PbO}(\text{s})) + 2RT [\ln(c_{\text{O}}) - \ln(c_{\text{O}, \text{sat}})] \quad (8.6)$$

Müller *et al.* [4] give a fit for the saturation concentration of oxygen in Pb, which is based on a data evaluation by Risold *et al.* [6]:

$$\log c_{\text{O}, \text{sat}} = 1.64 - \frac{3503}{T} \quad (8.7)$$

with  $c_{\text{O}, \text{sat}}$  in weight-% and valid in the temperature window  $623 < T(\text{K}) < 1323$ .

Number	Reaction	Gibbs energy equation
1	$\text{Pb(l)} + \text{Mo(s)} + 2\text{O}_2(\text{diss}) \rightleftharpoons \text{PbMoO}_4(\text{s})$	$\frac{\Delta G_{\text{O}_2}^{\text{eff}}(T)}{\text{O}_2} = RT \ln \frac{p_{\text{O}_2}}{p^{\text{O}_2}} = \frac{1}{2} \Delta_f G_m^{\text{O}}(\text{PbMoO}_4(\text{s}), T)$
2	$\text{Pb(l)} + \text{MoO}_2(\text{s}) + \text{O}_2(\text{diss}) \rightleftharpoons \text{PbMoO}_4(\text{s})$	$\Delta G_{\text{O}_2}^{\text{eff}}(T) = \Delta_f G_m^{\text{O}}(\text{PbMoO}_4(\text{s}), T) - \Delta_f G_m^{\text{O}}(\text{MoO}_2(\text{s}), T)$
3	$\text{Pb(l)} + \text{MoO}_3(\text{s,l}) + \frac{1}{2} \text{O}_2(\text{diss}) \rightleftharpoons \text{PbMoO}_4(\text{s})$	$\Delta G_{\text{O}_2}^{\text{eff}}(T) = 2[\Delta_f G_m^{\text{O}}(\text{PbMoO}_4(\text{s}), T) - \Delta_f G_m^{\text{O}}(\text{MoO}_3(\text{s,l}), T)]$
4	$2\text{Pb(l)} + \text{Mo(s)} + \frac{5}{2} \text{O}_2(\text{diss}) \rightleftharpoons \text{Pb}_2\text{MoO}_5(\text{s})$	$\Delta G_{\text{O}_2}^{\text{eff}}(T) = \frac{2}{5} \Delta_f G_m^{\text{O}}(\text{Pb}_2\text{MoO}_5(\text{s}), T)$
5	$2\text{Pb(l)} + \text{MoO}_2(\text{s}) + \frac{3}{2} \text{O}_2(\text{diss}) \rightleftharpoons \text{Pb}_2\text{MoO}_5(\text{s})$	$\Delta G_{\text{O}_2}^{\text{eff}}(T) = \frac{2}{3} [\Delta_f G_m^{\text{O}}(\text{Pb}_2\text{MoO}_5(\text{s}), T) - \Delta_f G_m^{\text{O}}(\text{MoO}_2(\text{s}), T)]$
6	$2\text{Pb(l)} + \text{MoO}_3(\text{s,l}) + \text{O}_2(\text{diss}) \rightleftharpoons \text{Pb}_2\text{MoO}_5(\text{s})$	$\Delta G_{\text{O}_2}^{\text{eff}}(T) = \Delta_f G_m^{\text{O}}(\text{Pb}_2\text{MoO}_5(\text{s}), T) - \Delta_f G_m^{\text{O}}(\text{MoO}_3(\text{s,l}), T)$
7	$2\text{Pb(l)} + \text{PbMoO}_4(\text{s}) + \frac{1}{2} \text{O}_2(\text{diss}) \rightleftharpoons \text{Pb}_3\text{MoO}_8(\text{s})$	$\Delta G_{\text{O}_2}^{\text{eff}}(T) = 2[\Delta_f G_m^{\text{O}}(\text{Pb}_3\text{MoO}_8(\text{s}), T) - \Delta_f G_m^{\text{O}}(\text{PbMoO}_4(\text{s}), T)]$
8	$5\text{Pb(l)} + \text{Mo(s)} + 4\text{O}_2(\text{diss}) \rightleftharpoons \text{Pb}_5\text{MoO}_8(\text{s})$	$\Delta G_{\text{O}_2}^{\text{eff}}(T) = \frac{1}{4} \Delta_f G_m^{\text{O}}(\text{Pb}_5\text{MoO}_8(\text{s}), T)$
9	$5\text{Pb(l)} + \text{MoO}_2(\text{s}) + 3\text{O}_2(\text{diss}) \rightleftharpoons \text{Pb}_5\text{MoO}_8(\text{s})$	$\Delta G_{\text{O}_2}^{\text{eff}}(T) = \frac{1}{3} [\Delta_f G_m^{\text{O}}(\text{Pb}_5\text{MoO}_8(\text{s}), T) - \Delta_f G_m^{\text{O}}(\text{MoO}_2(\text{s}), T)]$
10	$5\text{Pb(l)} + \text{MoO}_3(\text{s}) + \frac{5}{2} \text{O}_2(\text{diss}) \rightleftharpoons \text{Pb}_5\text{MoO}_8(\text{s})$	$\Delta G_{\text{O}_2}^{\text{eff}}(T) = \frac{2}{3} [\Delta_f G_m^{\text{O}}(\text{Pb}_5\text{MoO}_8(\text{s}), T) - \Delta_f G_m^{\text{O}}(\text{MoO}_3(\text{s}), T)]$
11	$4\text{Pb(l)} + \text{PbMoO}_4(\text{s}) + 2\text{O}_2(\text{diss}) \rightleftharpoons \text{Pb}_3\text{MoO}_8(\text{s})$	$\Delta G_{\text{O}_2}^{\text{eff}}(T) = \frac{1}{2} [\Delta_f G_m^{\text{O}}(\text{Pb}_3\text{MoO}_8(\text{s}), T) - \Delta_f G_m^{\text{O}}(\text{PbMoO}_4(\text{s}), T)]$
12	$3\text{Pb(l)} + \text{Pb}_2\text{MoO}_5(\text{s}) + \frac{3}{2} \text{O}_2(\text{diss}) \rightleftharpoons \text{Pb}_3\text{MoO}_8(\text{s})$	$\Delta G_{\text{O}_2}^{\text{eff}}(T) = \frac{2}{3} [\Delta_f G_m^{\text{O}}(\text{Pb}_3\text{MoO}_8(\text{s}), T) - \Delta_f G_m^{\text{O}}(\text{Pb}_2\text{MoO}_5(\text{s}), T)]$
13	$\text{Pb(l)} + 2\text{Cs(l)} + 2\text{Mo(s)} + 4\text{O}_2(\text{diss}) \rightleftharpoons \text{Cs}_2\text{Pb(MoO}_4)_2(\text{s})$	$\Delta G_{\text{O}_2}^{\text{eff}}(T) = \frac{1}{4} \Delta_f G_m^{\text{O}}(\text{Cs}_2\text{Pb(MoO}_4)_2(\text{s}), T)$
14	$\text{Pb(l)} + \text{Cs}_2\text{MoO}_4(\text{s}) + \text{Mo(s)} + 2\text{O}_2(\text{diss}) \rightleftharpoons \text{Cs}_2\text{Pb(MoO}_4)_2(\text{s})$	$\Delta G_{\text{O}_2}^{\text{eff}}(T) = \frac{1}{2} [\Delta_f G_m^{\text{O}}(\text{Cs}_2\text{Pb(MoO}_4)_2(\text{s}), T) - \Delta_f G_m^{\text{O}}(\text{Cs}_2\text{MoO}_4(\text{s}), T)]$
15	$\text{Pb(l)} + \text{Cs}_2\text{MoO}_4(\text{s}) + \text{MoO}_2(\text{s}) + \text{O}_2(\text{diss}) \rightleftharpoons \text{Cs}_2\text{Pb(MoO}_4)_2(\text{s})$	$\Delta G_{\text{O}_2}^{\text{eff}}(T) = \Delta_f G_m^{\text{O}}(\text{Cs}_2\text{Pb(MoO}_4)_2(\text{s}), T) - \Delta_f G_m^{\text{O}}(\text{Cs}_2\text{MoO}_4(\text{s}) - \Delta_f G_m^{\text{O}}(\text{MoO}_2(\text{s}), T)$
16	$\text{Pb(l)} + \text{Cs}_2\text{MoO}_4(\text{s}) + \text{MoO}_3(\text{s}) + \frac{1}{2} \text{O}_2(\text{diss}) \rightleftharpoons \text{Cs}_2\text{Pb(MoO}_4)_2(\text{s})$	$\Delta G_{\text{O}_2}^{\text{eff}}(T) = 2[\Delta_f G_m^{\text{O}}(\text{Cs}_2\text{Pb(MoO}_4)_2(\text{s}), T) - \Delta_f G_m^{\text{O}}(\text{Cs}_2\text{MoO}_4(\text{s}) - \Delta_f G_m^{\text{O}}(\text{MoO}_3(\text{s}), T)]$
17	$\text{Pb(l)} + \text{Cs}_2\text{Mo}_2\text{O}_7(\text{s,l}) + \frac{1}{2} \text{O}_2(\text{diss}) \rightleftharpoons \text{Cs}_2\text{Pb(MoO}_4)_2(\text{s})$	$\Delta G_{\text{O}_2}^{\text{eff}}(T) = 2[\Delta_f G_m^{\text{O}}(\text{Cs}_2\text{Pb(MoO}_4)_2(\text{s}), T) - \Delta_f G_m^{\text{O}}(\text{Cs}_2\text{Mo}_2\text{O}_7(\text{s,l}), T)]$

Table 8.1: Equilibrium reactions and the corresponding Gibbs energy equations for the formation of molybdate compounds in liquid Pb.

Combining Equation 8.6 with Equation 8.7 yields:

$$RT \ln(p_{O_2}) = 2\Delta_f G_m^o(\text{PbO(s)}) + 2RT[\ln(c_O) - (1.64 - \frac{3503}{T}) \cdot \frac{1}{\log_{10}(e)}] \quad (8.8)$$

Now, the oxygen potential in liquid Pb versus temperature can be calculated for relevant oxygen concentrations  $c_O$ .

### OXYGEN POTENTIAL UNDER OPERATIONAL CONDITIONS

Second, knowledge on the typical oxygen concentrations under operational conditions is necessary to answer the question whether the molybdates will form in operational conditions. According to Müller *et al.* [3], the operational window that prevents PbO precipitation and supports  $\text{Fe}_3\text{O}_4$  formation as protective oxide scale on the cladding or structural material is defined by:

$$2\Delta_f G^0(\text{PbO}) > RT \ln p_{O_2} > \frac{1}{2}\Delta_f G^0(\text{Fe}_3\text{O}_4) \quad (8.9)$$

This means that the operational window can be indicated on the diagrams by using the Gibbs energies of formation of PbO [6, 7] and  $\text{Fe}_3\text{O}_4$  [8]. The conditions of Equation 8.9 are fulfilled only in the white windows in Figures 8.1 and 8.2.

### GIBBS ENERGY EQUATIONS

To evaluate which oxygen concentration in liquid Pb is necessary for  $\text{PbMoO}_4$ ,  $\text{Pb}_2\text{MoO}_5$ ,  $\text{Pb}_3\text{MoO}_8$  and  $\text{Cs}_2\text{Pb}(\text{MoO}_4)_2$  to form, several reactions are written down in Table 8.1. The corresponding Gibbs energy equations for the formation of complex compounds from coolant, fission products or fission product compounds, and oxygen dissolved in the coolant are written down in Table 8.1 as well. Gibbs energy functions are taken from Smith *et al.* [9] and Van Hattem *et al.* [7] for the Cs-Mo-O and Pb-Mo-O compounds, while the Gibbs energy of  $\text{Cs}_2\text{Pb}(\text{MoO}_4)_2$  was calculated by summing the Gibbs energy equations for  $\text{Cs}_2\text{MoO}_4$  and  $\text{PbMoO}_4$  and the enthalpy of formation and entropy of formation from molybdates as given in Table 4.10. Metallic Mo(s) is assumed to have an activity of 1, although its real activity might be lower because it is dissolved in the white 5-metal phase. Cs(l) in reaction 13 is taken equivalent to elemental Cs(l) in the JOG at unit activity.

### IMPLICATIONS FOR REACTOR SAFETY

The minimum temperature limit of LFR operation is given by the melting point of Pb (600 K). The maximum expected temperature will differ per design and irradiation scheme. For instance, in the ALFRED design, the maximum coolant temperature in several transients was calculated to always stay below 1125 K, while the maximum cladding temperature is calculated to be about 1073 K in the ULOHS + ULOF (unprotected loss of heat sink + unprotected loss of flow) scenario [10]. The temperature range in Figures 8.1 and 8.2 therefore starts at 600 K and is limited to the melting point of the compounds or 1273 K. Within the maximum window for typical operational conditions, the four compounds under study can all form, though not all reaction pathways proposed in Table 8.1 are possible.

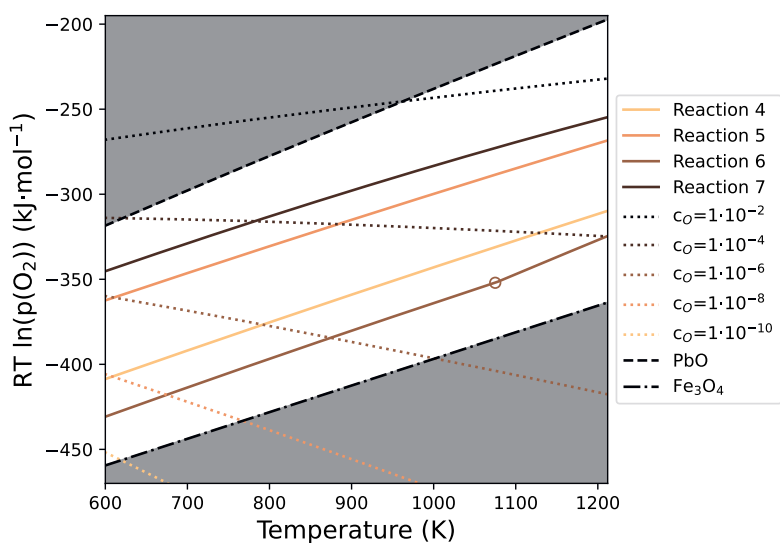
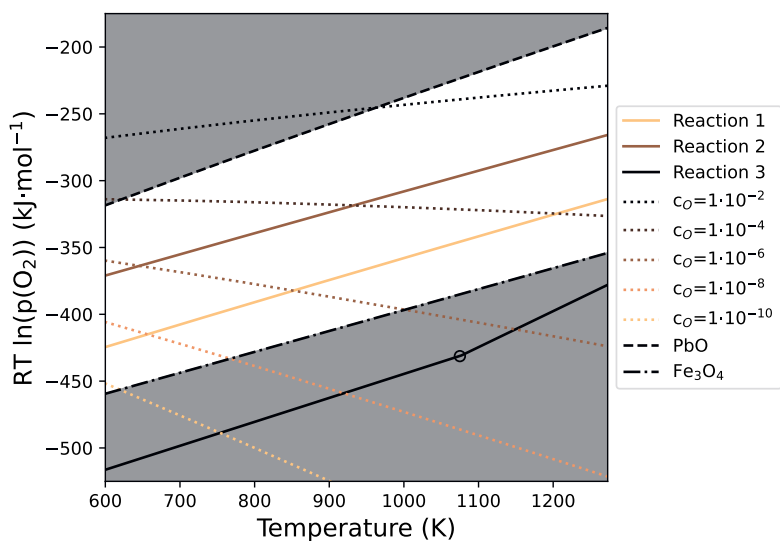


Figure 8.1: Threshold oxygen potential diagram for the formation of  $\text{PbMoO}_4$  (top) and  $\text{Pb}_2\text{MoO}_5$  (bottom). The non-filled area indicates a typical operational oxygen potential. Oxygen concentrations in wt-% O. The temperature window is chosen up to the melting point of the respective compounds. The circles in the figures indicate the melting of  $\text{MoO}_3$ . See for reactions Table 8.1 and for explanation the main text.

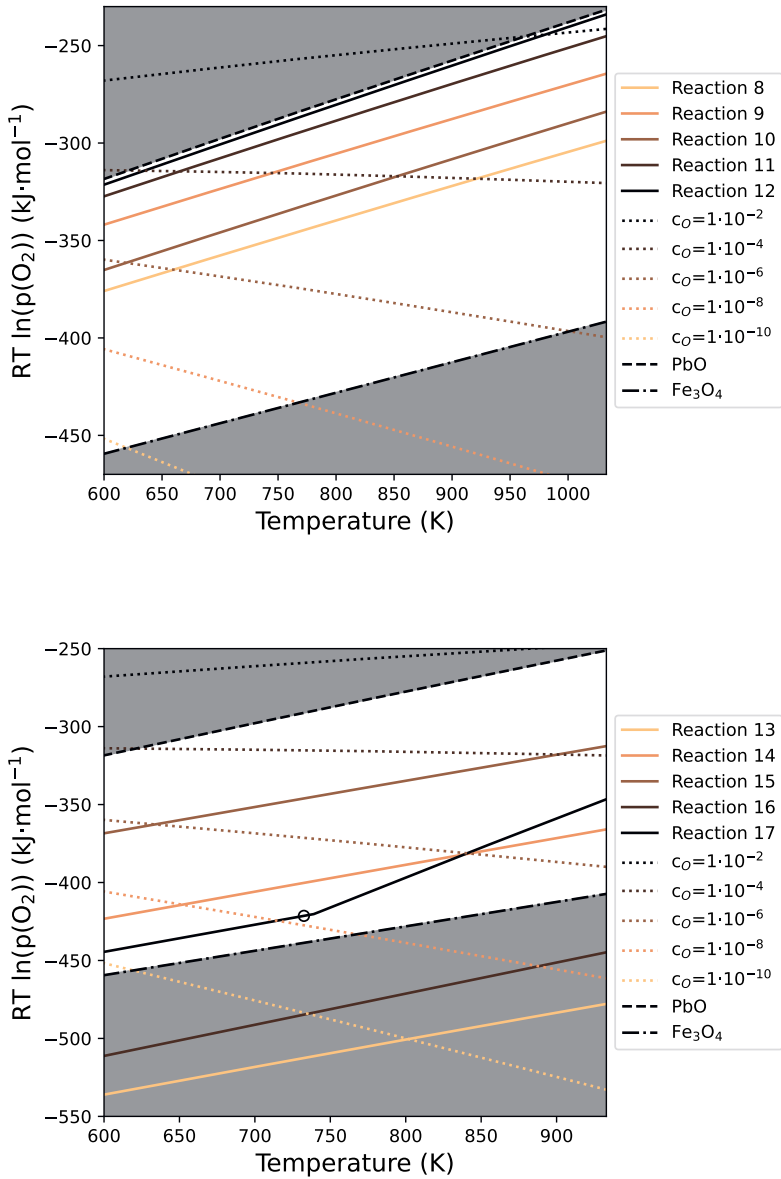


Figure 8.2: Threshold oxygen potential diagram for the formation of  $\text{Pb}_5\text{MoO}_8$  (top) and  $\text{Cs}_2\text{Pb}(\text{MoO}_4)_2$  (bottom). The non-filled area indicates a typical operational oxygen potential. Oxygen concentrations in wt-% O. The temperature window is chosen up to the melting point of the respective compounds. The circles in the figures indicate the melting of  $\text{Cs}_2\text{Mo}_2\text{O}_7$ . See for reactions Table 8.1 and for explanation the main text.

$\text{PbMoO}_4$  can form from the interaction between liquid Pb, dissolved O and Mo(s) or  $\text{MoO}_2$ , but not from the reaction of liquid Pb, dissolved O and  $\text{MoO}_3$ , as can be seen in Figure 8.1. On the other hand,  $\text{Pb}_2\text{MoO}_5$  can form via all 4 predicted pathways.

Cairang *et al.* [11] studied oxidation of refractory Mo by liquid lead-bismuth eutectic (LBE) at 873 K with  $c_{\text{O}} \approx 2 \cdot 10^{-3}$  wt.-%. They found multilayered oxide scale consisting of  $\text{MoO}_2$ ,  $\text{PbMoO}_4$  and  $\text{Pb}_2\text{MoO}_5$ . Ignoring the difference between oxygen solubility in liquid Pb and LBE momentarily and using Figure 8.1, this should be explained by reactions 2 and 7, *i.e.* a subsequent formation of  $\text{PbMoO}_4$  and  $\text{Pb}_2\text{MoO}_5$ .

From Figure 8.2, it follows that  $\text{Pb}_5\text{MoO}_8$  formation should be possible, although all reactions are favourable at the upper limit of the operational window. The slightly lower thermal stability should not hinder its formation at typical coolant temperatures, but its formation may be kinetically hindered.

Whereas the Pb-Mo-O system may be part of the structural materials-coolant interaction, the Pb-Cs-Mo-O system is only relevant in case of cladding failure. Figure 8.2 depicts the results of the calculations for the proposed equilibrium reactions towards the formation of  $\text{Cs}_2\text{Pb}(\text{MoO}_4)_2$ . Reactions 13 and 16 require an oxygen concentration too low to be feasible, whereas reactions 14, 15 and 17 are within the operational window. These reactions start from  $\text{Cs}_2\text{MoO}_4$  or  $\text{Cs}_2\text{Mo}_2\text{O}_7$ , phases typically present in the JOG. The melting point of  $\text{Cs}_2\text{Mo}_2\text{O}_7$  (732.5 K [9]) is indicated with an open circle on Figure 8.2 as well. The presented calculations imply that  $\text{Cs}_2\text{Pb}(\text{MoO}_4)_2$  is thermodynamically stable in a cladding failure scenario under typical LFR operational conditions.

## 8.2. COOLANT-JOG INTERACTION FOR LBE-COOLED SYSTEMS

A phase that could hypothetically form upon reaction between LBE-coolant and JOG-phase (approximated as  $\text{Cs}_2\text{MoO}_4$ ) was investigated in Chapter 5. This Chapter describes neutron diffraction experiments at low and high temperature that lead to solving the crystal structure of  $\text{CsBi}(\text{MoO}_4)_2$  at room temperature unambiguously. The crystal structure has a doubled cell parameter as compared to previous assignments. The XANES spectrum confirms the tetrahedral arrangement around Mo. The obtained results provide an interesting insight into the fundamental physics of the compound. Within the application scope of this thesis, it is observed that the compound has a similar thermal stability to  $\text{Cs}_2\text{Pb}(\text{MoO}_4)_2$ , and the remarks made above are applicable here as well, even though the research into the Bi-Cs-Mo-O is less advanced. In general, LBE-cooled nuclear systems are envisioned to operate at lower temperatures, implying the arguments on solid and volatile species can be applied even stronger here. At this stage, there is not enough data to carry out the application calculations for the formation of  $\text{CsBi}(\text{MoO}_4)_2$  or  $\text{Cs}_5\text{Bi}(\text{MoO}_4)_2$ , the other compound in the Bi-Cs-Mo-O system. Determination of the standard entropy and enthalpy of formation at 298.15 K, eventually supported by the high-temperature heat capacity, would allow these calculations.

## 8.3. COOLANT-VOLATILE FISSION PRODUCT INTERACTION

The elements Cs and I are present as fission products in the JOG-layer, and rather volatile by nature at typical temperatures at the fuel-cladding interface. In Chapter 6, the interaction between coolant and the volatile fission products in the JOG-layer (*i.e.* the Pb-Bi-

Cs-I system) was studied via the pseudo-ternary CsI-PbI<sub>2</sub>-BiI<sub>3</sub> system.

The standard entropy of  $\delta$ -CsPbI<sub>3</sub>, Cs<sub>4</sub>PbI<sub>6</sub> and Cs<sub>3</sub>Bi<sub>2</sub>I<sub>9</sub> was derived from the low-temperature heat capacity measured using a thermal-relaxation technique. These obtained thermodynamic data were used to constrain the standard entropies of the ternary compounds in the model of the ternary salt system CsI-PbI<sub>2</sub>-BiI<sub>3</sub> that was developed. To study the liquidus surface of the ternary system CsI-PbI<sub>2</sub>-BiI<sub>3</sub>, the constituting binary salt systems were investigated for the first time (BiI<sub>3</sub>-PbI<sub>2</sub>) or subjected to renewed investigation (CsI-PbI<sub>2</sub> and CsI-BiI<sub>3</sub>). Based on our DSC results, the BiI<sub>3</sub>-PbI<sub>2</sub> system seems to form a continuous solid solution over the whole composition range. In general, the CsI-PbI<sub>2</sub> and CsI-BiI<sub>3</sub> systems behave as reported previously in literature. The three binary systems were modelled and extrapolated to the ternary phase field. The predicted ternary eutectic points and the section Cs<sub>3</sub>Bi<sub>2</sub>I<sub>9</sub>-CsPbI<sub>3</sub> were experimentally measured. They agree well with the predictions by the CALPHAD model. Thus, the full liquidus surface was modelled and experimentally verified, yielding a complete assessment of the solid-liquid transitions in this system.

For Pb-cooled systems, the CsI-PbI<sub>2</sub> system becomes relevant. The lowest eutectic line here is at 621 K at the PbI<sub>2</sub>-rich side, indicating that in PbI<sub>2</sub>-rich systems the material would be (partially) liquid starting from this temperature. As liquid Pb-cooled systems inherently operate at temperatures above 600 K, Pb-Cs-I mixtures are expected to be at least partially liquid, although temperature-wise, PbI<sub>2</sub>, CsPbI<sub>3</sub>, Cs<sub>4</sub>PbI<sub>6</sub> and CsI can be expected to be present at solids.

The lowest ternary eutectic in the ternary phase diagram lies at 617 K. However, LBE-cooled systems select LBE because of a desired lower operating temperature. Using MYRRHA characteristics, the temperature window during operation for the current discussion is 400 to 550 K [12]. This means any mixture in the CsI-PbI<sub>2</sub>-BiI<sub>3</sub> system is expected to be solid.

There are several limitations to our current study of the Pb-(Bi-)Cs-I system for the safety assessment of the Pb- and LBE-cooled nuclear systems. First, with high operating temperatures or severe accident conditions, the properties of the gas phase become relevant. The temperature window of applicability of the current model can as a first estimation be bound to the maximum temperature in the coolant vessel, which is around 1115 K for ALFRED [13], but the gas phase will most probably be appreciable already before reaching this temperature. Second, only the ternary salt field, mainly focusing on the determination of the liquidus surface, was studied. Since most of the Pb and Bi will be present as liquid metal, thermodynamic studies into the coolant-Cs-I systems, *i.e.* Pb-Cs-I and LBE-Cs-I are also necessary, including elemental solubility of Cs and I in the coolant. Third, depending where the reaction takes place, even the presence of CsI should be questioned. This is not only an effect of the higher fission yield of Cs compared to I, but the most recent contribution to the question on the existence of CsI in irradiated fuel indicates that Cs and I are not present as CsI in irradiated fuel because radiolysis overrules the thermodynamic predictions [14]. Nevertheless, the radiolysis will be smaller at larger distances from the core. Fourth, the oxygen potential in the coolant seems to play a role on the iodine species released from LBE:I [15, 16]. This would imply there is a need to consider systems like Pb-I-O and others as well to make proper assumptions on release mechanisms.

Given these limitations, no application calculations are carried out like for the Pb-Cs-Mo-O system. In order to do so, one would need to have solubility or activity curves of Cs and I in coolant up to high temperatures, and this data seems incomplete.

Although the topic is not treated in this dissertation, the chemical physics of the Pb-Cs system is rather unique and is getting renewed attention [17], but the fundamental understanding of the chemistry of very low concentrations of Cs together with other elements in liquid Pb remains limited.

Despite all these limitations, the retention capacity or release of Cs and I in liquid coolant can be studied for practical purposes without answering all fundamental chemical questions [18, 19]. In general, translating a separate effect study to the reactor reality or even to experimental release measurements itself is complicated. For example, Liu *et al.* mention impurity potassium metal to act as a sink for iodine [20], so the combined release of Cs and I can be expected to be different than the effects of the separate elements. Kumelin *et al.* study the release of CsI and other relevant Cs-compounds and find a heterogeneity in release products. Density of interaction products seems to play a role in the release mechanisms, as compounds float on top of liquid Pb [21].

For the thermodynamic modelling community focussing on oxide fuels, the most important steps are to develop a thermodynamic model using a compatible formalism [22], and collecting experimental data into vapour phase speciation and vapour pressures, for the full quaternary system over a wide temperature window.

#### 8.4. COOLANT-GREY PHASE INTERACTION

The study of the Pb-Ba-Pu-O system resulted in a study of the Ba-Pu-O system, as described in **Chapter 7**. This chapter deals with a phase found in the attempt to synthesise  $\text{Ba}_3\text{PuO}_6$ . This alkaline-earth Pu-containing perovskite-related phase  $\text{Ba}_{2.875}\text{PuO}_{5.875}$  has been synthesised for the first time using solid state synthesis starting from  $\text{BaCO}_3$  and  $\text{PuO}_2$ . The positions of the heavy metal atoms Ba and Pu in the crystal structure were refined in space group  $I4/m$  instead of  $I4/mmm$  proposed for the U-analog, yielding an overall satisfactory model with ordered empty Ba-sites. The evolution of the space group with temperature was proposed based on high-temperature X-ray diffraction measurements. X-ray absorption spectroscopy at the Pu  $M_5$  and  $L_3$  edges showed Pu to be present as Pu(VI) and agreement for the local environment was found using EXAFS spectroscopy and FDMNES calculations. The  $\text{Ba}_{2.875}\text{PuO}_{5.875}$  spectra were like ‘-ate’ species, which is in line with expectations. The low-temperature heat capacity was measured, yielding the heat capacity and standard entropy at 298.15 K. Moreover, the magnetic susceptibility was measured, which is the first reported full temperature-dependent curve for a  $[\text{Rn}]5f^2$  Pu-based compound.

Whereas the Pb-Ba-Pu-O system was the targetted system, it was found that insights into the Ba-Pu-O system are too limited to proceed to this system directly. The results obtained in this Chapter are an important step to an enhanced understanding of the Ba-Pu-O system, and are necessary to update thermochemical tables on actinide materials. This starts from the very issue of the stoichiometry of the compound and the findings during the synthesis: Ba seems to be rather volatile in certain quite stable compositions. The findings in this chapter are applicable for the understanding of the grey phase in irradiated fuel in general, and not only LFRs. The rather high entropy obtained

for  $\text{Ba}_{2.875}\text{PuO}_{5.875}$  hints at a high stability of the compound, but its presence in irradiated nuclear fuel can only be ascertained after either studies of irradiated fuel, or calculations including a fuel database and defined oxygen potential.

## 8.5. GENERAL IMPLICATIONS AND OUTLOOK

Two general implications of this dissertation originate from the fundamental phase diagrams and thermochemical approach chosen. First, the herein reported phase diagrams describe the full studied (composition, temperature)-space. The scenario of cladding failure can lead to ingress of fission products in the coolant, or ingress of coolant inside the fuel pin, or a local interaction. In a phase diagram, these scenarios correspond to high Pb (and Bi) concentration, low Pb (or Bi) concentration, and intermediate Pb (or Bi) concentration. All cases are covered by the general phase diagram and thermodynamic assessment. This thesis provides the first answer to the possible phases that can form in case of coolant-JOG chemical interaction following cladding failure in LFRs using the thermodynamic approach. Thereby, it contributes to the Generation IV principle of safety, but also allows to better estimate the costs related to clean-up associated with this event.

Second, the herein reported phase diagrams describe the full studied (composition, temperature)-space independent of nuclear applications. This is emphasised in the introduction of several articles, but particularly evidenced by the chapter on CsI-PbI<sub>2</sub>(-BiI<sub>3</sub>), which deals with the same chemical compounds that are widely studied in the field of photovoltaics and beyond.



# BIBLIOGRAPHY

- (1) Sreedharan, O. M.; Gnanamoorthy, J. B. *Journal of Nuclear Materials* **1980**, *89*, 113–128.
- (2) Smith, A. L.; Gueneau, C.; Flèche, J.-L.; Chatain, S.; Beneš, O.; Konings, R. J. M. *The Journal of Chemical Thermodynamics* **2017**, *114*, 93–115.
- (3) Müller, G.; Schumacher, G.; Zimmermann, F. *Journal of Nuclear Materials* **2000**, *278*, 85–95.
- (4) Müller, G.; Heinzl, A.; Schumacher, G.; Weisenburger, A. *Journal of Nuclear Materials* **2003**, *321*, 256–262.
- (5) Sieverts, A. *Zeitschrift für Metallkunde* **1929**, *21*, 37–46.
- (6) Risold, D.; Nagata, J.-I.; Suzuki, R. O. *Journal of Phase Equilibria* **1998**, *19*, 213–233.
- (7) Van Hattem, A.; Dankelman, R.; Colineau, E.; Griveau, J.-C.; Dardenne, K.; Rothe, J.; Couweleers, S.; Konings, R. J. M.; Smith, A. L. *Journal of Alloys and Compounds* **2024**, *1003*, 175588.
- (8) Chase, M. W. *Journal of Physical and Chemical Reference Data* **1996**, *25*, 1069–1111.
- (9) Smith, A. L.; Thi, T. N. P.; Guéneau, C.; Dumas, J.-C.; Epifano, E.; van Burik, W.; Dupin, N. *Calphad* **2021**, *75*, 102350.
- (10) Bandini, G.; Bubelis, E.; Schikorr, M.; Stempnievicz, M.; Tucek, K.; Lázaro, A.; Kudinov, P.; Kööp, K.; Jeltsov, M.; Mansani, L. Safety analysis results of representative DEC accidental transients for the ALFRED reactor, 2013.
- (11) Cairang, W.; Ma, S.; Gong, X.; Zeng, Y.; Yang, H.; Xue, D.; Qin, Y.; Ding, X.; Sun, J. *Corrosion Science* **2021**, *179*, 109132.
- (12) Engelen, J.; Ait Abderrahim, H.; Baeten, P.; De Bruyn, D.; Leysen, P. *International Journal of Hydrogen Energy* **2015**, *40*, 15137–15147.
- (13) Alemberti, A.; Caramello, M.; Frignani, M.; Grasso, G.; Merli, E.; Morresi, G.; Tarantino, M. *Nuclear Engineering and Design* **2020**, *370*, 110884.
- (14) Colle, J.-Y.; Zappey, J.; Beneš, O.; Cologna, M.; Wiss, T.; Konings, R. J. M. *Journal of Nuclear Materials* **2025**, *608*, 155715.
- (15) Karlsson, E.; Neuhausen, J.; Eichler, R.; Aerts, A.; Danilov, I. I.; Vögele, A.; Türler, A. *Journal of Radioanalytical and Nuclear Chemistry* **2020**, *326*, 1249–1258.
- (16) Karlsson, E.; Neuhausen, J.; Eichler, R.; Danilov, I. I.; Vögele, A.; Türler, A. *Journal of Radioanalytical and Nuclear Chemistry* **2021**, *328*, 691–699.

- (17) Zaier, R.; van Hattem, A.; de Waal, B. N.; Konings, R. J. M.; Smith, A. L.; Zeller, P.; Gueneau, C. Thermodynamic Modelling of the Cs-Pb System, in preparation.
- (18) Bell, J. S.; Dickson, R. S.; Sheedy, J.; Peplinskie, R. T.; Gauthier, M. D.; Ruhnke, J.; Stoll, K. *Annals of Nuclear Energy* **2020**, *148*, 107683.
- (19) Wang, M.; Jiang, G.; Cheng, S.; Wang, K. *Nuclear Engineering and Design* **2024**, *419*, 112981.
- (20) Liu, L.; Zobnin, V.; Zivadinovic, I.; Eichler, R.; Vögele, A.; Herrmann, D.; Aerts, A.; Steinegger, P.; Neuhausen, J. *Journal of Radioanalytical and Nuclear Chemistry* **2025**, 1–16.
- (21) Kulemin, V. V.; Rumer, I. A.; Nevolin, Y. M.; Krasavina, E. P.; Kulyukhin, S. A. *Radiochemistry* **2024**, *66*, 64–72.
- (22) Gueneau, C.; Dupin, N.; Kjellqvist, L.; Geiger, E.; Kurata, M.; Gosse, S.; Corcoran, E.; Quaini, A.; Hania, R.; Smith, A. L., et al. *Calphad* **2021**, *72*, 102212.

# ACKNOWLEDGEMENTS

Almost five years have passed since the first digital job interviews with a chemist from Utrecht University that had never been in Delft before and who had no background in nuclear industry, and his future promoters. I would like to wholeheartedly express my gratitude to prof.dr. Rudy Konings and dr. Anna Smith for all their guidance, good advice and generosity. I am very grateful for the opportunities they offered me to explore the exciting realm of chemistry and physics all over the periodic table, including the actinides; and I am grateful for the opportunities I got by visiting experimental facilities and joining international conferences. Thinking on the past years, I can barely imagine it truly happened, and I am glad we can continue working together a while longer.

During the digital job interview, Rudy was probably not even in Delft but in Karlsruhe. The Joint Research Centre became my place to visit and re-visit. My first introduction to the JRC was into the basic property research by Jean-Christophe Griveau and Eric Colineau. Although you did not get me to learn French, you got me from 'I want a standard entropy value for my thermodynamic model' to revisit multiple chapters of solid state physics, and to start enjoying magnetism in actinide-containing compounds. I am sorry I did not (yet) deliver you single crystal intermetallic compounds. The synthesis of some complex oxides soon involved Karin Popa. You taught me what doing experimental nuclear chemistry means, and how it can be done efficiently in a highly demanding environment. Many thanks for your patience when I asked for another analysis or extra explanation. A thank you to all scientists and staff that contributed somehow to the research and to my development as a researcher, even if the results are not included in this dissertation. In alphabetical order, I want to name Pedro Amador Celdran, Ondrej Benes, Co Boshoven, Jean-Yves Colle, Eckhard Dahms, Herwin Hein, Ramon Carlos Marquez, Octavian Valu and Olaf Walter. I am very grateful for the many things I learned from all of you, and that my wishes to do actinide science were fulfilled over the limits one would think possible. Also, the secretaries Krisztina Varga and Petra Strube deserve a round of applause.

Karlsruhe not only has a fantastic institute for transuranium research in its JRC, but also a nice synchrotron facility on the KIT Campus. Thank you Kathy Dardenne, Jörg Rothe, Tim Pruessmann, Tonya Vitova and Bianca Schacherl for the fruitful collaboration and nice discussions – most often in Karlsruhe or via e-mail but funnily enough I met Tonya for the first time at a conference in Charleston, SC, to discuss the M-edge data that ended up in Chapter 7.

Crystallography was a recurring theme throughout this research, and Anna introduced me to the kind Parisian crystallographer Gilles Wallez. It took till the last part of my PhD before we finally met in person, but a fruitful collaboration was born since our first contact. Thank you for everything I learned from you, especially at the times you mentioned something over e-mail in which I found a lead for a deeper dive.

From my first day in Delft, I was drilled in the lab and coffee-time rhythm by the

technicians John Vlieland and Dick de Haas. I found great support with the technicians and instrument scientists in Delft (in alphabetic order): Sebastian Couweleers, Robert Dankelman, Indu Dhiman, Anton Lefering, Michel Steenvoorden and Michel Thijs. The radiation protection unit accepted the countless wipe tests, with probably the most exchanged word 'schoon'. Also, the friendly atmosphere in the Reactor Physics and Nuclear Materials group was very nice. Trudy Beentjes, thank you for helping me through a lot of administrative issues. In the past years and over many coffees, I think I learned a bit on reactor physics and the nuclear energy sector from Martin Rohde, Danny Lathouwers and Jan-Leen Kloosterman as well.

Initially, the times were not apt for having in-person meetings and conversations, but luckily this improved rather quickly. Time seems to have flown by when I write down the names of Jaen Ocadiz Flores and Thomas Dumaire – thank you for leading the way. Dennis Alders, we joined almost simultaneously and experienced the PhD journey together, in the same office (and we will continue to do so). Your molten salt modelling experience proved highly suitable for a nice collaboration in the framework of Lead-cooled Fast Reactors. Realising I am passing several persons, I want to mention our coffee-table guest from downstairs, Jasper van Blaaderen. Our shared article is a proof coffee breaks can result in fruitful scientific collaboration. Thank you to my office mates (or the office next door) Bouke Kaaks, Tiberiu Berlacu, Nicolo Magro, Ruben Dewes, Aron Selmecei, Anish Kumar, Ana Sacristan, Jocelyn Soppo, Laurent de Geus, Marc van den Berg, Nick ter Veer, Anand Sudha and all the others, for the lunches, table tennis, volleyball, and discussions on all thinkable topics and beyond.

The advice to supervise master thesis projects proved to be very fruitful. Nick ter Veer and Laurent de Geus, I am glad I somehow convinced you to do a PhD yourself, even though you decided to work on molten salt reactor chemistry. Jelte de Wit, you made the decision to go to nuclear industry and found a nice position at the Dutch nuclear power plant. Annika Duijn, your project ended rather recently and I hope you find your way to a position in the nuclear field to your liking. It is rewarding to see you all decided to stay in the nuclear field. Koen de Vries, your project is still running and hopefully we can finish it soon. I also want to thank the bachelor students I supervised and enjoyed working with: Brandon de Waal and Fleur van Koten. For all of you, the work contributed to nice theses and contributions that already ended up in a publication, are to be published or in publication, or should have been published (one day you will understand this last category).

The many back and forths between Karlsruhe and Delft/Nunspeet made it difficult to spend a lot of time with the many nice young persons I met in Karlsruhe. The memory of the last stays is the most vivid, but thank you, Daphne Cette (I decided to put you in the Karlsruhe list), Meghann Fucina, Leonard Floarea, Lisa Gubbels, Andrea Mariano, and all the others, for the many dinners and drinks. Michal Dutkiewicz, thank you for all the good advices, dinners and trips during all the stays. In your hands I will trust every chemical element.

Ik wil op deze plaats ook mijn ouders Dries en Gretha, mijn schoonouders en grootouders, mijn broer Jan en alle andere familieleden en vrienden die meeleeften bedanken voor de ondersteuning in de afgelopen jaren. Het zal niet altijd makkelijk geweest zijn als ik weer eens weg was naar Duitsland, of nog verder weg voor een conferentie. Be-

dankt voor alle ondersteuning, ook voor ons groeiende gezin. *Last but not least* wil ik mijn vrouw Sandra bedanken voor alle liefde en hulp. Jij was degene die mij in september 2020 op de vacature aan de TU Delft attendeerde en hebt daarmee het zaadje voor dit proefschrift geplant. Ik was vaak weg of zat lang boven en ik waardeer het dat je me daarvoor de gelegenheid en de tijd gegeven hebt. Bedankt voor alle goede zorgen, ook voor onze lieve dochters Jenthe en Gemma. Aan hen, als vertegenwoordigers van een nieuwe generatie, is dit proefschrift in de eerste plaats opgedragen.



# A

## SUPPORTING INFORMATION TO THE Pb-Mo-O SYSTEM

### HEAT CAPACITY PbO

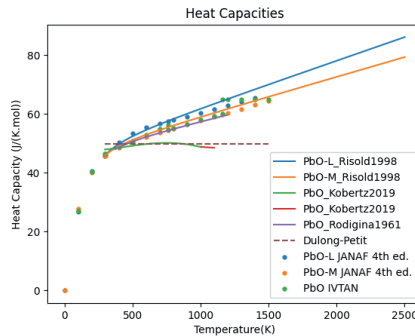


Figure A.1: The data set of Kobertz using DSC [1], Rodigina *et al.* using drop calorimetry [2], assessed equations in thermodynamic tables JANAF [3] and IVTAN [4] and modelled functions by Risold *et al.* [5] are compared. The data of Kobertz are not in line with the other data.

### EQUATIONS FOR WEIGHTED AVERAGE

Equations to calculate the weighted average (Equation 1) and its uncertainty (Equation 2) [6].

$$\bar{X} \equiv \frac{\sum_{i=1}^N \frac{X_i}{\sigma_i^2}}{\sum_{i=1}^N \frac{1}{\sigma_i^2}} \quad (\text{A.1})$$

$$\sigma_{\bar{X}} = \sqrt{\frac{1}{\sum_{i=1}^N \frac{1}{\sigma_i^2}}} \quad (\text{A.2})$$

## SOLUBILITY OF OXYGEN IN LEAD

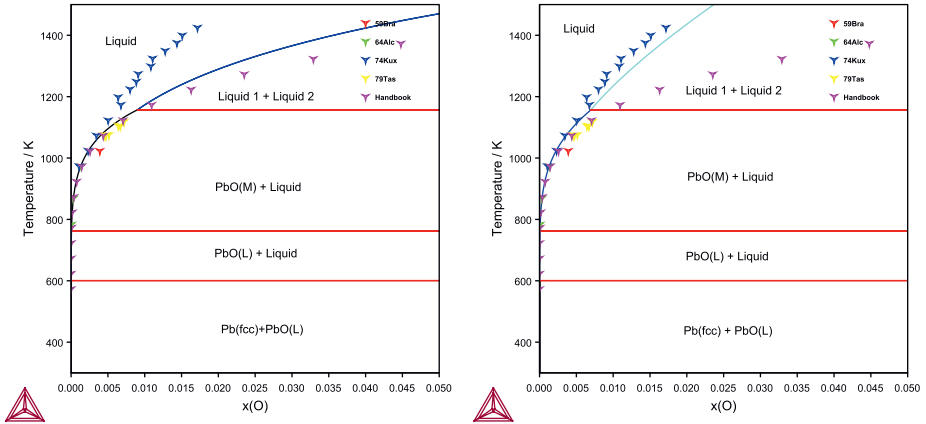


Figure A.2: Comparison of the oxygen (O) solubility in lead (Pb) data with the model by Vcanvarevic *et al.* [7] (Left) and the model as published by Risold *et al.* [5] and used in the current work (Right). For the experimental data underlying the Handbook recommendation, see the Handbook [8] and [9–12].

## THIRD-LAW ANALYSIS $\text{PbMoO}_4$ AND $\text{Pb}_2\text{MoO}_5$ DATA

Aiswarya *et al.* [13] derived the Gibbs formation energy of  $\text{PbMoO}_4(\text{s})$  and  $\text{Pb}_2\text{MoO}_5(\text{s})$  at high temperatures. The relationship between this obtained data and the current work was carefully examined, since at first glance the  $\text{PbMoO}_4$  Gibbs energy function formulation based on the optimized standard entropy and enthalpy of formation at 298.15 K, together with high-temperature heat capacity data by Aiswarya *et al.* [14] seemed to differ. Aiswarya *et al.* [13] use the following chemical equilibrium for their cell:



A third-law analysis using the free energy functions (FEF) of  $\text{Pb}(\text{cr,l})$ ,  $\text{MoO}_2(\text{s})$  and  $\text{O}_2(\text{g})$  as given in the JANAF tables [3], the high-temperature heat capacity for  $\text{PbMoO}_4(\text{s})$  reported by Aiswarya *et al.* [14] and the standard entropy at 298.15 K of  $\text{PbMoO}_4(\text{s})$  selected in this work, together with the original e.m.f.-cell data was made using the following equation:

$$T\Delta_r FEF + \Delta_r G(T) = \Delta_r H(298.15\text{K}) \quad (\text{A.4})$$

with  $\Delta_r G(T) = -4FE_{\text{cell}}$ .  $\Delta_f H(\text{PbMoO}_4, 298.15\text{K}) = \Delta_r H(298.15\text{K}) + \Delta_f H(\text{MoO}_2, 298.15\text{K})$ ; for the latter value the JANAF [3] value was taken as well. The result of the third law analysis is shown in Figure A.3.

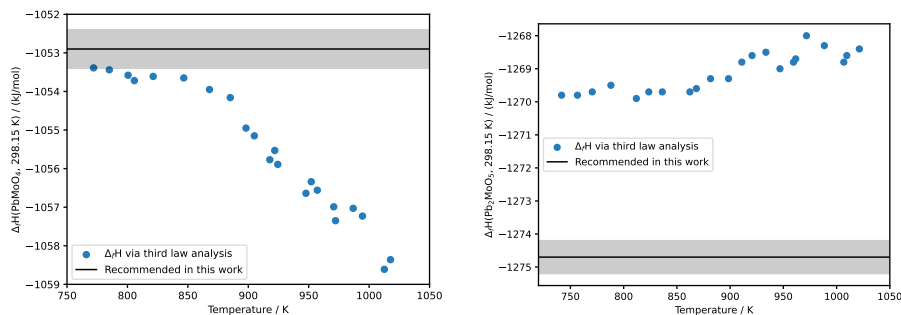
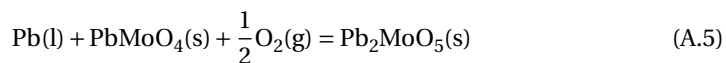


Figure A.3: Third law analysis for  $\text{PbMoO}_4$  (left) and  $\text{Pb}_2\text{MoO}_5$  (right).

As can be seen in this figure, the enthalpy of formation of  $\text{PbMoO}_4$  at 298.15 K obtained by this analysis shows a drift using the e.m.f.-data above 850 K, while the enthalpy of formation of  $\text{PbMoO}_4$  at 298.15 K obtained by the e.m.f.-data between 750 and 850 K are actually in good agreement with the selected value in this work. Thus, second law analysis as performed by Aiswarya *et al.* [13] yields a rather different result from the third law analysis performed herein. This indicates that the reaction of the cell is not valid anymore above 850 K, or there is a reaction involving the electrodes or electrolytes. The deviation above 850 K can account for a deviation up to -6 kJ/mol to the Gibbs energy function used in this work, as can be concluded from Figure A.3.

Moreover, for the actual comparison between the Gibbs energy function used in this work and the e.m.f.-data of Aiswarya *et al.*, the Gibbs energy functions used in the thermodynamic database of the current Pb-Mo-O model were used as auxiliary data. The comparison is shown in Figure A.4. The deviation at 770 K is about 3 kJ/mol, at 1020 K 7 kJ/mol. Taking into account the drift observed in the third law analysis, the e.m.f.-data can be considered to be in chemically accurate agreement with the assessed Gibbs energy function of  $\text{PbMoO}_4$ .

The analysis of  $\text{PbMoO}_4$  influences the  $\text{Pb}_2\text{MoO}_5$  analysis as well, since the calculations by Aiswarya *et al.* [13] made use of the equilibrium:



Again, a third-law analysis was made, which is shown in Figure A.3. The Gibbs energy curve of  $\text{Pb}_2\text{MoO}_5$  is compared to e.m.f results of Aiswarya *et al.* [13] in Figure A.4. This time, there is no drift visible, but the results differ by about 5 kJ/mol. As the third law analysis depends on the entropy, a test was made by change of the selected standard entropy of  $\text{Pb}_2\text{MoO}_5$  at 298.15 K. A change within the error margins can lead to an exact agreement between the selected formation enthalpy at 298.15 K and the value deduced from the e.m.f.-data. Again, a better agreement of the e.m.f.-data by Aiswarya *et al.* [13] was found than obtained by the second law analysis by those authors themselves.

The e.m.f.-data was converted to Gibbs energy using the thermodynamic database

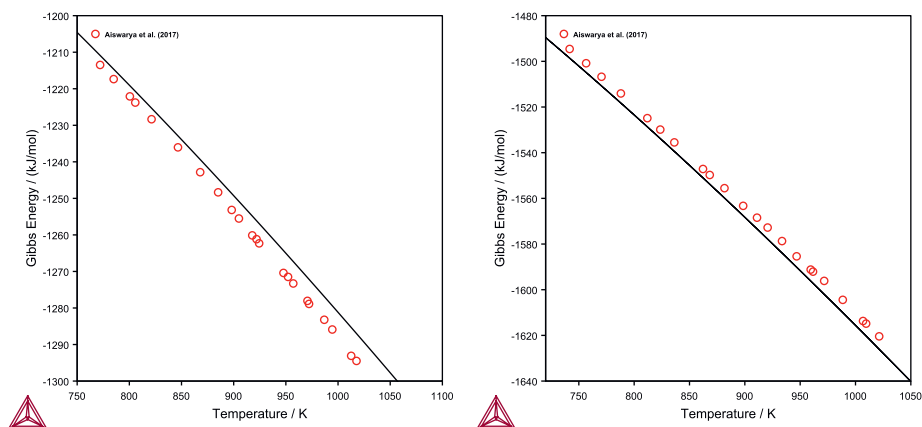


Figure A.4: Gibbs energy of  $\text{PbMoO}_4$  (left) and  $\text{Pb}_2\text{MoO}_5$  (right) as calculated using the model compared with experimental data of Aiswarya *et al.* [13].

of the current work as auxiliary functions and compared to the Gibbs energy function of  $\text{Pb}_2\text{MoO}_5$ . The result is shown in Figure A.4. A deviation up to 5 kJ/mol is observed, which is in line with the third law analysis and can probably be related to a deviation of the standard entropy at 298.15 K within the accuracy reported in this work.

### GAS PHASE FUNCTIONS Pb-Mo-O

On top of the binary gas phase species present in the binary phase diagrams Mo-O and Pb-O, the gas phase species as reported by Kunkel *et al.* [15] have been added to the thermodynamic database. Kunkel *et al.* calculated the thermodynamic properties, which were converted to Gibbs energy expressions and added to the database herein. No further calculations have been made with the gas phase species, as experimental vapour pressure data at various temperatures is, to the best of our knowledge, not reported in literature.

Molecule	$\Delta_f H^\circ$ (298.15 K) (kJ·mol <sup>-1</sup> )	$S_m^\circ$ (298.15 K) (J·K <sup>-1</sup> ·mol <sup>-1</sup> )	$C_p(T)$ (J·K <sup>-1</sup> ·mol <sup>-1</sup> )			Method
			a	b·10 <sup>3</sup>	c·10 <sup>-6</sup>	
$\text{PbMoO}_4$	-698.2	363.2	123.25	7.59	-2.44	QC, 298-1200 K
	-676.3±7.5					Exp.
$\text{PbMo}_2\text{O}_7$	-1406.0	500.1	213.09	15.21	-4.23	QC, 298-1200 K
	-1397.2±12.7					Exp.
$\text{PbMo}_3\text{O}_{10}$	-2072.9	635.0	301.90	23.64	-5.94	QC, 298-1200 K
	-2076.3±3.7					Exp.
$\text{Pb}_2\text{MoO}_5$	-874.9	472.8	171.83	8.57	-2.90	QC, 298-1200 K
	-888.0±18.3					Exp.

Table A.1: Calculated thermodynamic functions of the gas-phase lead-molybdenum oxides as reported by Kunkel *et al.* [15].  $C_p(T) = a + b \cdot T + c \cdot T^{-2}$ . QC = Quantum-chemical calculations.

CELL PARAMETERS OF  $\text{PbMoO}_4$  AND  $\text{Pb}_2\text{MoO}_5$ 

T (K)	a (Å)	c (Å)	V (Å <sup>3</sup> )
301	5.4365(1)	12.1109(3)	357.94(1)
373	5.4406(1)	12.1335(3)	359.16(1)
473	5.4467(1)	12.1659(3)	360.92(1)
573	5.4531(1)	12.2001(2)	362.79(1)
673	5.4597(1)	12.2362(2)	364.75(1)
773	5.4666(1)	12.2748(2)	366.82(1)
873	5.4735(1)	12.3147(2)	368.93(1)
973	5.4813(1)	12.3576(2)	371.28(1)
1073	5.4879(1)	12.4002(2)	373.45(1)
1173	5.4991(1)	12.4559(4)	376.66(2)
373	5.4421(2)	12.1405(6)	359.55(2)

Table A.2: Cell parameters of  $\text{PbMoO}_4$  at different temperatures. The statistically derived standard uncertainties obtained from the refinement were underestimated by about one order of magnitude and were thus multiplied by 10.

T (K)	a (Å)	b (Å)	c (Å)	$\beta$ (°)	V (Å <sup>3</sup> )
303	14.21678(5)	5.78663(2)	7.3292(2)	114.142(2)	550.218(3)
373	14.22527(4)	5.79681(2)	7.3462(2)	114.108(2)	552.942(3)
473	14.23473(4)	5.81036(2)	7.3701(2)	114.068(2)	556.581(3)
573	14.24670(3)	5.82603(2)	7.3979(2)	114.040(2)	560.782(2)
673	14.26042(3)	5.84341(1)	7.4293(2)	114.027(2)	565.438(2)
773	14.27449(3)	5.86202(1)	7.4628(2)	114.035(2)	570.322(2)
873	14.28722(3)	5.88225(1)	7.4984(2)	114.073(2)	575.361(2)
973	14.29942(4)	5.90393(1)	7.5344(2)	114.148(2)	580.411(2)
1073	14.31326(11)	5.92788(4)	7.5709(6)	114.270(4)	585.597(7)

Table A.3: Cell parameters of  $\text{Pb}_2\text{MoO}_5$  at different temperatures. The statistically derived standard uncertainties obtained from the refinement were underestimated by about one order of magnitude and were thus multiplied by 10.

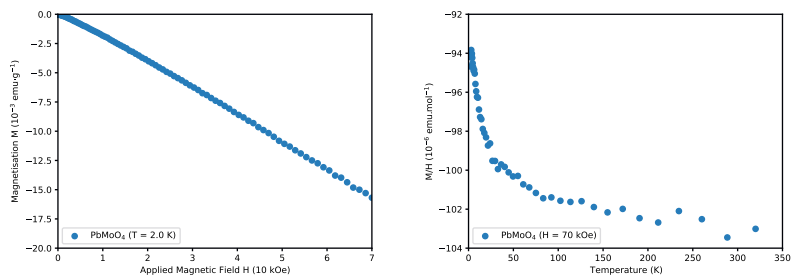
MAGNETIC SUSCEPTIBILITY OF  $\text{PbMoO}_4$  AND  $\text{Pb}_2\text{MoO}_5$ 

Figure A.5: Magnetic susceptibility of  $\text{PbMoO}_4$ .  $\text{PbMoO}_4$  displays diamagnetic behaviour in the full temperature range of study and can be considered as a temperature-independent diamagnet.

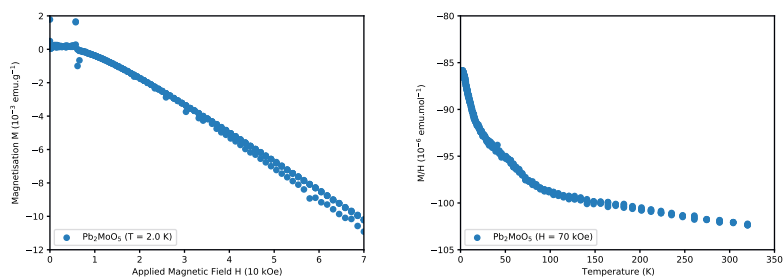


Figure A.6: Magnetic susceptibility of  $\text{Pb}_2\text{MoO}_5$ .  $\text{Pb}_2\text{MoO}_5$  displays diamagnetic behaviour in the full temperature range of study and can be considered as a temperature-independent diamagnet.

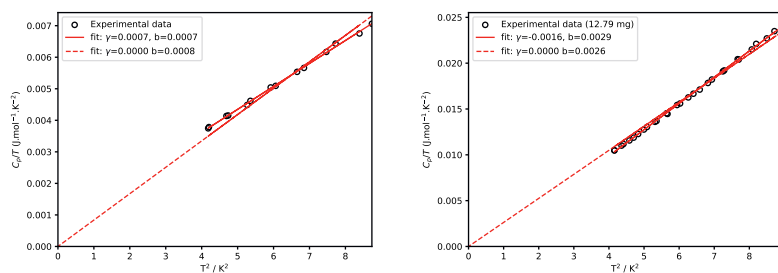
LOW-TEMPERATURE HEAT CAPACITY OF  $\text{PbMoO}_4$  AND  $\text{Pb}_2\text{MoO}_5$ 

Figure A.7: Heat capacity of  $\text{PbMoO}_4$  and  $\text{Pb}_2\text{MoO}_5$  as plotted in  $C_p/T$  vs  $T^2$  showing there is no additional contribution to the heat capacity.

## BIBLIOGRAPHY

- (1) Kobertz, D. *Calphad* **2019**, *65*, 155–164.
- (2) Rodigina, E. N.; Gomel'skii, K. Z.; Luginina, V. F. *Russian Journal of Physical Chemistry* **1961**, *35*, 884–886.
- (3) Chase, M. W.; National Information Standards Organization, U. S., *NIST-JANAF thermochemical tables*; American Chemical Society Washington, DC: 1998; Vol. 9.
- (4) Gurvich, L. V.; Polyshchuk, V. K.; Yorish, V. S.; Yungman, V. S., *The IVTAN data bank on the thermodynamic properties of individual substances*, 1981.
- (5) Risold, D.; Nagata, J.-I.; Suzuki, R. O. *Journal of Phase Equilibria* **1998**, *19*, 213–233.
- (6) Grenthe, I.; Fuger, J.; Konings, R. J. M.; Lemire, R. J.; Muller, A. B.; Nguyen-Trung, C.; Wanner, H., *Chemical thermodynamics of uranium*; Elsevier Amsterdam: 1992; Vol. 1.
- (7) Čančarevic, M.; Zinkevich, M.; Aldinger, F. *International Journal of Materials Research* **2005**, *96*, 879–887.
- (8) OECD–NEA, *Handbook on lead-bismuth eutectic alloy and lead properties, materials compatibility, thermalhydraulics and technologies*; Organisation for Economic Co-Operation and Development: 2015.
- (9) Bradhurst, D. H.; Buchanan, A. S. *Australian Journal of Chemistry* **1959**, *12*, 523–524.
- (10) Alcock, C. B.; Belford, T. N. *Transactions of the Faraday Society* **1964**, *60*, 822–835.
- (11) Kuxmann, U.; Fischer, P. *Erzmetall* **1974**, *27*, 181–190.
- (12) Taskinen, A. *Scandinavian Journal of Metallurgy* **1979**, *8*, 185–190.
- (13) Aiswarya, P. M.; Ganesan, R.; Gnanasekaran, T. *Journal of Nuclear Materials* **2017**, *493*, 310–321.
- (14) Aiswarya, P. M.; Ganesan, R.; Gnanasekaran, T. *The Journal of Chemical Thermodynamics* **2018**, *116*, 21–31.
- (15) Kunkel, K.; Milke, E.; Binnewies, M. *International Journal of Mass Spectrometry* **2014**, *374*, 12–19.



# B

## EXPERIMENTAL DATA IN THE CsI-PbI<sub>2</sub>-BiI<sub>3</sub> SYSTEM

### MAGNETIC SUSCEPTIBILITY CsPbI<sub>3</sub>

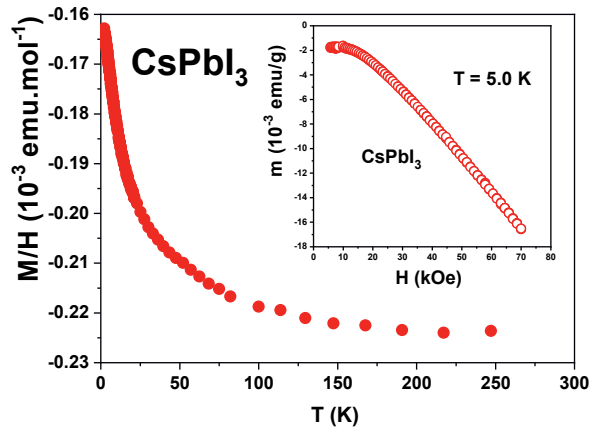


Figure B.1: Zero-field cooled magnetic susceptibility of  $\delta\text{-CsPbI}_3$  obtained at 70 kOe. Insert shows magnetisation dependence at fixed temperature 5.0 K.

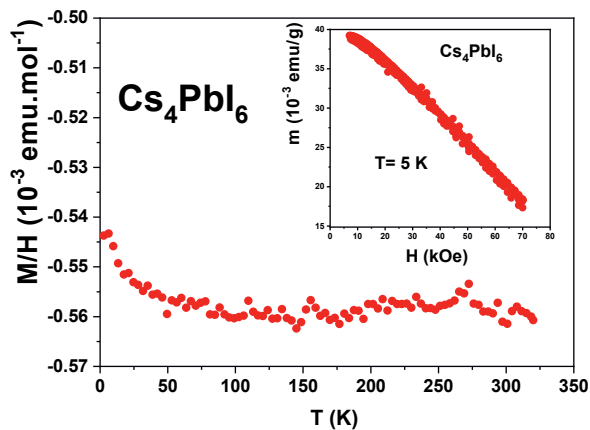
MAGNETIC SUSCEPTIBILITY  $\text{Cs}_4\text{PbI}_6$ 

Figure B.2: Zero-field cooled magnetic susceptibility of  $\text{Cs}_4\text{PbI}_6$  obtained at 70 kOe. Insert shows magnetisation dependence at fixed temperature 5.0 K. A Ni impurity contribution ordered above 300 K is subtracted from results.

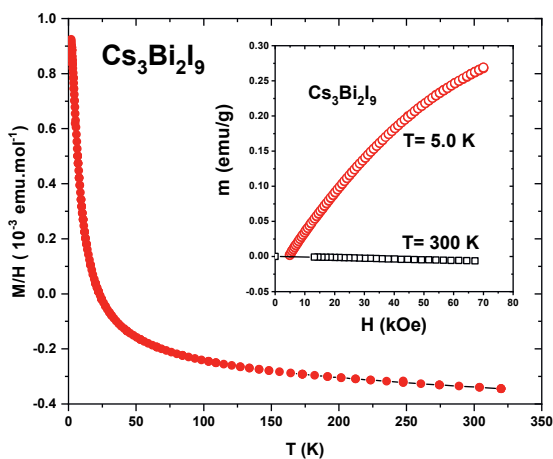
MAGNETIC SUSCEPTIBILITY  $\text{Cs}_3\text{Bi}_2\text{I}_9$ 

Figure B.3: Zero-field cooled magnetic susceptibility of  $\text{Cs}_3\text{Bi}_2\text{I}_9$  obtained at 70 kOe. Insert shows magnetisation dependence at fixed temperatures 5.0 K and 300 K. A Ni impurity contribution ordered above 300 K is subtracted from results.

## LOW TEMPERATURE HEAT CAPACITY OF $\delta$ -CsPbI<sub>3</sub> WITH DIFFERENT GRÜNEISEN PARAMETER

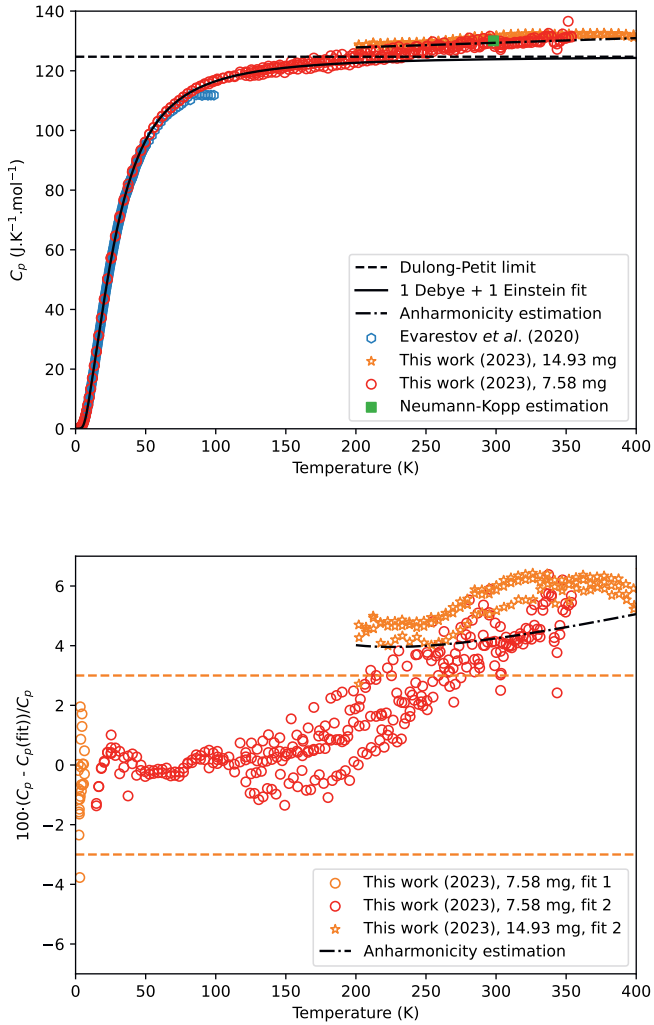
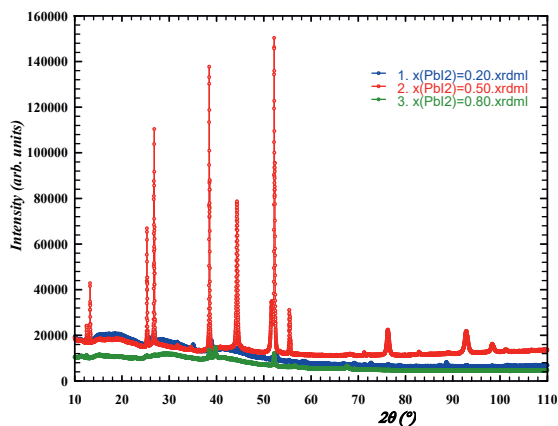


Figure B.4: Top: Low-temperature heat capacity of  $\delta$ -CsPbI<sub>3</sub> with anharmonicity estimation based on a Grüneisen parameter of 1. Bottom: Difference of models and measured data.

## PHASE ANALYSIS STUDIES IN THE BINARY SYSTEMS

System	Fraction	Phases	Experimental details
$\text{CsI-PbI}_2$	$x(\text{PbI}_2) = 0.20$	$\text{CsI}$ , $\text{Cs}_4\text{PbI}_6$ , $\text{CsPbI}_3$	Post-DSC XRD
	$x(\text{PbI}_2) = 0.50$	$\text{CsPbI}_3$	Post-DSC XRD
	$x(\text{PbI}_2) = 0.70$	$\text{CsPbI}_3$ , $\text{PbI}_2$	Post-DSC XRD
$\text{CsI-BiI}_3$	$x(\text{BiI}_3) = 0.20$	$\text{Cs}_3\text{Bi}_2\text{I}_9$ , $\text{CsI}$	Quenching from 873 K
	$x(\text{BiI}_3) = 0.25$	$\text{Cs}_3\text{Bi}_2\text{I}_9$ , $\text{CsI}$	Quenching from 748 K
	$x(\text{BiI}_3) = 0.25$	$\text{Cs}_3\text{Bi}_2\text{I}_9$ , $\text{CsI}$	Quenching from 973 K
	$x(\text{BiI}_3) = 0.30$	$\text{Cs}_3\text{Bi}_2\text{I}_9$ , $\text{CsI}$	Post-DSC XRD
	$x(\text{BiI}_3) = 0.40$	$\text{Cs}_3\text{Bi}_2\text{I}_9$	Post-DSC XRD
	$x(\text{BiI}_3) = 0.80$	$\text{Cs}_3\text{Bi}_2\text{I}_9$ , $\text{BiI}_3$	Post-DSC XRD
$\text{BiI}_3\text{-PbI}_2$	$x(\text{PbI}_2) = 0.20$	$\text{Pb}_{1-x}\text{Bi}_x\text{I}_{2+x}$	Post-DSC XRD
	$x(\text{PbI}_2) = 0.50$	$\text{Pb}_{1-x}\text{Bi}_x\text{I}_{2+x}$	Post-DSC XRD
	$x(\text{PbI}_2) = 0.80$	$\text{Pb}_{1-x}\text{Bi}_x\text{I}_{2+x}$	Post-DSC XRD

Table B.1: Summary of phase analysis studies in the binary systems. For explanation, see main text.

XRD MEASUREMENTS IN THE  $\text{BiI}_3\text{-PbI}_2$  PHASE DIAGRAMFigure B.5: X-ray diffraction patterns of post-DSC samples in the  $\text{BiI}_3\text{-PbI}_2$  system, exhibiting the (partial) crystalline nature of the products. The diffraction patterns are taken at  $x(\text{PbI}_2) = 0.20$  (blue), 0.50 (red) and 0.80 (green).

EXPERIMENTAL DATA IN THE CsI-BiI<sub>3</sub> SYSTEM

$x(\text{BiI}_3)$	T (K)	Equilibrium	Equilibrium reaction
0.000	904	Congruent melting	$\text{CsI} = L$
0.099	779	Eutectic	$\text{CsI} + \text{Cs}_3\text{Bi}_2\text{I}_9 = L$
0.099	871	Liquidus	$\text{CsI} + L' = L$
0.154	785	Eutectic	$\text{CsI} + \text{Cs}_3\text{Bi}_2\text{I}_9 = L$
0.154	846	Liquidus	$\text{CsI} + L' = L$
0.207	786	Eutectic	$\text{CsI} + \text{Cs}_3\text{Bi}_2\text{I}_9 = L$
0.251	787	Eutectic	$\text{CsI} + \text{Cs}_3\text{Bi}_2\text{I}_9 = L$
0.251	828	Liquidus	$\text{Cs}_3\text{Bi}_2\text{I}_9 + L' = L$
0.297	780	Eutectic	$\text{CsI} + \text{Cs}_3\text{Bi}_2\text{I}_9 = L$
0.297	854	Liquidus	$\text{Cs}_3\text{Bi}_2\text{I}_9 + L' = L$
0.400	867	Congruent melting	$\text{Cs}_3\text{Bi}_2\text{I}_9 = L$
0.503	636	Eutectic	$\text{BiI}_3 + \text{Cs}_3\text{Bi}_2\text{I}_9 = L$
0.503	858	Liquidus	$\text{Cs}_3\text{Bi}_2\text{I}_9 + L' = L$
0.600	636	Eutectic	$\text{BiI}_3 + \text{Cs}_3\text{Bi}_2\text{I}_9 = L$
0.600	816	Liquidus	$\text{Cs}_3\text{Bi}_2\text{I}_9 + L' = L$
0.699	636	Eutectic	$\text{BiI}_3 + \text{Cs}_3\text{Bi}_2\text{I}_9 = L$
0.699	725	Liquidus	$\text{Cs}_3\text{Bi}_2\text{I}_9 + L' = L$
0.746	638	Eutectic	$\text{BiI}_3 + \text{Cs}_3\text{Bi}_2\text{I}_9 = L$
0.798	633	Eutectic	$\text{BiI}_3 + \text{Cs}_3\text{Bi}_2\text{I}_9 = L$
0.897	636	Eutectic	$\text{BiI}_3 + \text{Cs}_3\text{Bi}_2\text{I}_9 = L$
0.897	664	Liquidus	$\text{BiI}_3 + L' = L$
1.000	665	Congruent melting	$\text{BiI}_3 = L$

Table B.2: Equilibrium data in the CsI-BiI<sub>3</sub> system as measured in this work by DSC. Standard uncertainties on composition are  $\pm 0.005$ ; standard uncertainties on temperature are  $\pm 5$  K for pure compounds and  $\pm 10$  K for mixtures. The measurements were performed at ambient pressure.

EXPERIMENTAL DATA IN THE BI<sub>3</sub>-PBI<sub>2</sub> SYSTEM

x(PbI <sub>2</sub> )	T (K)	Equilibrium	Equilibrium reaction
0.000	665	Congruent melting	BiI <sub>3</sub> = L
0.103	650	Solidus	Pb <sub>1-x</sub> Bi <sub>x</sub> I <sub>2+x</sub> = BiI <sub>3</sub> + L'
0.103	668	Liquidus	BiI <sub>3</sub> + L' = L
0.207	635	Solidus	Pb <sub>1-x</sub> Bi <sub>x</sub> I <sub>2+x</sub> = BiI <sub>3</sub> + L'
0.207	657	Liquidus	BiI <sub>3</sub> + L' = L
0.300	640	Solidus	Pb <sub>1-x</sub> Bi <sub>x</sub> I <sub>2+x</sub> = BiI <sub>3</sub> + L'
0.300	654	Liquidus	BiI <sub>3</sub> + L' = L
0.402	641	Solidus	Pb <sub>1-x</sub> Bi <sub>x</sub> I <sub>2+x</sub> = BiI <sub>3</sub> + L'
0.402	652	Liquidus	BiI <sub>3</sub> + L' = L
0.513	641	Solidus	Pb <sub>1-x</sub> Bi <sub>x</sub> I <sub>2+x</sub> = PbI <sub>2</sub> + L'
0.513	653	Liquidus	PbI <sub>2</sub> + L' = L
0.602	644	Solidus	Pb <sub>1-x</sub> Bi <sub>x</sub> I <sub>2+x</sub> = PbI <sub>2</sub> + L'
0.602	656	Liquidus	PbI <sub>2</sub> + L' = L
0.695	648	Solidus	Pb <sub>1-x</sub> Bi <sub>x</sub> I <sub>2+x</sub> = PbI <sub>2</sub> + L'
0.695	662	Liquidus	PbI <sub>2</sub> + L' = L
0.798	649	Solidus	Pb <sub>1-x</sub> Bi <sub>x</sub> I <sub>2+x</sub> = PbI <sub>2</sub> + L'
0.798	669	Liquidus	PbI <sub>2</sub> + L' = L
0.887	657	Solidus	Pb <sub>1-x</sub> Bi <sub>x</sub> I <sub>2+x</sub> = PbI <sub>2</sub> + L'
0.887	678	Liquidus	PbI <sub>2</sub> + L' = L
1.000	687	Congruent melting	PbI <sub>2</sub> = L

Table B.3: Equilibrium data in the BiI<sub>3</sub>-PbI<sub>2</sub> system as measured in this work by DSC. Standard uncertainties on composition are  $\pm 0.005$ ; standard uncertainties on temperature are  $\pm 5$  K for pure compounds and  $\pm 10$  K for mixtures. The measurements were performed at ambient pressure. The measured peak onset temperature was taken as the temperature of the solidus, while the temperature of the peak maximum was taken for the liquidus.

EXPERIMENTAL DATA IN THE CSI-PBI<sub>2</sub> SYSTEM

(see next page)

$x(\text{PbI}_2)$	T (K)	Equilibrium	Equilibrium reaction
0.000	904	Congruent melting	$\text{CsI} = L$
0.039	753	Peritectic	$\text{Cs}_4\text{PbI}_6 = \text{CsI} + L'$
0.039	898	Liquidus	$\text{CsI} + L' = L$
0.101	754	Peritectic	$\text{Cs}_4\text{PbI}_6 = \text{CsI} + L'$
0.101	873	Liquidus	$\text{CsI} + L' = L$
0.200*	759	Peritectic	$\text{Cs}_4\text{PbI}_6 = \text{CsI} + L'$
0.248	604	Polymorphism	$\delta\text{-CsPbI}_3 = \alpha\text{-CsPbI}_3$
0.248	716	Eutectic	$\alpha\text{-CsPbI}_3 + \text{Cs}_4\text{PbI}_6 = L$
0.248	753	Peritectic	$\text{Cs}_4\text{PbI}_6 = \text{CsI} + L'$
0.301	604	Polymorphism	$\delta\text{-CsPbI}_3 = \alpha\text{-CsPbI}_3$
0.301	717	Eutectic	$\alpha\text{-CsPbI}_3 + \text{Cs}_4\text{PbI}_6 = L$
0.301	753	Liquidus	$\text{Cs}_4\text{PbI}_6 + L' = L$
0.350	607	Polymorphism	$\delta\text{-CsPbI}_3 = \alpha\text{-CsPbI}_3$
0.350	718	Eutectic	$\alpha\text{-CsPbI}_3 + \text{Cs}_4\text{PbI}_6 = L$
0.407	604	Polymorphism	$\delta\text{-CsPbI}_3 = \alpha\text{-CsPbI}_3$
0.407	718	Eutectic	$\text{Cs}_4\text{PbI}_6 + \alpha\text{-CsPbI}_3 = L$
0.448	600	Polymorphism	$\delta\text{-CsPbI}_3 = \alpha\text{-CsPbI}_3$
0.448	714	Eutectic	$\alpha\text{-CsPbI}_3 + \text{Cs}_4\text{PbI}_6 = L$
0.448	758	Liquidus	$\alpha\text{-CsPbI}_3 + L' = L$
0.500	599	Polymorphism	$\delta\text{-CsPbI}_3 = \alpha\text{-CsPbI}_3$
0.500	758	Congruent melting	$\alpha\text{-CsPbI}_3 = L$
0.606	594	Polymorphism	$\delta\text{-CsPbI}_3 = \alpha\text{-CsPbI}_3$
0.606	618	Eutectic	$\alpha\text{-CsPbI}_3 + \text{PbI}_2 = L$
0.606	748	Liquidus	$\alpha\text{-CsPbI}_3 + L' = L$
0.649	595	Polymorphism	$\delta\text{-CsPbI}_3 = \alpha\text{-CsPbI}_3$
0.649	620	Eutectic	$\alpha\text{-CsPbI}_3 + \text{PbI}_2 = L$
0.649	735	Liquidus	$\alpha\text{-CsPbI}_3 + L' = L$
0.694	596	Polymorphism	$\delta\text{-CsPbI}_3 = \alpha\text{-CsPbI}_3$
0.694	617	Eutectic	$\alpha\text{-CsPbI}_3 + \text{PbI}_2 = L$
0.776	596	Polymorphism	$\delta\text{-CsPbI}_3 = \alpha\text{-CsPbI}_3$
0.776	618	Eutectic	$\alpha\text{-CsPbI}_3 + \text{PbI}_2 = L$
0.800	595	Polymorphism	$\delta\text{-CsPbI}_3 = \alpha\text{-CsPbI}_3$
0.800	617	Eutectic	$\alpha\text{-CsPbI}_3 + \text{PbI}_2 = L$
0.825	596	Polymorphism	$\delta\text{-CsPbI}_3 = \alpha\text{-CsPbI}_3$
0.825	620	Eutectic	$\alpha\text{-CsPbI}_3 + \text{PbI}_2 = L$
0.825	640	Liquidus	$\text{PbI}_2 + L' = L$
0.902	594	Polymorphism	$\delta\text{-CsPbI}_3 = \alpha\text{-CsPbI}_3$
0.902	620	Eutectic	$\alpha\text{-CsPbI}_3 + \text{PbI}_2 = L$
0.902	665	Liquidus	$\text{PbI}_2 + L' = L$
1.000	687	Congruent melting	$\text{PbI}_2 = L$

Table B.4: Equilibrium data in the CsI-PbI<sub>2</sub> system as measured in this work by DSC. Standard uncertainties on composition are  $\pm 0.005$ ; standard uncertainties on temperature are  $\pm 5$  K for pure compounds and  $\pm 10$  K for mixtures. The measurements were performed at ambient pressure. All compositions except the end-members and \* are measured by mixing CsI with PbI<sub>2</sub>; \* was first synthesised.

EXPERIMENTAL DATA OF THE CsPbI<sub>3</sub>-Cs<sub>3</sub>Bi<sub>2</sub>I<sub>9</sub> SECTION

$x(\text{CsPbI}_3)$	T (K)	Equilibrium	Equilibrium reaction
0.05	840	Unknown	-
0.05	871	Liquidus	$\text{Cs}_3\text{Bi}_2\text{I}_9 + L' = L$
0.1	865	Liquidus	$\text{Cs}_3\text{Bi}_2\text{I}_9 + L' = L$
0.20	719	Eutectic	$\alpha\text{-CsPbI}_3 + \text{Cs}_3\text{Bi}_2\text{I}_9 = L$
0.20	860	Liquidus	$L' + \text{Cs}_3\text{Bi}_2\text{I}_9 = L$
0.40	714	Eutectic	$\alpha\text{-CsPbI}_3 + \text{Cs}_3\text{Bi}_2\text{I}_9 = L$
0.40	843	Liquidus	$L' + \text{Cs}_3\text{Bi}_2\text{I}_9 = L$
0.60	738	Eutectic	$\alpha\text{-CsPbI}_3 + \text{Cs}_3\text{Bi}_2\text{I}_9 = L$
0.60	826	Liquidus	$L' + \text{Cs}_3\text{Bi}_2\text{I}_9 = L$
0.70	671	Unknown	-
0.70	741	Eutectic	$\alpha\text{-CsPbI}_3 + \text{Cs}_3\text{Bi}_2\text{I}_9 = L$
0.70	809	Liquidus	$L' + \text{Cs}_3\text{Bi}_2\text{I}_9 = L$
0.80	740	Eutectic	$\alpha\text{-CsPbI}_3 + \text{Cs}_3\text{Bi}_2\text{I}_9 = L$
0.80	787	Liquidus	$L' + \text{Cs}_3\text{Bi}_2\text{I}_9 = L$
0.90	744	Eutectic	$\alpha\text{-CsPbI}_3 + \text{Cs}_3\text{Bi}_2\text{I}_9 = L$
0.95	747	Eutectic	$\alpha\text{-CsPbI}_3 + \text{Cs}_3\text{Bi}_2\text{I}_9 = L$
0.95	756	Liquidus	$\alpha\text{-CsPbI}_3 + L' = L$

Table B.5: Equilibrium data in the CsPbI<sub>3</sub>-Cs<sub>3</sub>Bi<sub>2</sub>I<sub>9</sub> system as measured in this work by DSC. Standard uncertainties on composition are  $\pm 0.005$ ; standard uncertainties on temperature are  $\pm 5$  K for pure compounds and  $\pm 10$  K for mixtures. The measurements were performed at ambient pressure. All compositions are measured by mixing appropriate ratios of BiI<sub>3</sub>, CsI and PbI<sub>2</sub>.

## CALCULATED MIXING ENTHALPIES

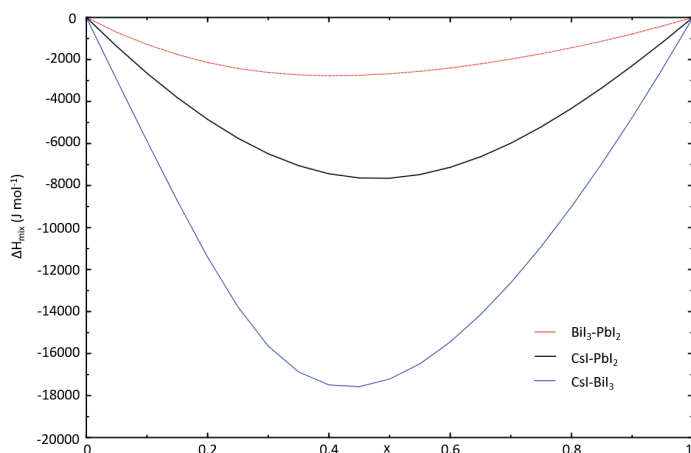


Figure B.6: Mixing enthalpies of the systems investigated in this work calculated with the thermodynamic model presented here. The enthalpy of mixing was calculated at  $T = 1000$  K, and is not observed to be significantly temperature dependent. The mole fractions on the x-axis correspond to  $\text{PbI}_2$  ( $\text{BiI}_3$ – $\text{PbI}_2$  system),  $\text{PbI}_2$  ( $\text{CsI}$ – $\text{PbI}_2$  system) and  $\text{BiI}_3$  ( $\text{CsI}$ – $\text{BiI}_3$  system).

## UNIDENTIFIED EVENTS AT 724 K IN THE $\text{CsI}$ – $\text{BiI}_3$ SYSTEM

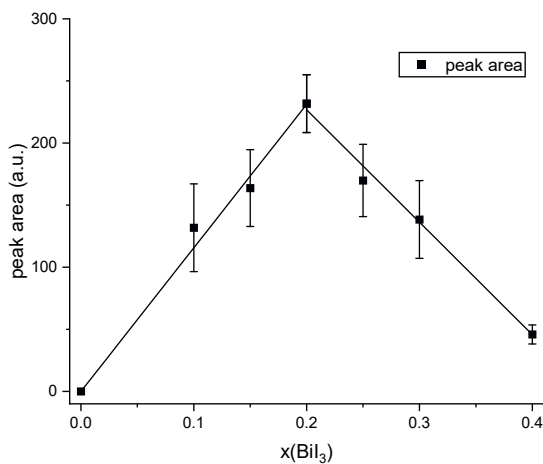


Figure B.7: Investigation of the peak area of the unidentified peaks measured at 724 K in the  $\text{CsI}$ – $\text{BiI}_3$  system. Based on the trend in the peak areas, a phase change is expected at  $x(\text{BiI}_3) = 0.2$ . No such transition has been found by quenching and post-XRD, however, as shown in Table B.1.



# C

## THERMODYNAMIC MODEL OF THE CsI-PbI<sub>2</sub>-BiI<sub>3</sub> SYSTEM

The thermodynamic modelling of the binaries CsI–PbI<sub>2</sub>, CsI–BiI<sub>3</sub> and BiI<sub>3</sub>–PbI<sub>2</sub>, as well as the ternary system CsI–PbI<sub>2</sub>–BiI<sub>3</sub>, was performed based on the CALPHAD method [1] using the FactSage software, version 8.2 [2]. Experimental data obtained in this work was used in combination with data reported in the literature as a basis for optimisation of the excess Gibbs energy functions of the salt systems of interest.

### STOICHIOMETRIC COMPOUNDS

The Gibbs energy function for the stoichiometric compounds CsI, PbI<sub>2</sub>, BiI<sub>3</sub>, CsPbI<sub>3</sub>, Cs<sub>4</sub>PbI<sub>6</sub> and Cs<sub>3</sub>Bi<sub>2</sub>I<sub>9</sub> is given by Equation C.1.

$$G^\phi(T) - \sum_i n_i^{\phi} H_i^{SER}(298.15K) = a + b \cdot T + c \cdot T \cdot \ln T + \sum d_n T^n \quad (C.1)$$

### LIQUID SOLUTION

The excess Gibbs energy terms of the liquid solutions are modelled using the quasi-chemical formalism in the quadruplet approximation as proposed by Pelton *et al.* [3]. This method is well-suited to the modelling of chloride and fluoride molten salt systems and was applied herein to a new class of halide salts, namely iodide salts. In the liquid phase, the lead and bismuth cations are taken to be symmetric with respect to each other, whereas the monovalent Cs is taken to be asymmetric.

This description of the melt assumes the existence of quadruplets in the liquid, allowing for the incorporation of short-range ordering into the thermodynamic model. A schematic depiction of a quadruplet is given in Figure C.1. This formalism allows for the selection of the composition of maximum short-range ordering, often found at the lowest eutectic or the congruent melting point of an intermediate, through the choice of

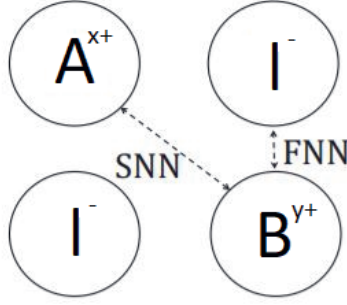


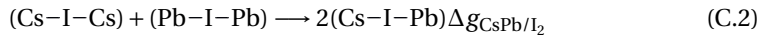
Figure C.1: Schematic representation of a quadruplet used in the quadruplet approximation. In this figure,  $A^{x+}$  and  $B^{y+}$  are the cations in a system, while  $I^{-}$  is the anion. The first-nearest neighbour (FNN) and second-nearest neighbour (SNN) are also shown.

$A^{x+}$	$B^{y+}$	$Z_{AB/I_2}^A$	$Z_{AB/I_2}^B$	$Z_{AB/I_2}^I$
$\text{Cs}^+$	$\text{Cs}^+$	6	6	6
$\text{Pb}^{2+}$	$\text{Pb}^{2+}$	6	6	3
$\text{Bi}^{3+}$	$\text{Bi}^{3+}$	6	6	2
$\text{Cs}^+$	$\text{Pb}^{2+}$	6	6	4
$\text{Cs}^+$	$\text{Bi}^{3+}$	3	6	2.4
$\text{Pb}^{2+}$	$\text{Bi}^{3+}$	6	6	2.4

Table C.1: Coordination numbers used in the CALPHAD models presented in this work.

cation-cation coordination numbers. The anion-anion coordination numbers are subsequently fixed through the electroneutrality rule. The coordination numbers used in this work are given in Table C.1.

The change in energy associated with the second-nearest neighbour exchange reaction, given in Eq. C.2 for the system  $\text{CsI-PbI}_2$ , is given in Eq. C.3. This excess Gibbs energy parameter is one of the optimisation parameters used in this work.



$$\Delta g_{\text{CsPb/I}_2} = \Delta g_{\text{CsCs/I}_2}^o + \sum_{i \geq 1} g_{\text{CsPb/I}_2}^{i0} \chi_{\text{CsPb/I}_2}^i + \sum_{j \geq 1} g_{\text{CsPb/I}_2}^{0j} \chi_{\text{PbCs/I}_2}^j \quad (\text{C.3})$$

In Eq. C.3 the terms  $\Delta g_{\text{CsPb/I}_2}^o$ ,  $g_{\text{CsPb/I}_2}^{i0}$  and  $g_{\text{PbCs/I}_2}^{0j}$  are composition-independent coefficients that may depend on temperature. The composition dependence of the Gibbs energy is apparent through  $\chi_{\text{CsPb/I}_2}$  as these are defined per Eq. C.4. In this equation  $X_{\text{CsCs/I}_2}$  is the cation-cation pair fraction, or the molar fraction of the quadruplet containing two cations Cs. For a binary system such as  $\text{CsI-PbI}_2$ ,  $\{X_{\text{CsCs/I}_2} + X_{\text{CsPb/I}_2} + X_{\text{PbPb/I}_2}\}$  is equal to one.

$$\chi_{\text{CsPb/I}_2} = \frac{X_{\text{CsCs/I}_2}}{X_{\text{CsCs/I}_2} + X_{\text{CsPb/I}_2} + X_{\text{PbPb/I}_2}} \quad (\text{C.4})$$

The excess Gibbs energy functions used in this work are given in Eq. C.5 for the CsI–PbI<sub>2</sub> system, in Eq. C.6 for the CsI–BiI<sub>3</sub> system and in Eq. C.7 for the BiI<sub>3</sub>–PbI<sub>2</sub> system. The ternary phase diagram is calculated by extrapolation from the constituting binary sub-systems using the asymmetric Kohler-Toop formalism [4]. No ternary interaction parameters were used for the extrapolation of these binaries to the ternary phase diagram.

$$\Delta g_{\text{CsPb/I}_2} = -8000 + \chi_{\text{CsPb/I}_2}(-1500) \quad (\text{C.5})$$

$$\Delta g_{\text{CsBi/I}_2} = -20200 + \chi_{\text{CsBi/I}_2}(400) + \chi_{\text{BiCs/I}_2}(-13000) \quad (\text{C.6})$$

$$\Delta g_{\text{PbBi/I}_2} = -2800 + \chi_{\text{BiPb/I}_2}(-2200) \quad (\text{C.7})$$

### SOLID SOLUTION DESCRIPTION OF THE BiI<sub>3</sub>–PbI<sub>2</sub> SYSTEM

Thermodynamic modelling of the complete solid solution in the BiI<sub>3</sub>–PbI<sub>2</sub> binary system and the homogeneity range in the CsI–BiI<sub>3</sub> binary system around Cs<sub>3</sub>Bi<sub>2</sub>I<sub>9</sub> is done using the compound energy formalism (CEF). Using this formalism, the assumption is that the solid is composed of sublattices with a fixed stoichiometry, with random mixing on each sublattice [1].

The atomic scale order of the BiI<sub>3</sub>–PbI<sub>2</sub> system poses the question on the proper choice of sublattices. In general, one should use the least number of optimization parameters while describing the experimental results well and resembling the physical nature. Since there is not enough experimental data available to fit the model to a brick structure, a simpler model reflecting the single-crystal XRD and EDS data from Alexander *et al.* [5] is selected. Their measurements indicated that Pb<sup>2+</sup>, Bi<sup>3+</sup> and vacancies share the same site, while iodine has a fully occupied position. Therefore, the BiI<sub>3</sub>–PbI<sub>2</sub> system is modelled herein as (Pb<sup>2+</sup>, Bi<sup>3+</sup>, Va)(I)<sub>2</sub>. The Gibbs energy of this phase is expressed in Eq. C.8; the excess Gibbs energy of the system is given in Eq. C.9. The values used for the interaction <sup>0</sup>L-terms in this equation are given in Table C.2.

$$G - \sum n_i^o H_i^{SER}(298.15\text{K}) = y_{\text{Pb}^{2+}} y_{\text{I}^-} \cdot {}^o G_{(\text{Pb}^{2+})_1(\text{I})_2} + y_{\text{Bi}^{3+}} y_{\text{I}^-} \cdot {}^o G_{(\text{Bi}^{3+})_1(\text{I})_2} + y_{\text{Va}} y_{\text{I}^-} \cdot {}^o G_{(\text{Va})_1(\text{I})_2} + RT(y_{\text{Pb}^{2+}} \ln y_{\text{Pb}^{2+}} + y_{\text{Bi}^{3+}} \ln y_{\text{Bi}^{3+}} + y_{\text{Va}} \ln y_{\text{Va}}) + G^{\text{excess}} \quad (\text{C.8})$$

$$G^{\text{excess}} = {}^0L_{(\text{Pb}^{2+}, \text{Bi}^{3+})_1(\text{I})_2} y_{\text{Pb}^{2+}} y_{\text{Bi}^{3+}} + {}^0L_{(\text{Pb}^{2+}, \text{Va})_1(\text{I})_2} y_{\text{Pb}^{2+}} y_{\text{Va}} \quad (\text{C.9})$$

In Eq. C.8,  $y_i$  are the fractions of species  $i$  in the sublattice, and  ${}^o G_{(i)_1(j)_2}$  are the Gibbs energies of the different end-members composed of species  $i$  on the first sublattice and species  $j$  on the second sublattice. The configurational entropy term accounts for ideal mixing on the cationic sublattice.

A schematic representation of the model is given in Figure C.2. In this figure, the neutral line shows at which points in this diagram the system has a net charge of zero, as this is the domain in which this model has a physical meaning. The end points of this neutral line are the end-members of this system, namely BiI<sub>3</sub> and PbI<sub>2</sub>.

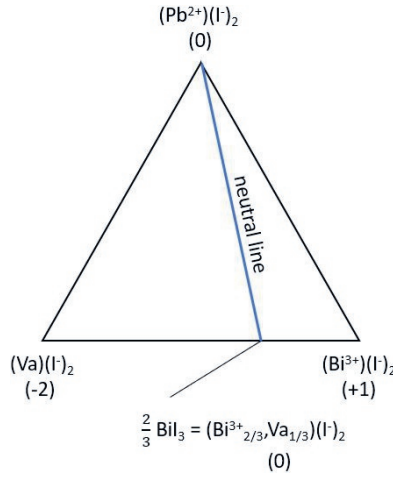


Figure C.2: Graphical representation of the model for the solid solution  $\text{BiI}_3\text{-PbI}_2$  using the compound energy formalism.

The Gibbs energies of the neutrally charged end-members  $\text{BiI}_3$  and  $\text{PbI}_2$  can be expressed as in Eqs. C.10 and C.11, respectively. Eq. C.11 can be simplified to Eq. C.12:

$${}^oG_{\text{PbI}_2} = {}^oG_{(\text{Pb}^{2+})_1(\Gamma)_2} \quad (\text{C.10})$$

$$\frac{2}{3} {}^oG_{\text{BiI}_3} = \frac{2}{3} {}^oG_{(\text{Bi}^{3+})_1(\Gamma)_2} + \frac{1}{3} {}^oG_{(\text{Va})_1(\Gamma)_2} + RT\left(\frac{1}{3} \ln \frac{1}{3} + \frac{2}{3} \ln \frac{2}{3}\right) \quad (\text{C.11})$$

$${}^oG_{\text{BiI}_3} = {}^oG_{(\text{Bi}^{3+})_1(\Gamma)_2} + \frac{1}{2} {}^oG_{(\text{Va})_1(\Gamma)_2} + RT\left(\ln 2 - \frac{3}{2} \ln 3\right) \quad (\text{C.12})$$

The description of the three end-members of this model are given by Eqs. C.13-C.15:

$${}^oG_{(\text{Pb}^{2+})_1(\Gamma)_2} = {}^oG_{\text{PbI}_2} \quad (\text{C.13})$$

$${}^oG_{(\text{Bi}^{3+})_1(\Gamma)_2} = {}^oG_{\text{BiI}_3} - {}^oG_I^{\text{SER}} - 50000 - RT\left(\ln 2 - \frac{3}{2} \ln 3\right) \quad (\text{C.14})$$

$${}^oG_{(\text{Va})_1(\Gamma)_2} = 2{}^oG_I^{\text{SER}} + 100000 \quad (\text{C.15})$$

#### SOLID SOLUTION DESCRIPTION IN THE TERNARY SYSTEM

To describe the entire ternary system using the CEF, the Cs-ion is also incorporated on the cationic sublattice. A vacancy is then introduced on the anionic sublattice to be able to define the CsI end-member. The ionic species used to describe the solid solution in the ternary system are therefore  $(\text{Cs}^+, \text{Pb}^{2+}, \text{Bi}^{3+}, \text{Va})(\Gamma, \text{Va})_2$ . The corresponding Gibbs energy functions used to describe this system is given in Eq. C.16:

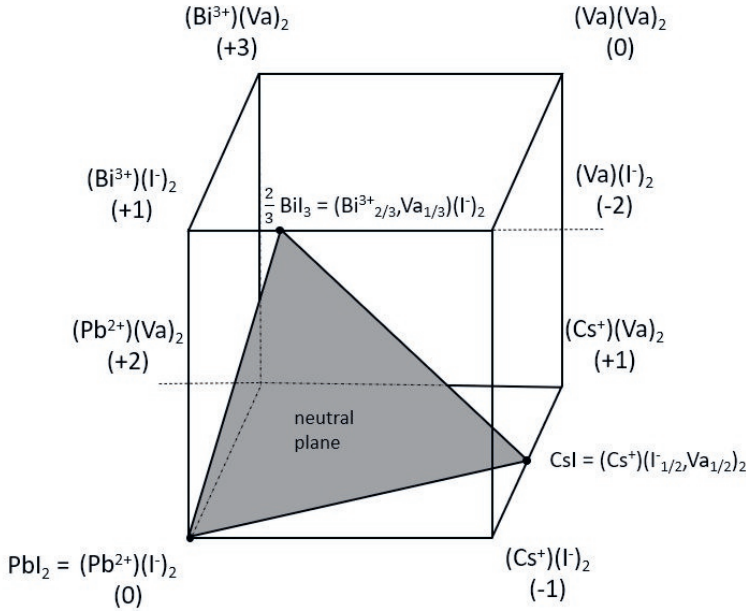


Figure C.3: Graphical representation of the  $(\text{Cs}^+, \text{Pb}^{2+}, \text{Bi}^{3+}, \text{Va})(\Gamma^-, \text{Va})_2$  sublattice model in the compound energy formalism. The neutral plane is the plane along which the phase diagrams of the binaries are calculated.

$$\begin{aligned}
 G - \sum_i n_i^o H_i^{SER}(298.15\text{K}) &= y_{\text{Cs}^+} y_{\Gamma^-} \cdot {}^o G_{(\text{Cs}^+)_1(\Gamma)_2} + y_{\text{Cs}^+} y_{\text{Va}} \cdot {}^o G_{(\text{Cs}^+)_1(\text{Va})_2} \\
 &+ y_{\text{Pb}^{2+}} y_{\Gamma^-} \cdot {}^o G_{(\text{Pb}^{2+})_1(\Gamma)_2} + y_{\text{Pb}^{2+}} y_{\text{Va}} \cdot {}^o G_{(\text{Pb}^{2+})_1(\text{Va})_2} \\
 &+ y_{\text{Bi}^{3+}} y_{\Gamma^-} \cdot {}^o G_{(\text{Bi}^{3+})_1(\Gamma)_2} + y_{\text{Bi}^{3+}} y_{\text{Va}} \cdot {}^o G_{(\text{Bi}^{3+})_1(\text{Va})_2} \\
 &+ y_{\text{Va}} y_{\Gamma^-} \cdot {}^o G_{(\text{Va})_1(\Gamma)_2} + y_{\text{Va}} y_{\text{Va}} \cdot {}^o G_{(\text{Va})_1(\text{Va})_2} \\
 &+ RT(y_{\text{Cs}^+} \ln y_{\text{Cs}^+} + y_{\text{Pb}^{2+}} \ln y_{\text{Pb}^{2+}} + y_{\text{Bi}^{3+}} \ln y_{\text{Bi}^{3+}} + y_{\text{Va}} \ln y_{\text{Va}}) \\
 &+ 2RT(y_{\Gamma^-} \ln y_{\Gamma^-} + y_{\text{Va}} \ln y_{\text{Va}}) + G^{\text{excess}}
 \end{aligned} \tag{C.16}$$

with the excess Gibbs energy function,  $G^{\text{excess}}$  as defined in Eq. C.17. The values used for the interaction parameters  ${}^oL$  are given in Table C.2.

$$\begin{aligned}
 G^{\text{excess}} &= {}^oL_{(\text{Pb}^{2+}, \text{Bi}^{3+})_1(\Gamma)_2} y_{\text{Pb}^{2+}} y_{\text{Bi}^{3+}} + {}^oL_{(\text{Pb}^{2+}, \text{Va})_1(\Gamma)_2} y_{\text{Pb}^{2+}} y_{\text{Va}} \\
 &+ {}^oL_{(\text{Cs}^+, \text{Pb}^{2+})_1(\Gamma)_2} y_{\text{Cs}^+} y_{\text{Pb}^{2+}} + {}^oL_{(\text{Cs}^+, \text{Pb}^{2+})_1(\text{Va})_2} y_{\text{Cs}^+} y_{\text{Pb}^{2+}} \\
 &+ {}^oL_{(\text{Cs}^+, \text{Bi}^{3+})_1(\Gamma)_2} y_{\text{Cs}^+} y_{\text{Bi}^{3+}}
 \end{aligned} \tag{C.17}$$

A graphical representation of the system is given in Figure C.3.

In addition to the Gibbs energy functions given in Eqs. C.13-C.15, Gibbs energy functions for the other end-members are given in Eqs. C.18-C.22. The end-member consisting exclusively of vacancies, Eq. C.22, has been destabilized using a large positive excess

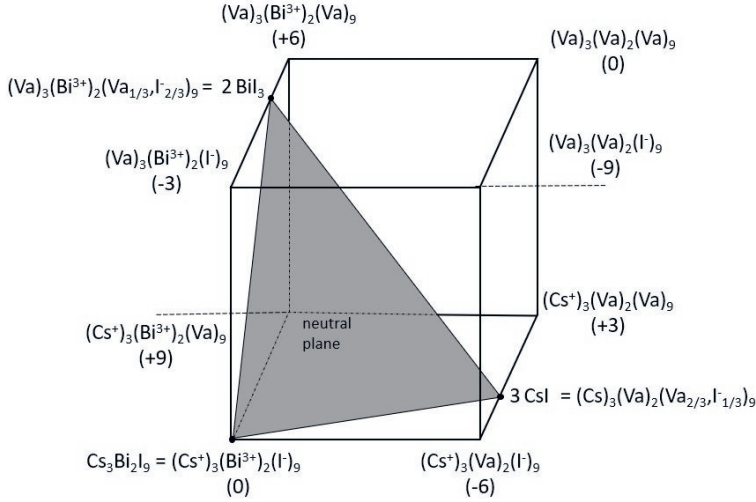


Figure C.4: Graphical representation of the  $(\text{Cs}^+, \text{Va})_3(\text{Bi}^{3+}, \text{Va})_2(\text{I}^-, \text{Va})_9$  sublattice model in the compound energy formalism. The neutral plane is the plane along which the homogeneity range around  $\text{Cs}_3\text{Bi}_2\text{I}_9$  is constructed.

energy term as recommended by Lukas, Fries and Sundman [1].

$${}^oG_{(\text{Cs}^+)_1(\text{Va})_2} = {}^oG_{\text{CsI}} - {}^oG_I^{\text{SER}} - 2RT\left(\frac{1}{2}\ln\frac{1}{2} + \frac{1}{2}\ln\frac{1}{2}\right) \quad (\text{C.18})$$

$${}^oG_{(\text{Cs}^+)_1(\text{I}^-)_2} = {}^oG_{\text{CsI}} + {}^oG_I^{\text{SER}} - 2RT\left(\frac{1}{2}\ln\frac{1}{2} + \frac{1}{2}\ln\frac{1}{2}\right) \quad (\text{C.19})$$

$${}^oG_{(\text{Pb}^{2+})_1(\text{Va})_2} = {}^oG_{\text{PbI}_2} - 2 \cdot {}^oG_I^{\text{SER}} \quad (\text{C.20})$$

$${}^oG_{(\text{Bi}^{3+})_1(\text{Va})_2} = {}^oG_{\text{BiI}_3} - 3 \cdot {}^oG_I^{\text{SER}} - 50000 - RT(\ln 2 - \frac{3}{2}\ln 3) \quad (\text{C.21})$$

$${}^oG_{(\text{Va})_1(\text{Va})_2} = 100000 \quad (\text{C.22})$$

### MODELLING THE $\text{Cs}_3\text{Bi}_2\text{I}_9$ HOMOGENEITY RANGE IN THE CEF FORMALISM

In the system  $\text{CsI-BiI}_3$ , the intermediate  $\text{Cs}_3\text{Bi}_2\text{I}_9$  exhibits a homogeneity range spanning several mole percent. In order to model this in the CEF, an expression for this intermediate compound is used with three sublattices:  $(\text{Cs}^+, \text{Va})_3(\text{Bi}^{3+}, \text{Va})_2(\text{I}^-, \text{Va})_9$ . A graphical representation of this model is given in Figure C.4.

The Gibbs energy of the homogeneity range of  $\text{Cs}_3\text{Bi}_2\text{I}_9$  is defined in Eq. C.23, with the term  $G^{\text{excess}}$  as defined in Eq. C.24 and the individual Gibbs energy terms for each end-member defined in Eqs C.25-C.32. The end-member consisting exclusively of vacancies, Eq. C.32, has been destabilized using a large positive excess energy term as recommended by Lukas, Fries and Sundman [1]. The values for the  ${}^oL$  and  ${}^1L$  parameters

used in Eq. C.24 are given in Table C.2.

$$\begin{aligned}
 G - \sum n_i^0 H_i^{SER}(298.15K) = & y_{Cs^+} y_{Bi^{3+}} y_{I^-} \cdot {}^0G_{(Cs^+)_3(Bi^{3+})_2(I^-)_9} + y_{Cs^+} y_{Bi^{3+}} y_{Va} \cdot {}^0G_{(Cs^+)_3(Bi^{3+})_2(Va)_9} \\
 & + y_{Cs^+} y_{Va} y_{I^-} \cdot {}^0G_{(Cs^+)_3(Va)_2(I^-)_9} + y_{Cs^+} y_{Va} y_{Va} \cdot {}^0G_{(Cs^+)_3(Va)_2(Va)_9} \\
 & + y_{Va} y_{Bi^{3+}} y_{I^-} \cdot {}^0G_{(Va)_3(Bi^{3+})_2(I^-)_9} + y_{Va} y_{Bi^{3+}} y_{Va} \cdot {}^0G_{(Va)_3(Bi^{3+})_2(Va)_9} \\
 & + y_{Va} y_{Va} y_{I^-} \cdot {}^0G_{(Va)_3(Va)_2(I^-)_9} + y_{Va} y_{Va} y_{Va} \cdot {}^0G_{(Va)_3(Va)_2(Va)_9} \\
 & + 3RT(y_{Cs^+} \ln y_{Cs^+} + y_{Va} \ln y_{Va}) + 2RT(y_{Bi^{3+}} \ln y_{Bi^{3+}} + y_{Va} \ln y_{Va}) \\
 & + 9RT(y_{I^-} \ln y_{I^-} + y_{Va} \ln y_{Va}) + G^{\text{excess}}
 \end{aligned} \tag{C.23}$$

$$\begin{aligned}
 G^{\text{excess}} = & y_{I^-} y_{Va} ({}^0L_{(Cs^+)_3(Va)_2(I^-,Va)_9} + {}^1L_{(Cs^+)_3(Va)_2(I^-,Va)_9} (y_{I^-} - y_{Va})) \\
 & + y_{I^-} y_{Va} ({}^0L_{(Va)_3(Bi^{3+})_2(I^-,Va)_9} + {}^1L_{(Va)_3(Bi^{3+})_2(I^-,Va)_9} (y_{I^-} - y_{Va}))
 \end{aligned} \tag{C.24}$$

$$\begin{aligned}
 & + y_{I^-} y_{Va} ({}^0L_{(Cs^+)_3(Bi^{3+})_2(I^-,Va)_9} + y_{Bi^{3+}} y_{Va} {}^0L_{(Cs^+)_3(Bi^{3+},Va)_2(I^-)_9} \\
 & \quad {}^0G_{(Cs^+)_3(Bi^{3+})_2(I^-)_9} = {}^0G_{Cs_3Bi_2I_9}
 \end{aligned} \tag{C.25}$$

$${}^0G_{(Cs^+)_3(Bi^{3+})_2(Va)_9} = {}^0G_{Cs_3Bi_2I_9} - 9 \cdot {}^0G_I^{SER} \tag{C.26}$$

$${}^0G_{(Cs^+)_3(Va)_2(I^-)_9} = 3 \cdot {}^0G_{CsI} + 6 \cdot {}^0G_I^{SER} - 3RT(2 \ln 2 - 3 \ln 3) \tag{C.27}$$

$${}^0G_{(Cs^+)_3(Va)_2(Va)_9} = 3 \cdot {}^0G_{CsI} - 3 \cdot {}^0G_I^{SER} - 3RT(2 \ln 2 - 3 \ln 3) \tag{C.28}$$

$${}^0G_{(Va)_3(Bi^{3+})_2(I^-)_9} = 2 \cdot {}^0G_{BiI_3} + 3 \cdot {}^0G_I^{SER} - 3RT(2 \ln 2 - 3 \ln 3) \tag{C.29}$$

$${}^0G_{(Va)_3(Bi^{3+})_2(Va)_9} = 2 \cdot {}^0G_{BiI_3} - 6 \cdot {}^0G_I^{SER} - 3RT(2 \ln 2 - 3 \ln 3) \tag{C.30}$$

$${}^0G_{(Va)_3(Va)_2(I^-)_9} = 9 \cdot {}^0G_I^{SER} + {}^0G_{(Va)_3(Va)_2(Va)_9} \tag{C.31}$$

$${}^0G_{(Va)_3(Va)_2(Va)_9} = 100000 \tag{C.32}$$

Phase	Gibbs energy (J·mol <sup>-1</sup> )	Source	
Solid solution	${}^0G_{(\text{Bi}^{3+})_1(\Gamma)_2} - 2 \cdot {}^0H_I^{SER} - {}^0H_{\text{Bi}}^{SER} = {}^0G_{\text{BiI}_3} - {}^0G_I^{SER} + 7.9384 \cdot T - 50,000$	*	
(Cs <sup>+</sup> , Pb <sup>2+</sup> , Bi <sup>3+</sup> , Va) <sub>1</sub> (Γ, Va) <sub>2</sub>	${}^0G_{(\text{Bi}^{3+})_1(\text{Va})_2} - {}^0H_{\text{Bi}}^{SER} = {}^0G_{\text{BiI}_3} - 3 \cdot {}^0G_I^{SER} + 7.9384 \cdot T - 50,000$	*	
	${}^0G_{(\text{Pb}^{2+})_1(\Gamma)_2} - 2 \cdot {}^0H_I^{SER} - {}^0H_{\text{Pb}}^{SER} = {}^0G_{\text{PbI}_2}$	*	
	${}^0G_{(\text{Pb}^{2+})_1(\text{Va})_2} - {}^0H_{\text{Pb}}^{SER} = {}^0G_{\text{PbI}_2} - 2 \cdot {}^0G_I^{SER}$	*	
	${}^0G_{(\text{Cs}^+)_1(\text{Va})_2} - 3 \cdot {}^0H_{\text{Cs}}^{SER} = {}^0G_{\text{CsI}} - {}^0G_I^{SER} + 11.5263 \cdot T$	*	
	${}^0G_{(\text{Cs}^+)_1(\Gamma)_2} - 2 \cdot {}^0H_I^{SER} - {}^0H_{\text{Cs}}^{SER} = {}^0G_{\text{CsI}} + {}^0G_I^{SER} + 11.5263 \cdot T$	*	
	${}^0G_{(\text{Va})_1(\Gamma)_2} - 2 \cdot {}^0H_I^{SER} = 2 \cdot {}^0G_I^{SER} + \mathbf{100,000}$	*	
	${}^0G_{(\text{Va})_1(\text{Va})_2} = \mathbf{100,000}$	*	
	${}^0L_{(\text{Pb}^{2+}, \text{Bi}^{3+})_1(\Gamma)_2} = \mathbf{2,500}$	*	
	${}^0L_{(\text{Pb}^{2+}, \text{Va})_1(\Gamma)_2} = \mathbf{-3,000}$	*	
	${}^0L_{(\text{Bi}^{3+}, \text{Cs}^+)_1(\Gamma)_2} = \mathbf{100,000}$	*	
	${}^0L_{(\text{Cs}^+, \text{Pb}^{2+})_1(\Gamma)_2} = \mathbf{60,000}$	*	
	${}^0L_{(\text{Cs}^+, \text{Pb}^{2+})_1(\text{Va})_2} = \mathbf{60,000}$	*	
	Homogeneity range (Cs <sup>+</sup> , Va) <sub>3</sub> (Bi <sup>3+</sup> , Va) <sub>2</sub> (Γ, Va) <sub>9</sub>	${}^0G_{(\text{Cs}^+)_3(\text{Bi}^{3+})_2(\Gamma)_9} - 3 \cdot {}^0H_{\text{Cs}}^{SER} - 2 \cdot {}^0H_{\text{Bi}}^{SER} - 9 \cdot {}^0H_I^{SER} = {}^0G_{\text{Cs}_3\text{Bi}_2\text{I}_9}$	*
		${}^0G_{(\text{Cs}^+)_3(\text{Bi}^{3+})_2(\text{Va})_9} - 3 \cdot {}^0H_{\text{Cs}}^{SER} - 2 \cdot {}^0H_{\text{Bi}}^{SER} = {}^0G_{\text{Cs}_3\text{Bi}_2\text{I}_9} - 9 \cdot {}^0G_I^{SER}$	*
		${}^0G_{(\text{Cs}^+)_3(\text{Va})_2(\Gamma)_9} - 3 \cdot {}^0H_{\text{Cs}}^{SER} - 9 \cdot {}^0H_I^{SER} = 3 \cdot {}^0G_{\text{CsI}} + 6 \cdot {}^0G_I^{SER} + 47.6278 \cdot T$	*
		${}^0G_{(\text{Cs}^+)_3(\text{Va})_2(\text{Va})_9} - 3 \cdot {}^0H_{\text{Cs}}^{SER} = 3 \cdot {}^0G_{\text{CsI}} - 3 \cdot {}^0G_I^{SER} + 47.6278 \cdot T$	*
${}^0G_{(\text{Va})_3(\text{Bi}^{3+})_2(\Gamma)_9} - 2 \cdot {}^0H_{\text{Bi}}^{SER} - 9 \cdot {}^0H_I^{SER} = 2 \cdot {}^0G_{\text{BiI}_3} + 3 \cdot {}^0G_I^{SER} + 47.6278 \cdot T$		*	
${}^0G_{(\text{Va})_3(\text{Bi}^{3+})_2(\text{Va})_9} - 2 \cdot {}^0H_{\text{Bi}}^{SER} = 2 \cdot {}^0G_{\text{BiI}_3} - 6 \cdot {}^0G_I^{SER} + 47.6278 \cdot T$		*	
${}^0G_{(\text{Va})_3(\text{Va})_2(\Gamma)_9} - 9 \cdot {}^0H_I^{SER} = 9 \cdot {}^0G_I^{SER} + {}^0G_{(\text{Va})_3(\text{Va})_2(\text{Va})_9}$		*	
${}^0G_{(\text{Va})_3(\text{Va})_2(\text{Va})_9} = \mathbf{100,000}$		*	
${}^0L_{(\text{Cs}^+)_3(\text{Va})_2(\Gamma, \text{Va})_9} = \mathbf{200,000}$		*	
${}^1L_{(\text{Cs}^+)_3(\text{Va})_2(\Gamma, \text{Va})_9} = \mathbf{120,000}$		*	
${}^0L_{(\text{Va})_3(\text{Bi}^{3+})_2(\Gamma, \text{Va})_9} = \mathbf{100,000}$		*	
${}^1L_{(\text{Va})_3(\text{Bi}^{3+})_2(\Gamma, \text{Va})_9} = \mathbf{150,000}$		*	
${}^0L_{(\text{Cs}^+, \text{Va})_3(\text{Bi}^{3+})_2(\Gamma)_9} = \mathbf{70,000}$		*	
${}^0L_{(\text{Cs}^+)_3(\text{Bi}^{3+}, \text{Va})_2(\Gamma)_9} = \mathbf{110,000}$		*	
Functions		${}^0G_I^{SER} = 100565.721 - 41.4565742 \cdot T - 20.78611 \cdot T \cdot \ln T \quad (298 < T < 900 \text{ K})$	[6]
		${}^0G_I^{SER} = 100490.766 - 39.9796783 \cdot T - 21.02293 \cdot T \cdot \ln T - 0.0002889215 \cdot T^2 - 5.92257 \cdot 10^{-8} \cdot T^3 + 4271.7805 \cdot T^{-1} \quad (900 < T < 2400 \text{ K})$	[6]
	${}^0G_{\text{BiI}_3} = -157970.93 + 65.731 \cdot T - 40.95 \cdot T \cdot \ln T - 0.0543366 \cdot T^2 + 5.865 \cdot 10^{-9} \cdot T^3 - 1444860 \cdot T^{-1} \quad (298 < T < 681.8 \text{ K})$	[7, 8]	
	${}^0G_{\text{PbI}_2} = -208180.225 + 565.688 \cdot T - 114.6362 \cdot T \ln T + 0.06491 \cdot T^2 - 2.2958 \cdot 10^{-5} \cdot T^3 + 471266.95 \cdot T^{-1} \quad (298 < T < 683 \text{ K})$	[6]	
	${}^0G_{\text{CsI}} = -361484.671 + 176.752 \cdot T - 43.815 \cdot T \ln T - 0.0109211 \cdot T^2 - 4.15961 \cdot 10^{-7} \cdot T^3 - 100123.85 \cdot T^{-1} \quad (298 < T < 905 \text{ K})$	[9]	
	${}^0G_{\delta\text{-CsPbI}_3} = -589169.342 + 744.645685 \cdot T - 158.4512 \cdot T \ln T + 0.05399 \cdot T^2 - 2.3333 \cdot 10^{-5} \cdot T^3 + 371143 \cdot T^{-1} \quad (298 < T < 681.8 \text{ K})$	*	
	${}^0G_{\alpha\text{-CsPbI}_3} = -574969.342 + 720.739961 \cdot T - 158.4512 \cdot T \ln T + 0.05399 \cdot T^2 - 2.3333 \cdot 10^{-5} \cdot T^3 + 371143 \cdot T^{-1} \quad (298 < T < 594 \text{ K})$	*	
	${}^0G_{\text{Cs}_4\text{PbI}_6} = -1684327.59 + 1278.02264 \cdot T - 289.8962 \cdot T \ln T + 0.02123 \cdot T^2 - 2.4666 \cdot 10^{-5} \cdot T^3 + 70771.5 \cdot T^{-1} \quad (594 < T < 770 \text{ K})$	*	
	${}^0G_{\text{Cs}_3\text{Bi}_2\text{I}_9} = -1552006.97 + 678.544824 \cdot T - 211.365 \cdot T \ln T - 0.142803 \cdot T^2 - 0.124833 \cdot 10^{-5} \cdot T^3 - 300374.5 \cdot T^{-1} \quad (298 < T < 872 \text{ K})$	*	

Table C.2: Summary of the thermodynamic data used in the present work to model the solid phases of the CsI-PbI<sub>2</sub>-BiI<sub>3</sub> system. SER refers to the phase of the element stable at 298.15 K. The optimised values are marked in bold. \* = This work.

# BIBLIOGRAPHY

- (1) Lukas, H. L.; Fries, S. G.; Sundman, B., *Computational Thermodynamics: the Calphad method*; Cambridge University Press: 2007; Vol. 131.
- (2) Centre for Research in Computational Thermochemistry FactSage 8.2, Date of last access: June 9, 2023, 20222.
- (3) Pelton, A. D.; Chartrand, P.; Eriksson, G. *Metallurgical and Materials Transactions A* **2001**, 32, 1409–1416.
- (4) Pelton, A. D. *Calphad* **2001**, 25, 319–328.
- (5) Alexander, G. C. B. Exploratory synthesis and characterization of heavy metal halide semiconductors: unveiling new properties and structures, Ph.D. Thesis, Northwestern University, 2020.
- (6) Chase, M. W.; National Information Standards Organization, U. S., *NIST-JANAF thermochemical tables*; American Chemical Society Washington, DC: 1998; Vol. 9.
- (7) Cubicciotti, D. *Inorganic Chemistry* **1968**, 7, 211–213.
- (8) Barin, I.; Knacke, O.; Kubaschewski, O. In *Thermochemical properties of inorganic substances*; Springer: 1977, pp 1–861.
- (9) Capelli, E.; Beneš, O.; Konings, R. J. M. *Journal of Nuclear Materials* **2018**, 501, 238–252.



# D

## SUPPORTING INFORMATION TO BAO-DEFICIENT $\text{Ba}_3\text{PuO}_6$

### $\text{PuO}_2$ PREPARATION

Nanopowder  $\text{PuO}_2$  was obtained by thermal decomposition of Pu-oxalate at 873 K in air, yielding a product with  $a = 5.400(3)$  Å cell parameter and a particle size of  $20 \pm 3$  nm based on XRD measurements. The isotopic ratio is 92.49% Pu-239, 7.08% Pu-240, 0.395% Pu-241 and 0.03% Pu-242 as determined by ICP-MS. The stock was virtually free of Am.

### X-RAY DIFFRACTION

Remark on the remaining CheckCif alerts: As explained in the main text, owing to the measurement conditions and extreme Z contrast, the structural analysis did not aim at localizing the oxygen atoms, which were fixed on ideal positions. This is necessary, although this simplification contributes to reducing the accuracy of the cations array, in particular concerning the atomic displacement parameters, of which some of them are negative, or exceedingly high.

### THERMOGRAVIC-DIFFERENTIAL THERMAL ANALYSIS

After an initial buoyancy effect, there is no mass loss till 1050 K. The curve shows a mass loss starting with a simultaneous peak in the heat flow at 1080 K. The mass loss due to  $\text{CO}_2$  equals 15.3 %, while the mass gain of 0.5  $\text{O}_2$  towards full  $\text{Ba}_3\text{PuO}_6$  from air is 1.8 %. This means a total mass loss of about 13.5 % is expected. Above 1650 K, the heat flow changes direction, accompanied by a small decrease in the mass curve. On cooling, no effects on both the heat flow and the mass curve are visible. To account for the deficiency of 0.125 BaO in the synthesised material compared to  $\text{Ba}_3\text{PuO}_6$ , an additional 2.5 % loss was expected. The TG-DTA did not show such a loss.

An XRD pattern after the thermal analysis was measured. The obtained material seems to have a rather high symmetry, but is not the same as  $\text{Ba}_{2.875}\text{PuO}_{5.875}$ , nor can

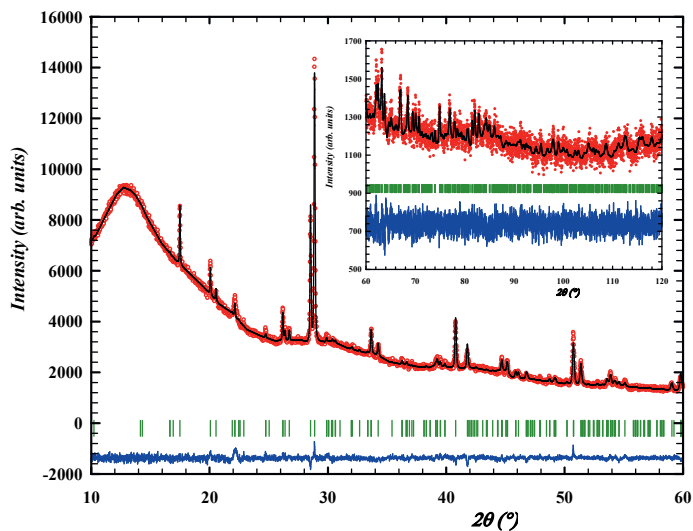


Figure D.1: Experimental ( $Y_{obs}$ , in red) and calculated ( $Y_{calc}$ , in black) powder XRD patterns of  $\text{Ba}_{2.875}\text{PuO}_{5.875}$  from synthesis 1 after 1270 K at ambient temperature. The difference between the calculated and the experimental intensities  $Y_{obs} - Y_{calc}$  is shown in blue. The angular positions of the Bragg reflections are shown in green. Measurement at  $\lambda = \text{Cu K}\alpha$ . Rietveld refinement in space group  $I4/m$ .

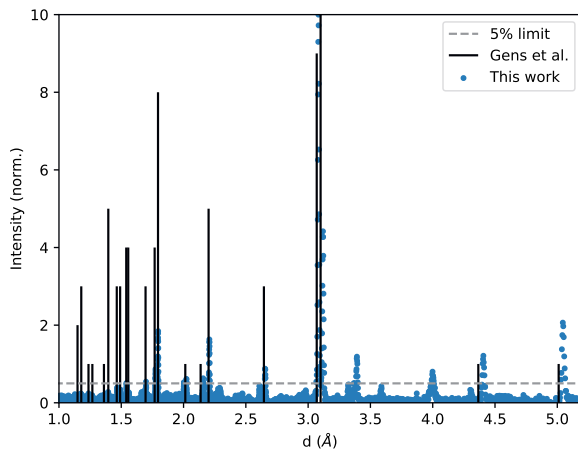


Figure D.2: Comparison of the diffraction pattern of  $\text{Ba}_{2.875}\text{PuO}_{5.875}$  obtained in this work compared with the diffraction lines reported by Gens *et al.* [1]. The background is subtracted for easier comparison.

be matched with the pattern obtained at 1473 K in the high-temperature XRD measurements. A Rietveld refinement with  $\text{Ba}_3\text{PuO}_6$  (space group 225 [2]) and  $\text{BaPuO}_3$  has been made, which yields 96.6 mass-%  $\text{Ba}_3\text{PuO}_6$  and 3.4 mass-%  $\text{BaPuO}_3$ , although a minor presence of  $\text{PuO}_2$  can be seen as well. Although the maximum temperature reached in the DTA experiment was substantially higher than in the synthesis, the heating rate was much faster. Thus, the kinetics to a Ba:Pu ratio of 2.875:1 may not have been achieved.

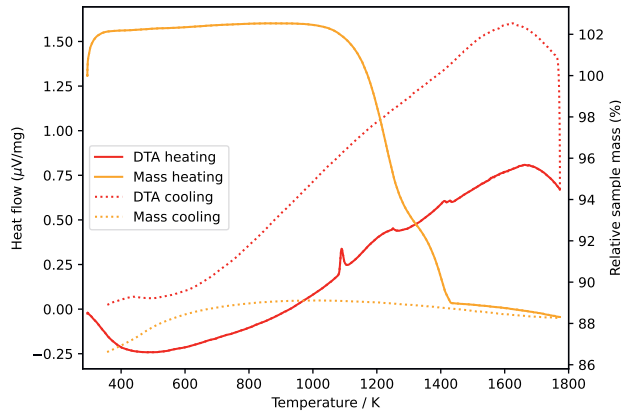


Figure D.3: Thermogravimetric-Differential Thermal Analysis of the mixture of  $3 \text{BaCO}_3 + \text{PuO}_2$  in air.

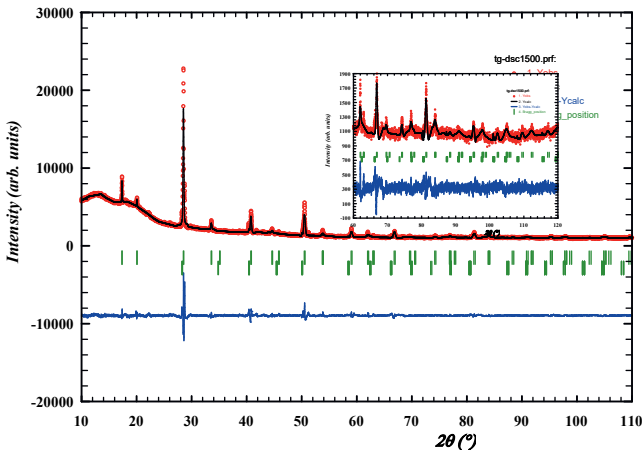


Figure D.4: Experimental powder XRD patterns of the post-TG-DTA sample at ambient temperature. Measurement at  $\lambda = \text{Cu K}\alpha$ .

## LANDAU MODEL FOR THERMAL EXPANSION

The distortion of the  $c$ -axis from a straight chain model was quantified by extrapolating the high-temperature trend in the  $c$ -axis and calculating  $c_{\text{linear}} - c_{\text{real}}$ . A Landau model should be proportional to  $(T_c - T)^{1/2}$ .  $T_c$  was optimised to the data points about 200 degrees below the transition, yielding  $T_c = 758$  K.

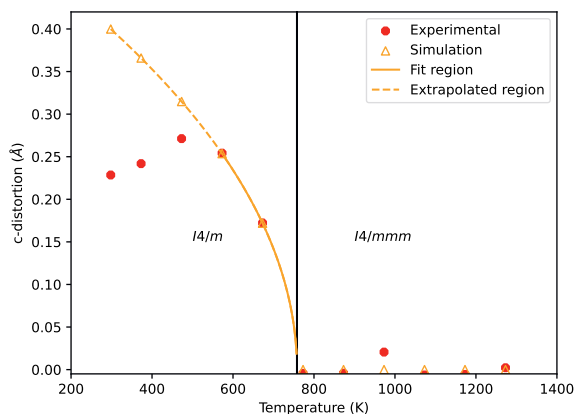


Figure D.5: Tentative Landau model for the antiferrodistorsive transition in  $\text{Ba}_{2.875}\text{PuO}_{5.875}$  with  $T_c = 758$  K.

## COMPARISON LOW-TEMPERATURE HEAT CAPACITY DATA

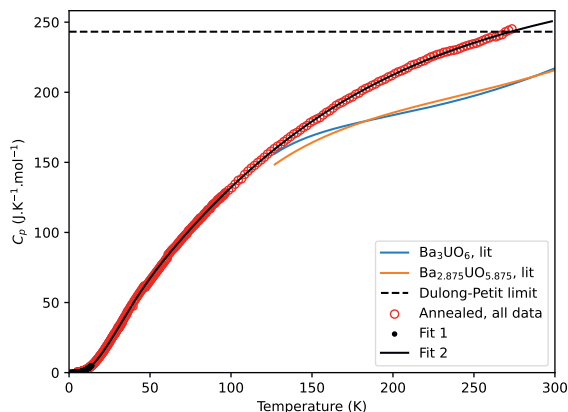


Figure D.6: Comparison of the low-temperature heat capacity data reported for  $\text{Ba}_3\text{UO}_6$  and  $\text{Ba}_{2.875}\text{UO}_{5.875}$  using DSC [3] with the data obtained in this work.

# BIBLIOGRAPHY

- (1) Gens, R.; Fuger, J.; Morss, L. R.; Williams, C. W. *Journal of Chemical Thermodynamics* **1985**, *17*, 561–573.
- (2) Keller, C. *Nukleonik* **1962**, *4*, 271–277.
- (3) Dash, S.; Singh, Z. *Journal of Nuclear Materials* **2010**, *404*, 9–18.



# CURRICULUM VITÆ- NL

## **Andries VAN HATTEM**

08-10-1996 Geboren in Doornspijk, Nederland.

### OPLEIDING

- 2021–2025 Promovendus  
Technische Universiteit Delft, Delft  
Verschillende onderzoeksstages bij het Joint Research Centre van de Europese Commissie in Karlsruhe
- 2017–2019 Master of Science  
Chemische wetenschappen  
Programma Nanomaterials Science  
Universiteit Utrecht, Utrecht
- 2014–2017 Bachelor of Science  
Scheikunde  
Universiteit Utrecht, Utrecht
- 2008–2014 VWO / Gymnasium  
Pieter Zandt scholengemeenschap, Kampen

### WERKERVARING

- 2025–(heden) Post-doctoraal onderzoeker  
Technische Universiteit Delft
- 2019–2021 Docent en toa  
Pieter Zandt scholengemeenschap, Kampen
- 2018–2021 Practicumbegeleider  
Universiteit Utrecht, Utrecht

## WETENSCHAPPELIJKE PRESENTATIES

2024-12	Chains conference, Veldhoven (presentatie)
2024-09	Plutonium Futures, Charleston (presentatie)
2024-04	Journées des Actinides, Lille (presentatie)
2023-11	NuFuel, Marseille (poster)
2023-08	IUPAC-Chains conference, Den Haag (poster)
2023-04	Journées des Actinides, Dresden (poster, prijs voor beste poster)
2022-10	NuMat, Gent (presentatie)
2021-09	NuFuel (poster, online)

# CURRICULUM VITÆ- EN

## **Andries VAN HATTEM**

08-10-1996            Born in Doornspijk, The Netherlands.

### EDUCATION

2021–2025            PhD-candidate  
Delft University of Technology, Delft  
Several research internships at the Joint Research Centre  
of the European Commission in Karlsruhe

2017–2019            Master of Science  
Chemical Sciences  
Program Nanomaterials Science  
Utrecht University, Utrecht

2014–2017            Bachelor of Science  
Chemical Sciences  
Utrecht University, Utrecht

2008–2014            Pre-university education / grammar school  
Pieter Zandt scholengemeenschap, Kampen

### WORK EXPERIENCE

2025–(current)        Post-doctoral researcher  
Delft University of Technology, Delft

2019–2021            Teacher and technical teaching assistant  
Pieter Zandt scholengemeenschap, Kampen

2018–2021            Teaching Assistant  
Utrecht University, Utrecht

## SCIENTIFIC PRESENTATIONS

- 2024-12 Chains conference, Veldhoven (oral presentation)
- 2024-09 Plutonium Futures, Charleston (oral presentation)
- 2024-04 Journées des Actinides, Lille (oral presentation)
- 2023-11 NuFuel, Marseille (poster presentation)
- 2023-08 IUPAC-Chains conference, The Hague (poster presentation)
- 2023-04 Journées des Actinides, Dresden (poster presentation, best poster prize)
- 2022-10 NuMat, Ghent (oral presentation)
- 2021-09 NuFuel (poster presentation, online)

# LIST OF PUBLICATIONS

10. **A. van Hattem**, G. Wallez, N.T.H. ter Veer, I. Dhiman, K. Dardenne, J. Rothe, R.J.M. Konings, A.L. Smith *Crystallographic Study into the Antiferroelectricity Mechanism in CsBi(MoO<sub>4</sub>)<sub>2</sub>* (submitted).
9. R. Zaier, **A. van Hattem**, B.N. de Waal, R.J.M. Konings, A.L. Smith, P. Zeller, C. Guéneau, *A Thermodynamic Model of the Cs-Pb System* (submitted).
8. **A. van Hattem**, J. Vlieland, E. Colineau, J-C. Griveau, R.J.M. Konings and A.L. Smith *Thermodynamic Study of  $\alpha$ -Cs<sub>2</sub>Pb(MoO<sub>4</sub>)<sub>2</sub> and Safety Assessment of the Pb-JOG Interaction in Lead-cooled Fast Reactors* (under review).
7. **A. van Hattem**, K. Popa, G. Wallez, J. Boshoven, E. Colineau, E. Dahms, J-C. Griveau, H. Hein, O. Walter, B. Schacherl, T. Vitova, K. Dardenne, T. Pruessmann, J. Rothe, A.L. Smith, and R.J.M. Konings *Structural and Physical Investigation of Ordered BaO-deficient Ba<sub>3</sub>PuO<sub>6</sub>*, *Communications Chemistry* **8** (2025): 270.
6. **A. van Hattem**, L.M.T. de Geus, A. Sacristán, R. Dankelman, S.D. Couweleers, C. Hennig, J-C. Griveau, E. Colineau, K. Dardenne, J. Rothe, T. Pruessmann, R.J.M. Konings and A.L. Smith *Elucidation of the Off-Center Displaced Mo in Octahedral Coordination in Ba<sub>2</sub>MoO<sub>5</sub>*, *Inorganic Chemistry* **64**, 1 (2025): 674-681.
5. J.J. van Blaaderen, **A. van Hattem**, J.T. Mulder, D. Biner, K. Krämer and P. Dorenbos, *Photoluminescence and Scintillation Mechanism of Cs<sub>4</sub>PbBr<sub>6</sub>*, *The Journal of Physical Chemistry C* **128**, 46 (2024): 19921-19932.
4. **A. van Hattem**, R. Dankelman, E. Colineau, J-C. Griveau, K. Dardenne, J. Röthe, S.D. Couweleers, R.J.M. Konings and A.L. Smith, *Experimental investigations and thermodynamic modelling of the ternary system Pb-Mo-O*, *Journal of Alloys and Compounds* **1003** (2024): 175588 .
3. **A. van Hattem**, J-C. Griveau, E. Colineau, A.J.E. Lefering, R.J.M. Konings and A.L. Smith, *Low-Temperature Heat Capacity of CsPbI<sub>3</sub>, Cs<sub>4</sub>PbI<sub>6</sub>, and Cs<sub>3</sub>Bi<sub>2</sub>I<sub>9</sub>*, *The Journal of Physical Chemistry C* **127**, 46 (2023): 22808-22816.
2. **A. van Hattem**, D. Alders, R.J.M. Konings and A.L. Smith *Ternary System CsI-PbI<sub>2</sub>-BiI<sub>3</sub> and Thermodynamic Stability of Cesium Metal Halide Perovskites*, *The Journal of Physical Chemistry C* **127**, 35 (2023): 17482-17496.
1. **A. van Hattem**, J. Vlieland, R. Dankelman, M. Thijs, G. Wallez, K. Dardenne, J. Röthe, R.J.M. Konings and A.L. Smith, *Structural Studies and Thermal Analysis in the Cs<sub>2</sub>MoO<sub>4</sub>-PbMoO<sub>4</sub> System with Elucidation of  $\beta$ -Cs<sub>2</sub>Pb(MoO<sub>4</sub>)<sub>2</sub>*, *Inorganic Chemistry* **62**, 18 (2023): 6981-6992.





